# CHARACTERIZATION OF ALKALI ION BATTERY MATERIALS BY NMR

# CHARACTERIZATION OF CATHODE MATERIALS FOR ALKALI ION BATTERIES BY SOLID-STATE NUCLEAR MAGNETIC RESONANCE METHODS

BY DANIELLE L. SMILEY, B.SC.

A Thesis Submitted to the School of Graduate Studies in Partial Fulfillment of the Requirements for the Degree Doctor of Philosophy

McMaster University DOCTOR OF PHILOSOPHY (2018) Hamilton, Ontario
(Chemistry)

TITLE: Characterization of Cathode Materials for Alkali Ion Batteries by Solid-State Nuclear Magnetic Resonance Methods

AUTHOR: Danielle L. Smiley, B.Sc. (McMaster University)

SUPERVISOR: Professor Gillian R. Goward

NUMBER OF PAGES: xxvii, 253

# Lay Abstract

Lithium ion batteries are considered to be at the forefront of current energy storage development, offering high energy density in a small and lightweight package. This thesis delineates the investigation of materials for both lithium and sodium ion batteries via nuclear magnetic resonance methods. Slow Li ion dynamics were investigated and quantified in three lithium-conducting materials: $Li_2MnP_2O_7$, $Li_2SnO_3$, and $LiFeV_2O_7$ via the use of selective inversion NMR experiments. In the case of the latter, the ion dynamics were probed *ex situ* during the course of battery cycling, where a maximum in Li mobility is observed approximately half way through the charge-discharge cycle. Additionally, a potential Na ion cathode material, $Na_2FePO_4F$, was found by *ex situ* methods to reveal a biphasic mechanism for the desodiation of the electrode during charging. This mechanism and the NMR data used to discover it were further supported by *ab initio* calculations.

# Abstract

This thesis concerns the use of advanced solid-state NMR methods to investigate local structural features and ion dynamics in a series of paramagnetic cathode materials for lithium and sodium ion batteries. A variety of polyanionic phosphate and fluorophosphate derivatives were explored to identify characteristics that ultimately improve battery performance. Solid-state NMR is an excellent method to probe such materials, as it offers the unique ability to track the charge-carrying alkali ion (Li or Na) over the course of the electrochemical process, adding insight not obtainable by bulk characterization techniques. Selective inversion exchange experiments were used to elucidate ion diffusion pathways in low-mobility Li ion conductors $Li_2MnP_2O_7$ and $Li_2SnO_3$. Contrasting experimental results highlight significant differences observed when the method is applied to paramagnetic versus diamagnetic systems, with the former being much more complicated to study with traditional exchange spectroscopy methods. Selective inversion was similarly applied to a new lithium iron vanadate framework, $LiFeV_2O_7$, where the changing ion dynamics as a function of electrochemical state of charge were quantified, allowing for the development of a model to explain the corresponding phase changes in the material. This represents the first example of an *ex situ* Li-Li exchange study for a cathode material, particularly where the conductivity changes are linked directly to a change of ion exchange rates. Additionally, $^{23}$Na NMR spectroscopy was additionally used to investigate $Na_2FePO_4F$ as a potential Na ion battery cathode, where *ex situ* NMR measurements successfully determined the local Na ion distribution in the electrode as a function of electrochemical cycling. In combination with density functional theory (DFT) calculations, the NMR results lead to the construction of a biphasic desodiation model for $Na_2FePO_4F$ cathodes. Finally, possible defect formation in sodium iron fluorophosphate was investigated with a variety of methods including $^{23}$Na NMR, DFT calculations, powder X-ray diffraction and Mössbauer spectroscopy.

# Acknowledgements

First and foremost, I wish to thank my supervisor, Prof. Gillian Goward, for her mentorship, patience, and encouragement throughout both my undergraduate and graduate degrees. Not only has she taught me how to be a scientist, but she has also exemplified what it means to be successful both in career and in life. Her kindness throughout this process has made all the difference in this experience for me, and I will be forever grateful. I would also like to thank Prof. Yurij Mozharivskyj for his support both as a committee member and as a teacher. Thank you to Prof. Darren Brouwer not only for his involvement in my committee towards the end of my degree, but also for his guidance as a talented NMR spectroscopist throughout the last 6 years. A very special thank you goes to Prof. Alex Bain; the NMR world is not the same without you, and your passion for the field ignited in me the interest that has driven the bulk of this thesis. I wish to thank Prof. Dany Carlier for welcoming me in Bordeaux, and teaching me so much about NMR and DFT in such a short time. The example that you have set for me as a researcher will certainly impact me over the course of my career.

To my fellow Goward group members: it wasn't until the last few years that I realized it's true when people say you make lifelong friends in grad school. I couldn't have done this without all of you, and you've made my time here absolutely unforgettable. I must give a special thank you to Blossom Yan; not everyone gets to experience this with their best friend and I can't imagine not having you there with me. Thank you also to the NMR staff, Bob, Hilary, and Megan, as well as Jim Garrett for their endless assistance.

Thank you to my loving, supportive, amazing parents who I know would have supported me in whatever I chose to do. Also thank you to my siblings; you inspire me in many ways, and I couldn't be more thankful to have you. Finally, thank you to Nick Andreychuk for supporting me and talking me out of any and all rash decisions. Your love and encouragement have meant everything to me, and your passion for chemistry has been a constant source of inspiration. I don't know where life will take us next, but I can't wait to experience it together.

# Table of Contents

## Chapter 6: Structure and Dynamic Properties of $Na_2FePO_4F$ As Determined by $^{23}$Na Solid-State NMR ............................................................ 155

## Chapter 7: *Ab Initio* Calculations using Density Functional Theory to Investigate Layered $Na_2FePO_4F$ ..................................................................... 181

# List of Tables

# List of Figures

# List of Abbreviations and Symbols

| | |
|---|---|
| GHG | Greenhouse Gas |
| ICE | Internal Combustion Engine |
| V | Volt |
| LCO | Lithium Cobalt Oxide, $LiCoO_2$ |
| LFP | Lithium Iron Phosphate, $LiFePO_4$ |
| PHEV | Plug-in Hybrid Electric Vehicle |
| EV | Electric Vehicle |
| UPS | Uninterruptible Power Source |
| NMC | Nickel Manganese Cobalt Oxide, $LiNi_{0.33}Mn_{0.33}Co_{0.33}O_2$ |
| NCA | Nickel Cobalt Aluminum Oxide, $LiNi_{0.8}Co_{0.15}Al_{0.05}O_2$ |
| EC | Ethylene Carbonate |
| DMC | Dimethyl Carbonate |
| SEI | Solid-electrolyte Interface |
| LIB | Lithium Ion Battery |
| ZEBRA | Zeolite Battery Research Africa Project |
| TFSI | bis(tri-fluoromethanesulfonyl)imide |
| TM | Transition Metal |
| NMR | Nuclear Magnetic Resonance |

| | |
|---|---|
| ssNMR | Solid-state NMR |
| NIB | Sodium Ion Battery |
| DFT | Density Functional Theory |
| $\mu$ | Spin magnetic moment |
| $\gamma$ | Gyromagnetic Ratio |
| I | nuclear spin number |
| $\hbar$ | Reduced Planck’s constant |
| $B_0$ | External Magnetic Field |
| $\Delta E$ | Energy Difference |
| $k_B$ | Boltzmann’s Constant |
| $\omega_0$ | Larmor Frequency |
| RF | Radiofrequency |
| $\hat{H}$ | Hamiltonian |
| $I_z$ | Nuclear spin along z-axis |
| $\Omega$ | Frequency Precession in the Rotating Frame |
| $B_1$ | Magnetic Field Generated by the RF pulse |
| FID | Free Induction Decay |
| $T_1$ | Longitudinal Nuclear Relaxation (Spin-lattice Relaxation) |
| $T_2$ | Transverse Nuclear Relaxation (Spin-spin Relaxation) |

|  |  |
|---|---|
| $M_y^{nuc}$ | Magnetization of nuclei along the y-axis |
| $M_x^{nuc}$ | Magnetization of nuclei along the x-axis |
| CSA | Chemical Shift Anisotropy |
| MAS | Magic Angle Spinning |
| EFG | Electric Field Gradient |
| eQ | Quadrupole Moment |
| $C_Q$ | Quadrupole Coupling Constant |
| $\eta_Q$ | Asymmetry Parameter |
| $\nu$ | Frequency |
| $P_2,P_4$ | Legendre Polynomials |
| $\mu_e$ | Electron Magnetic Moment |
| $\mathbf{S}$ | Electron Spin Angular Momentum |
| $\mathbf{A}$ | Hyperfine Coupling Tensor |
| EPR | Electron Paramagnetic Resonance |
| $\chi_M$ | Magnetic Susceptibility |
| $\langle S_z \rangle$ | Time-averaged Electron Spin Density |
| $\sigma_{CS}$ | Chemical Shielding |
| $A_{FC}$ | Fermi Contact Hyperfine Interaction |
| $A_D$ | Dipolar Hyperfine Interaction |

| | |
|---|---|
| $\delta_{FC,iso}$ | Isotropic Fermi Contact Shift |
| $\rho_i$ | Spin Density at Nucleus |
| MQMAS | Multiple Quantum Magic Angle Spinning |
| FWHM | Full Width at Half Maximum |
| EXSY | Exchange Spectroscopy |
| NOESY | Nuclear Overhauser Effect Spectroscopy |
| 2D | Two-dimensional |
| SI | Selective Inversion |
| ΔS | Entropy Change |
| ΔH | Enthalpy Change |
| $t_{mix}$ | Mixing Time |
| $M_i(t)$ | Magnetization of site *i* at time t |
| $M_i(\infty)$ | Magnetization of site *i* at equilibrium |
| $R_i$ | Relaxation Time Constant for site *i* |
| $k_{ij}$ | Rate Constant for *i-j* Exchange |
| NSI | Non-selective Inversion |
| CIFIT | Selective Inversion Fitting Program |
| FC | Fermi Contact |
| LDA | Local Density Approximation |

|  |  |
|---|---|
| GGA | Generalized Gradient Approximation |
| PAW | Projector Augmented Wave |
| $V_{KS}(r)$ | Kohn-Sham Potential |
| $V_H(r)$ | Hartree Potential |
| $V_{xc}(r)$ | Exchange-Correlation Potential |
| VESTA | Visualization for Electronic and Structural Analysis |
| CASTEP | Cambridge Serial Total Energy Package |
| CB | Carbon Black |
| PVDF | Polyvinylidene Fluoride |
| NMP | N-Methyl Pyrrolidone |
| PITT | Potentiostatic Intermittent Titration Technique |
| PXRD | Powder X-ray Diffraction |
| eV | Electron Volt |
| SOLA | Solids Lineshape Analysis Tool |
| VASP | Vienna Ab-Initio Simulation Package |
| PBE | Perdew-Burke-Ernzerhof |
| SQUID | Superconducting Quantum Interference Device |
| DOS | Density of States |
| $\Delta G_{rxn}$ | Gibbs Free Energy Change |

| | |
|---|---|
| F | Faraday’s Constant |
| ppm | Parts per Million |
| C | Curie Constant |
| $\Theta_{CW}$ | Curie Temperature |
| $\Delta_f E$ | Formation Energy |
| NVPF | $Na_3V_2(PO_4)_2F_3$ |
| IS | Isomer Shift |
| QS | Quadrupole Shift |
| HMS | Hyperfine Magnetic Shift |

# Declaration of Academic Achievement

The study of Li ion dynamics in $Li_2MnP_2O_7$ was initiated by former student, X. He under the supervision of Prof. Gillian Goward. His initial efforts regarding the synthesis and selective inversion experiments guided the work presented herein on $Li_2MnP_2O_7$. In particular, X. He assigned the sites in the Li NMR spectrum to their corresponding crystallographic environments, the results of which are discussed in this thesis. Julia Langer, visiting student from Graz, provided the $Li_2SnO_3$ sample and worked in collaboration to perform the CIFIT analysis and obtain Li-Li hopping rates. Pristine samples of $LiFeV_2O_7$ were provided by Yasmine Benabed and Mickael Dollé (Université de Montréal). They additionally shared *ex situ* diffraction data for samples cycled in the Montréal lab. Prof Dany Carlier (Bordeaux) was instrumental in the design of the Density Functional Theory calculations performed at the Université de Bordeaux under her supervision. Alain Wattiaux and Mathieu Duttine carried out all Mössbauer measurements and subsequent spectral interpretation. Yurij Mozharivskyj performed the Rietveld refinement of the powder X-ray diffraction pattern for $Na_2FePO_4F$. All other results, experimental or computational, were obtained and interpreted by D.L. Smiley.

# Chapter 1: Introduction to Cathode Materials for Alkali Ion Batteries

## 1.1 History and Motivation

The combination of post-industrial revolution society and an ongoing technological revolution have created a larger-than-ever dichotomy between the lifestyles of the first and third worlds. Massive global population growth has only served to exacerbate the issue, with developed nations largely taking the ease of access to unlimited energy for granted. This contrast was precipitated in large part by the discovery of fossil fuels and their subsequent exploitation. The limited nature of these non-renewable natural resources make their global impact unsustainable, leading to the current global inequality experienced today.

In addition to societal factors, the current status of the earth's climate change issue necessitates a major shift away from the current energy construct. The pervasive use of fossil fuels to sustain the modern world has had a devastating irreversible environmental impact that requires mitigation before global warming renders sections of the earth completely uninhabitable.[1] Like many countries around the world, the Canadian government has in recent years vowed to implement economic measures to combat climate change via the use of methods such as carbon taxing or cap-and-trade programs in an effort to reduce the national carbon footprint and meet global emission reduction targets. Making up 23% of total national greenhouse gas (GHG) emissions, the transportation sector represents a large fraction of Canada's emissions with 170 megatons of $CO_2$ released in 2014.[2] A significant change in this sector in particular would therefore have a considerable impact on creating a sustainable future. The replacement of the internal combustion engine (ICE) in the automotive industry by an alternative energy storage medium could thus be one of the most significant advances toward decreased fossil fuel reliance.

Researchers have long been investigating alternative methods for energy storage with fuel cells and batteries being the most obvious frontrunners for portable applications such as transportation methods. Before the use of fossil fuels, lead acid and nickel-iron batteries were manufactured over a century ago due largely to significant interest from Thomas Edison and Henry Ford and their concerted effort to make automobiles commonplace.[3] Although now re-gaining popularity, electric vehicles in the interim fell out of use with the uprising of gasoline-powered automobiles and the internal combustion engine. The discovery and commercialization of the modern lithium ion battery (LIB) by Sony Corporation in 1991 was one of the most significant breakthroughs in the field, with the current battery construct very closely resembling that first iteration even to this day. Although the lithium ion battery conceptually predated this discovery, the inclusion of a carbonaceous anode material rather than dangerous lithium metal necessarily improved the stability of the battery, allowing it to be commercially viable.

Due to the relative practical ease of incorporating a battery on board a vehicle as an alternative to the ICE, lithium ion batteries have gained significant traction in both research and commercial markets as the most likely candidate for automotive applications. The prevalent use of the lithium ion battery is motivated by the high gravimetric and volumetric energy densities afforded by the lightweight Li materials relative to other battery substitutes as demonstrated in **Figure 1.1**. There has correspondingly been a massive research effort devoted to the continued study and development of materials for lithium ion batteries, with a focus on commercial viability for large-scale applications.

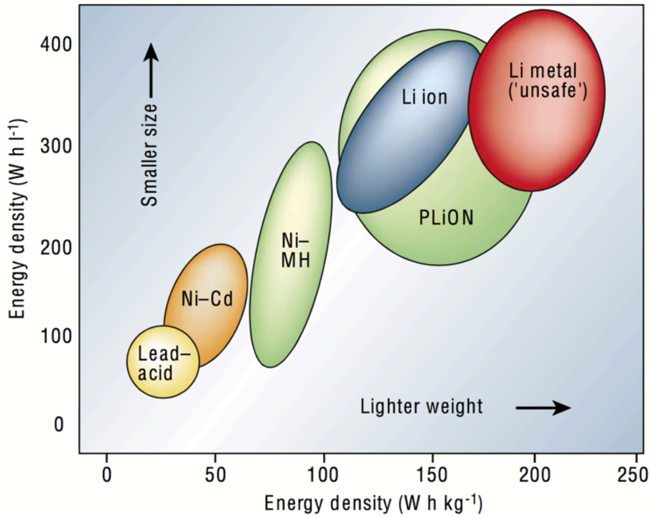

**Figure 1.1:** Comparison of gravimetric (Whkg$^{-1}$) and volumetric (Whl$^{-1}$) energy densities of various battery systems. Reprinted with permission from *Nature*, 'Issues and challenges facing rechargeable lithium batteries', Tarascon, J-M., and Armand, M., ©2001.

Despite the various advances made in battery technology since Edison and Ford's efforts in the early 1900s, many of the same challenges persist in 2018. Ford is quoted as saying "*The problem so far has been to build a storage battery of light weight which would operate for a long distance without recharging"* (Jan 11, 1914; ***New York Times***). While the state of the situation is vastly improved, as full-electric lithium-powered vehicles are manufactured by numerous automotive companies as of 2018, the current battery capacity limits still fall short of targets that aim to reduce the so-called ‘range anxiety’ of the average consumer when considering electric vehicles.

Recent commercial success of the lithium ion battery has also motivated the expansion of similar energy storage constructs to significantly larger scale applications such as electrical grid storage. In the face of the global effects of climate change, the overwhelming evidence suggests that a shift to non-fossil fuel based energy is inevitable and therefore an amplified interest in renewable or ‘green’ energy sources is apparent. These renewable sources such as wind or solar are already viable, however the intermittent nature of energy production by such means has remained a stumbling block for existing state-of-the-art technology. The ability to store energy generated during peak production would allow renewable energy to realistically compete with fossil fuels on a large-scale basis. The lack of a weight constraint and a decreased risk for extreme conditions for such energy storage devices means that alternatives beyond extremely light-weight lithium ion batteries can reasonably be considered; an extensive body of research is dedicated to various other energy storage formulations such as high temperature Na cells, sodium ion batteries, fuel cells, redox flow batteries, among others.[4-7] In this exciting field, all efforts are focused on the same goal of reducing, and ultimately abandoning, fossil fuel reliance.

## 1.2 Lithium Ion Batteries

Rechargeable lithium ion batteries consist of a positive and a negative electrode separated by an electrolyte solution containing a lithium salt. Lithium ions are shuttled back and forth between the electrodes through the electrolyte, while electrons simultaneously travel through an external circuit, creating usable current to power a device. A schematic of a typical lithium ion battery is depicted in **Figure 1.2**, where the electrodes are represented by the structure of a commonly used intercalation cathode compound, $LiCoO_2$, and a layered graphitic anode into which Li ions can be inserted between individual sheets. As the total amount of usable current from a given electrochemical cell is directly related to the number of Li atoms that can be simultaneously removed from the cathode and incorporated into the anode, the stoichiometry and capacity of the electrode material are the determining factors for an overall batteries capacity. This is often referred to as specific capacity, generally

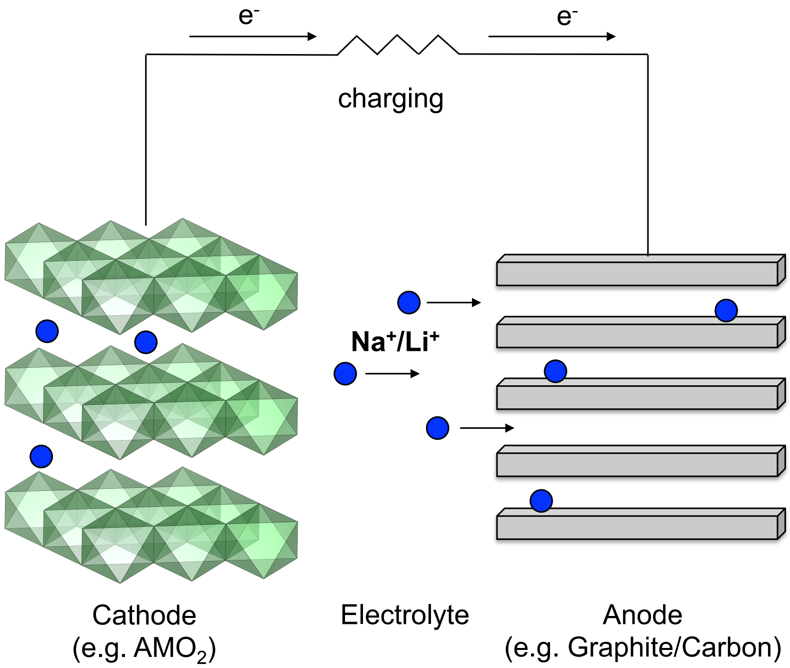

**Figure 1.2:** Schematic of a modern lithium ion battery comprising a cathode (pictured here as $LiCoO_2$), Li –salt electrolyte, and a graphitic anode. The charging state occurs when Li ions leave the cathode and travel to the anode, accompanied by the flow of electrons through an external circuit in the same direction.

considered to be the current produced per gram of active material. Specific capacity is most effectively expressed with the units of mAhg$^{-1}$, referring to the amount of charge that will allow 1 mA of current to flow through the external circuit over the course of a single hour per gram of active material. The current state-of-the-art lithium ion batteries provide between 160-180 mAhg$^{-1}$ (**Table 1.1**) in a typical cell with a common commercial cathode and graphitic anode.[3,4] This capacity is also commonly expressed, especially for consumer products, as a specific energy with units of Whkg$^{-1}$ denoting the total amount of energy per kilogram of active material that a single electrochemical cell or battery pack can provide.

**Table 1.1:** Comparison of average voltage and theoretical capacities of common commercial battery systems.

| **Battery Type** | **Average Operating Voltage (V)** | **Theoretical Specific Capacity (mAh g$^{-1}$)** | **Commercialization** |
|---|---|---|---|
| Lead-Acid | 2.1 | 83 | Various[a] |
| Ni-Metal Hydride | 1.35 | 162 | PHEVs |
| Li Ion (LCO)[b] | 3.7 | 158 | EVs |
| Li Ion (Spinel)[b] | 4.0 | 104 | EVs |
| Li Ion (LFP)[b] | 3.4 | 117 | EVs |
| Na-S[c] | 2.0 | 377 | Stationary Storage |
| Na-NiCl$_2$[c] | 2.58 | 305 | Stationary Storage |

[a]Various applications including backup power storage, uninterruptable power supplies (UPS) and automobile starters for ICEs. [b]In a typical Li ion cell with a Li$_x$C$_6$ anode. [c]High temperature operation only (270-350 °C).

A typical cathode material consists of a redox-active structural network into which Li ions can be easily intercalated. This redox activity primarily defines the voltage at which charging or discharging occurs, ultimately translating to a theoretical power output from a single electrochemical cell. The framework of the cathode also determines the overall reversibility and structural stability of a material, especially after multiple charge-discharge cycles wherein Li ions are moving in and out of the structure relatively quickly. Other factors such as ionic and electronic conductivities and compatibility with the electrolyte, and commercial considerations such as cost and toxicity all play crucial roles in the development of a suitable cathode material for lithium ion batteries.

Most current commercial cathode materials are part of a larger class of structures known as ‘metal oxides’. Since the initial use of $LiCoO_2$ (commonly referred to as LCO) in the first commercial cells developed by Sony, this structural motif wherein Li atoms are housed between layers of metal-oxide octahedra (as shown in **Figure 1.3)** has been modified to create the most successful modern commercial materials, namely $LiNi_{1-x-y}Mn_xCo_yO_2$ (NMC) and $LiNi_{0.8}Co_{0.15}Al_{0.05}O_2$ (NCA). As of 2018, the consumer electric vehicle (EV) sector predominantly employs one of these two cathode structures, as high capacity and high power are necessary in such applications. In its current state, the commercial battery market sees only incremental improvements in the active cathode material, where small stoichiometric modifications and materials engineering developments dominate the changes implemented in practice. Despite some brief success with $LiFePO_4$ (LFP), where the structural stability provided by the robust phosphate framework cannot be reproduced in the layered oxides, NMC and NCA remain preferred materials for automotive applications due to superior capacity and charging rates.

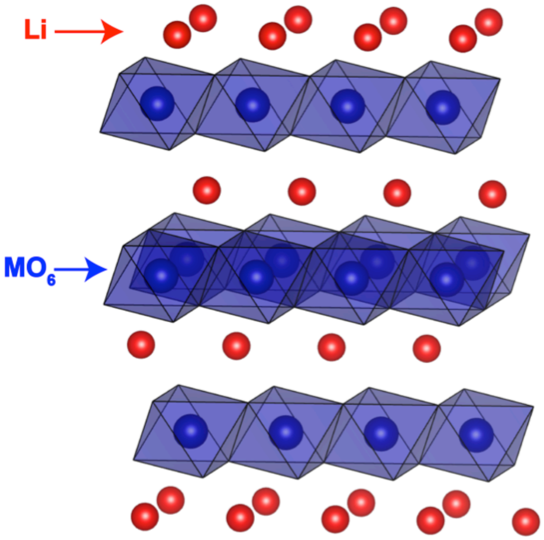

**Figure 1.3:** General structure of the lithium layered oxides of the form $LiMO_2$, where M=Co, Ni, $Ni_{1-x-y}Mn_xCo_yO_2$. Lithium atoms are shown in red, with the metal octahedral units in blue.

While theoretical considerations of capacity and voltage limits are widely used for screening and discovery of new materials, in practice it is often a complex issue. Despite a desire for a high voltage cathode in order to increase the power density of a cell, modern electrolytes have a limited voltage window over which they remain stable. The most commonly employed electrolyte is comprised $LiPF_6$ salt dissolved in an organic solvent, usually similar to an ethylene carbonate/dimethyl carbonate (or EC/DMC) mixture or neat propylene carbonate (PC). The voltage window over which this solvent system is stable approaches a maximum at approximately 4.9 V under normal operating conditions, and therefore regardless of the theoretical benefit to high voltage, cathodes that approach or exceed this limit are rendered useless. Despite considerable research efforts to develop high voltage electrolyte composites, no new high voltage battery systems have been developed as of 2018.

The anode also plays a critical role in battery function and performance, and current graphitic anodes wherein Li intercalates between graphite sheets to give a composition of $Li_xC_6$ has proven rather successful. In current battery systems, graphitic anodes are the most widely used, as they offer high mechanical stability on multiple charge-discharge cycles and good electrical and ionic conductivity. Despite these properties, the incompatibility of graphite with PC based electrolytes has motivated the search for alternatives such as conversion materials where Li creates an alloy or undergoes a chemical reaction with the anode to store energy.[3,8] While there have been some advances in the area of alternative anode materials, graphitic carbon remains the dominant choice for lithium ion batteries in consumer products at the time of writing.

Despite significant progress since the batteries of Ford and Edison, the NMC-graphite secondary lithium battery is a long way from ideality. In order to reach many of the targets put forth for full incorporation into the automotive market, several areas must first be addressed, most notably: increasing charging rates, maximizing capacity density, and improving electrode and electrolyte stabilities. In order to overcome these obstacles, materials chemists are working toward understanding the structural motifs that give rise to desirable LIB properties at the molecular level. In particular the construction of a cathode material that can quickly and reversibly intercalate/deintercalate Li ions without major structural changes is highly sought-after, as it would result in high energy density batteries with rapid charging rates.

## 1.3 Sodium Ion Batteries

Although not yet widely utilized commercially, battery concepts using Na as the charge-carrying ion have been in existence since the 1960s.[5,9,10] An early discovery at the Ford Motor Company in 1967 demonstrated that beta-alumina, with a chemical formula of $11Al_2O_3 \cdot xNa_2O$, exhibited unexpectedly high ionic conductivity at elevated temperatures, making it an excellent solid-state electrolyte candidate. Thus began the first wave of commercialization of sodium battery derivatives: Na-S[11] and Na-$NiCl_2$, (also called ZEBRA)[12] cells. These systems are unusual in that they comprise a liquid Na metal negative electrode and a highly conductive solid-state Na-ion conducting electrolyte (beta-alumina). Both exhibit very high theoretical specific capacities of 300-375 $mAhg^{-1}$ (**Table 1.1**) when operating near 350 °C, reaching nearly twice of what is achievable by even the most promising lithium ion battery cells. Their high temperature requirements and significant safety concerns, however, have relegated their use almost entirely to stationary-storage applications.

As early as the 1970s-80s cathode materials for room temperature sodium batteries were being actively studied.[5,10,13,14] With the commercialization of Li ion batteries in 1991, attention was quickly diverted to the more electrochemically promising candidate for rechargeable battery systems. Nonetheless, a resurgence of interest in sodium battery systems is motivated by concerns regarding the geographical location and limited amount of the global lithium reserves. Although hindered by the relatively larger size and weight of the mobile charge-carrying Na atom, sodium ion batteries are especially appealing as a safer alternative for stationary energy storage solutions. Between 1990 and 2017, the number of peer-reviewed articles on the topic 'sodium ion batteries' increased by over 700%, putting this field approximately 10 years behind lithium in terms of overall research interest. Despite the resumed attention, the major barrier to sodium ion battery commercialization remains a lack of suitable electrode materials that can reasonably compete with existing systems.

Theoretically sodium ion batteries are perfectly analogous to lithium ion batteries in both configuration and operation, comprising a cathode and an anode separated by an electrolyte salt solution over which $Na^+$ ions travel between electrodes. The main difference comes with choice of appropriate electrode materials; however, this is not simply accomplished by implementing sodiated versions of successful lithium cathodes. Moreover, the graphitic anode used in Li ion batteries is unusable in the case of Na, as intercalation of the Na ions between graphite layers is less thermodynamically favourable than Na plating on the surface of the negative electrode. This effect is believed to stem from the weak interaction between intercalated Na atoms and the graphitic layers of the anode. Without a favourable interaction, there is no energetic benefit to the intercalation of sodium into graphite as opposed to deposition at the electrode surface.[15,16] Nevertheless, the lack of graphitic intercalation behaviour doesn't preclude other carbonaceous materials from use as anode materials in sodium ion batteries. Indeed, carbon has been highly successful in the lithium systems largely because of the low cost and environmental concerns associated with other materials that work reasonably well. Stevens and Dahn[16] reported in the early 2000s on the ability of Na incorporation into hard carbon materials containing a mixture of nano-sized pore domains and parallel graphene sheet regions. An adsorption-like process is possible for sodium into the porous domains of hard carbons as well as insertion between graphene layers. Although sodium capacity is inescapably lower than the smaller and lighter weight lithium counterpart, capacities for Na insertion into hard carbons is sufficient for cell operation.[16] Notably, the hard carbon material 'C1600' was recently found to exhibit a capacity of over 300 mAh $g^{-1}$, with excellent retention over 50 cycles.[17] Although there is certainly room for further improvement in this area, hard carbon anodes are currently at the forefront of modern sodium ion battery technologies.

Unlike the anodes for sodium ion batteries, choice of electrolyte is relatively straightforward, and more easily extrapolated based on what is already used for lithium ion batteries. Important factors for electrolyte choice include ionic conductivity, thermal stability and electrochemical voltage window. Most common are organic-based liquid electrolytes incorporating a dissociated Na-salt such as $NaClO_4$, $NaPF_6$, and sodium bis(tri-fluoromethanesulfonyl)imide (abbreviated to NaTFSI), all of which are frequently used in Na ion batteries currently in development. Although the perchlorate salt has demonstrated the most stable cycling performance and rate capability, the $NaPF_6$ system features improved SEI thermal stability. Both have similar voltage stability windows (maximum of ~5 V), and thus are largely interchangeable, offering only very slight differences in cell performance.

With effective choices for both the anode and electrolyte materials, the cathode remains the last major barrier in the development of a commercialized room temperature sodium ion battery. Much like cathodes for lithium ion batteries, an ideal sodium cathode material has high gravimetric capacity, thermal and electrochemical stability, and high rate capability. Perhaps the most obvious starting point in the search for a high performance sodium ion battery cathode is the layered oxide family of materials that has enjoyed significant commercial success in lithium ion cells. In the early 1980s, Delmas *et al.*[14] reported on the electrochemical intercalation of sodium ions into $Na_xCoO_2$ bronzes. These structures consist of a lattice of edge-shared metal-oxide octahedra that form layers between which Na ions can intercalate into two unique environments; prismatic (*P*) or octahedral (*O*). Compositions of $Na_{0.8}CoO_2$ showed most promising electrochemical performance, with higher sodium concentrations giving very low reversible cycling capacities (intercalation/deintercalation of less than 0.2 Na equivalents per formula unit). Still, the total Na content in this structure type is not ideal, with at most 50% removal upon charging. Furthermore, the voltage profiles of $Na_xCoO_2$ materials reveal considerable structural transitions upon cycling, likely resulting from the gliding of oxygen layers relative to each other as Na is removed from the lattice. These structural changes often lead to poor reversibility in electrochemical cycling either in terms of capacity or voltage hysteresis on charge and discharge, and are therefore undesirable for commercial applications. In contrast to cobalt oxides, manganese oxides have actually demonstrated good cycling performance, with Billaud *et al.*[18] reaching 190 mAh $g^{-1}$ of capacity with the $\beta$-$NaMnO_2$ polymorph. In almost all cases, however, the voltage of the layered oxides was found to be lower for Na relative to Li derivatives, owing to a decreased energy benefit obtained upon Na insertion into the lattice. This effect is most prominent in the layered oxides, and decreases their benefit relative to other structure families that are perhaps more stable during the cycling process.[19]

**Table 1.2:** Comparison of experimental voltage, capacity, and cycle life of selected cathode materials for sodium ion batteries.

| **Cathode Material** | **Average Operating Voltage (V)** | **Experimental Capacity (mAh g$^{-1}$)** | **Number of Cycles (Max. Reported)** |
|---|---|---|---|
| $Na_{0.44}MnO_2$ | 2.0-3.8 | 120 | 1000[20] |
| $Na_3V_2(PO_4)_3$ | 3.4 | 114 | >1000[21] |
| $Na_xFe_yMn_{1-y}O_2$ | 2.5-3.5 | 190 | 30-40[22] |
| $\alpha$-$NaMnO_2$ | 2.75-3.5 | 120-200 | 20[23] |
| $\beta$-$NaMnO_2$ | 2.7-3.5 | 150-190 | 100[18] |
| $Na_3V_2(PO_4)_2F_3$ | 3.7-4.2 | 115-128 | 250[24] |
| $Na_2FePO_4F$ | 3.0-3.7 | 155 | 50[25] |

This lack of an immediate frontrunner in the sodium ion battery field is not necessarily a discouraging result; in fact, computational results suggest that in many cases the $Na^+$ migration barrier can actually be lower than that for $Li^+$ in certain structure types.[19] Moreover, despite a difference in the types of morphologies favoured by sodium-containing materials, there is no theoretical evidence to suggest that Na cannot compete with lithium ion frameworks. Along with sodium-containing layered oxides, polyanion-derived arrangements such as phosphates, fluorophosphates, pyrophosphates and fluorosulphates have all demonstrated promising sodium intercalation properties.[9,10] These polyanionic structures all share the stability benefit offered from the robust network of $XO_4$ units (X=P, S) that do an excellent job of maintaining structural integrity of the lattice across a range of Na stoichiometries. Although exhibiting markedly lower capacities and operating voltages as compared to layered oxides for lithium, the disparity between oxides and polyanions is reduced for sodium intercalation materials on account of the voltage drop exhibited by the sodium metal oxides. Many of these polyanionic materials (for both lithium and sodium) additionally offer the use of more cost-effective, low toxicity metals such as iron and manganese, which when combined with the greater stability inherent to these systems, make them an excellent candidate for both lithium and sodium ion batteries. In that vein, the focus of this thesis will be the investigation of various new and inexpensive polyanionic cathode materials for both lithium and sodium ion batteries, using a combination of $^{7}$Li and $^{23}$Na solid-state nuclear magnetic resonance methods to elucidate structural and dynamics properties before, after, and during electrochemical cycling.

## 1.4 Materials Studied In This Thesis

Although layered oxide frameworks are still actively being studied in the context of both lithium and sodium ion battery cathodes, significant attention has turned toward novel intercalation compounds based on a multi-dimensional phosphate-linked network that provides excellent structural support during electrochemical cycling. In general, these materials consist of tetrahedral $PO_4^{3-}$ units and $MO_6$ or $MO_4F_2$ octahedra that effectively resist significant changes to lattice parameters, ultimately improving the reversibility of the alkali ion deintercalation process. The diverse way in which these polyanionic units can be arranged creates an assortment of structural architechtures involving many different transition metals (TMs). Of the possibilities, iron and manganese are generally sought after as they are inexpensive and non-toxic relative to some of the other metals used, namely cobalt. Iron and manganese also tend to exhibit $M^{2+}$-$M^{3+}$ redox voltages within an acceptable range for use with current electrolyte systems. Polyanionic frameworks have the added benefit of an inductive effect of the phosphate polyhedra that increases the redox potential of the TM relative to typical oxides. This increased voltage allows for the use of favourable TMs that exhibit redox couples deemed too low for oxides, such as Fe in $\alpha$-$LiFeO_2$ which has an average charge voltage of 3.0 V.[26] Where these materials tend to suffer is in their decreased overall theoretical capacity (due to the presence of extra structural atoms in addition to oxygen) and reduced ionic and electronic kinetics. Fortunately, these properties are entirely material-dependent, and thus the search for an ideal combination of high stability, high capacity and improved kinetics is ongoing.

Given the large complexity of these structures as compared to a simple layered arrangement, the particular chemical environment of the alkali ions during cycling is not necessarily obvious and acquiring such information can provide significant insight into the mechanism underlying a material's bulk electrochemical performance. Unfortunately, this type of local atomic information is not readily attainable by many techniques. Microscopy and powder X-ray diffraction methods have proven excellent for bulk structural characterization, providing an excellent picture of the overall changes to the lattice structure for a given material over temperatures or cycling conditions. Other spectroscopic techniques such as Mössbauer have been extensively used to understand the important changes occurring at the transition metal ion (in the case where Fe is the redox active site). Unfortunately, these techniques are unable to capture details regarding the charge-carrying alkali ions, especially lithium, and site-specific motion is essentially invisible to these methods.

Solid-state nuclear magnetic resonance (ssNMR) offers the ability to probe both the bulk structural atomic arrangement as well as the local dynamics of the mobile alkali ions. The ability to track differences between the unique chemical environments occupied by the Li or Na ion allow for experimental validation of structure and dynamics processes that occur during charging. NMR has been well established as a method from which kinetics information can be extracted, and thus rate constants and energy barriers can be elucidated without concern for bulk effects such as grain boundaries that are unavoidable in bulk conductivity measurements. Moreover, the dynamics of the Li or Na ions in different chemical environments can be compared, ultimately generating a detailed ion diffusion pathway for complex three-dimensional networks. This thesis will focus exclusively on alternative polyanionic cathode materials for lithium and sodium ion batteries, and how they can be characterized and understood with the aid of advanced solid-state nuclear magnetic resonance methods.

### 1.4.1 Lithium Pyrophosphates, $Li_2MnP_2O_7$

The pioneering discovery of lithium iron phosphate derivatives came from Goodenough and coworkers in the late 1990s as a structurally robust polyanionic alternative to the layered oxides for Li cathode frameworks.[27,28] To date, $LiFePO_4$ (LFP) remains the model example for polyanionic materials in general, as it boasts a competitive capacity, is environmentally friendly, and has excellent stability for long term cycling applications.[27] These properties have propelled it to the forefront of the polyanionic materials development field, with successful implementation into electric vehicle applications, the first non-oxide based cathode material to do so. All of this success comes in spite of poor electronic conductivity, and defect-induced limits on ionic conductivity.[29] Furthermore, it has inspired the burgeoning research efforts in this field, expanding the class of polyanionic materials to include pyrophosphates ($Li_2MP_2O_7$),[30-32] fluorophosphates ($Li_2MPO_4F$),[33-36] and fluorosulfates ($LiMSO_4F$),[37-39] where in all cases the Fe-containing substituent is often desirable due to the low associated cost and low environmental impact relative to other metals.

The pyrophosphate family of materials of the type $Li_2MP_2O_7$, where M=Fe or Mn, have a high operating voltage combined with the ability to house two charge carrying Li ions per transition metal center, thus increasing theoretical capacities.[30-32,40-43] This high voltage and possibility for an extended capacity based on a second $M^{3+}$-$M^{4+}$ redox couple could in theory improve on the groundwork laid by LFP in the discovery of a commercially viable phosphate-based cathode. Zhou *et al.*[32] have reported highly reversible electrochemical cycling of the Fe-based pyrophosphate, with the ability to reproducibly remove a single lithium ion from the structure to generate a metastable $LiFeP_2O_7$ phase. However, despite promisingly high redox potentials, the Mn-containing phase (**Figure 1.4**) appeared to exhibit consistently poor cycling behaviour. This lack of electrochemical ability in $Li_2MnP_2O_7$ is in agreement with observations for other Mn phosphates, for example $LiMnPO_4$, where electrochemical performance pales in comparison to its LFP counterpart.[44,45] The mechanism for poor cyclability in the Mn pyrophosphate analog is not well understood, although it has been hypothesized to result from either a structural distortion during charging, or high kinetic barriers.[31,32] Tamaru *et al.*[31] have demonstrated that the Mn phase does in fact exhibit redox activity at 4.45 V with slow cycling rates, albeit with limited capacity, supporting the hypothesis of a possible kinetic barrier for Li ion diffusion through the cathode material. The encouragingly high redox potential of the entire $Li_2Mn_{1-y}Fe_yP_2O_7$ class of materials prompts the elucidation of their ion diffusion pathways as this would provide valuable insight into structural properties that contribute to electrochemical performance.

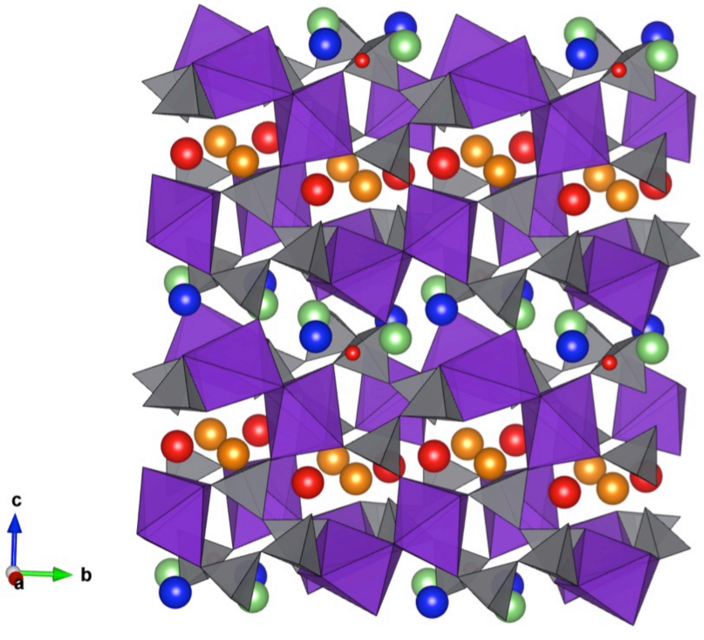

**Figure 1.4:** Structure of monoclinic $Li_2MnP_2O_7$ with space group $P2_1/a$. $PO_4$ and $FeO_6$ units are depicted as grey and purple polyhedra respectively. Li atoms are shown as blue, green, orange, and red to depict the four unique crystallographic sites.

### 1.4.2 Lithium Iron Vanadate: $LiFeV_2O_7$

Despite the overwhelming attention given to phosphate and sulphate polyanion alternatives, more recent studies indicate that the use of a vanadate foundation with Fe as the redox active metal has yielded promising results.[46-48] Of those reported thus far, the extent of the vanadium redox activity is highly varied, in some cases being the primary redox active site, while in others playing a more minor role. In the latter case, the full redox activity of the $Fe^{2+}/Fe^{3+}$ couple is complemented by additional capacity due to partial V activation. Although some of the voltage gain afforded by the larger inductive effect in $PO_4^{3-}$ relative to $VO_4^{3-}$ is lost, the result is somewhat mitigated by increased conductivity of the vanadate framework. A recent report by collaborators at Université de Montreal presented a novel lithium iron vanadate, $LiFeV_2O_7$, that undergoes reversible Li intercalation-deintercalation between 2.4 and 2.8 V.[47] The structure crystallizes in the monoclinic space group *Cc*, and consists of extended V-O chains that create layers between which Li and Fe-O units alternate (**Figure 1.5**). Based on a refinement of the single crystal X-ray structure, the Li ions are expected to be involved in a three-dimensional Li transport network during cycling. The presence of several unique plateaus also indicates multiple possible structural evolutions occuring reversibly during cycling, as evidenced by the very small hysteresis in the electrochemical curve. With a theoretical capacity of 97 mAh $g^{-1}$ corresponding to the full conversion of $Fe^{3+}$ to $Fe^{2+}$, the authors discovered an anomalous 'extra' capacity, to ultimately insert 1.1 Li atoms per structural unit.

The promising behaviour of this unique structure type as a lithium ion battery cathode encourages in-depth investigation into the rate behaviour of the Li ions as well as a structural investigation to determine the cause of the unique shape observed for the electrochemical cycling curve. In this thesis, these properties are investigated by $^7$Li solid-state NMR techniques. *Ex situ* NMR studies were carried out in an attempt to characterize the structural evolution of $Li_{1+x}FeV_2O_7$ during lithium insertion/deinsertion, as well as probe ion dynamics during this change.

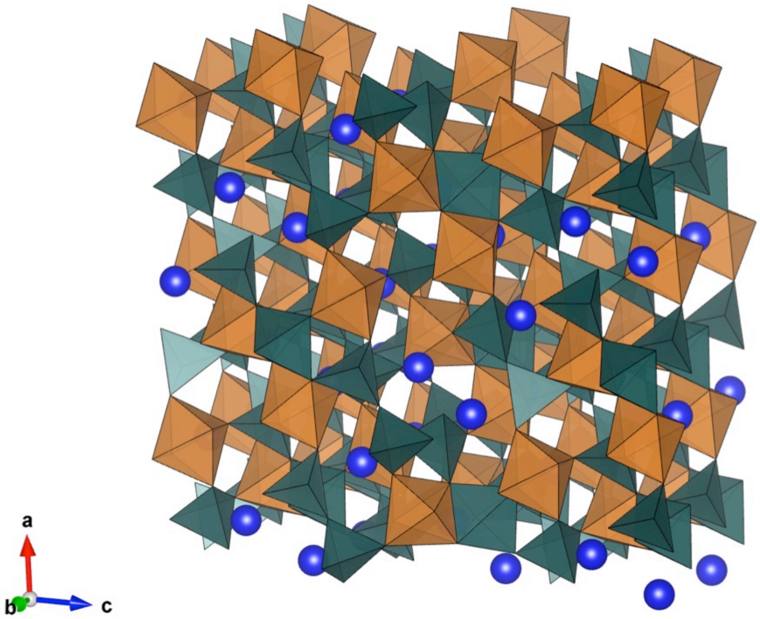

**Figure 1.5:** Structure of monoclinic $LiFeV_2O_7$. $VO_4$ and $FeO_6$ units are depicted by green and orange polyhedra respectively. Lithium ions housed in three crystallographic sites are shown in teal.

### 1.4.3 Sodium Fluorophosphates; $Na_2MPO_4F$

The layered fluorophosphate-type intercalation material $A_2FePO_4F$ (A=Li, Na) has great potential as a cathode material for both LIBs and NIBs.[25,49] The Na variant crystallizes in the orthorhombic *Pbcn* space group where face-sharing $FeO_4F_2$ octahedra are connected via bridging F atoms to form bioctahedral units that are joined by $PO_4$ anions to make up the layered structure (see **Figure 1.6**).[49] $Na^+$ ions are housed in two unique crystallographic positions, Na1 and Na2, both of which exhibit a [6+1] type coordination to 4 O atoms and 2 F atoms with each having an additional long range contribution to the bond valence sum from a neighbouring oxygen atom.[25,49] The Na2 environment is slightly more compact, having shorter Na-O and Na-F distances on average.[29] Favourable electrochemical performance of this material was demonstrated by Nazar and coworkers when cycled versus Li metal, forming a novel Na-Li ion battery hybrid that exhibited an average charge potential of 3.3 V *vs* Li and a reputable 115 $mAhg^{-1}$ capacity.[25,33,35,36,49] Chemical oxidation of the parent $Na_2FePO_4F$ phase yielded a near-identical $NaFePO_4F$ structure with only the Na1 positions occupied, implying that the Na2 site houses the more mobile of the two ions.[37-39]

Following the initial proposal and synthesis of this material, several studies have expanded upon the work of Nazar and coworkers. A variety of modified synthetic methods for preparation of $Na_2FePO_4F$ with improved electrochemical performance have been proposed, including new synthetic pathways for nanosizing the material, as well as an assortment of carbon-containing methods that both act as a particle growth inhibitor as well as deposit a conductive carbon coating for improved electronic conductivity. [30-32,40-43] In addition, this promising electrochemical behaviour has prompted the modeling of diffusion pathways in an effort to identify the mechanism of Na ion migration in this material.[44,45] In 2013, Tripathi *et al.*[31] were able to demonstrate the possibility for $Na^+$ diffusion along the a- and c-axes, explaining the improvement in Na intercalation properties relative to the poorly performing $NaFePO_4$ material and confirming the earlier predictions of Ellis *et al*.[32] Their results suggest a network of Na ions that include $Na^+$ hops between connecting Na1-Na1 and Na1-Na2 sites that form an extensive diffusion pathway throughout the material with sufficiently low activation energy barriers for alkali ion hopping.[50]

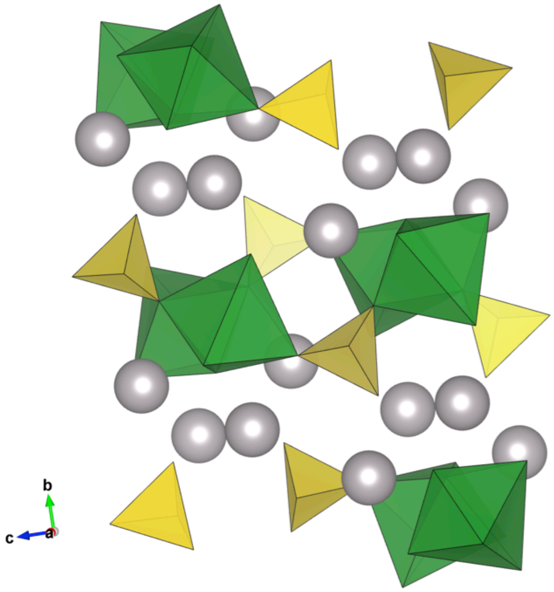

**Figure 1.6:** Structure of orthorhombic, layered fluorophosphate, $Na_2FePO_4F$. Shown above is a single unit cell containing two crystallographic Na positions (shown in grey) and interconnected $PO_4$ and $FeO_4F_2$ polyhedra, shown in yellow and green respectively.

## 1.5 Summary

The energy storage research field is incredibly diverse and broad, nonetheless, very few materials actually achieve commercial success. Much of this comes down to the unique chemistry involved for each different material, and as such, understanding this is imperative for the production of better batteries to bring about the next era of success. A detailed awareness of structural and dynamics features of materials before, after, and during the charging and discharging processes would help to design the next generation of cathode materials for lithium and sodium ion batteries. Solid-state NMR is recognized as an excellent tool to do this with, on account of the detailed site-specific information that can be obtained from it. This thesis will discuss the ways in which solid-state NMR has been applied to study unique mobility information in alternative Li cathode materials, $Li_2MnP_2O_7$, $Li_2SnO_3$, and $LiFeV_2O_7$ both in the pristine states and during cycling through *ex situ* NMR studies. Subsequent chapters will then discuss a potential cathode for sodium ion batteries, $Na_2FePO_4F$, where a detailed *ex situ* NMR study is used to characterize the sodium distribution in the bulk structure by observation of local environment changes. Further, the application of density functional theory will be discussed in the context of a complementary technique to NMR for understanding difficult NMR spectra and validation of experimental results.

## 1.6 Thesis Outline

This thesis will broadly cover the fields of lithium and sodium ion battery cathode materials, and the use of solid-state NMR methods to characterize them. The investigation of several Mn or Fe containing polyanionic materials will be discussed in detail, with a focus on NMR results that give rise to an improved understanding of both structural and dynamics properties of these materials both before and during electrochemical cycling. Chapter 1 has outlined the broad context of the thesis including the overarching motivations for the characterization of cathode materials for lithium and sodium ion batteries. This chapter also briefly introduced the specific materials of interest throughout the thesis, with a brief summary of what was previously studied. Chapter 2 will discuss in detail the technique of solid-state magnetic resonance, with a focus on the theoretical basis from which all NMR experiments are derived, as well as a description of the benefits and limitations of $^{7}$Li and $^{23}$Na NMR including a brief discussion of their respective quadrupolar parameters among other effects. Chapter 3 will explain in greater detail the challenges associated with solid-state NMR of paramagnetic materials, and the specific techniques used within this thesis to elucidate structural and ion dynamics information. This chapter will also introduce the concept of density functional theory as a complement to NMR spectroscopy of paramagnetic materials. Chapter 4 will discuss the study of slow lithium ion dynamics in $Li_2MnP_2O_7$ as compared to $Li_2SnO_3$ by $^{6}$Li ssNMR methods, including an exploration of the limitations in terms of timescale for studying ion exchange in paramagnetic materials by NMR. Continuing with the theme of ion dynamics, Chapter 5 presents a combined electrochemical and *ex situ* NMR study of $Li_{1+x}FeV_2O_7$ wherein Li-Li hopping rate changes as a function of state of charge are elucidated and discussed. Chapter 6 will focus on an *ex situ* $^{23}$Na NMR study of a potential sodium ion cathode material, $Na_2FePO_4F$. Specifically, NMR is used in this case to understand the Na ion distribution in the bulk electrode as a function of electrochemical cycling. A brief discussion of the use of $^{23}$Na NMR in the context of paramagnetic cathode materials will be included in this chapter. Chapter 7 presents results from *ab initio* density functional theory calculations of structure parameters and paramagnetic shifts in $Na_2FePO_4F$, linking heavily back to experimental NMR data presented in the preceding chapter. Chapter 8 summarizes efforts to identify and characterize compositional defects in $Na_2FePO_4F$ materials combining several techniques, notably ssNMR, DFT, Mossbauer, and X-ray diffraction. Finally, chapter 9 will summarize the key results, and propose future work for the specific projects presented within this thesis, as well as a discussion of the future direction of the field in general.

## 1.7 References

(1) Hansen, J. E.; Sato, M. In *Climate Change*; Springer, Vienna: Vienna, 2012; pp 21–47.

(2) National Energy Board. *Canada's Renewable Power Landscape - Energy Market Analysis 2016 - October 2016*; 2016; pp 1–39.

(3) Thackeray, M. M.; Wolverton, C.; Isaacs, E. D. *Energy Environ. Sci.* **2012**, *5* (7), 7854.

(4) Blomgren, G. E. *J. Electrochem. Soc.* **2016**, *164* (1), A5019.

(5) Sawicki, M.; Shaw, L. L. *RSC Adv.* **2015**, *5*, 53129.

(6) Kundu, D.; Talaie, E.; Duffort, V.; Nazar, L. F. *Angew. Chem. Int. Ed.* **2015**, *54* (11), 3431.

(7) Saha, P.; Datta, M. K.; Velikokhatnyi, O. I.; Manivannan, A.; Alman, D.; Kumta, P. N. *Progress in Materials Science* **2014**, *66* (C), 1.

(8) Nitta, N.; Wu, F.; Lee, J. T.; Yushin, G. *Biochemical Pharmacology* **2015**, *18* (5), 252.

(9) Yabuuchi, N.; Kubota, K.; Dahbi, M.; Komaba, S. *Chem. Rev.* **2014**, *114* (23), 11636.

(10) Ellis, B. L.; Nazar, L. F. *Current Opinion in Solid State & Materials Science* **2012**, *16* (4), 168.

(11) Sudworth, J.; Tiley, A. R. *The Sodium Sulphur Battery*; Springer Science & Business Media, 1985.

(12) Sudworth, J. L. *Journal of Power Sources* **2001**, *100* (1), 149.

(13) Parant, J.-P.; Olazcuaga, R.; Devalette, M.; Fouassier, C.; Hagenmuller, P. *J. Solid State Chem.* **1971**, *3* (1), 1.

(14) Delmas, C.; Braconnier, J.; Fouassier, C.; Hagenmuller, P. *Solid State Ionics* **1981**, *3-4*, 165.

(15) DiVincenzo, D. P.; Mele, E. J. *Phys. Rev. B* **1985**, *32* (4), 2538.

(16) Stevens, D. A.; Dahn, J. R. *J. Electrochem. Soc.* **2001**, *148* (8), A803.

(17) Zhao, J.; Zhao, L.; Chihara, K.; Okada, S.; Yamaki, J.-I.; Matsumoto, S.; Kuze, S.; Nakane, K. *Journal of Power Sources* **2013**, *244* (c), 752.

(18) Billaud, J.; Clément, R. J.; Armstrong, A. R.; Canales-Vázquez, J.; Rozier, P.; Grey, C. P.; Bruce, P. G. *J. Am. Chem. Soc.* **2014**, *136* (49), 17243.

(19) Ong, S. P.; Chevrier, V. L.; Hautier, G.; Jain, A.; Moore, C.; Kim, S.; Ma, X.; Ceder, G. *Energy Environ. Sci.* **2011**, *4* (9), 3680.

(20) Cao, Y.; Xiao, L.; Wang, W.; Choi, D.; Nie, Z.; Yu, J.; Saraf, L. V.; Yang, Z.; Liu, J. *Adv. Mater.* **2011**, *23* (28), 3155.

(21) Saravanan, K.; Mason, C. W.; Rudola, A.; Wong, K. H.; Balaya, P. *Adv. Energy Mater.* **2012**, *3* (4), 444.

(22) Yabuuchi, N. *Nat. Mater.* **2012**, *11* (6), 512.

(23) Ma, X.; Chen, H.; Ceder, G. *J. Electrochem. Soc.* **2011**, *158* (12), A1307.

(24) GOVER, R.; Bryan, A.; Burns, P.; Barker, J. *Solid State Ionics* **2006**, *177* (17-18), 1495.

(25) Ellis, B. L.; Makahnouk, W. R. M.; Rowan-Weetaluktuk, W. N.; Ryan, D. H.; Nazar, L. F. *Chem. Mater.* **2010**, *22* (3), 1059.

(26) Li, J. G.; Li, J. J.; Luo, J.; Wang, L.; He, X. *J Electrochem Sci* **2011**.

(27) Padhi, A. K.; Nanjundaswamy, K. S.; Goodenough, J. B. *J. Electrochem. Soc.* **1997**, *144* (4), 1188.

(28) Padhi, A. K.; Nanjundaswamy, K. S.; Masquelier, C.; Masque; Okada, S.; Goodenough, J. B. *J. Electrochem. Soc.* **1997**, *144* (5), 1609.

(29) Ait Salah, A.; Mauger, A.; Zaghib, K.; Goodenough, J. B.; Ravet, N.; Gauthier, M.; Gendron, F.; Julien, C. M. *J. Electrochem. Soc.* **2006**, *153* (9), A1692.

(30) Adam, L.; Guesdon, A.; Raveau, B. *J. Solid State Chem.* **2008**, *181* (11), 3110.

(31) Tamaru, M.; Barpanda, P.; Yamada, Y.; Nishimura, S.-I.; Yamada, A. *J. Mater. Chem.* **2012**, *22* (47), 24526.

(32) Zhou, H.; Upreti, S.; Chernova, N. A.; Hautier, G.; Ceder, G.; Whittingham, M. S. *Chem. Mater.* **2011**, *23* (2), 293.

(33) Ramesh, T. N.; Lee, K. T.; Ellis, B. L.; Nazar, L. F. *Electrochem. Solid-State Lett.* **2010**, *13* (4), A43.

(34) Ellis, B. L.; Makahnouk, W. R. M.; Rowan-Weetaluktuk, W. N.; Ryan, D. H.; Nazar, L. F. *Chem. Mater.* **2010**, *22* (3), 1059.

(35) Kim, S.-W.; Seo, D.-H.; Kim, H.; Park, K.-Y.; Kang, K. *Phys. Chem. Chem. Phys.* **2012**, *14* (10), 3299.

(36) Lee, S.; Park, S. S. *J. Solid State Chem.* **2013**, *204* (C), 329.

(37) Barpanda, P.; Ati, M.; Melot, B. C.; Rousse, G.; Chotard, J.-N.; Doublet, M.-L.; Sougrati, M. T.; Corr, S. A.; Jumas, J.-C.; Tarascon, J.-M. *Nat. Mater.* **2011**, *10* (10), 772.

(38) Recham, N.; Chotard, J.-N.; Dupont, L.; Delacourt, C.; Walker, W.; Armand, M.; Tarascon, J.-M. *Nat. Mater.* **2009**, *9* (1), 68.

(39) Tripathi, R.; Ramesh, T. N.; Ellis, B. L.; Nazar, L. F. *Angew. Chem. Int. Ed.* **2010**, *49* (46), 8738.

(40) Furuta, N.; Nishimura, S.-I.; Barpanda, P.; Yamada, A. *Chem. Mater.* **2012**, *24* (6), 1055.

(41) Shimizu, D.; Nishimura, S.-I.; Barpanda, P.; Yamada, A. *Chem. Mater.* **2012**, *24* (13), 2598.

(42) Barpanda, P.; Rousse, G.; Ye, T.; Ling, C. D.; Mohamed, Z.; Klein, Y.; Yamada, A. *Inorg. Chem.* **2013**, *52* (6), 3334.

(43) Tamaru, M.; Chung, S. C.; Shimizu, D.; Nishimura, S.-I.; Yamada, A. *Chem. Mater.* **2013**, *25* (12), 2538.

(44) Delacourt, C.; Laffont, L.; Bouchet, R.; Wurm, C.; Leriche, J.-B.; Morcrette, M.; Tarascon, J.-M.; Masquelier, C. *J. Electrochem. Soc.* **2005**, *152* (5), A913.

(45) Li, G.; Azuma, H.; Tohda, M. *Electrochem. Solid-State Lett.* **2002**, *5* (6), A135.

(46) Patoux, S.; Richardson, T. J. *Electrochemistry Communications* **2007**, *9* (3), 485.

(47) Benabed, Y.; Castro, L.; Penin, N.; Darriet, J.; Dollé, M. *Chem. Mater.* **2017**, *29* (21), 9292.

(48) Poizot, P.; Baudrin, E.; Laruelle, S.; Dupont, L.; Touboul, M.; Tarascon, J.-M. *Solid State Ionics* **2000**, *138* (1-2), 31.

(49) Ellis, B. L.; Makahnouk, W. R. M.; Makimura, Y.; Toghill, K.; Nazar, L. F. *Nat. Mater.* **2007**, *6* (10), 749.

(50) Tripathi, R.; Wood, S. M.; Islam, M. S.; Nazar, L. F. *Energy Environ. Sci.* **2013**, *6* (8), 2257.

# Chapter 2: Introduction to Solid-State NMR Spectroscopy

## 2.1 Introduction

Nuclear Magnetic Resonance (NMR) is a routinely useful tool in many diverse areas of scientific investigation from the physical sciences to medical research. Discovered and developed throughout the late 1930s and 1940s,[1,2] their discovery of magnetic resonance won Bloch and Purcell the Nobel prize for their observation of this physical phenomenon. In the decades following, solid-state NMR has been implemented to investigate a wide range of materials in the energy storage domain, and has been applied to probe local properties of NMR-active nuclei in various cathode materials for lithium ion batteries.[3-14] This technique is the primary method used throughout this thesis to study both structural and dynamics properties of cathode materials for alkali ion batteries. The present chapter will briefly review the theoretical basis for the NMR experiment and introduce the various complex interactions that affect the spectra of materials investigated within this thesis.

## 2.2 The Basics: Nuclear Spin in a Magnetic Field

### 2.2.1 Nuclear Spin and Nuclear Magnetic Moments

NMR spectroscopy relies on the property of spin arising from an inherent angular momentum of the nucleus. As the seemingly vague idea of *spin* is far from intuitive, it is useful to first consider the more familiar classical concept of angular momentum. Any rotating object possesses angular momentum that can be represented by a vector quantity perpendicular to the rotational plane. Particles can possess a similar property, called *spin* *angular momentum*, which does not result from a physical rotation, but rather is an intrinsic quality of the particle itself.[15-17] Many of the elementary particles that comprise the matter in our world possess this abstract property of spin, and as nuclei are made up of multiple smaller particles, they can also exhibit an inherent spin angular momentum that depends upon the exact combination of neutrons and protons of which it is composed.[15] Nuclei also possess a *magnetic moment*, that is closely related to its spin angular momentum *via* an appropriately named proportionality constant: the gyromagnetic ratio, γ.

$$\hat{\boldsymbol{\mu}} = \gamma \hat{\boldsymbol{I}} \tag{2.1}$$

where μ is the nuclear magnetic moment related to the spin angular momentum, I.

### 2.2.2 Nuclear Zeeman Splitting and Precession

For a nucleus with spin I under the influence of an external magnetic field, there are 2I+1 spin states, quantized according to the 2I+1 values of the nuclear spin magnetic quantum number, $m$.[18] The separation between energy levels, also called *Zeeman splitting*,[19] depends on the strength of the external field and the nuclear gyromagnetic ratio as demonstrated by the following relationship:[15]

$$E_{I,m} = -\gamma \hbar B_0 m \tag{2.2}$$

Consider a simple example such as the $^1$H nucleus where $I = \frac{1}{2}$; there are two available spin states with $m = \pm\frac{1}{2}$ and, following from Equation 2.2, the energy difference between the two states is $\gamma\hbar \mathrm{B}_0$. These energy levels are referred to as α and β to refer to the low and high energy spin states respectively with magnetic quantum numbers $m = +\frac{1}{2}$ and $m = -\frac{1}{2}$. A schematic illustrating the effect of nuclear Zeeman splitting for a set of spin-1/2 nuclei is provided in **Figure 2.1**, demonstrating the energy difference between the spin states.[15] The energy difference induced by the presence of $B_0$ creates a population difference between the α and β states, where the population in each is described by the Boltzmann distribution and depends on the energy of the nuclear spin-state. Although the energy differences are small, and thus the population differences are near-negligible, the relative difference between these populations is measurable, and gives rise to the bulk magnetization observed in the NMR experiment. The relative difference in population between the α and β spin states is governed by:

$$\frac{N_\beta}{N_\alpha} = e^{-\Delta E/kT} \tag{2.3}$$

where ΔE refers to the difference between energy levels, $N_\alpha$ and $N_\beta$ are the spin populations of the α and β states respectively, $k_B$ is the Boltzmann constant and T the temperature in units of K.

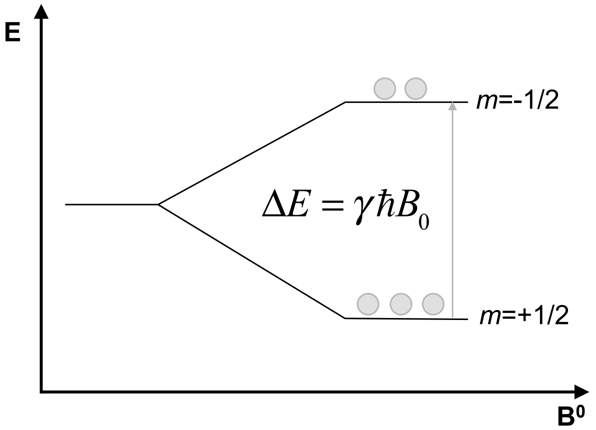

**Figure 2.1:** Schematic depicting the energy levels for spin-1/2 nuclei in the presence of an external magnetic field, $B_0$. The difference in energy between the two levels is shown, and is related to the Larmor frequency of the nucleus. This energy separation creates a population difference between the energy levels that can be described by the Boltzmann distribution.

### 2.2.3 Precession and The Larmor Frequency

In the absence of a magnetic field, the distribution of magnetic moments in a sample is isotropic at equilibrium; i.e. they are completely randomized with no concerted directional dependence. Imposing an external field causes the spins to rotate about the magnetic field at a fixed frequency due to the combination of the spin's magnetic moment and angular momentum. This rotation, or precession, occurs at a rate defined by the *Larmor frequency* ($\omega_0$), and is a function of the external magnetic field ($B_0$) and the gyromagnetic ratio ($\gamma$) of the nucleus:

$$\omega_0 = -\gamma B_0 \tag{2.4}$$

This frequency is directly related to the energy difference for the $\alpha \rightarrow \beta$ spin-state transition shown above, and consequently, for a single isolated spin in a magnetic field there is a single transition that results in a single spectroscopic line at a fixed frequency, specifically the Larmor frequency. In practice, nuclear spins are fixed within a complex molecule, and the exact precession frequency depends on the chemical environment of that nucleus. This environment-driven frequency dependence on environment is the basis for all NMR spectroscopy in the chemical sciences, and is why NMR is such a widely used method for chemical identification and characterization. By fixing the gyromagnetic ratio (and thus the reference Larmor frequency) to that of a single isolated spin, the amount by which the actual precession frequency differs from the reference provides an environment-dependent frequency shift, more commonly known as the chemical shift.

### 2.2.4 The NMR Experiment: Radiofrequency Pulses

At this point we have defined the nuclear spin states in terms of energy levels of nuclear spin states, and precessing magnetic moments about an external magnetic field. In the former description, it is relatively easy to imagine that we might want to induce transitions between these states to probe the energy levels of our sample. In fact this is exactly what one sets out to do in an NMR experiment, a feat that is accomplished by the administration of a radiofrequency (rf) *pulse* (manifesting as a time-dependent magnetic field perpendicular to the external field, termed $B_1$), tuned to the energy difference between the nuclear spin states.

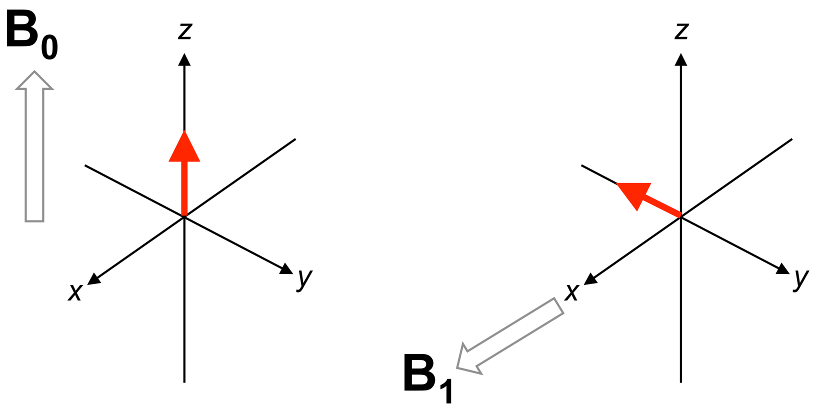

**Figure 2.2:** The bulk magnetization vector is initially aligned parallel to the $B_0$ field (external magnetic field). With the application of a RF pulse, a $B_1$ field is generated along *x*, effectively rotating the magnetization of the sample around the *x*-axis to end up in the –*y* direction.

Returning to our description of the precessing nuclear magnetic moments, the oscillating $B_1$ field generated perpendicular to the z-axis of the external static field rotates the bulk magnetization vector from the *z* to the *y* axis as demonstrated in **Figure 2.2**[17]. This rotation acts to move the bulk magnetization into the xy-plane, where a current is induced in the coil as the magnetization continues to precess about the static $B_0$ field. For a field applied along the x-direction that is oscillating at a frequency of $\omega_{RF}$ , the Hamiltonian can be written as[20]

$$\hat{H} = \omega_0 \boldsymbol{I_z} + 2\omega_1 \cos(\omega_{RF} t) \boldsymbol{I_x} \qquad (2.5)$$

where in the above equation the first term ($\omega_0\boldsymbol{I_z}$) is a result of the nuclear magnetic moment interacting with the external $B_0$ field, and the second term represents the rotation resulting from the interaction with the $B_1$ field generated by the rf pulse.

Here, it becomes much simpler to think about the NMR experiment in an altered reference frame known as the 'rotating frame'. In this new field of view, the precessing spin is itself considered the reference point such that the magnetization actually appears to be stationary. Adopting this frame of reference, the apparent Larmor precession frequency (i.e. the precession frequency as observed from the point of view of the rotating frame) of the spins becomes ($\omega_0 - \omega_{\mathrm{rf}}$), simply called the *offset frequency* ($\Omega$). This has the fortunate consequence of removing the time-dependence of the rf pulse, allowing Equation 2.5 to be rewritten as:

$$\widehat{\mathrm{H}} = (\omega_0 - \omega_{rf})\boldsymbol{I_z} + \omega_1\boldsymbol{I_x} \tag{2.6a}$$

$$\widehat{\mathrm{H}} = \Omega\boldsymbol{I_z} + \omega_1\boldsymbol{I_x} \tag{2.6b}$$

Considering that there are now two magnetic fields acting on the spin magnetic moments, the static and the $B_1$ field, the concept of an effective field is introduced, i.e. the field about which the magnetization actually precesses upon application of the $B_1$ field, denoted $B_{\mathrm{eff}}$. The angle between the reduced and effective fields creates what is known as the 'tilt angle', and is routinely referred to in NMR experiments as a 90° (π/2) or 180° (π) pulse for a pulse that rotates the magnetization vector into the *xy*-plane and –*z*-axis respectively.

Following the rf pulse, the bulk magnetic moment continues to precess at the inherent resonant frequency characteristic of the spins within the sample, inducing a current in the same coil used to deliver the rf power. This signal, known as the *free induction decay* (FID), can be analyzed in modern experiments by a Fourier transform of this time-domain information to yield a spectrum in the frequency domain. Notably, the lifetime of the bulk magnetization vector in the *xy*-plane is not infinite. In other words, this rotation of the precession axis occurs only during the course of the $B_1$ field, and once removed, effects due to the external magnetic field will induce a return to thermal equilibrium. This phenomenon and its effect of reorienting the bulk magnetization vector after the rf pulse is referred to as nuclear spin relaxation.

### 2.2.5 Nuclear Spin Relaxation

In physical chemistry relaxation traditionally refers to the mechanism by which any system restores its equilibrium state from some perturbed or excited state. For nuclear spins in a magnetic field the equilibrium state is that in which there is no net transverse magnetization (*xy*-plane), whereas there is a very small but observable net magnetization along the *z*-direction, parallel to the external field. Immediately following the application of an rf pulse that generates coherent transverse magnetization, the spins are far from equilibrium, and relaxation is the process by which those spins return to their equilibrium state. The primary cause of this relaxation is the interaction of individual nuclear magnetic moments with local fields present in the sample that can interact with and ultimately rotate the nuclear magnetic moments to new orientations, much the way the rf pulse rotates the bulk magnetization. The extent of these interactions can vary significantly from one magnetic moment to another within a single sample as the local fields affect only microscopic distances and are highly orientation-dependent. The primary sources by which these local fields are generated to induce relaxation are (i) dipolar interactions, (ii) chemical shift anisotropy, (iii) paramagnetic species, and (iv) quadrupolar effects, with the latter being applicable only to nuclei with spin > ½ and significant quadrupole coupling.

In his pioneering article published in 1946,[2] Bloch describes the decay of magnetization back to $M_0$, thermal equilibrium via a series of equations through which he demonstrated the exponential decay of the magnetization parallel (z-axis) and perpendicular (xy-plane) to $M_0$ using two different time constants. These time constants are routinely denoted $T_1$ for the relaxation of $M_z$ (magnetization along the z-axis) and $T_2$ for relaxation of $M_y$ and $M_x$ (magnetization along the y and x axes respectively). The simple time dependence of the magnetization derived by Bloch is demonstrated by the series of equations (2.7a-c) shown below. [2,18]

$$\frac{dM_z}{dt} = {-(M_z - M_0)}/{T_1} \tag{2.7a}$$

$$\frac{dM_x}{dt} = {-M_x}/{T_2} \tag{2.7b}$$

$$\frac{dM_y}{dt} = {-M_y}/{T_2} \tag{2.7c}$$

A full relaxation of the system to return to equilibrium in an NMR experiment involves two components: relaxation of the longitudinal magnetization component, i.e. the recovery of the net z-magnetization from zero, and relaxation of the transverse magnetization in the *xy*-plane to yield a random distribution of spin-orientations in this plane. These descriptions of relaxation are typically denoted spin-lattice ($T_1$) and spin-spin ($T_2$) relaxation as the former involves a transfer of energy from the spins to the molecular motion of the sample, and the latter a dephasing of the spins relative to each other as they precess at different frequencies. In the commonly used vector model to visualize the spin magnetic moments in an NMR experiment, $T_1$ is described by the return of the net polarization vector to $+z$ alignment from the transverse plane, leaving no overall transverse magnetic moment. Conversely, $T_2$ can be visualized as the randomization of individual spin vectors within the transverse plane, ultimately resulting in a total magnetic moment of zero in this plane. These vector pictures of relaxation are demonstrated in **Figure 2.3** to depict the difference between spin-lattice and spin-spin relaxation mechanisms in NMR.

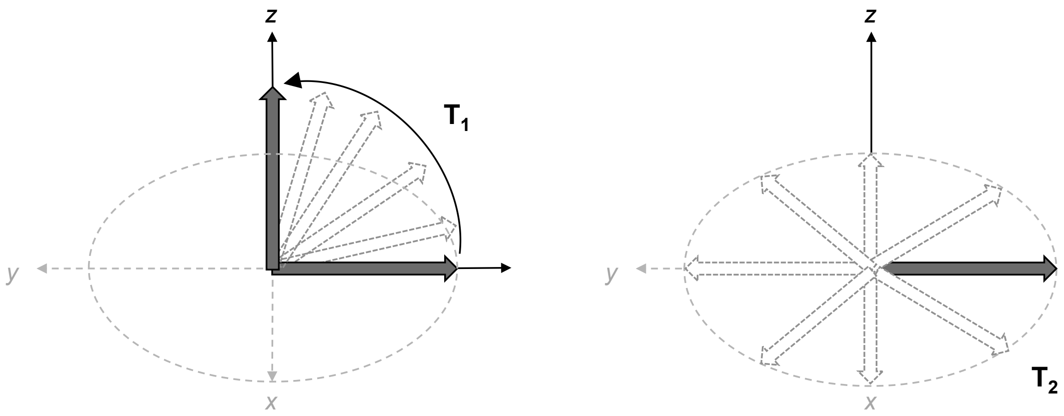

**Figure 2.3:** Vector representations of the two types of relaxation in an NMR experiment. Spin-lattice relaxation ($T_1$) depicted on the left shows the natural return of transverse magnetization to the +*z*-axis to align with the external $B_0$ field. Spin-spin relaxation ($T_2$) is conversely depicted as relaxation within the *xy*-plane to yield a net zero magnetization in the *x* or *y* directions.

## 2.3 Nuclear Spin Interactions of Spin-1/2 Nuclei

In the simplest experiment, the nuclei in a sample are perturbed and their precession in the *xy*-plane is detected to produce a spectrum with a single peak at the oscillatory frequency of the nucleus defined by the electronic environment in which these nuclei are found. From a practical perspective, it is rarely this straightforward, and a variety of influences on the behaviour of the spins in the magnetic field can have drastic effects on the outcome of the experiment. The role of these influencing interactions cannot be overstated in the application of *solid-state* NMR spectroscopy, which, being the primary technique employed in this thesis, is of great interest to the author. The lack of rapid molecular tumbling associated with molecules in a solution means that many of the interactions that are sufficiently averaged in the solution-state remain present in the solid-state such that they significantly affect experimental spectra. The remainder of this chapter will work through the descriptions of these interactions and their implications on the solid-state NMR experiment.

### 2.3.1 Chemical Shift Anisotropy (CSA)

The chemical shift typically observed in NMR results from a shielding of the nucleus by surrounding electrons.[16,21-24] Electrons, like nuclei, possess magnetic moments, and when placed in an external magnetic field, circulate to produce small magnetic fields that either add to or subtract from the overall $B_0$ field felt by the nucleus. The electron cloud that surrounds the nucleus is very often non-spherical; being a direct reflection of bonding environment. It is easy to imagine that the residual magnetic field felt at the nucleus will depend strongly on the orientation of this non-spherical electron cloud relative to the external field, which is to say that it depends strongly on the orientation of the molecule with respect to the external field. The orientation-dependence of the shielding is expressed mathematically by the chemical shielding tensor, $\boldsymbol{\sigma}$, as follows:

$$\sigma = \begin{bmatrix} \sigma_{xx} & \sigma_{xy} & \sigma_{xz} \\ \sigma_{yx} & \sigma_{yy} & \sigma_{yz} \\ \sigma_{zx} & \sigma_{zy} & \sigma_{zz} \end{bmatrix}$$

Note that the above tensor is described in terms of components relative to the laboratory axis frame, with coordinates $x, y, z$. It is useful, however, to express this in terms of the symmetry elements of the environment around the nucleus, called the PAF, or principal axis frame. By convention this frame of reference is chosen such that the chemical shielding tensor is diagonalized, and the values along the diagonal are therefore referred to as the principal values ($\sigma_{xx}^{PAF}, \sigma_{yy}^{PAF}, \sigma_{zz}^{PAF}$) of the chemical shielding tensor. Various compositions of these principal values yield the *isotropic shielding*, $\sigma_{iso}$, the *shielding anisotropy*, $\mathit{\Delta}$, and the *asymmetry*, $\eta$, all of which are defined as follows:[16,23,25]

$$\sigma_{iso} = \tfrac{1}{3}(\sigma_{xx}^{PAF} + \sigma_{yy}^{PAF} + \sigma_{zz}^{PAF}) \tag{2.8}$$

$$\mathit{\Delta} = \sigma_{zz}^{PAF} - \sigma_{iso} \tag{2.9}$$

$$\eta = {(\sigma_{xx}^{PAF} - \sigma_{yy}^{PAF})}\big/{\sigma_{zz}^{PAF}} \tag{2.10}$$

The above components can be used to define the chemical shift frequency that depends on both the isotropic and anisotropic interactions in a general expression:[16,25]

$$\omega_{CS}(\theta, \phi) = -\omega_0\sigma_{iso} - \tfrac{1}{2}\omega_0\mathit{\Delta}\{3\cos^2\theta - 1 + \eta\sin^2\theta\cos 2\phi\} \tag{2.11}$$

where $-\omega_0\sigma_{iso}$is the isotropic, or *orientation independent*, chemical shift frequency of the nucleus and $\theta$ and $\phi$ are the angles that describe the orientation of the molecule with respect to the external $B_0$ field (see the inset of **Figure 2.4**). Imagining the case for an axially symmetric molecule, the problem is reduced to two components; $\sigma_{zz}$ which lies along the symmetry axis of the molecule and $\sigma_{yy} = \sigma_{xx}$ which are perpendicular to the molecular axis, simplifying the expression for chemical shift frequency to:

$$\omega_{CS}(\theta, \phi) = -\omega_0\sigma_{iso} - \tfrac{1}{2}\omega_0(\sigma_{zz}^{PAF} - \sigma_{iso})\{3\cos^2\theta - 1\} \tag{2.12}$$

We can now consider what this will look like for a real powder sample, where there are many $\theta$ angles for which the principal axis frame (defined relative to the molecule) is oriented with respect to the external field. This gives rise to many unique chemical shift frequencies corresponding to the various crystallite orientations in a powder sample, resulting in the observation of a so-called powder pattern such as the simulated spectrum depicted in **Figure 2.4**. The shape of this powder pattern is defined by the asymmetry parameter $\eta$ defined above, where the three main features of the peak correspond to the situation in which each of three axes of the principal axis frame lie along the magnetic field direction.[16,25]

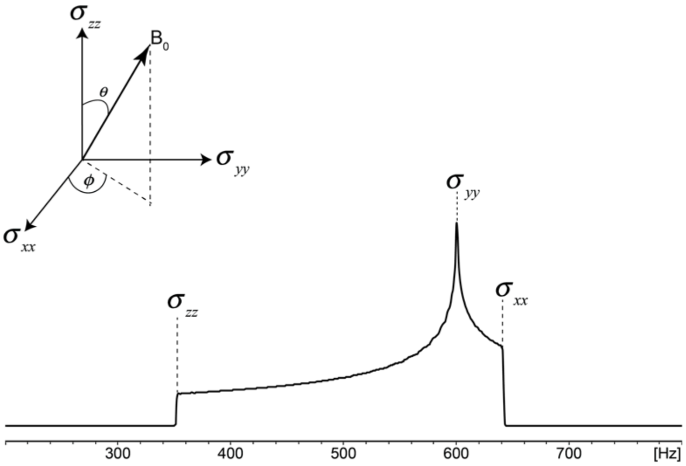

**Figure 2.4:** Simulated static powder pattern for a molecule with non-axial symmetry. The relative geometry of the PAF with respect to the external field, $B_0$, as defined by angles $\theta$ and $\phi$ is shown in the inset.

### 2.3.2 Dipolar Coupling

Much like chemical shielding, dipolar coupling is an orientation dependent effect that disproportionately affects solid-state NMR experiments due to a lack of inherent averaging mechanisms for a static powder sample. This effect can be easily visualized by imagining the small, localized magnetic field generated by a single nuclear magnetic moment in a sample, for example spin S. If a nearby spin (e.g. labeled I) is fortunate enough to be close to $S$ and lie within this microscopic field, the magnetic field experienced by I will be affected not only by the external field, but also by the local S field in which it resides. This effect is through-space in that it does not require or even use chemical bonding, thus nuclei in different molecules can experience a dipole-dipole interaction should they be sufficiently proximal to one another.

The Hamiltonian describing this dipolar coupling interaction can be written as follows:[25]

$$\widehat{\mathrm{H}} = -\frac{\mu_0}{4\pi}\frac{\gamma_I\gamma_S\hbar}{{r_{IS}}^3}[\mathrm{A} + \mathrm{B} + \mathrm{C} + \mathrm{D} + \mathrm{E} + \mathrm{F}] \tag{2.13}$$

where:

$$\begin{aligned} A &= \hat{\mathrm{I}}_z\hat{\mathrm{S}}_z(3\cos^2\theta - 1) \\ B &= -\frac{1}{4}[\hat{\mathrm{I}}_+\hat{\mathrm{S}}_- + \hat{\mathrm{I}}_-\hat{\mathrm{S}}_+](3\cos^2\theta - 1) \\ C &= -\frac{3}{2}\left[\hat{\mathrm{I}}_z\hat{\mathrm{S}}_+ + \hat{\mathrm{I}}_+\hat{\mathrm{S}}_z\right]\sin\theta\cos\theta\, e^{-i\phi} \\ D &= -\frac{3}{2}\left[\hat{\mathrm{I}}_z\hat{\mathrm{S}}_- + \hat{\mathrm{I}}_-\hat{\mathrm{S}}_z\right]\sin\theta\cos\theta\, e^{+i\phi} \\ E &= -\frac{3}{4}\left[\hat{\mathrm{I}}_+\hat{\mathrm{S}}_+\right]\sin^2\theta\, e^{-2i\phi} \\ F &= -\frac{3}{4}\left[\hat{\mathrm{I}}_-\hat{\mathrm{S}}_-\right]\sin^2\theta\, e^{+2i\phi} \end{aligned} \tag{2.14}$$

In the above expression $\mu_0$ is the permeability of free space, $\gamma_I$ and $\gamma_S$ are the gyromagnetic ratios of the coupled I and S spins, $r_{IS}$ is the internuclear distance between the I and S spins, with θ being the angle of the I-S internuclear vector with respect to the

$B_0$ field. The I and S operators in the above series of equations denote the various angular momentum components of the I and S spins respectively. Fortunately, the potentially complex problem is vastly simplified when considering that only the A and B terms of the above dipolar 'alphabet' will non-negligibly affect the Zeeman levels, and thus need to be considered. Notably, there is a distinction between heteronuclear and homonuclear dipolar coupling effects, where in the case of the former the B term is additionally dropped from the equation. This yields the first order average Hamiltonians for heteronuclear and homonuclear dipolar coupling effects respectively as:[16,25]

$$\widehat{\mathrm{H}}_d^{hetero} = -\mathrm{d}(3\cos^2\theta - 1)\hat{I}_z\hat{S}_z \tag{2.15}$$

$$\widehat{\mathrm{H}}_d^{homo} = -\mathrm{d}\frac{1}{2}(3\cos^2\theta - 1)[3\hat{I}_z\hat{S}_z - \hat{\boldsymbol{I}}\cdot\widehat{\boldsymbol{S}}] \tag{2.16}$$

where d is the collection of defined terms that make up the *dipolar coupling constant*: [16,23]

$$d = \left(\frac{\mu_0}{4\pi}\right)\frac{\gamma_I\gamma_S\hbar}{{r_{IS}}^3} \tag{2.17}$$

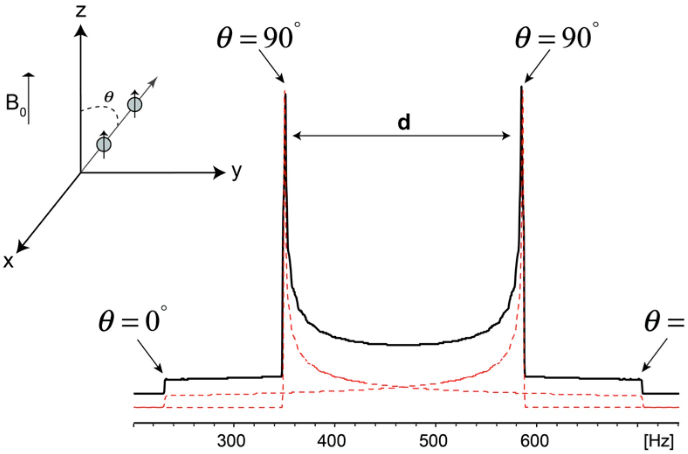

**Figure 2.5:** Simulated powder pattern of a two-spin system dipolar coupled to each other. The total signal is the superposition of two powder patterns. The angle theta shown on the spectrum is the angle between the internuclear vector joining the two coupled spins and the external magnetic field $B_0$. This classic lineshape, known as a Pake doublet, arises from the various orientations, θ, of the internuclear spin vector.

This difference arises from the fact that the B term in the dipolar alphabet (Equation 2.14) will only play a role when the transverse component of the S spin's magnetic dipole has a precession frequency close enough to spin I such that it can cause transitions. As this is only reasonably true when I and S are the same nucleus, and thus this term is only significant for homonuclear dipolar coupling. Additionally, the strength of this effect scales linearly with gyromagnetic ratio, in solid-state NMR experiments with higher $\gamma$ nuclei the effect is much larger, and therefore requires more effort to remove. For reference, the spin numbers and gyromagnetic ratios for relevant NMR nuclei are provided in **Table 2.1**.

**Table 2.1:** Nuclear Spins and gyromagnetic ratios for common and relevant nuclei studied in this thesis.

| Isotope | Spin Number (I) | Gyromagnetic Ratio ($10^6$ rad $s^{-1}$ $T^{-1}$) |
|---|---|---|
| **$^1$H** | 1/2 | 267.52 |
| **$^{31}$P** | 1/2 | 108.41 |
| **$^6$Li** | 1 | 39.37 |
| **$^7$Li** | 3/2 | 103.96 |
| **$^{23}$Na** | 3/2 | 70.70 |
| **Electron** | 1/2 | ~170000 |

A typical static solid-state NMR line shape for an isolated dipolar coupled spin pair is simulated in **Figure 2.5**, where the classic line shape, called a Pake pattern, is observed.[26] This pattern is in actuality the sum of two powder patterns, where the angle generated by the internuclear vector that joins the two coupled spins relative to the external $B_0$ field determines the observed shift. The result is this powder pattern, where when the angle, θ, relative to the field is 90°, intensity is at a maximum, yielding the 'horns' of the spectrum in **Figure 2.5**. Although the orientation-dependence is easily averaged in solution-state NMR by the rapid tumbling of molecules in the sample, this is not the case in solid-state NMR where a stationary sample is made up of many crystallites with random orientations with respect to the external field.

## 2.4 Magic Angle Spinning (MAS)

Upon reviewing the shielding and dipolar interactions that serve to broaden and seemingly complicate NMR spectra of solids, it might be difficult to imagine how this technique can provide any useful information for real, complex samples. Indeed, observing static powder patterns where samples have contributions from CSA, dipole-dipole coupling and in some cases also quadrupolar interactions (see below), the spectra can be very complicated. Fortunately, by manipulating the known orientation-dependence of many of the interactions described above, the spectra can be somewhat simplified. In solution-state NMR, these interactions are not observed due to the averaging of the recurring $3\cos^2\theta - 1$ term that occurs on the timescale of the NMR experiment as the molecules sample all possible orientations due to molecular tumbling. A similar effect can be produced in solids by rotating the sample at the so-called *magic angle* of 54.74° relative to the external field, thus averaging this term to zero. This effectively averages the anisotropic interactions from both chemical shielding and heteronuclear dipolar coupling (refer to Equations 2.12 and 2.15) provided the spinning rate is sufficiently faster than the anisotropy. This technique of *magic angle spinning* (MAS), is frequently used to average, either fully or partially, the various orientation-dependent interactions that show up in solid-state spectra.[27,28]

In practice, this averaging is often incomplete, resulting in visible spinning sidebands, expressed as additional peaks in the NMR spectrum that flank the isotropic shift and are separated by the MAS rotation frequency, as shown in **Figure 2.6**. These typically appear in samples with large anisotropic interactions that are not completely averaged by an MAS rate slower than that of the strength of the interaction in Hz. Even in cases where the averaging by MAS is incomplete, the isotropic chemical shift can be identified by the resonance that does not change its resonance position with changing MAS rotation rate. Current state-of-the-art equipment can routinely achieve rotation speeds of 40-60 kHz, with specialty equipment reaching >100 kHz in some cases. These speeds are often more than enough to average anisotropic interactions in a typical $^{1}$H or $^{7}$Li spectrum, however, as will be demonstrated in this thesis, there are many complex cases where averaging of anisotropic interactions are impossible with current equipment.

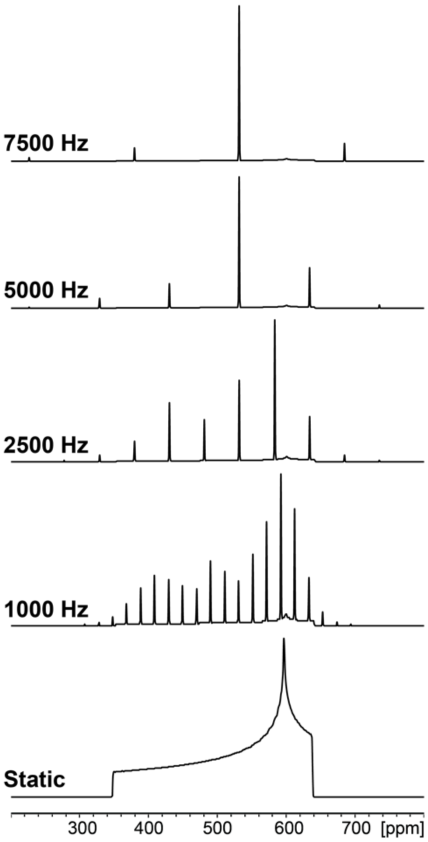

**Figure 2.6:** Simulated NMR solid-state spectra broadened by chemical shift anisotropy at various MAS rotation rates. The broad powder pattern observed at $\nu_r$=0 Hz is broken into discrete frequency bins located exactly the spinning frequency away from the isotropic chemical shift, known as spinning sidebands. At faster MAS rates the intensity converges into the isotropic resonance, until the anisotropy is sufficiently averaged such that only the orientation-independent chemical shift ($\delta_{iso}$) is observed.

## 2.5 The Quadrupole Interaction

Thus far we have limited our description of NMR to nuclei with spin-1/2. This is perhaps misleading, as the periodic table is flush with nuclei that have spin greater than ½. These quadrupolar nuclei possess a non-spherically symmetric charge distribution at the nucleus that can interact with the electronic environment created by the molecular structure called the electric field gradient (EFG) to produce the *quadrupolar coupling interaction*. Similar to chemical shielding, the EFG is a second-rank tensor that can be diagonalized with principal elements $V_{xx}, V_{yy}$, and $V_{zz}$. As one might imagine, this interaction between the quadrupole moment of the nucleus and the EFG tensor depends necessarily on molecular symmetry. For example, when placed in a site with perfect cubic symmetry, the quadrupolar interaction is completely diminished regardless of the nuclear quadrupole moment, as all three principal elements of the EFG tensor are reduced to zero. The quadrupolar interaction is most frequently described by two parameters, the qudarupolar coupling constant, $C_Q$, and the asymmetry parameter, $\eta_Q$ as defined by:

$$C_Q = \frac{e^2 Q V_{zz}}{h} \tag{2.18}$$

$$\eta_Q = \frac{V_{yy} - V_{xx}}{V_{zz}} \tag{2.19}$$

This close relationship between magnitude of the spectroscopically observed interaction and chemical environment by way of the EFG tensor makes the quadrupolar interaction a highly effective tool for studying and understanding molecular bonding in a wide variety of materials.

Recall from the earlier discussion that any nucleus with spin I has 2I+1 possible energy levels that when placed in a magnetic field become equally separated by way of the Zeeman interaction. These energy levels created by Zeeman splitting are further shifted by the first order element of the quadrupolar interaction Hamiltonian, $H_Q^{(1)}$. For a typical $I = \frac{3}{2}$ example depicted in **Figure 2.7**, the shift causes no change in the energy splitting (i.e. the resonance frequency) of the central transition ($\frac{1}{2} \rightarrow -\frac{1}{2}$), and the resulting spectrum differs from that of a spin-1/2 nucleus only in the presence of equally spaced satellite transitions (ST) due to the equal but opposite energy shift of the $\frac{3}{2} \rightarrow \frac{1}{2}$ and $-\frac{1}{2} \rightarrow -\frac{3}{2}$ transitions. This is the extent of the energy splitting in many cases where the quadrupolar interaction is on the order of the Zeeman splitting; however, should the quadrupole coupling become significant (again with respect to Zeeman) a second order term in the Hamiltonian must be considered. This second-order perturbation of the energy levels (**Figure 2.5**, $H_Q^{(2)}$) will invariably affect the frequency of the central transition, and the orientation-dependence of the EFG tensor will affect the observed NMR line shape.

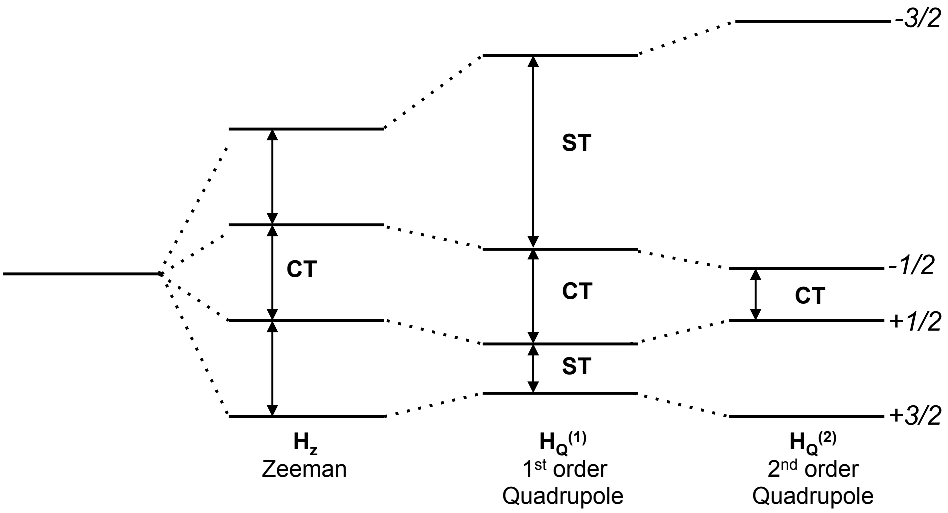

**Figure 2.7:** Energy level splitting due to Zeeman, 1st order quadrupole and 2nd order quadrupole interactions. The central transition and satellite transitions are labeled as CT and ST respectively.

While the use of MAS is highly effective at increasing the resolution of solid-state spectra, the effect of magic angle spinning on NMR spectra of quadrupolar nuclei is complex, and depends in part on the strength of the interaction, and thus whether or not the second order quadrupole effect needs to be considered. In general, the resonance frequency for a spinning sample can be described by[29]:

$$\nu = \nu_{\mathrm{iso}} + C_0 \nu_{\mathrm{QIS}} + C_2 P_2(\cos\theta) * \nu_2(\alpha, \beta) + C_4 P_4(\cos\theta) * \nu_4(\alpha, \beta) \tag{2.20}$$

where in the above expression the second-order polynomial that corresponds to the first-order quadrupole effect is defined as:[29]

$$P_2(\cos(\theta)) = \frac{1}{2}[3\cos^2\theta - 1] \tag{2.21}$$

and the fourth-order term describing the second-order quadrupolar interaction is:[29]

$$P_4(\cos(\theta)) = \frac{1}{8}[35\cos^4\theta - 30\cos^2\theta + 3] \tag{2.22}$$

There is evidently no single value of θ that satisfies the condition to remove the orientation dependent terms from the frequency dependence, and thus magic angle spinning completely averages only the first-order effects. Therefore, while spinning at the magic angle alone does affect the spectra in some way, the broadening and characteristic line shapes are not completely removed. Some very talented NMR spectroscopists have come up with ways to mitigate or remove orientation-dependent effects of the quadrupole interaction, including feats of engineering such as spinning the sample at two rotation angles (double rotation, or DOR) or complex pulse sequences that filter out the anisotropic interactions through coherence pathway selection (Multiple Quantum Magic Angle Spinning, or MQMAS).[29-33]

Thus far the response of the bulk nuclear magnetization vector to the rf pulse has only very briefly been discussed, specifically in the context of a '90°' or '180°' pulse. For a standard nucleus with spin $I = \frac{1}{2}$, changing the length of the rf pulse directly influences the tilt angle of the magnetization vector in a perfect sinusoidal fashion. This behaviour, called nutation, cannot always be assumed for quadrupolar nuclei, and in fact depends largely on the strength of the quadrupole interaction. It is thus closely related to the molecular environment of the nucleus, and can in theory be used to discern information about molecular environments.[29,34] In general, there are three possible conditions that give rise to differences in nutation behaviour; a $C_Q$ that is much smaller than the radiofrequency, a $C_Q$ that is much larger than the rf, and a $C_Q$ value comparable to the rf.

In the initial case, if the quadrupolar coupling interaction is insignificant relative to the rf pulse, the nutation frequency will equal the frequency of the pulse as is observed in a typical spin-1/2 situation. In the opposite scenario where the $C_Q$ is very large relative to the rf, the nutation frequency is still sinusoidal in nature, but simply scaled by a factor of I+1/2. The most difficult case arises when $C_Q$ is the same order of magnitude as the rf, and in this case non-sinusoidal complex nutation response is observed.[34] **Figure 2.8** demonstrates this effect, where the nutation behaviour of a spin-5/2 nucleus is observed with respect to rf pulse length.

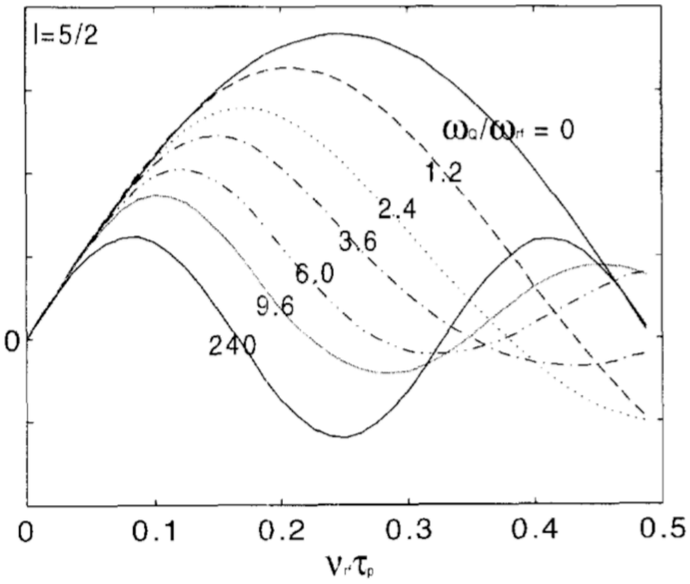

**Figure 2.8:** Plot of the calculated signal intensity versus rf pulse length for various $\omega_Q/\omega_{rf}$ (quadrupole coupling/radiofrequency). The curves illustrate the effect on the nutation of the quadrupolar spin as a function of the quadrupole coupling interaction strength relative to the rf pulse. Reprinted from *Geoderma*, 80, Kentgens, A.P.M., 'A practical guide to solid-state NMR of half-integer quadrupolar nuclei with some applications to disordered systems', ©1997 with permission from Elsevier.

Quadrupolar nuclei make up the majority of atoms, and thus being able to study them and in some cases use their unique properties to glean information is extremely valuable.[29,35] Somewhat surprisingly, while the majority of this thesis deals with nuclei that have a quadrupole moment ($^{23}$Na, $^{7}$Li) the obvious effects are often overshadowed by the much more significant interaction of the nuclei with the unpaired electrons in the paramagnetic samples studied. Nevertheless, particularly in the case of $^{23}$Na, the quadrupole coupling interaction can have an effect that increases the complexity of these spectra. Specifically, $^{23}$Na nutation behaviour and how it could be useful to characterize environments will be discussed in greater detail in Chapter 8 of this thesis.

## 2.6 Paramagnetism in Solid-State NMR

### 2.6.1 Unpaired Electrons in a Magnetic Field

Electrons, much like nuclei, possess spin angular momentum that gives rise to a magnetic moment that causes them to behave similarly in a magnetic field. In diamagnetic materials, the pairing of electrons in filled atomic orbitals acts to cancel the magnetic effects yielding a net zero magnetic moment. Paramagnetic materials, by definition, contain singly populated orbitals, leaving unpaired electrons whose magnetic moments are not effectively cancelled by pairing. These electrons act as small bar magnets, analogous to nuclei that can interact with nearby magnetic fields. The magnetic moment of an electron is defined by the term $\mu_e$ and is related to the electron spin angular momentum ($\mathbf{S}$) as defined by:

$$\boldsymbol{\mu}_\mathbf{e} = -\mu_B g_e \mathbf{S} \tag{2.23}$$

where $g_e$ is the electron g factor and $\mu_B$ is the electron Bohr magneton.[36] In electron paramagnetic resonance (essentially the electron equivalent to NMR), or EPR, this hyperfine interaction leads to a splitting effect. Due to the extremely fast relaxation of the electron spins relative to the observed nuclear spins, there is an overall averaging of the electron magnetic moment to produce a net shift to the nuclear resonance frequency in the NMR experiment. The nucleus is therefore coupling to the time-averaged electron spin that is dependent on the molar magnetic susceptibility ($\chi_M$) of the material: [36]

$$\langle S_z \rangle = \frac{-B_0}{\mu_0 g_e N_0 \mu_B} \chi_M \tag{2.24}$$

where $B_0$ is the external field, $\mu_0$ the permeability, and $N_0$ is Avogadro's number. Just as two nuclear magnetic moments can interact with each other through, for example, a nuclear dipolar interaction, nuclei and electrons can analogously communicate via a *hyperfine coupling interaction.* The second-rank tensor **A** can be used to describe this nuclear-electron interaction and can be conveniently separated into contributions from the Fermi Contact ($A_{FC}$) and dipolar ($A_{dip}$), only the latter of which is anisotropic.[37]

$$\boldsymbol{A} = A_{FC} + \boldsymbol{A_{dip}} \tag{2.25}$$

### 2.6.2 The Fermi Contact Shift

The isotropic paramagnetic shift to the NMR frequency is governed by the Fermi Contact shift due to the transfer of unpaired electron spin density to the observed nucleus.

The magnitude of this shift contribution can be expressed in terms of the hyperfine coupling constant and magnetic susceptibility by:[36]

$$\delta_{FC,iso} = \frac{A_{FC}}{\hbar}\frac{\chi_M}{\mu_0\gamma_N\mu_B g_e} \tag{2.26}$$

The FC coupling constant, $A_{FC}$, depends on the electron spin density at the nucleus, $\rho_s$ (N) via[37]

$$A_{FC} = \frac{\mu_0}{3S}\hbar\gamma_N\mu_B g_e\rho_S(N) \tag{2.27}$$

By combining Equations 2.29 and 2.30 a final solution for the isotropic paramagnetic shift from the Fermi contact contribution can be expressed as:

$$\delta_{FC,iso} = \frac{1}{3S}\rho_S(N)\chi_M \tag{2.28}$$

where $\rho_S(N)$ is the spin density transferred to a nucleus with spin I via the FC interaction.[37] The ability to determine the electron spin density at the nucleus *via* the FC hyperfine coupling constant using first principles calculations has allowed for the accurate prediction of paramagnetic NMR shifts in a variety of solids, including many related to energy storage applications.[13,38,39]

### 2.6.3 The Pseudocontact Shift

Whereas the Fermi contact shift can be approximated by the transfer of unpaired electron spin density to the site of the nucleus, the *pseudocontact shift* (PCS) results from a dipolar coupling interaction between the nuclear and electron magnetic moments.[40,41]

The total paramagnetic contribution to the chemical shift should formally be written as follows:

$$\delta_{para} = \delta_{FC} + \delta_{PCS} \tag{2.29}$$

where $\delta_{FC}$ and $\delta_{PCS}$ are the Fermi contact and pseudocontact contributions to the shift respectively. The latter of the two is a result of through-space interactions between the magnetic anisotropy at the transition metal center and anisotropic hyperfine interactions.[42] The PCS shift depends directly on the principal components of the electron g-tensor and by assuming it is isotropic, the PCS shift is reduced to zero. For symmetric transition metal environments this assumption is typically valid. In general for inorganic paramagnetic solids, the Fermi contact term is considered the dominant shift contribution, and throughout this thesis it will be used exclusively to predict paramagnetic shifts in transition metal compounds.

## 2.7 Summary

This chapter provides some of the essential fundamental elements of NMR spectroscopy of solid-state materials and a brief introduction to effects of paramagnetism on NMR. The experimental findings presented throughout this thesis rely on the principals outlined here that allow nuclear magnetic resonance to work as an effective method for many types of scientific investigation. In particular, this thesis focuses on paramagnetic solid-state materials and their study by ssNMR in order to understand the properties that contribute to their electrochemical performance. While the physical concepts that give rise to NMR phenomena have been presented here, Chapter 3 aims to demonstrate how these concepts are used in practice to obtain useful information from complex samples. It will also provide practical aspects such as how to determine coupling constants to assign experimental NMR shifts in paramagnetic materials.

## 2.8 References

(1) Rabi, I. I.; Zacharias, J. R.; Millman, S.; Kusch, P. *Physical Review* **1938**, *53* (4), 318.

(2) Bloch, F. *Physical Review* **1946**, *70* (7), 460.

(3) Grey, C. P.; Dupré, N. *Chem. Rev.* **2004**, *104* (10), 4493.

(4) Grey, C. P.; Lee, Y. J. *Solid State Sciences* **2003**, *5* (6), 883.

(5) Lee, Y. J.; Wang, F.; Grey, C. P. *J. Am. Chem. Soc.* **1998**, *120* (48), 12601.

(6) Davis, L. J. M.; Goward, G. R. *J. Phys. Chem. C* **2013**, *117* (16), 7981.

(7) Davis, L. J. M.; Heinmaa, I.; Ellis, B. L.; Nazar, L. F.; Goward, G. R. *Phys. Chem. Chem. Phys.* **2011**, *13* (11), 5171.

(8) Smiley, D. L.; Tessaro, M. Z.; He, X.; Goward, G. R. *J. Phys. Chem. C* **2015**, *119* (29), 16468.

(9) Smiley, D. L.; Davis, L. J. M.; Goward, G. R. *J. Phys. Chem. C* **2013**, *117* (46), 24181.

(10) Langer, J.; Smiley, D. L.; Bain, A. D.; Goward, G. R.; Wilkening, M. *J. Phys. Chem. C* **2016**, *120* (6), 3130.

(11) Ruprecht, B.; Wilkening, M.; Uecker, R.; Heitjans, P. *Phys. Chem. Chem. Phys.* **2012**, *14* (34), 11974.

(12) Carlier, D.; Blangero, M.; Ménétrier, M.; Pollet, M.; Doumerc, J.-P.; Delmas, C. *Inorg. Chem.* **2009**, *48* (15), 7018.

(13) Carlier, D.; Ménétrier, M.; Grey, C.; Delmas, C.; Ceder, G. *Phys. Rev. B* **2003**, *67* (17), 174103.

(14) Clément, R. J.; Pell, A. J.; Middlemiss, D. S.; Strobridge, F. C.; Miller, J. K.; Whittingham, M. S.; Emsley, L.; Grey, C. P.; Pintacuda, G. *J. Am. Chem. Soc.* **2012**, *134* (41), 17178.

(15) Levitt, M. H. *Spin Dynamics*, 2nd ed.; John Wiley & Sons: West Sussex, England, 2008.

(16) Duer, M. J. *Introduction to Solid-State NMR Spectroscopy*; Blackwell Publishing Ltd.: Oxford, 2004.

(17) Keeler, J. *Understanding NMR Spectroscopy*; John Wiley & Sons, 2011.

(18) Harris, R. K. *Nuclear Magnetic Resonance Spectroscopy*; Pittman: London, 1983.

(19) Zeeman, P. *Nature* **1897**, *55* (1), 347.

(20) Keeler, J., Lecture Notes. Cambridge, 1998.

(21) Ramsey, N. F. *Physical Review* **1950**, *78* (6), 699.

(22) Facelli, J. C. *Progress in Nuclear Magnetic Resonance Spectroscopy* **2011**, *58* (3-4), 176.

(23) Laws, D. D.; Bitter, H.; Jerschow, A. *Angew. Chem. Int. Ed.* **2002**, *41* (17), 3096.

(24) Apperley, D. C.; Harris, R. K.; Hodgkinson, P. *Solid State NMR Basic Principles and Practice*; Momentum Press: New York, NY, 2014.

(25) Duer, M. J. *Solid state NMR spectroscopy: principles and applications*; Blackwell Science Ltd.: London, 2002.

(26) Pake, G. E. *J. Chem. Phys.* **1948**, *16* (4), 327.

(27) Andrew, E. R.; Bradbury, A.; Eades, R. G. *Nature* **1958**, *182* (4), 1659.

(28) Andrew, E. R.; Bradbury, A.; Eades, R. G. *Nature* **1959**, *183* (4), 1802.

(29) Kentgens, A. P. M. *Geoderma* **1997**, *80*, 271.

(30) Medek, A.; Harwood, J. S.; Frydman, L. *J. Am. Chem. Soc.* **1995**, *117* (51), 12779.

(31) Edén, M.; Grinshtein, J.; Frydman, L. *J. Am. Chem. Soc.* **2002**, *124* (33), 9708.

(32) Samoson, A.; Pines, A. *Review of Scientific Instruments* **1989**, *60* (10), 3239.

(33) Cochon, E.; Amoureux, J. P. *Solid State Nucl. Magn. Reson.* **1993**, *2* (5), 205.

(34) Spencer, T. L.; Goward, G. R.; Bain, A. D. *Can. J. Chem.* **2011**, *89* (7), 764.

(35) Koller, H.; Engelhardt, G.; Kentgens, A. *The Journal of Physical …* **1994**.

(36) Bertini, I.; Luchinat, C.; Parigi, G. *Progress in Nuclear Magnetic Resonance Spectroscopy* **2002**, *40* (3), 249.

(37) Kaupp, M.; Köhler, F. H. *Coordination Chemistry Reviews* **2009**, *253* (19-20), 2376.

(38) Castets, A.; Carlier, D.; Trad, K.; Delmas, C.; Ménétrier, M. *J. Phys. Chem. C* **2010**, *114* (44), 19141.

(39) Broux, T.; Bamine, T.; Fauth, F.; Simonelli, L.; Olszewski, W.; Marini, C.; Ménétrier, M.; Carlier, D.; Masquelier, C.; Croguennec, L. *Chem. Mater.* **2016**, *28* (21), 7683.

(40) Bertini, I.; Luchinat, C.; Parigi, G. *Concepts Magn. Reson.* **2002**, *14* (4), 259.

(41) McConnell, H. M.; Robertson, R. E. *J. Chem. Phys.* **1958**, *29* (6), 1361.

(42) Mondal, A.; Gaultois, M. W.; Pell, A. J.; Iannuzzi, M.; Grey, C. P.; Hutter, J.; Kaupp, M. *J. Chem. Theory Comput.* **2017**, *14* (1), 377.

# Chapter 3: Solid-State NMR Spectroscopy Techniques for the Study of Energy Storage Materials

## 3.1 Introduction

In the current global energy climate, there is more motivation than ever to replace fossil fuels with viable alternative energy solutions. One part of this global shift involves the use of energy storage materials to replace gasoline in the transportation sector. Although lithium ion batteries have achieved considerable success in the commercial market, there is much room for improvement, especially in the areas of long-term cycling stability, rate performance, and storage capacity. Solid-state NMR has become a highly valued method in the study of existing commercial electrode materials, as it offers a unique view of the local chemical environments that are ultimately responsible for bulk performance. This is being further extended to new electrode materials that have not been tested commercially, in an effort to identify molecular properties that overall benefit the battery performance, and can thus be incorporated into the design of new materials. Despite the ability of ssNMR to probe these properties, there are many challenges associated with the use of this technique, many of which arise from the presence of unpaired electrons at the redox active transition metal in most cathode materials. This chapter aims to introduce the specific NMR experiments utilized within this thesis to effectively study structural and dynamics properties in paramagnetic cathode materials for lithium and sodium ion batteries. It will review the differences between the Li and Na nuclei as it relates to the NMR experiment, and the ways that these differences manifest experimentally. Furthermore, a brief review of *ab initio* calculation methods utilized in the work presented here will be undertaken, with an emphasis on the current methods used to calculate chemical shifts in paramagnetic solids by density functional theory.

## 3.2 Challenges in the Study of Paramagnetic Materials by Solid-State NMR

### 3.2.1 Comparing Experimental NMR Methods for $^7$Li *versus* $^{23}$Na

Lithium cathode materials have been investigated using $^{6,7}$Li solid-state NMR for over a decade, with the first experiments roughly correlating with the commercialization of the lithium ion battery in 1990.[1-4] More recently, the renewed interest in sodium ion batteries, especially for large-scale stationary storage applications, has prompted the exploration of $^{23}$Na NMR as a viable technique for characterizing electrode materials in this realm.[5-9] Due to the similar nature of the cathodic structures for both Li and Na batteries, many of the challenges related to the paramagnetic nature of the redox-active transition metal are applicable to both nuclei. A comparison of relevant NMR parameters for $^7$Li, $^6$Li and $^{23}$Na nuclides is shown in **Table 3.1**, highlighting the similarities between the nuclei of interest.

**Table 3.1:** Comparison of some common NMR parameters for relevant Li and Na isotopes.

| Nucleus | Ionic Radius (Å)[10] | Spin Number | Gyromagnetic Ratio ($10^6$ rad $s^{-1}T^{-1}$) | Quadrupole Moment[11] ($10^{-25}$ $m^2$) |
|---|---|---|---|---|
| **$^6$Li** | 0.76 | 1 | 39.37 | -8.08 |
| **$^7$Li** | 0.76 | 3/2 | 103.96 | -40.1 |
| **$^{23}$Na** | 1.02 | 3/2 | 70.70 | 104 |

The major difference in the table above is evident in the nuclear quadrupole moments, where *Q* for $^{23}$Na is an order of magnitude larger than either of the NMR-active lithium isotopes. This is especially obvious in the NMR spectra of some common Na salts, such as $Na_2CO_3$ or $Na_2SO_3$, that exhibit observable second-order quadrupolar lineshapes in the solid state.[12,13] This is in contrast to the equivalent Li counterparts, where the quadrupole coupling constants are not large enough to manifest these second-order effects in $^{7}$Li NMR spectra.[14,15]

In practice, the quadrupole coupling constants in lithium salts are very minimal, and simple MAS is usually enough to achieve the resolution necessary to observe isotropic spectra.[15] In contrast, things are not quite so simple for sodium, where a variety of methods are frequently needed to decouple the quadrupolar parameters from the isotropic shifts, even for spectra of relatively simple molecules.[13,16] In 1995 Medek *et al.*[17] introduced the popular Multiple-Quantum Magic Angle Spinning (MQMAS) technique that is now routinely used to aid in the investigation of quadrupolar nuclei in solids. This technique uses a clever sequence of rf pulses to manipulate the spin coherence such that only transitions filtered through multiple quantum coherence orders are observed. This allows one to observe a two-dimensional spectrum in which the second frequency dimension contains purely isotropic chemical shift information. The method is especially useful for samples with multiple Na environments, as it separates overlapping quadrupole-broadened lineshapes by chemical shift.

In general, with the exception of the larger quadrupole interaction for the $^{23}$Na nucleus, the similarities between $^{23}$Na and $^{6}$Li or $^{7}$Li NMR tend to outweigh the differences, and thus in practice they can in many cases be treated equivalently. This is especially true for samples containing unpaired electrons, where the electron spin density tends to be the most significant factor in terms of line broadening and chemical shift contributions. These interactions are independent of quadrupole moment, and are thus comparable for the alkali ions, allowing many of the approaches used for $^{6,7}$Li to be extended to $^{23}$Na NMR of paramagnetic cathode materials.

### 3.2.2 NMR of Paramagnetic Cathode Materials for Alkali Ion Batteries

The theoretical impact of unpaired electrons on the NMR experiment were outlined in Chapter 2; in this section the practical manifestation of these effects will be discussed. Many of the cathode materials for lithium or sodium ion batteries contain first-row transition metals (e.g. Co, Fe, Mn) that contain unpaired electrons in at least one redox-accessible oxidation state. The synthesis of structural analogues with a diamagnetic metal to replace the paramagnetic center offers the unique opportunity to establish the effect arising purely from unpaired electrons on the $^{7}$Li or $^{23}$Na spectrum. The spectra in **Figure 3.1** demonstrate this effect in a pair of sodium fluorophosphates, where the most obvious differences are apparent in the total span of the spinning sideband manifold and the breadth of the isotropic shift, or Full-Width at Half-Maximum (FWHM). These effects arise from different components of the hyperfine interaction, with the former being a manifestation of the anisotropic dipolar interaction, the latter relating to the orientation-dependence of the magnetic susceptibility that contributes to the isotropic Fermi Contact shift.

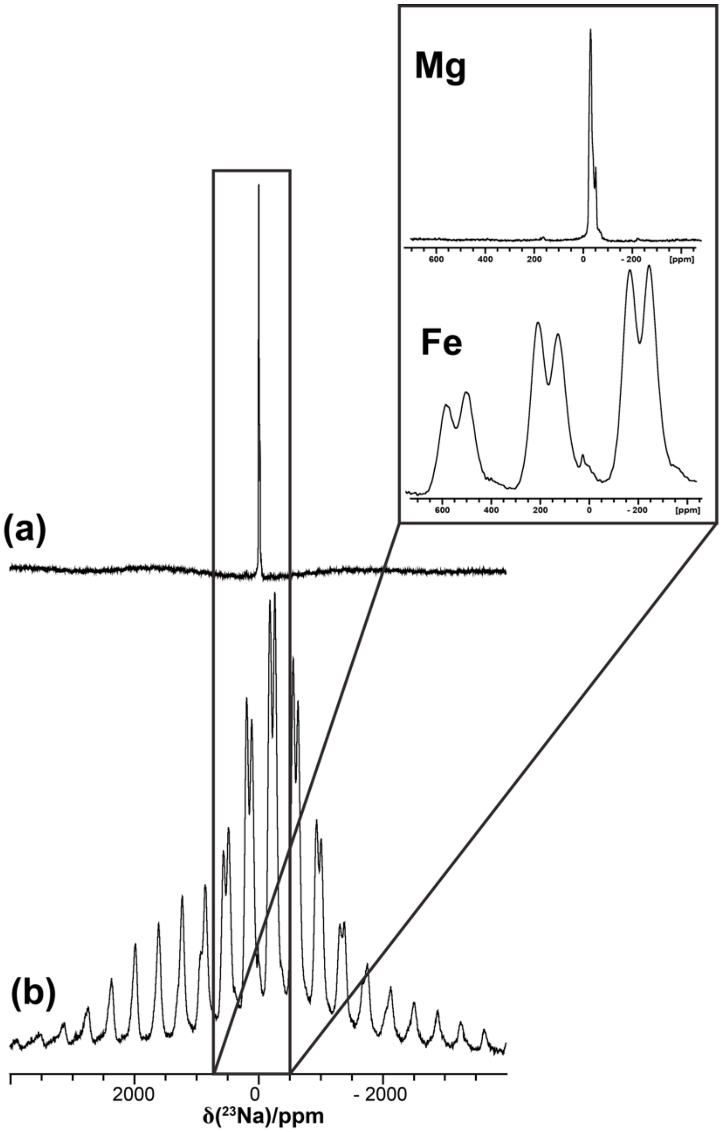

**Figure 3.1:** Comparison of the 1D $^{23}$Na NMR spectra (30 kHz MAS) of **(a)** $Na_2MgPO_4F$ ($d^0$, no unpaired electrons) and **(b)** $Na_2FePO_4F$ ($d^6$, 4 unpaired electrons). The regions surrounding the isotropic peaks in $Na_2FePO_4F$ is magnified to demonstrate the significantly larger FWHM for the paramagnetic sample.

In addition to the major effect of both isotropic and anisotropic broadening due to unpaired electron spin density, relaxation effects can severely limit measureable dynamics timescales by NMR for paramagnetic materials. The strong local fields generated by the unpaired electrons in the sample induce relaxation that is in some cases several orders of magnitude faster than for an equivalent diamagnetic sample. As will become evident in later sections of this thesis, this fast relaxation imposes an upper limit on the exchange rates that are observable experimentally using traditional exchange spectroscopy techniques. Furthermore, the large spinning sideband manifolds often require MAS on the upper limit of what is commercially available, usually 40-60 kHz, that can make observation of even the isotropic shifts nontrivial. Despite these apparent drawbacks, the electron-nuclear interaction can actually benefit the spectroscopy, especially for small non-polarizable nuclei such as lithium or sodium that exhibit a typical chemical shift range on the order of ±10 ppm. While Na has the benefit of a more significant quadrupole moment that can induce unique changes to the central transition depending on bonding environment, this often requires more advanced techniques such as MQMAS to make sense of experimental data. The vastly expanded chemical shift range afforded by the electron-nuclear hyperfine interaction causes the resonant frequency to be highly sensitive to the surrounding environment. Although not necessarily interpretable by simple rules regarding chemical shielding, this offers the opportunity for site-specific information to be gleaned from relatively complex solid-state materials. Furthermore, the fast relaxation effects actually allow for rapid signal averaging, requiring very short recycle delays between pulses in the NMR experiment. The site resolution unique to paramagnetic materials is useful not only for obtaining structural insight, but also for observing ion hopping between individual crystallographic sites.

## 3.3 Investigating Chemical Exchange in Energy Storage Materials by Solid-State NMR

NMR has been used extensively to study chemical exchange in both the solution and solid-state fields. One of the most basic and fundamental principles in NMR, the sensitivity of the resonance frequency to the magnetic environment, is in many ways the key to observing chemical exchange. However, the way in which any dynamic process affects a particular magnetic environment can vary dramatically. The process of chemical exchange can be specifically differentiated from other dynamics processes in that it occurs at a state of macroscopic equilibrium, i.e. no chemical changes are occurring on the lab scale, and the sample itself is not changing over the course of the NMR experiment. Rather, the chemical exchange occurs such that otherwise magnetically inequivalent atoms effectively swap positions, thus maintaining the state of the sample before and after exchange. This dynamic process can manifest in a variety of ways, ranging from a simple ring flip of a molecule in solution to the hopping of ions from one crystallographic site to another in a solid lattice.[18,19]

Perhaps the most important aspect to consider when embarking on a study chemical exchange is the timescale of the exchange process relative to the timescale of the NMR experiment. As both chemical exchange and nuclear relaxation are treated in similar ways by most NMR exchange experiments, the timescale of the experiment is largely determined by the nuclear relaxation properties of the nuclei undergoing the dynamic process of interest. The exchange timescales can therefore be described generally by three categories: fast, intermediate, and slow exchange, where the bracket into which a particular dynamic process can be classified often determines the specific NMR experiment(s) that should be implemented to study kinetics in that system.

While a significant number of dynamics processes fall into the fast and intermediate exchange classifications and therefore have been extensively studied,[20,21] the primary focus of this section will be the slow chemical exchange timescale. The dynamic process is considered ‘slow’ if exchange rates are much smaller than the frequency difference between the NMR shifts of the exchanging sites. In this regime, there is no observable coalescence and the peaks are often well separated, permitting the use of a suite of rather elegant spectroscopic methods to study such systems. Perhaps most widely used among these methods is a two-dimensional exchange spectroscopy experiment (2D EXSY) that takes advantage of a nuclear Overhauser effect spectroscopy (NOESY) pulse sequence that cleverly uses the change in magnetic environment of a set of spins during the course of the experiment’s mixing time to observe the chemical exchange process via the existence of an off-diagonal peak in the 2D spectrum.[22] Despite its ability to provide excellent visual confirmation of chemical exchange, and its practical use as a method for qualitative identification of exchange pairs, it is not necessarily the most efficient or effective method for quantitative determination of exchange rates. A seemingly simpler method, selective inversion recovery (or more generally, selective perturbation), allows one to measure exchange rates for any number of sites much more efficiently than the series of 2D EXSY experiments required to obtain precisely the same information. Both of these experimental methods and related data analysis will be discussed in detail in subsequent sections.

Before commencing a description of exchange spectroscopy methods, it is helpful to see how this information might be used to understand physical processes. Regardless of the exchange timescale or method used to measure rates, one of the many benefits of the ability to quantitatively investigate chemical exchange using NMR spectroscopy is the potential to gain a deep understanding of molecular and chemical processes in a variety of systems. A simple model of the exchange process can be described as the equilibrium between two states, A and B as shown below:

$$A \underset{k_r}{\overset{k_f}{\rightleftharpoons}} B \tag{3.1}$$

where $k_f$ and $k_r$ are the rate constants for the forward ($A \rightarrow B$) and reverse ($B \rightarrow A$) conversion reactions respectively. The reaction rate dependence on temperature (T) is described simply by Eyring's formula relating the rate constant ($k$) and the free energy of activation ($\Delta G^{\dagger}$):[23]

$$k = \frac{k_B T}{h} exp\left(-\frac{\Delta G^{\dagger}}{RT}\right) \tag{3.2}$$

where in the above equation $k_B$, $h$ and R denote the Boltzmann, Planck, and molar gas constants respectively.

Eyring's equation can then be expanded and rewritten as a function of entropy of activation ($\Delta S^{\dagger}$) and enthalphy of activation ($\Delta H^{\dagger}$) as follows:

$$k = \frac{k_B T}{h} \exp\left(\frac{\Delta S^{\dagger}}{R} - \frac{\Delta H^{\dagger}}{RT}\right) \tag{3.3}$$

For atoms undergoing true chemical exchange in the solid state i.e. no macroscopic change in the structure, the entropy difference between the ground and activated state is expected to be very small and thus can be removed from the above equation to yield the simplified equation below:

$$k = \frac{k_B T}{h} \exp\left(-\frac{\Delta H^{\dagger}}{RT}\right) \tag{3.4}$$

where the enthalpy of activation, $\Delta H^{\dagger}$, can be treated as the energy barrier required to achieve the exchange process associated with the measured rate constant. This relationship suggests that by plotting experimentally determined rate constants in the form of ln($k$/T) as a function of inverse temperature, the slope of the graph gives the solution to $\frac{\Delta H^{\dagger}}{R}$. This enthalpy of activation can be useful for experimental comparison to molecular structure calculations of energy barriers, where bulk methods such as conductivity measurements, cannot.

The increasing importance of lithium ion batteries in the fields of portable electronics and electric vehicles has generated significant motivation to understand the individual components of the battery and the chemical or molecular processes that govern performance. The lithium ion diffusion mechanism and associated timescale is especially relevant as it can be indicative of a material's ability to charge or discharge quickly. The 1990s saw the first implementation of NMR spectroscopy to study Li cathode materials, with an early focus on layered and spinel-like oxide structures.[1-4,24] Although Grey and coworkers were some of the first to demonstrate the use of NMR to probe ion dynamics in Li cathode materials specifically,[24] the extension of the technique to study dynamics properties in mobile Li-containing solids was reported by Xu and Stebbins[25] in 1995 whereby the authors used 2D EXSY to quantify Li motion in lithium orthosilicate. Their goal with this work was to use exchange spectroscopy to generate a quantitative understanding of Li diffusion in the crystalline silicate material, and ultimately define a Li diffusion pathway. In the two decades following these pioneering studies, the use of $^{6,7}$Li NMR has become established as an essential tool for studying Li battery materials in general, and to date remains the ideal method to quantitatively measure Li-Li hopping rates experimentally.

In general, the importance of the exchange rates relative to the timescale of the particular NMR experiment will principally govern the effect on the spectrum and subsequent treatment of the exchange. One of the greatest challenges in observing chemical exchange in paramagnetic materials is the typically very fast relaxation rate of nuclei in close proximity to a transition metal comprising unpaired d-electrons. Regardless of pulse sequence used to treat chemical exchange by NMR, the upper limit for measurable exchange rates will always be inherent nuclear relaxation rates. The ways in which $T_1$ affects both 2D and 1D exchange experiments will be discussed thoroughly herein.

### 3.3.1 2D Methods to Study Exchange in Li Battery Materials

Two-dimensional Exchange Spectroscopy (2D EXSY) has become one of the most common NMR methods for studying chemical exchange in the slow motion regime. This experiment has been used to study Li ion dynamics in a number of Li cathode materials for energy storage applications, including oxides ($LiMn_2O_4$)[18], nitrides ($Li_7MnN_4$)[26], and phosphates ($Li_3M_2(PO_4)_3$, M=V or Fe).[27,28]

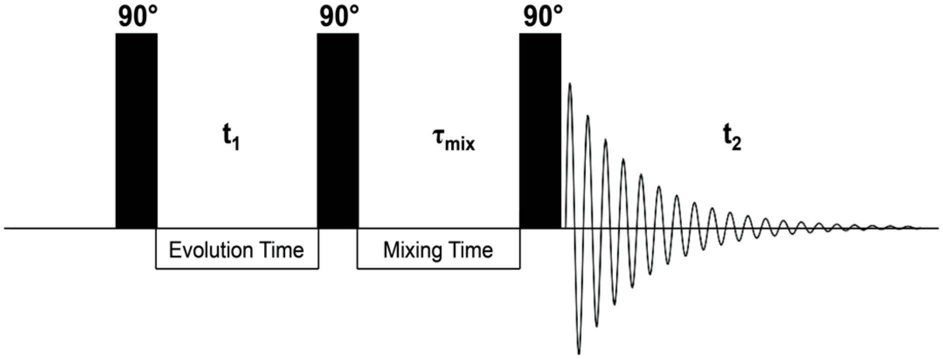

**Figure 3.2:** The 2D EXSY pulse sequence (also called NOESY) used to observe chemical exchange by NMR. The initial $t_1$ period stores chemical shift information before exchange, and this information in combination with the exchange allowed to occur during $\tau_{mix}$ is ultimately observed during $t_2$.

The pulse sequence for the 2D EXSY experiment is illustrated in **Figure 3.2**, where the initial 90° pulse generates coherence in the *xy*-plane, after which an evolution period ($t_1$) occurs where the spins are allowed to precess. A second 90° pulse re-aligns the magnetization in the z-direction. The subsequent mixing time ($\tau_{mix}$) is used to let the spins experience chemical exchange, where they will ultimately take on the precession frequency of the new chemical environment in which they reside. Finally, the signal is observed following a final 90° read-out pulse that brings the magnetization back into the transverse plane. The signal that results has two characteristic frequency components ($\omega_1$ and $\omega_2$) that correspond to the precession rates of the original and new site respectively. If exchange occurs on the timescale of the mixing time, crosspeaks are observed in the 2D spectrum as shown schematically in **Figure 3.3**, where the intensity of the cross peak relative to the diagonal peak intensity is the sum of chemical and spin exchange between two nuclei.[22] Under fast MAS conditions (>40 kHz), spin exchange is not likely to be observed for $^6$Li or $^7$Li due to the tendency of the MAS to average any spin diffusion effects resulting from homonuclear dipolar coupling between small-γ $^7$Li or $^6$Li nuclei.

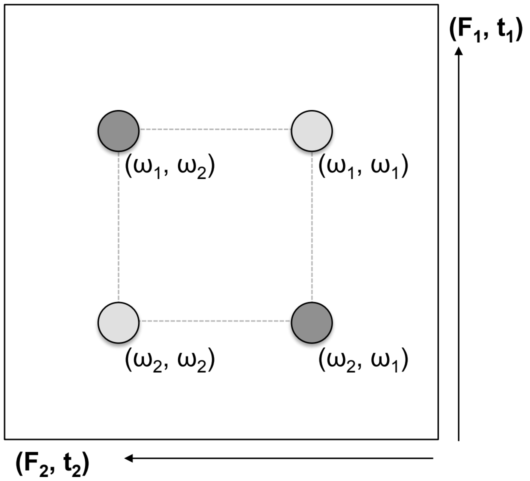

**Figure 3.3:** Schematic of a 2D EXSY spectrum, where the diagonal peaks are located at the resonant frequencies of site 1 and site 2 respectively at $\omega_1$ and $\omega_2$. Conversely, the crosspeaks that have arisen due to exchange between sites 1 and 2 have frequency components from both $\omega_1$ and $\omega_2$.

The effects of relaxation in the 2D EXSY experiment are unavoidable, and can pose an experimental challenge for paramagnetic materials. If relaxation occurs during the allowed mixing time, the signal will decay either partially or completely before the final readout pulse, leaving little (if any) detectable polarization at the end of the experiment. This results in a loss of intensity in both the cross peaks and diagonal peaks in both dimensions; a loss that can be particularly pronounced for slowly exchanging nuclei where cross peak intensity is low even in the absence of relaxation. This introduces the essential caveat alluded to earlier, where exchange rates must be faster than or on the order of the relaxation rates in order to observe significant cross peak intensity in the 2D spectrum.

The unfortunate effect of relaxation on the spectra yielded from a 2D EXSY experiment is not the only drawback of this method. In fact, the limitation that applies more generally is actually the large amount of experiment time devoted to a series of 2D experiments at enough unique mixing times to accurately fit the data with an exchange model. For samples with low natural abundance or unusually broad lineshapes, the required experiment time can extend to several days for a single sample.[29] When this is coupled with short $T_2$ relaxation times as is the case for many paramagnetic solids, loss of signal due to relaxation at longer mixing times necessitates increased signal averaging to obtain useful spectra. One-dimensional experiments are commonly less time consuming, yielding inherently higher signal-to-noise relative to analogous 2D experiments. In some situations, it may be prudent to use 2D EXSY as a qualitative tool for identification of possible exchange pairs in multi-site systems, followed by 1D methods to obtain quantitative kinetics information. In general, one-dimensional selective inversion experiments can provide reliable, quantitative data in the time required for a single mixing time of the 2D EXSY experiment. This massive efficiency increase is especially attractive for solids or complex molecules where experiment times for 2D spectra are often unwieldy.

### 3.3.2 Selective Inversion Experiment

For all its utility as a robust method of measuring chemical exchange rates by NMR, selective inversion is a beautifully simple experiment. In its most general form wherein there are two resolved peaks corresponding to nuclei engaged in slow exchange, one peak is selectively inverted, often using a long, Gaussian-shaped 180-degree pulse. Following this inversion, the nuclei are allowed to exchange during an imposed mixing time, $t_{mix}$, before being brought into the *xy*-plane for detection by a $\pi/2$ readout pulse. The typical pulse sequence used for a simple selective inversion recovery experiment using a Gaussian inversion pulse is shown in **Figure 3.4**. Rate constants are obtained by measuring the intensity of each site as a function of mixing time and fitting the data to a coupled relaxation model describing the build up of magnetization.

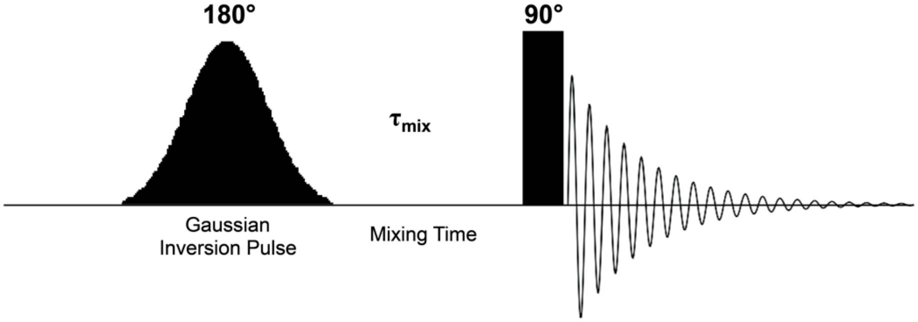

**Figure 3.4:** The pulse sequence used for one variation of the selective inversion experiment where the initial inversion of a selective frequency range is accomplished by the use of a 180° inversion pulse.

The two peaks in a two-site, single exchange process selective inversion experiment exhibit a characteristic intensity dependence on mixing time based on the initial conditions generated by the selective pulse. Typically, the intensity at the irradiated frequency will experience an exponential build-up of magnetization until the magnetization reaches a maximum after relaxation by $T_1$. The rate of this build-up process depends strongly on both $T_1$ and the rate constant for chemical exchange with the unperturbed peak. Conversely, the site that is not directly irradiated via the inversion procedure will experience a transient decrease in intensity, followed by relaxation back to equilibrium due to $T_1$ at longer mixing times. A fit of both the inverted and unperturbed resonances as a function of mixing time reveal both the time constant associated with spin-lattice relaxation and the rate constant for chemical exchange between the two sites.

The analysis of SI data is accomplished by varying the parameters involved in the mathematical model of the coupled relaxation of a spin system until a minimum of the sum of the squares of the differences between calculated and observed data is achieved. The model for a system with *n* sites that describes the process of spin relaxation coupled with exchange is described by a differential equation where the magnetization of a site *i* at time t ($M_i(t)$) and at equilibrium ($M_i(\infty)$) have the following time dependence:

$$\frac{\partial}{\partial t}\begin{pmatrix} M_1(\infty) - M_1(t) \\ \vdots \\ M_n(\infty) - M_n(t) \end{pmatrix} = \boldsymbol{A}\begin{pmatrix} M_1(\infty) - M_1(t) \\ \vdots \\ M_n(\infty) - M_n(t) \end{pmatrix} \tag{3.5}$$

where

$$\boldsymbol{A} = \begin{pmatrix} R_1 & -k_{2i} & \cdots & -k_{n1} \\ -k_{12} & R_2 & \cdots & -k_{n2} \\ \vdots & & & \\ -k_{1n} & -k_{2n} & \cdots & R_n \end{pmatrix}$$

and $R_i$ is defined as:

$$R_i = \frac{1}{T_{1i}} + \sum_{l \neq i} k_{il} \tag{3.6}$$

In the above equation $T_{1i}$ is the spin-lattice relaxation time for site *I* in the absence of chemical exchange and $k_{ij}$ is the rate constant describing exchange between sites *i* and *j*.

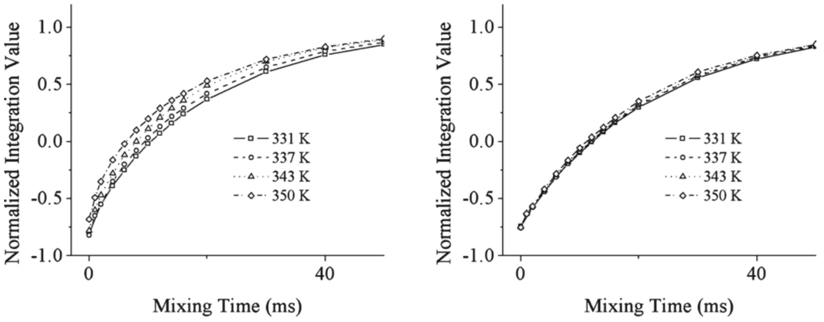

**Figure 3.5:** Comparison between the build-up curves of magnetization as a function of mixing time for a SI (left) *versus* NSI (right) experiment. In the former, a dependence on temperature is observed due to the inclusion of a rate process in the relaxation matrix. Reprinted with permission from Davis, L.J.M et al., '$^6$Li 1D EXSY NMR Spectroscopy: A new tool for studying lithium dynamics in paramagnetic materials applied to monoclinic $Li_2VPO_4F$', *J. Phys. Chem. C,* 115, ©2011 American Chemical Society.

This model is implemented in A.D. Bain's program, CIFIT, for fitting of selective inversion data uses the above relationship to best fit the experimental data accounting for the initial conditions created experimentally. Barring significant differences in $T_1$ rates, for a two-site exchange process between equal populations a non-selective inversion (NSI) recovery experiment (i.e. both sites are equally perturbed) the relaxation back to equilibrium is governed by the each site's inherent nuclear relaxation mechanism. The plot in **Figure 3.5** demonstrates the difference in time dependence of the magnetization between the SI and NSI experiments, where in the NSI experiment a lack of temperature dependence is observed due to the decreased contribution of the temperature dependent relaxation mechanism, chemical exchange. This difference in build-up of magnetization as a function of mixing time occurs because in practice the choice of initial conditions largely determine the extent of the contribution on the elements in the relaxation matrix. In an NSI experiment there is a much larger contribution from the diagonal elements of the matrix (comprising relaxation time constants) compared to the off-diagonal elements, resulting in an almost negligible effect from exchange rate constants on NSI build up curves. This exemplifies the importance of experimentally generating various sets of initial conditions with a combination of selective and non-selective pulses in order to best determine the rate and relaxation parameters for a system. **Figure 3.6** demonstrates the time-dependence of peak-area in the $Li_2VPO_4F$ system, with the fits obtained via the CIFIT program overlaid with experimental results. The inclusion and fitting of both the initial and final magnetization conditions into the model allow for analysis of data even under 'non-ideal' circumstances where targeted selective inversion of a single peak is imperfect due to experimental constraints.

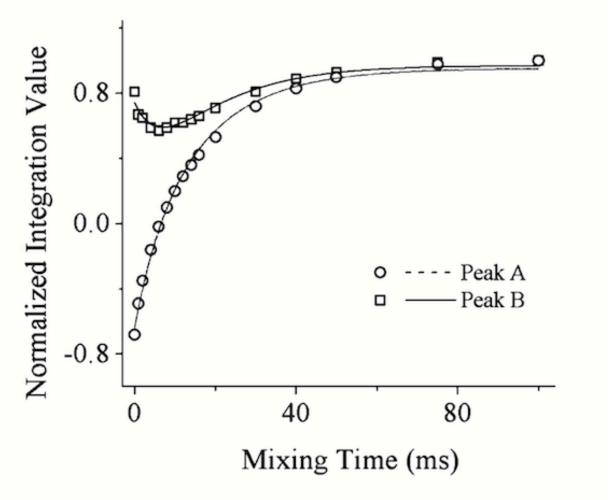

**Figure 3.6:** Experimental results for a selective inversion experiment in $Li_2VPO_4F$ wherein Peak A is inverted. The characteristic behaviour of Peak B, where an initial attenuation of the peak area is observed, is indicative of an exchange process with the inverted site A. Reprinted with permission from Davis, L.J.M et al., '$^6$Li 1D EXSY NMR Spectroscopy: A new tool for studying lithium dynamics in paramagnetic materials applied to monoclinic $Li_2VPO_4F$', *J. Phys. Chem. C,* 115, ©2011 American Chemical Society.

Selective inversion is an ideal method for quantifying ion exchange rates in paramagnetic cathode materials for both lithium and sodium ion batteries. Knowledge of exchange rates for specific ion pairs can lead to a rich understanding of ion diffusion pathways throughout a lattice, details that help to identify why materials behave more or less favourably in real applications. The dynamics information is especially powerful when combined with accurate assignment of the chemical shifts in paramagnetic materials. The complex interactions that give rise to the unusual shifts that are frequently observed in many cases require advanced techniques such as density functional theory calculations to accurately predict the NMR shifts for unique crystallographic sites.

## 3.4 Assigning Paramagnetic Shifts to Local Environments in NMR

### 3.4.1 Empirical Methods to Assign Paramagnetic NMR Shifts in Li Oxides

In Chapter 2 the mathematical basis for the paramagnetic shifts was outlined, including a discussion of the Fermi Contact hyperfine interaction as it relates to the observed paramagnetic shift. This contribution is strongly dependent on electron spin density at the Li (or Na) nucleus being observed, where the geometry dependence of this interaction can be explained *via* the Goodenough-Kanamori rules for spin superexchange.[30,31] This set of rules aims to describe the coupling that occurs between two cations through a bridging, non-magnetic anion, and is generally applicable to a majority of the cathode materials, where there is typically a transition metal center found with octahedral coordination oriented relative to Li or Na through a bridging oxygen or fluorine atom. The rules for the superexchange interaction state that the coupling between an occupied and vacant orbital via a bridging anion can be either ferromagnetic or antiferromagnetic in nature, with a general preference for ferromagnetic coupling.

This rule manifests as a set of general guidelines for the specific M-O-Li (Metal-Oxygen-Lithium) interaction in oxides depending on the atomic geometry as depicted in **Figure 3.7**. The mechanisms that give rise to either ferromagnetic or antiferromagnetic coupling are respectively labeled *delocalization* and *polarization*.[32-34] The delocalization mechanism, which is the more common of the two, causes the *sign* of the spin to be unchanged when the spin density is transferred, ultimately increasing the frequency of the paramagnetic NMR shift. When the M-O-Li atoms for a 90° interaction, bonding $t_{2g}$ orbitals transfer electron density to the Li atom through the oxygen 2p orbitals engaged in a π-type bonding motif. When this atomic arrangement is 180°, the $e_g$ orbitals are engaged in the bonding interaction, and are responsible for the spin density transfer via σ-bonded oxygen 2p orbitals to the Li nucleus. In contrast to the delocalization mechanism for spin density transfer, the polarization mechanism changes the sign of the spin density on Li, resulting in a decrease of the NMR frequency.

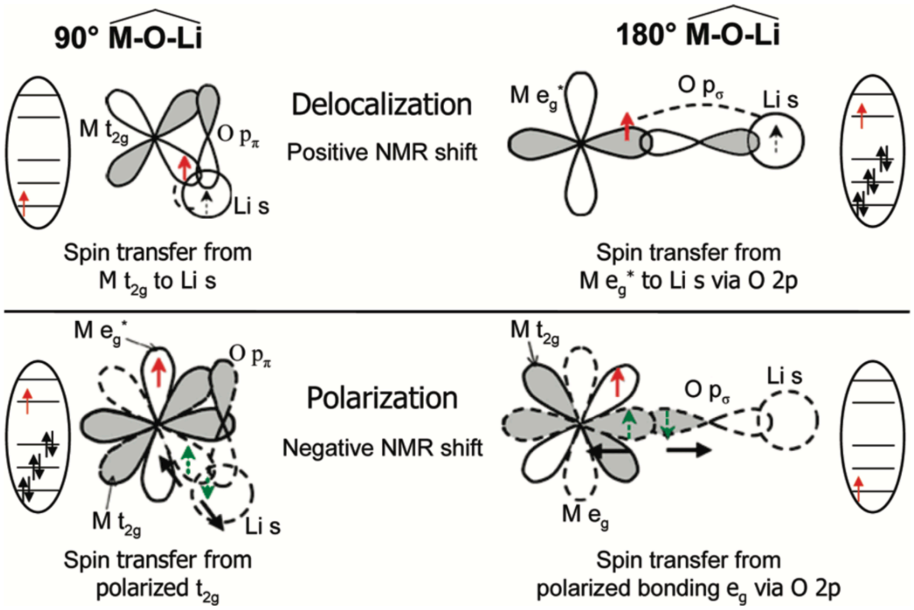

**Figure 3.7:** Schematic diagram showing visual representations of the two mechanisms for electron spin transfer to the Li s orbital in a typical lithium metal oxide structure. Reprinted with permission from Castets, A. et al., ‘Analysis of the $^7$Li NMR signals in the Monoclinic $Li_3Fe_2(PO_4)_3$ and $Li_3V_2(PO_4)_3$ Phases’, *J. Phys. Chem. C,* 114, ©2010 American Chemical Society.

In materials where the M-O-Li geometry is very close to 90° or 180°, the relative NMR shifts can be predicted on the basis of the polarization and delocalization mechanisms. The additive nature of these shift contributions makes it relatively straightforward to assign multiple shifts in an experimental NMR spectrum on the basis of the geometry. This method has been especially effective in the $LiMO_2$ layered-type materials where empirically determined contributions to the overall shift can be combined for a reasonable prediction of the NMR shift depending on the Li-O-M contacts.[32,35-38] Notably, this approach relies heavily on the 90° or 180° nature of the Li-M interaction, and deviations from this can create difficulties even with use as a qualitative assignment method. In polyanionic-derived structures such as phosphates or fluorophosphates, there are very rarely such predictable geometries, and assignment of the shifts in these materials has proven difficult using this technique.[39,40] In the past decade, the use of more advanced calculation methods, such as density functional theory, have been introduced in an effort to assign the Li NMR shifts in lattices with irregular Li-O-M arrangements quantitatively.[33,34,39-41]

### 3.4.2 Direct Calculation of Paramagnetic NMR Shifts by *Ab Initio* Methods

The contribution to the overall NMR shift of a Li or Na atom in a lattice containing a nearby paramagnetic transition metal ion is affected primarily by the hyperfine coupling interaction between the Na/Li nucleus and the unpaired electron spin density transferred to that nucleus through the Fermi Contact interaction. Calculation of the FC hyperfine coupling constant therefore gives a good theoretical approximation of the overall shift, as per the set of equations described in Chapter 2. Density functional theory is an effective method for calculating the strength of this FC hyperfine interaction that can ultimately be used to calculate theoretical paramagnetic shift contributions.

### *3.4.2.1 Basics of DFT*

The essential idea upon which density functional theory rests is that the electron density can be treated as a basic variable rather than dealing with the many-electron wavefunction to describe any electronic system.[42,43] In 1964, Hohenberg and Kohn[42] were able to prove two fundamental theorems for which a set of essential equations were derived by Kohn and Sham[44] the following year. The first theorem proposed by Hohenberg and Kohn states that *the ground state energy for any system of non-interacting particles can be described fully and uniquely by a functional of the electron density.*[42,43] This theorem sets up the direct relationship between the ground state wavefunction and the ground state electron density, which allows the Schrödinger equation to be solved by determination of the electron density. Their second theorem posits that *the electron density for which the ground state energy is minimized is the true electron density.*[42] While their work alone rephrases the problem of solving the Schrödinger equation in a more practical way, it did not provide a solution to this problem, a task that was later accomplished by Kohn and Sham.[44,45] Using their derivations, the ground state electron density can be expressed using equations involving only non-interacting electrons.[43]

$$\left[\frac{h^2}{2m}\nabla^2 + V(r) + V_H(r) + V_{XC}(r)\right]\psi_i(r) = \varepsilon_i\psi_i(r) \tag{3.7}$$

where the terms within brackets in the above equation refer to (in order): the kinetic energy, the electron-nuclear interaction potential, the Hartree potential that describes the Coulomb repulsion between a single electron and the total electron density, and the exchange-correlation functional. All of these terms can be defined exactly with the exception of the exchange correlation functional, which is the functional derivative of the exchange correlation energy and includes all quantum mechanical effects in the system that are not precisely known. As one might imagine, much of the development of DFT is focused on this undefined exchange correlation functional and how to best approximate this contribution so as to understand, and indeed predict, experimental findings.

#### *3.4.2.2 The Exchange Correlation Functional*

The most significant problem with density functional theory is that the exchange correlation functional is not known exactly, and the use of an approximation is necessary in all cases to solve the Kohn-Sham equations and describe the electronic structure of a system. Of the available approximations, there are varying levels of accuracy depending on the extent to which the approximation describes a real system. As might be expected, the caveat is that more accurate approximations for the exchange correlation functional are more computationally expensive and consequently compromises are necessary when choosing an appropriate functional to use in practice. Two of the most common approximations are the local density approximation (LDA) and Generalized Gradient Approximation (GGA) of which the latter is applied in the context of this thesis. The LDA method treats the electron density simply as a homogeneous electron gas, for which the exchange-correlation functional can be solved exactly. This is not, however, representative of most real systems and thus GGA, which takes into account both the local electron density as well as a local gradient in electron density, is considered a better approximation of a real system.

### *3.4.2.3 Pseudopotential and PAW Methods for Solving the Kohn-Sham Equations*

The most time-consuming component of the application of DFT to a real electronic system is the solving of the Kohn-Sham potential defined as the sum of the three potentials introduced above as follows:

$$V_{KS}(r) = V(r) + V_H(r) + V_{xc}(r) \tag{3.8}$$

In many examples, and indeed in all cases discussed throughout this thesis, DFT is used to describe the electronic structure of a periodic arrangement of atoms in a lattice. One of the ways to minimize computational effort is therefore to use a *plane-wave* basis set, which treats the potential acting on the electrons, and thus the electron density, as a periodic function. This vastly reduces the computational costs compared to other basis sets, especially for large unit cells. Despite this improvement, an unreasonably large number of plane waves would still be necessary to fully describe the rapid oscillation of the wavefunctions at and near atomic nuclei. One common method for dealing with this problem is to introduce pseudopotentials that approximate a fixed value for the potential of the nucleus, and effectively treating only the valence electrons. This type of method is often referred to as a 'frozen-core' approach. A more recent frozen-core method was introduced by Blöchl in 1994, called the Projector Augmented Wave (PAW) method,[46,47] that typically does a better job of approximating the electron core of a nucleus while still reducing overall computational energy. Although not technically as accurate as all-electron calculations that do not rely on a fixed potential to approximate the nucleus, the frozen core approach is useful and in some cases necessary when describing large periodic systems.

#### *3.4.2.4 DFT+U for Transition Metal Complexes*

Application of DFT, especially using LDA or GGA functionals, poses a problem for many transition metal complexes. The lack of an orbital-dependent potential in the LDA and GGA approaches means that they often fail to correctly describe strongly correlated systems such as d or f-block metals.[48-51] This tends to inappropriately delocalize the electron density of these metals, in many cases incorrectly predicting Li insertion voltages and phase changes.[49,50] One common method that is implemented in this thesis is the use of DFT+U (specifically GGA+U in this context) where an additional orbital-dependent term is included in the total energy to describe d-electron Coulomb interactions thus accounting for the strong electron correlation effects with a correction term.[51-54] The added $U$ is a Hubbard-type interaction term[53,54] that accounts for the potential energy of onsite repulsion arising from electron charges. This method has been used in examples of transition metal oxides or phosphates to correctly reproduce experimental parameters relative to DFT methods alone, and is used throughout this thesis for similar lattice structures.[55]

#### *3.4.2.5 Using DFT to Calculate Paramagnetic Shifts*

The benefit of density functional theory in the context of assigning paramagnetic NMR shift contributions is that the determination of the total electron density in a system allows for the quantification of the hyperfine coupling interaction that ultimately produces the large shifts observed in NMR. Upon calculation of this coupling strength, the sequence of equations detailed in Chapter 2 can be utilized in combination with magnetic susceptibility properties to calculate the full paramagnetic contribution to the shift. For nuclei such as $^{23}$Na, $^{6}$Li or $^{7}$Li the paramagnetic contribution is much larger than any inherent chemical shielding contributions, and thus can be approximated as the overall theoretical shift.

## 3.5 Summary

The conclusions and interpretations presented throughout the entirety of this thesis are based on the use of the experimental and computational methods described in this chapter. The strong paramagnetism in the materials studied presents a unique challenge for their investigation by NMR that are compensated for by experimental techniques such as fast MAS and interpreted with DFT computational methods. Knowledge of chemical shift environments are necessary to fully interpret spectra and understand important structural changes that occur in both Na and Li cathode materials, as will become evident in the *ex situ* NMR study of $Na_2FePO_4F$ described in Chapters 6 and 7. Further, both 2D and 1D methods for probing chemical exchange by NMR are used to identify and quantify ion dynamics in cathode materials with multiple crystallographic Li environments including $Li_2MnP_2O_7$, $Li_2SnO_3$, and $LiFeV_2O_7$ as in Chapters 4 and 5. Knowledge of the practices outlined in this chapter allow for the interpretation of the experimental findings throughout the entirety of this thesis.

## 3.6 References

(1) Carewska, M. *Solid State Ionics* **1997**, *93* (3-4), 227.

(2) Kumagai, N.; Fujiwara, T.; Tanno, K.; Horiba, T. *J. Electrochem. Soc.* **1996**, *143* (3), 1007.

(3) Ménétrier, M.; Rougier, A.; Delmas, C. *Solid State Communications* **1994**, *90* (7), 439.

(4) Colson, S.; SZU, S.; KLEIN, L.; TARASON, J. *Solid State Ionics* **1991**, *46* (3-4), 283.

(5) Carlier, D.; Blangero, M.; Ménétrier, M.; Pollet, M.; Doumerc, J.-P.; Delmas, C. *Inorg. Chem.* **2009**, *48* (15), 7018.

(6) Carlier, D.; Cheng, J. H.; Berthelot, R.; Guignard, M.; Yoncheva, M.; Stoyanova, R.; Hwang, B. J.; Delmas, C. *Dalton Trans.* **2011**, *40* (36), 9306.

(7) Billaud, J.; Clément, R. J.; Armstrong, A. R.; Canales-Vázquez, J.; Rozier, P.; Grey, C. P.; Bruce, P. G. *J. Am. Chem. Soc.* **2014**, *136* (49), 17243.

(8) Xu, J.; Lee, D. H.; Clément, R. J.; Yu, X.; Leskes, M.; Pell, A. J.; Pintacuda, G.; Yang, X.-Q.; Grey, C. P.; Meng, Y. S. *Chem. Mater.* **2014**, *26* (2), 1260.

(9) Smiley, D. L.; Goward, G. R. *Chem. Mater.* **2016**, *28* (21), 7645.

(10) Shannon, R. D.; IUCr. *Acta Crystallogr Sect A Cryst Phys Diffr Theor Gen Crystallogr* **1976**, *32* (5), 751.

(11) Pyykkö, P. *Mol. Phys.* **2008**, *106* (16-18), 1965.

(12) Jones, A. R.; Winter, R.; Greaves, G. N.; Smith, I. H. *J. Phys. Chem. B* **2005**, *109* (49), 23154.

(13) Koller, H.; Engelhardt, G.; Kentgens, A. *The Journal of Physical …* **1994**.

(14) Göbel, E.; Müller-Warmuth, W.; Olyschläger, H.; Dutz, H. *Journal of Magnetic Resonance (1969)* **1979**, *36* (3), 371.

(15) Leskes, M.; Drewett, N. E.; Hardwick, L. J.; Bruce, P. G.; Goward, G. R.; Grey, C. P. *Angew. Chem. Int. Ed.* **2012**, *51* (34), 8560.

(16) Kentgens, A. P. M. *Geoderma* **1997**, *80*, 271.

(17) Medek, A.; Harwood, J. S.; Frydman, L. *J. Am. Chem. Soc.* **1995**, *117* (51), 12779.

(18) Verhoeven, V. W.; de Schepper, I. M.; Nachtegaal, G.; Kentgens, A. P.; Kelder, E. M.; Schoonman, J.; Mulder, F. M. *Phys. Rev. Lett.* **2001**, *86* (19), 4314.

(19) Bain, A. D.; DUNS, G. J.; TERNIEDEN, S.; MA, J.; WERSTIUK, N. H. *J. Phys. Chem.* **1994**, *98* (31), 7458.

(20) Bain, A. D. *Progress in Nuclear Magnetic Resonance Spectroscopy* **2003**, *43* (3-4), 63.

(21) Fauconnier, T.; Lock, C. J. L.; Bell, R. A.; Britten, J. F.; Rainsford, K. D. *Can. J. Chem.* **1994**, *72* (2), 382.

(22) Jeener, J.; Meier, B. H.; Bachmann, P.; Ernst, R. R. *J. Chem. Phys.* **1979**, *71* (11), 4546.

(23) Eyring, H. *J. Chem. Phys.* **1935**, *3* (2), 107.

(24) Lee, Y. J.; Wang, F.; Grey, C. P. *J. Am. Chem. Soc.* **1998**, *120* (48), 12601.

(25) Xu, Z.; Stebbins, J. F. *Science* **1995**, *270* (5), 1332.

(26) Cabana, J.; Dupré, N.; Rousse, G.; Grey, C.; Palacin, M. R. *Solid State Ionics*

**2005**, *176* (29-30), 2205.

(27) Cahill, L. S.; Chapman, R. P.; Britten, J. F.; Goward, G. R. *J. Phys. Chem. B* **2006**, *110* (14), 7171.

(28) Davis, L. J. M.; Heinmaa, I.; Goward, G. R. *Chem. Mater.* **2010**, *22* (3), 769.

(29) Hodgkinson, P.; Hampson, M. R. *Solid State Nucl. Magn. Reson.* **2006**, *30* (2), 98.

(30) Goodenough, J. B. *Journal of Physics and Chemistry of Solids* **1958**, *6* (2-3), 287.

(31) Kanamori, J. *Progress of Theoretical Physics* **1957**, *17* (2), 177.

(32) Grey, C. P.; Dupré, N. *Chem. Rev.* **2004**, *104* (10), 4493.

(33) Castets, A.; Carlier, D.; Trad, K.; Delmas, C.; Ménétrier, M. *J. Phys. Chem. C* **2010**, *114* (44), 19141.

(34) Carlier, D.; Ménétrier, M.; Grey, C.; Delmas, C.; Ceder, G. *Phys. Rev. B* **2003**, *67* (17), 174103.

(35) Zeng, D.; Cabana, J.; Bréger, J.; Yoon, W.-S.; Grey, C. P. *Chem. Mater.* **2007**, *19* (25), 6277.

(36) Pan, C.; Lee, Y. J.; Ammundsen, B.; Grey, C. P. *Chem. Mater.* **2002**, *14* (5), 2289.

(37) Marichal, C.; Hirschinger, J.; Granger, P.; Ménétrier, M.; Rougier, A.; Delmas, C. *Inorg. Chem.* **1995**, *34* (7), 1773.

(38) Harris, K. J.; Foster, J. M.; Tessaro, M. Z.; Jiang, M.; Yang, X.; Wu, Y.; Protas, B.; Goward, G. R. *Chem. Mater.* **2017**, *29* (13), 5550.

(39) Kim, J.; Middlemiss, D. S.; Chernova, N. A.; Zhu, B. Y. X.; Masquelier, C.;

Grey, C. P. *J. Am. Chem. Soc.* **2010**, *132* (47), 16825.

(40) Middlemiss, D. S.; Ilott, A. J.; Clément, R. J.; Strobridge, F. C.; Grey, C. P. *Chem. Mater.* **2013**, *25* (9), 1723.

(41) Clément, R. J.; Pell, A. J.; Middlemiss, D. S.; Strobridge, F. C.; Miller, J. K.; Whittingham, M. S.; Emsley, L.; Grey, C. P.; Pintacuda, G. *J. Am. Chem. Soc.* **2012**, *134* (41), 17178.

(42) Hohenberg, P.; Kohn, W. *Physical Review* **1964**, *136* (3B), B864.

(43) Sholl, D. S.; Steckel, J. A. *Density functional theory: a practical introduction*; John Wiley & Sons, Inc: Hoboken, New Jersey, 2009; pp 1–253.

(44) Kohn, W.; Sham, L. J. *Physical Review* **1965**, *140* (4A), A1133.

(45) Kohn, W.; Becke, A. D.; Parr, R. G. *J. Phys. Chem.* **1996**, *100* (31), 12974.

(46) Blöchl, P. E. *Phys. Rev. B* **1994**, *50* (24), 17953.

(47) Kresse, G.; Joubert, D. *Physical Review B (Condensed Matter and Materials Physics)* **1999**, *59* (3), 1758.

(48) Aydinol, M. K.; Kohan, A. F.; Ceder, G.; Cho, K.; Joannopoulos, J. *Physical Review B (Condensed Matter)* **1997**, *56* (3), 1354.

(49) Zhou, F.; Cococcioni, M.; Marianetti, C. A.; Morgan, D.; Ceder, G. *Phys. Rev. B* **2004**, *70* (23), 15.

(50) Zhou, F.; Marianetti, C. A.; Cococcioni, M.; Morgan, D.; Ceder, G. *Phys. Rev. B* **2004**, *69* (20), 201101.

(51) Kulik, H. J.; Cococcioni, M.; Scherlis, D. A.; Marzari, N. *Phys. Rev. Lett.* **2006**, *97* (10), 435.

(52) Anisimov, V.; Zaanen, J.; Andersen, O. *Phys. Rev. B* **1991**, *44* (3), 943.

(53) Dudarev, S. L.; Botton, G. A.; Savrasov, S. Y.; Humphreys, C. J.; Sutton, A. P. *Phys. Rev. B* **1998**, *57* (3), 1505.

(54) Dudarev, S. L.; Botton, G. A.; Savrasov, S. Y.; Szotek, Z.; Temmerman, W. M.; Sutton, A. P. *physica status solidi (a)* **1998**, *166* (1), 429.

(55) Zhou, F.; Maxisch, T.; Ceder, G. *Phys. Rev. Lett.* **2006**, *97* (15), 155704.

# Chapter 4: Measuring Slow Li ion Dynamics in $Li_2MnP_2O_7$ and $Li_2SnO_3$ by Selective Inversion NMR

## 4.1 Introduction

Within the last decade, selective inversion (SI) NMR experiments were applied for the first time to measure Li exchange processes in paramagnetic cathode materials by the Goward research group.[1-3] These first examples all involved exchange that was well within the measurable range as defined by their specific relaxation parameters, making them ideal for study by this method. In this chapter, two unique cases wherein the SI experiment was applied to materials for Li ion batteries that exhibit slow Li-Li exchange will be explored, with an emphasis on contrasting experimental methods and data treatment required due to inherent differences in the NMR properties of the materials. First, an example whereby very slow Li diffusion is probed in a model pyrophosphate compound, $Li_2MnP_2O_7$, will be discussed, where the fast nuclear relaxation coupled with slow exchange makes quantitative determination of Li hopping rates difficult.[4] Moreover, the poor site resolution in the $^6$Li NMR spectroscopy for this sample compromises the achievable selectivity of the Gaussian inversion pulse used in the SI experiment. The ultimate effects of these practical disadvantages on the results will be discussed, as well a proposal of the overall Li diffusion mechanism in this material that is found to ultimately be limited by poor ion motion. This example will then be compared to the study of another slow Li ion conductor, where $Li_2SnO_3$ is investigated by the same NMR method and the long spin lifetimes of the Li nuclei allow for the use of a much more selective pulse, ultimately permitting the accurate quantification of very slow Li-Li exchange rate constants, in contrast to the earlier pyrophosphate example.[5]

The work presented this chapter was published as two separate manuscripts. The investigation of ion exchange in Li metal pyrophosphates, was published in the *Journal of Physical Chemistry C* in 2015 with authors D.L. Smiley, M.Z. Tessaro, X. He, and G.R. Goward. The solid-state synthesis of this material as well as all NMR experiments and subsequent data analysis were carried out at McMaster University under the supervision of Prof. G. Goward. The second manuscript was published in 2016 in the *Journal of Physical Chemistry C* with authorship of J. Langer, D.L. Smiley, A.D. Bain, G.R. Goward, and M. Wilkening. The SI exchange NMR spectroscopy and data analysis was completed at McMaster University under the supervision of Prof. Bain and Prof. Goward. The sample preparation and additional NMR studies with $Li_2SnO_3$ were carried out by J. Langer at Graz University of Technology under the supervision of Prof. M. Wilkening.

## 4.2 Experimental

### 4.2.1 Solid-state Synthesis of $Li_2MnP_2O_7$

$^6$Li enriched $Li_2MnP_2O_7$ was prepared by the "wet" method described by Zhou *et al*.[6] Stoichiometric amounts of $^6Li(CH_3CO_2)$, $Fe(CH_3CO_2)_2$, $Mn(CH_3CO_2)_2$, and $NH_4H_2PO_4$ were stirred in aqueous solution (0.02 M Li) and heated until dry. The sample was placed in an evacuated drying oven at 90 °C for 12 hours. Using a tube furnace with a constant flow of 5% $H_2/N_2$ at 5 psi, the sample was heated to 600 °C for 30 hours. The sample was subsequently reground and heated to 600 $^{o}$C for 12 hours. Powder X-ray diffraction was used to confirm formation of the desired phase.

### 4.2.2 Solid-State NMR

All $^{6}$Li MAS NMR spectra of $Li_2MnP_2O_7$ were acquired at a Larmor frequency of 44.1 MHz on a Bruker AV-300 spectrometer using 1.8 mm diameter rotors in a double-resonance probe. In most cases a Hahn-echo pulse sequence with a 90$^{o}$ pulse of 3.5 μs and a recycle delay of 200 ms was used. $^{6}$Li selective inversion experiments were accomplished using a $180^{o}$-$\tau_{mix}$ -$90^{o}$ pulse sequence, where the 180$^{o}$ Gaussian shaped pulse was 1 ms in duration with a soft pulse power of 0.109 W. The mixing time was varied across a series of experiments ranging from 5 μs to 200 ms. $^{6}$Li NMR spectra were referenced to a 1M solution of $^{6}$LiCl at 0 ppm. Temperatures were calibrated using $Sm_2Sn_2O_7$ according to the method discussed previously by Grey *et al.*[7]

NMR spectra of $Li_2SnO_3$ that were collected at McMaster University utilized a Bruker triple-resonance probe housing rotors with 2.5 mm diameter. One-dimensional selective inversion experiments were performed on a Bruker Avance III spectrometer operating at a $^{6}$Li Larmor frequency of 74 MHz with a MAS frequency of 30 kHz. Sample cooling was achieved by fresh evaporation of liquid nitrogen using a heat- exchange coil. The 1D NMR spectra were obtained using a one-pulse experiment with a (90°) solid pulse of 5 μs and recycle delays ranging from 160 to 300 s; the spectra were referenced to a solution of 1 M $^{6}$Li-enriched LiCl at a chemical shift of 0 ppm.

### 4.2.3 Data Analysis with CIFIT

Spectra acquired as a function of mixing time by the SI experiment were analyzed by the CIFIT program developed by Bain *et al.*[8] Peaks were fit using a Mathematica notebook developed by Prof. D. Brouwer at Redeemer University. Integrated peak areas were normalized to the integration values at the longest mixing time. CIFIT utilizes a rate matrix describing the relaxation properties of each spin under the influence of chemical exchange, the theory of which is discussed in greater detail in Chapter 3 and elsewhere.[9,10] The mixing time delay periods were chosen for the experiment based on the independently measured $T_1$ values for each material to ensure complete relaxation of both sites to equilibrium at the longest mixing times. The quality of the fit to the experimental data was evaluated by a chi-squared value and an error range associated with the calculated rate constant.

## 4.3 Results and Discussion

### 4.3.1 Motivation

Selective inversion experiments provide an excellent alternative to traditional 2D exchange NMR spectroscopy techniques as they vastly increase the efficiency with which useful data can be obtained.[11,12] Although traditionally used to study dynamic processes of molecules in the solution state, in 2012 Davis *et al.*[2] first applied the technique to several paramagnetic cathodes for Li ion batteries, proving the effectiveness of this method in the solid state. This method, as with any NMR method that relies on site resolution of two sites exchanging with one another, is used to study exchange that falls within the slow exchange regime (see Chapter 3), and in some cases, the exchange is so slow that it is simply not observable on the timescale of the NMR experiment. Whether or not it is possible to obtain rate information for any given sample using this method is determined by a variety of experimental parameters defined largely by the specific samples being studied. Here, $Li_2MnP_2O_7$ and $Li_2SnO_3$ are compared and contrasted, and although they both are shown to exhibit slow Li ion exchange at room temperature, the experimental parameters and subsequent data analysis varies greatly.

### 4.3.2 SI Experiments to Study Li Exchange in $Li_2MnP_2O_7$

Lithium metal pyrophosphates have been proposed as alternative Li cathode materials due to their structural stability and the potential to access two Li atoms per formula unit.[6,13-16] The manganese analog, $Li_2MnP_2O_7$, was originally synthesized by Adam *et al.*[14] in 2008, exhibiting a three-dimensional pyrophosphate framework that is composed of $MnO_5$ and $MnO_6$ polyhedra interconnected through $P_2O_7$ groups as shown in **Figure 4.1**; this arrangement generates a tunnel-like structure that houses the four crystallographically unique Li ions, with ions in Li1 and Li2 positions sharing one tunnel and Li3 and Li4 occupying another. Although the structural features have been thoroughly characterized by diffraction methods, the mechanism by which Li atoms diffuse through the pyrophosphate network is relatively ill defined. Furthermore, the origin of the disappointing electrochemical performance in the $Li_2MnP_2O_7$ variant relative to other transition metal analogues is not well understood. A structural deformation unique to the Mn phase or sluggish Li ion kinetics have both been proposed as possible mechanisms for this behaviour, although neither has been confirmed experimentally. Solid-state NMR is implemented here as a tool to investigate the latter of these theories by measuring Li ion exchange rates in $Li_2MnP_2O_7$.

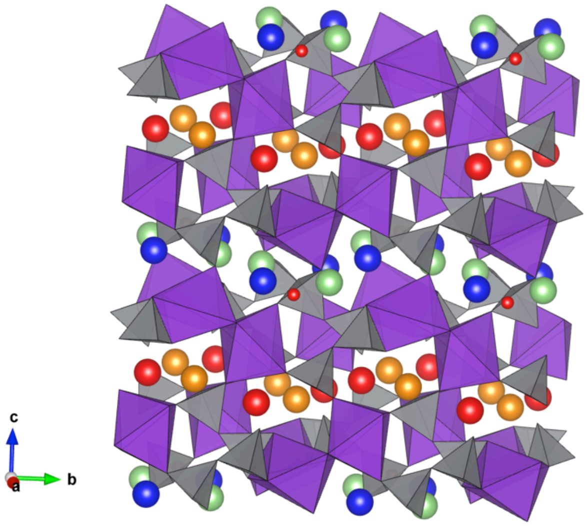

**Figure 4.1:** Reported structure of $Li_2MnP_2O_7$ with Mn-oxide polyhedra shown in purple and $PO_4$ tetrahedra in grey. The Li atoms reside in distinct layers in four unique crystallographic positions labeled Li1, Li2, Li3, and Li4 depicted as blue, green, red, and orange spheres respectively.

The $^6$Li MAS NMR spectrum of $Li_2MnP_2O_7$ is shown in **Figure 4.2**, where the four Li peaks corresponding to the distinct crystallographic positions in $Li_2MnP_2O_7$ are partially resolved. The four peaks (at 44, 32, 7 and 2.5 ppm) have been assigned to their respective crystallographic positions based on the Goodenough-Kanamori rules, as previously employed for the assignment of Li resonances in a variety of other paramagnetic compounds.[17] It is expected that the transfer of electron spin density from the half-filled $t_{2g}$ orbital of paramagnetic Mn (II) to the empty Li 2s orbital via a delocalization mechanism causes a shift in the Li resonance where the efficiency of this transfer is maximized when the Li-O-Mn orbitals overlap at angles close to 90 or 180°.[18] After consideration of all Li-O-Mn contacts in $Li_2MnP_2O_7$, Li3, having two Li-O-Mn angles approaching 90° (89.53° and 94.85°) and the shortest Li-Mn distances (3.01 Å), is assigned to the highest frequency site at 44 ppm due to the increased paramagnetic shift contribution caused by efficient orbital overlap. In contrast Li2, having no bond angles close to 90°, is ascribed to the lowest frequency resonance at 2.5 ppm. The same logic was applied to assign the remaining two peaks at 32 ppm and 7 ppm to Li4 and Li1 respectively. A deconvolution of the peaks in the $^6$Li MAS spectrum of $Li_2MnP_2O_7$ enables the determination of relative site occupancies with integration over the entire spinning sideband manifold revealing an equal population of the two sites in each of the two tunnels, although the integrated intensities of Li3 and Li4 are 84% that of Li1 and Li2. Of the four isotropic peaks, Li3 and Li4 are reasonably well resolved, whereas Li1 is present as a small but visible shoulder on the Li2 site.

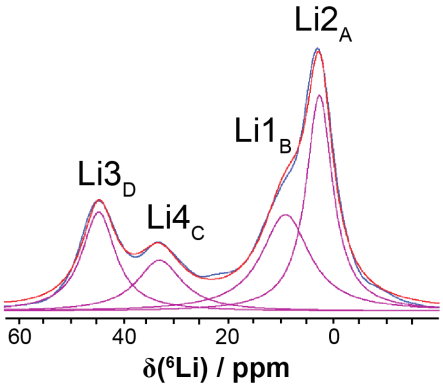

**Figure 4.2:** Deconvolution of $^6$Li MAS NMR spectrum of $Li_2MnP_2O_7$ with site assignment.

Selective inversion experiments to probe Li-Li exchange rates focused on Li3 in particular, as its relative separation from the rest of the isotropic region was most promising for achieving maximum inversion. The lack of optimal site resolution in the 1D MAS spectrum of $Li_2MnP_2O_7$ makes the successful application of a purely selective pulse near impossible, thus despite attempting to invert only a single resonance the nearby peak(s) are invariably affected by the inversion pulse, as depicted in **Figure 4.3**. The selectivity of the pulse is further limited by fast nuclear relaxation rates in this paramagnetic material. The spin-lattice relaxation times average to ~3 ms for all four sites, with $T_2$ constants even shorter at about 1 ms on average. The use of excessively long Gaussian inversion pulses was therefore avoided despite their potential to narrow the excitation bandwidth and improve selectivity. This is in contrast to work with other phosphates that have enjoyed sufficient site-resolution to achieve near-perfect selectivity as was true for $Li_3Fe_2(PO_4)_3$ or $LiVOPO_4F$. [2,3] A summary of peak widths and separation for $Li_2MnP_2O_7$ is provided in **Table 4.2**, where these values are compared to those of $Li_2SnO_3$. The poor peak separation coupled with limitations on pulse selectivity resulted in a maximum inversion efficiency of approximately 60% with a significant perturbation of the neighbouring site under these conditions. Fortunately, this can be accounted for in the relaxation matrix used to fit the experimental data by including the initial attenuated intensity of the affected peaks in the fit. In fact, upon testing various selective pulse lengths and shapes the extent to which nearby sites were affected by the selective pulse had little effect on the resulting rate constant obtained from the fit. Two examples are provided in **Table 4.1** where despite a difference in inversion efficiency, rate constants are found to be equal within error. For nuclei that are readily in exchange with each other, a plot of the intensity as a function of mixing time should give a series of "build-up" and "transient well" curves for the inverted and non-inverted sites respectively. This transient decrease in intensity arises from the exchange between the inverted and non-inverted sites, and the fit of this portion of the curve yields a rate constant for this exchange process.  As will be demonstrated here, the inability to qualitatively observe this transient attenuation of signal does not completely prohibit the experiment from capturing pieces of ion hopping rates and construct an overall Li diffusion mechanism.

**Table 4.1:** Effect of inversion efficiency on obtained rate constant and goodness of fit as measured by a $\chi^2$ value.

| **Inversion Percentage for Site D** | **Rate Constant, $k_{CD}$ ($s^{-1}$)** | **$\chi^2$ (from CIFIT)** |
|---|---|---|
| 41% | 35 ± 25 | 0.023 |
| 63% | 50 ± 25 | 0.029 |

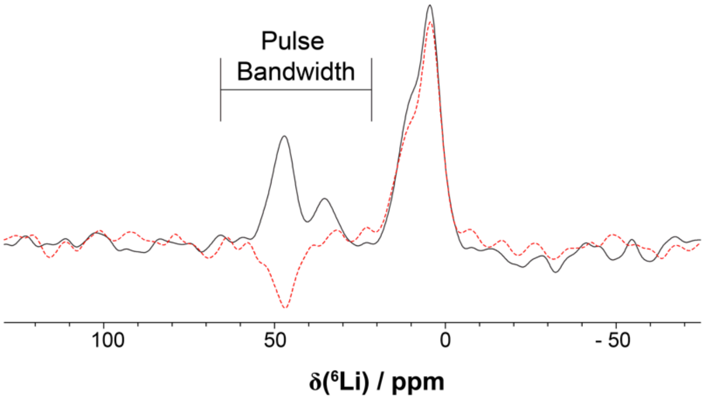

**Figure 4.3:** A demonstration of the effect of Selective Pulse Bandwidth on the MAS spectrum of $Li_2MnP_2O_7$ at room temperature. The spectrum shown in black is the typical 1D $^6$Li spectrum for $Li_2MnP_2O_7$ with no inversion pulse, compared to the red spectrum that uses a 1000 microsecond Gaussian inversion pulse centered around ~45 ppm.

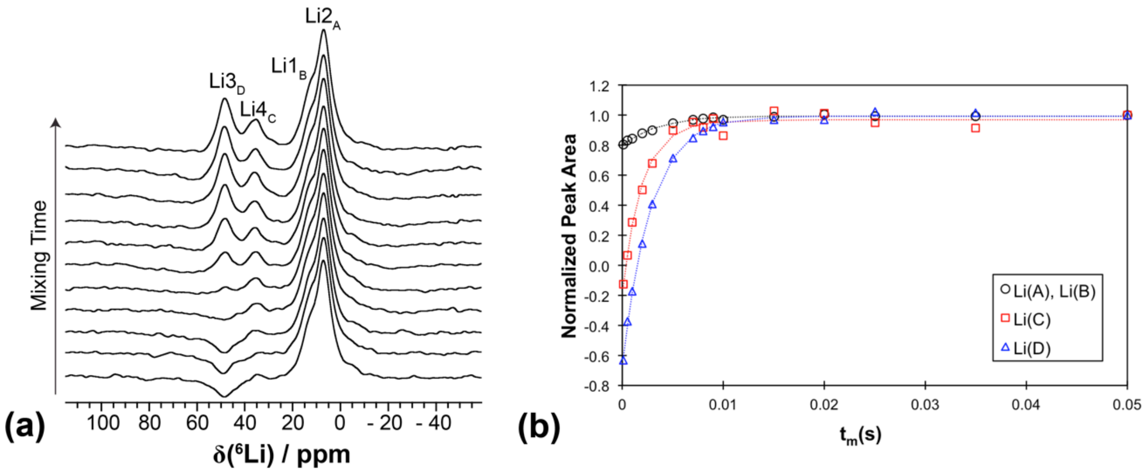

**Figure 4.4: (a)** Stack of 1D MAS spectra with increasing mixing time demonstrating the effect of inversion and recovery in an SI experiment, and **(b)** the normalized integration of each of the deconvoluted peaks in the SI experiment at room temperature.

As is depicted in **Figure 4.5**, both of the non-inverted peak regions are perturbed to varying extents by the inversion pulse. Moreover, no attenuation of the peak intensity after the shortest mixing time is observed. This is attributed to the combination of short nuclear relaxation times with relatively slow exchange rates for the mobile Li sites. Despite a lack of defined transient-well behaviour for non-inverted spins, the intensity as a function of mixing time is still effectively modeled by CIFIT using an estimated rate constant in combination with predetermined nuclear relaxation rates. At all available temperatures, resonances $\mathrm{Li_A}$ and $\mathrm{Li_B}$ remained too significantly overlapped to obtain any Li ion hopping rates between these sites. Initially allowing all rate constants to be varied by the CIFIT fitting procedure yielded results with unreasonably high error bars (>100%) and even negative rate constants in some instances. This prompted a reevaluation of the procedure in which all parameters included in the rate matrix were allowed to vary, and indeed by limiting the available exchange partners more reasonable fits and error bars were obtained. The exchange pairs were therefore restricted in the rate matrix to fit only $Li_C$-$Li_D$ exchange, as fits for other exchange pairs consistently gave rise to a negligible and/or negative rate constant from CIFIT and were thus assumed to be zero. However, the rate constant for $Li_D$-$Li_C$ exchange was found to sit between 45 – 100 Hz over the investigated temperature range. The exchange rates effectively corroborate the aforementioned site assignment in this material, where Li resonances were initially assigned to crystallographic positions by analysis of Li-O-Mn contacts. It is worth acknowledging that $Li_A$-$Li_B$ exchange is not quantified herein due to a lack of spectral resolution, however, as a result of their geometric similarity to the $Li_C$-$Li_D$ pair there is no reason to believe that they should not exchange with each other on a similar timescale. The observed rate constant, or lack thereof, implies that the exchangeable Li ions reside within the same two-dimensional tunnel rather than in opposing tunnels. In light of the fact that Li ions sharing a tunnel are ~3 Å apart, compared to >5 Å for cross-tunnel distances, it would be unlikely to observe exchange between Li ions residing in different tunnels without any within-tunnel ion hopping. The selective inversion results therefore support the initial peak assignment, where we can ascribe the low frequency region to Li1 and Li2 respectively and similarly, the high frequency sites to Li3 and Li4. As Li1 and Li2 share a tunnel, with Li3 and Li4 in a separate, distinct tunnel, the exchange experiments suggest that Li ion mobility occurs only within tunnels in the $Li_2MnP_2O_7$ structure, and not between them.

While the combination of slow Li ion hopping and fast nuclear relaxation makes exchange studies by NMR challenging, it is demonstrated here that reasonable kinetics information can still be obtained to provide some insight into Li ion diffusion pathways in the monoclinic pyrophosphate structures. The poor Li ion kinetics in the manganese pyrophosphate framework are likely at least partially to blame for the poor electrochemical performance observed elsewhere. Additionally, by limiting Li diffusion to distinct tunnels, motion can conceivably be impeded by defect ions as is observed for the olivine $LiFePO_4$ phase.[19,20]

### 4.3.3 SI Experiments to Study Li Exchange in $Li_2SnO_3$

The exchange rates that are measurable by NMR are determined almost entirely by the lifetime of spin polarization as defined by the relaxation parameters for a given sample. While for paramagnetic materials with fast-relaxing nuclei such as $Li_2MnP_2O_7$ it is difficult to quantify slow ion exchange, this quantitative limit is not inherent to the method, but rather the sample. Such is the case for diamagnetic slow Li ion conductors such as $Li_2TiO_3$ and $Li_2ZrO_3$, where although dynamics are known to be slow in these materials, their relatively long spin lifetimes produce improved quantitative results by exchange NMR experiments.[21-23] The selective inversion method was applied to study the ion hopping rates in $Li_2SnO_3$, where the rates are expected to be relatively slow based on the isostructural Ti and Zr analogues. Although other NMR techniques had been implemented to study Li ion hopping in $Li_2SnO_3$, quantitative rate determination requires a method that accounts for and models all three sites requires sophisticated data analysis such as that offered by CIFIT.[5]

Lithium tin oxide ($Li_2SnO_3$) is part of a class of oxide materials that are known to be lithium ion conductors. While examples of ion exchange in similar materials have been explored, there had been no previous examples of the ion exchange rates in $Li_2SnO_3$, and importantly, the diffusion mechanism had not been thoroughly investigated. As was demonstrated for $Li_2MnP_2O_7$ above, an improved understanding of Li ion hopping trends is absolutely essential in the development of new materials for a range of applications, especially if the ion mobility rates can be tuned so as to fit a particular application and temperature range. At room temperature, $Li_2SnO_3$ crystallizes in the monoclinic space group *C2/c*, analogous to the known $Li_2TiO_3$ and $Li_2ZrO_3$ polymorphs.[24] The structure of $Li_2SnO_3$ is depicted in **Figure 4.6**, where the lattice is made up of alternating Li-rich and Sn-rich layers, where in the Li-rich layer a distorted cubic close-packed network of oxygen houses two fully occupied Li atoms in the 8f and 4d positions (denoted Li1 and Li2). This arrangement alternates with $LiSn_2$ layers, where a third Li crystallographic position, Li3, resides.

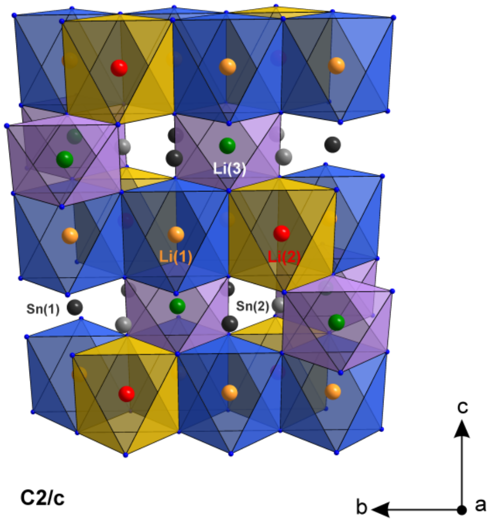

**Figure 4.5:** Crystal structure of monoclinic $Li_2SnO_3$. The three Li positions are labeled Li1, Li2 and Li3. The two unique crystallographic environments for Sn are labeled and depicted as grey and black spheres, with coordinated oxygen atoms as blue.

All three lithium sites exhibit octahedral coordination, and are thus in very similar electronic environments. Nevertheless, below room temperature there are three distinct Li resonances visible in the $^6$Li MAS spectrum of $Li_2SnO_3$, with all three peaks very close to 0 ppm. The three sites begin to coalesce above 285 K, indicating ion hopping rates that are comparable to the frequency separation between the peaks in the $^6$Li NMR spectrum. On the basis of CASTEP calculations performed by J. Langer at Graz University of Technology, the peak at 0.51 ppm was assigned to Li3, and the two low frequency sites at -0.48 ppm and -0.63 ppm to Li2 and Li1 respectively. The ideal stoichiometry for $Li_2SnO_3$ yields Li1 with 50% of the total Li in the structure, and Li2 and Li3 each with 25%. This ratio is consistent with the NMR intensities of the three sites, with a 0.93:0.96:2 ratio for Li3:Li2:Li1.

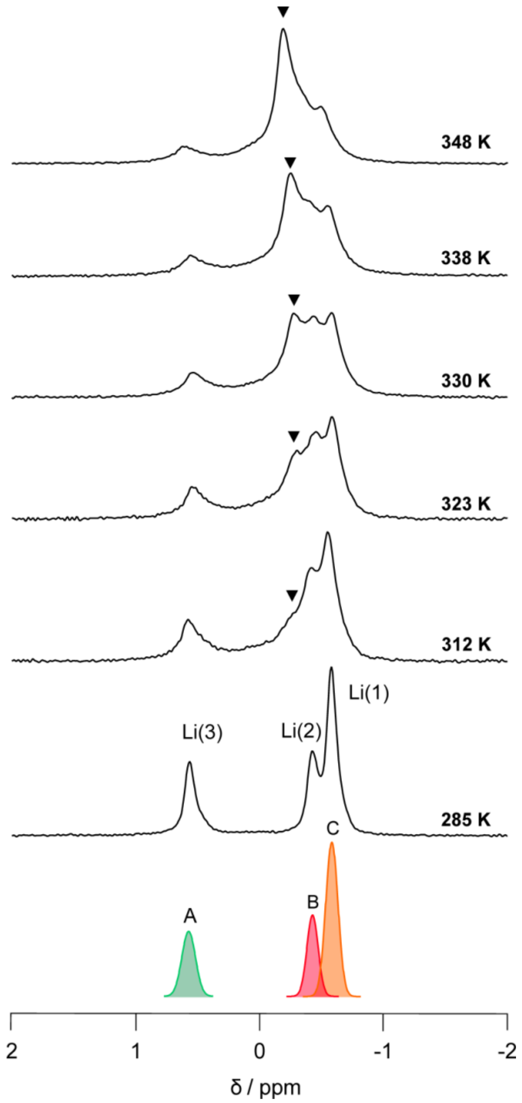

**Figure 4.6:** Variable temperature $^6$Li NMR spectra of monoclinic $Li_2SnO_3$ between 285-348 K. A deconvolution of the three sites in the spectrum at 285 K into peaks $Li3_A$, $Li2_B$, and $Li1_C$ is shown at the bottom. 1D VT NMR experiments were carried out by J. Langer at Graz University of Technology.

**Table 4.2:** Peak Widths (FWHM) and Peak Separation for $^6$Li resonances in $Li_2MnP_2O_7$ and $Li_2SnO_3$ compared to the pulse width of the selective Gaussian pulse used for SI experiments.

| Phase | Peak Label | FWHM (Hz) | Peak Separation (Hz) | | Pulse Width (Hz) |
|---|---|---|---|---|---|
| **$Li_2MnP_2O_7$** | A | 274 | A-B | 275 | **1000**[a] |
| | B | 317 | B-C | 1070 | |
| | C | 241 | C-D | 560 | |
| | D | 356 | | | |
| **$Li_2SnO_3$** | A | 14 | A-B | 73 | **40** |
| | B | 16 | B-C | 10 | |
| | C | 9 | | | |

[a]Limited by nuclear relaxation rates for Li ions in $Li_2MnP_2O_7$

Initial exchange NMR experiments were carried out on $Li_2SnO_3$ using 2D EXSY to identify possible exchange pairs. Exchange between the Li1 and Li3 sites is readily observed in the 2D spectrum, even at 0.1 s mixing times. Any exchange between Li1 and Li2 is not observed, likely due to the significant overlap between these peaks in the 1D spectrum making the observation of a crosspeak difficult. Furthermore, the lack of full Li1-Li2 coalescence by variable temperature NMR measurements indicates that the ion diffusion between these sites is very slow. The site resolution exhibited in the room temperature $^6$Li spectrum of $Li_2SnO_3$ makes it an ideal candidate for quantitative selective inversion exchange studies. Despite the expectation that Li diffuses slowly in this material, the comparable inefficient nuclear relaxation broadens the window over which dynamics can be observed.

A series of SI experiments using a 180-τ-90 pulse sequence with a Gaussian shaped inversion pulse were carried out over a range of temperatures for $Li_2SnO_3$. Accurate rate constants were not obtained for spectra collected above 285 K due to the onset of a complex coalescence process (**Figure 4.6**). Conversely, low temperatures slowed ion dynamics such that rate constants were immeasurable. A lack of variable temperature rate constants precludes energy barrier calculations, however, analysis at a single temperature enables determination of the Li ion exchange pathway through this complex structural network. Of the three sites, only that corresponding to Li3 is easily inverted in the $^6$Li spectrum of $Li_2SnO_3$ at 285 K. A long inversion pulse was used to select for the desired frequency band, where pulses as long as 25 milliseconds were used to select for the site of interest without perturbing nearby resonances (see **Table 4.2**). The ability to use a longer, and therefore more selective, inversion pulse is afforded by the slow $^6$Li relaxation rates in $Li_2SnO_3$ as compared to $Li_2MnP_2O_7$. The latter having a $T_1$ of a few milliseconds limits the length of the Gaussian pulse that can be used in the experiment due to relaxation effects during the application of the radiofrequency pulse. A comparison between the peak width and separation for each of the sites in $Li_2SnO_3$ and $Li_2MnP_2O_7$ is provided in **Table 4.2**, demonstrating the relative ease with which selective pulses can be applied in the tin oxide system.

The inversion and subsequent recovery of the Li3 site in the $^6$Li NMR spectrum of $Li_2SnO_3$ was plotted as a function of mixing time, along with the intensity of the Li1 and Li2 sites. The latter two exhibited the expected behaviour for sites in exchange with the inverted resonance, where a transient decrease in intensity is readily observed due to the chemical exchange between the inverted and unperturbed $^6$Li nuclei. By fitting the experimental curves using the CIFIT program, rate constants for Li3-Li1 and Li3-Li2 exchange are measured as 3 $s^{-1}$ and 0.7 $s^{-1}$ respectively, in good agreement with preliminary 2D EXSY measurements. A lack of sufficient resolution between Li1 and Li2 resonances prevented the quantification of any exchange between these sites, however a lack of coalescence despite the relative closeness in chemical shift implies that any mobility of Li ions between the two sites is negligible compared to exchange of either site with lithium ions residing in the Li3 position.

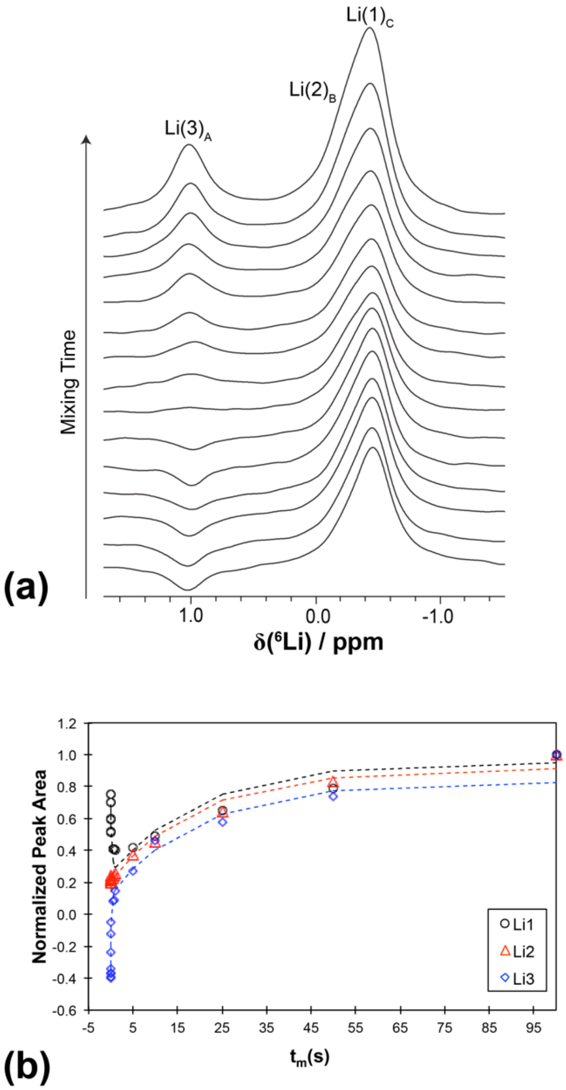

**Figure 4.7: (a)** Example stack of $^{6}$Li SI spectra for $Li_2SnO_3$ at 250 K. **(b)** Selected example of CIFIT fitting results for $Li_2SnO_3$ at 285 K. The inverted peak (Li3) exhibits an exponential build-up with mixing time ($t_m$) while the Li1 and Li2 resonances are attenuated due to exchange with the inverted site.

Given the known structural arrangement of Li atoms in $Li_2SnO_3$, the results of the exchange experiments are somewhat surprising. The Li1 and Li2 sites share the ‘lithium rich’ plane, and thus would be expected to readily exchange with one another, while the Li3 position is in a separate, Sn-rich layer. The markedly improved propensity for both

Li1 and Li2 to hop out of the plane to the Li3 site indicates that in-plane hopping is actually suppressed in this structure. Upon closer consideration of the site occupancies, the increased probability of Li3 site vacancies compared to either Li1 or Li2 likely drives the diffusion of the Li ions out of the lithium rich layer, to reside on the Li3 position. Furthermore, a slight preference for vacancy formation at the Li2 position relative to Li1 accounts for the faster Li2-Li3 hopping rate compared to Li1-Li3. The result is an unexpected vacancy-driven out-of-plane diffusion mechanism in this material, where the increased likelihood of finding a vacant Li3 site drives the overall ion diffusion in this structural motif. Not only does this allow for the understanding of the specific ion hopping pathway in this particular class of ion conductors, but it also provides valuable insight when it comes to materials development and design where the role of site vacancies demonstrably plays an important role in the overall diffusion mechanism within a complex structure.

## 4.4 Summary

As demonstrated by the examples of paramagnetic $Li_2MnP_2O_7$ and diamagnetic $Li_2SnO_3$ discussed herein, the ability of the selective inversion method to extract quantitative rate information depends entirely on the inherent nuclear relaxation properties of the material studied. Not only are smaller rate constants obtainable due to the longer window over which spin coherence endures, but also the selectivity of the pulse can be improved when relaxation parameters are not limiting.

In the first example, a lithium manganese pyrophosphate compound was investigated by ssNMR spectroscopy in an effort to understand ion dynamic effects on electrochemical performance in this class of materials. It was ascertained that slow ion hopping occurs between Li ions residing within the same tunnel, but not between tunnels. The relatively slow ion exchange between only the closest Li ion pairs is consistent with the poor electrochemical performance exhibited by the Mn-containing analog, particularly at fast cycling rates. This result provides important insight into the Li ion mobility pathways in the pyrophosphate class of materials, an observation that could be extended to other, similar structural motifs.

The extension of this method to another known slow lithium ion conductor, $Li_2SnO_3$ proved very successful in the quantification of rate constants for two unique Li ion hopping processes in this structure. Interestingly, it was determined that the overall ion diffusion is largely facilitated by the site vacancies at site Li3, ultimately resulting in increased Li diffusion out of the plane to cross layers rather than within the Li-rich plane. This unexpected result emphasizes the need for accurate, quantitative methods to study Li diffusion pathways in order to improve and facilitate the development of ion conductors of varying rates for a wide number of applications.

In general, the selective inversion method has in the past been applied to paramagnetic Li cathode materials, where ideal peak separation and relatively fast ion dynamics allow for determination of ion hopping rates. In this chapter, the use of the method to explore slow ion conductors demonstrates both the power and the limitations of the technique as it applies to solid-state materials.

## 4.5 References

(1) Davis, L. J. M.; Goward, G. R. *J. Phys. Chem. C* **2013**, *117* (16), 7981.

(2) Davis, L. J. M.; He, X. J.; Bain, A. D.; Goward, G. R. *Solid State Nucl. Magn. Reson.* **2012**, *42* (C), 26.

(3) Smiley, D. L.; Davis, L. J. M.; Goward, G. R. *J. Phys. Chem. C* **2013**, *117* (46), 24181.

(4) Smiley, D. L.; Tessaro, M. Z.; He, X.; Goward, G. R. *J. Phys. Chem. C* **2015**, *119* (29), 16468.

(5) Langer, J.; Smiley, D. L.; Bain, A. D.; Goward, G. R.; Wilkening, M. *J. Phys. Chem. C* **2016**, *120* (6), 3130.

(6) Zhou, H.; Upreti, S.; Chernova, N. A.; Hautier, G.; Ceder, G.; Whittingham, M. S. *Chem. Mater.* **2011**, *23* (2), 293.

(7) Grey, C. P.; Cheetham, A. K.; Dobson, C. M. *J. Magn. Reson., Ser. A* **1993**, *101* (3), 299.

(8) Bain, A. D.; Cramer, J. A. *J. Magn. Reson., Ser. A* **1996**, *118* (1), 21.

(9) Bain, A. D.; Fletcher, D. A. *Mol. Phys.* **1998**, *95* (6), 1091.

(10) Bain, A. D.; Cramer, J. A. *J. Magn. Reson., Ser. A* **1993**, *103* (2), 217.

(11) Bain, A. D.; Cramer, J. A. *J. Magn. Reson., Ser. A* **1993**, *103* (2), 217.

(12) Gesmar, H.; Led, J. J. *Journal of Magnetic Resonance (1969)* **1986**, *68* (1), 95.

(13) Masquelier, C.; Croguennec, L. *Chem. Rev.* **2013**, *113* (8), 6552.

(14) Adam, L.; Guesdon, A.; Raveau, B. *J. Solid State Chem.* **2008**, *181* (11), 3110.

(15) Tamaru, M.; Barpanda, P.; Yamada, Y.; Nishimura, S.-I.; Yamada, A. *J. Mater.*

*Chem.* **2012**, *22* (47), 24526.

(16) Tamaru, M.; Chung, S. C.; Shimizu, D.; Nishimura, S.-I.; Yamada, A. *Chem. Mater.* **2013**, *25* (12), 2538.

(17) Grey, C. P.; Lee, Y. J. *Solid State Sciences* **2003**, *5* (6), 883.

(18) Grey, C. P.; Dupré, N. *Chem. Rev.* **2004**, *104* (10), 4493.

(19) Axmann, P.; Stinner, C.; Wohlfahrt-Mehrens, M.; Mauger, A.; Gendron, F.; Julien, C. M. *Chem. Mater.* **2009**, *21* (8), 1636.

(20) Chung, S.-Y.; Kim, Y.-M.; Choi, S.-Y. *Adv. Funct. Mater.* **2010**, *20* (24), 4219.

(21) Baklanova, Y. V.; Arapova, I. Y.; Buzlukov, A. L.; Gerashenko, A. P.; Verkhovskii, S. V.; Mikhalev, K. N.; Denisova, T. A.; Shein, I. R.; Maksimova, L. G. *J. Solid State Chem.* **2013**, *208* (C), 43.

(22) Bottke, P.; Freude, D.; Wilkening, M. *J. Phys. Chem. C* **2013**, *117* (16), 8114.

(23) Ruprecht, B.; Wilkening, M.; Uecker, R.; Heitjans, P. *Phys. Chem. Chem. Phys.* **2012**, *14* (34), 11974.

(24) Hodeau, J. L.; Marezio, M.; Santoro, A.; Roth, R. S. *J. Solid State Chem.* **1982**, *45* (2), 170.

# Chapter 5: Identifying Phase Transformations and Ion Hopping Rates in $LiFeV_2O_7$ by $^7$Li Solid-State NMR During Electrochemical Cycling

## 5.1 Introduction

With the massive growth and commercialization of lithium ion batteries, the development of unique materials has similarly escalated. While the use of phosphates, fluorophosphates, pyrophosphates, and sulfates have been extensively studied for Li cathode materials, a relatively unexplored class of cathodes is the vanadate derived structure where vanadium is not designed to be the redox active metal but rather a part of the structural polyanionic network. Vanadates such as $LiFeV_2O_7$ and $Li_{1.98}Fe_{5.33}(VO_4)_6$ have been proposed by M. Dollé and co-workers, where they have demonstrated reversible insertion of Li ions into these novel structures at competitive voltages. In particular, $LiFeV_2O_7$ was identified as a possible candidate electrode material as it boasts the ability to insert a single Li equivalent with high reversibility.[1] Although initial results were rather promising, the structure is not yet well characterized and thus the mechanism for Li ion diffusion and intercalation in this material is not fully understood.

This chapter demonstrates the use of $^7$Li solid-state NMR to probe both the as-prepared $LiFeV_2O_7$ structure as well as phase changes and ion dynamics in electrochemically cycled $Li_{1+x}FeV_2O_7$ electrodes. A combination of one and two-dimensional *ex situ* NMR methods are employed to identify changes to local Li environments and quantify the Li ion exchange processes throughout cycling. As will be discussed herein, NMR proves to be an incredibly sensitive tool relative to other methods for differentiating between distinct Li environments in $LiFeV_2O_7$. For example, the presence of Li-site disorder, which had not been identified previously, is evident by $^7$Li NMR experiments of the pristine material. Furthermore, distinct changes to the Li environments during electrochemical cycling are identified by *ex situ* $^7$Li NMR, and, in combination with diffraction experiments, confirm a phase transformation at approximately half way through the discharge process. This structural reorientation coincides with a significant boost to Li ion mobility and thus overall Li diffusion. These changes are carefully characterized and quantified where possible, lending insight into the unique properties of this novel cathode material.

The results presented in this chapter are reported as part of a collaboration with Y. Benabed under the supervision of Prof. M. Dollé at Université de Montréal. Sample preparation, powder X-ray diffraction, and extensive electrochemical testing was performed by Y. Benabed, with separate electrochemical and subsequent NMR characterization carried out entirely at McMaster University under supervision of Prof. G. Goward. This project is ongoing, particularly aspects relating to structural characterization methods of cycled phases using diffraction methods to identify the structural changes of the framework atoms upon insertion of Li ions electrochemically. As this is not yet well understood, the focus of this chapter will be primarily on the NMR results and the significant insight that this method brings to this material.

## 5.2 Experimental Methods

### 5.2.1 Solid-State $^7$Li NMR

Lithium-7 NMR spectra were collected on a wide bore 300 MHz spectrometer at a resonant frequency of 116.64 MHz with a 1.4 μs π/2 pulse. A Bruker 1.3mm double resonance probe was employed for fast MAS rates of 50-65 kHz. Two-dimensional EXSY experiments were carried out at room temperature for all spectra using the standard 90-$t_1$-90-$t_{mix}$-90 pulse sequence. Selective inversion experiments utilized a 500 μs selective Gaussian pulse with 0.01 W power for inversion, followed by a variable mixing time and a final 90° read out pulse of 1.4 μs. Temperatures were calibrated by the accepted method using a $Sm_2Sn_2O_7$ chemical shift thermometer.[2] All spectra were referenced to 1M LiCl at 0 ppm.

### 5.2.2 Electrochemical Cycling

Electrodes were prepared by grinding the active material ($LiFeV_2O_7$) obtained from collaborators at Université de Montréal in an 85:10:5 weight % ratio with carbon black (CB) and polyvinylidene fluoride (PVDF). A solution of 2.00% PVDF in N-methyl-2-pyrrolidone (NMP) was added to ground active material and CB, and let stir for 2 hours. This slurry was then cast onto Al foil and dried under vacuum for 12 hours at 120 °C. This casted slurry was then punched into discs 1.27 cm in diameter, and assembled in coin cells with 1M $LiPF_6$ in a 1:1 wt% ethylene carbonate:dimethylcarbonate solution (Novolyte) as the electrolyte and Li-metal as the counter electrode. Cells were cycled at a rate of C/100, corresponding to the current rate to achieve a single charge cycle over 100 hours. Cathodes were extracted for NMR experiments by disassembly in an argon filled glove box, followed by washing with dimethylcarbonate to remove Li salts accumulated at the surface of the electrode.

## 5.3 Results and Discussion

### 5.3.1 Motivation and Background

The use of vanadium oxides have been explored in the field of electrochemistry as they generally offer rich redox chemistry allowing for the transfer of multiple alkali ions per formula unit.[3] The ability to form complex structures combining V-O polyhedra with additional redox active transition metals creates a multitude of opportunities for designing structural motifs that exhibit ideal electrochemical properties tuned to a specific application. A number of vanadium oxide derivatives have been successfully developed and in some cases implemented commercially, including $Ag_2V_4O_{11}$, $V_2O_5$, $LiV_3O_8$, and $LiVO_3$.[4-7] More recently, Patoux and Richardson[3] demonstrated the ability to insert lithium into a series of lithium vanadates that exhibit capacities between 160-200 mAh/g. Building upon this success, the ternary phase diagram involving $Li_2O$, $Fe_2O_3$, and $V_2O_5$ has been explored in an effort to discover novel iron vanadate phases exhibiting favourable electrochemical properties. In 2017 Dollé and coworkers successfully synthesized the novel phase, $LiFeV_2O_7$, identified as the first viable cathode material from the $Li_2O$-$Fe_2O_3$-$V_2O_5$ phase diagram. This iron vanadate structure crystallizes in the monoclinic *Cc* space group consisting of redox-active corner-shared $FeO_6$ octahedra connected to $V_4O_{18}$ structural units as depicted in **Figure 5.1**. Synthesized by a high temperature solid-state route, the material exhibits approximately 100 mAh/g capacity on the first cycle, with retention of 85% of this capacity after 60 cycles. As the full reduction of the $Fe^{3+}$ cation corresponds to a theoretical capacity of 97 mAh/g, there is some added capacity possibly afforded by participation of vanadium in the redox process. In their recent report on this phase, Benabed *et al.*[1] used potentiostatic intermittent titration (PITT) electrochemical measurements to loosely characterize some of the electrochemical features observed between 2.8 and 2.35 V. Despite slow electrochemical cycling at rates of C/100, kinetic limitations still appear to plague the material. Furthermore, in combination with the observation of solid-solution behaviour during cycling, characterized by a gradual shift of the structure over time, biphasic domains were identified along the voltage profile. There is thus a complex electrochemical process that occurs at the $Li_{1+x}FeV_2O_7$ electrode during the charge and discharge processes, and these initial electrochemical studies and structural characterization are the first steps in understanding this unique class of iron vanadate materials. Nevertheless, properties such as ion dynamics and Li disorder are yet to be fully explored, compelling the use of $^{7}Li$ solid-state NMR to uniquely probe the mobile ion over the course of the electrochemical process.

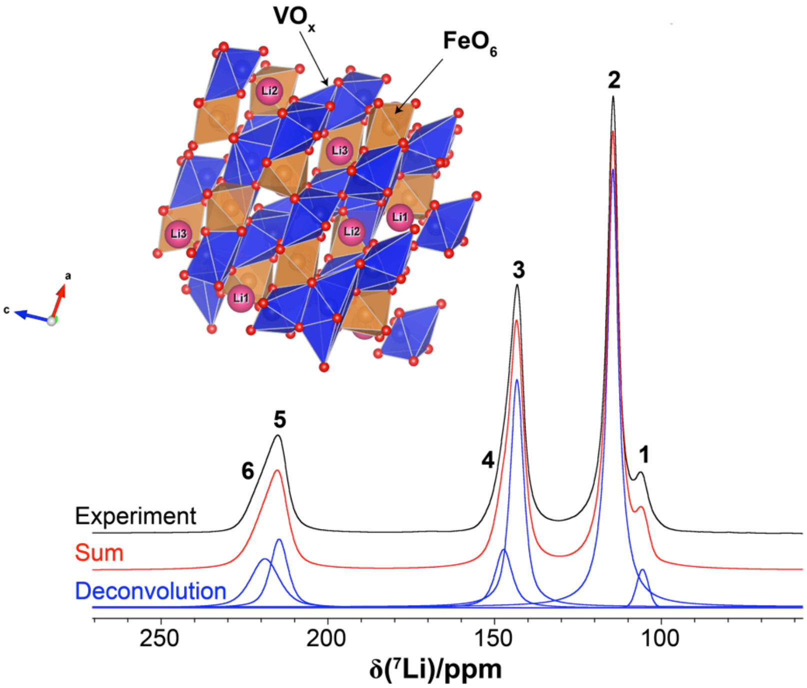

**Figure 5.1:** $^7$Li MAS ssNMR spectrum of pristine $LiFeV_2O_7$ using a Hahn Echo experiment. The spectrum was deconvoluted into 6 unique resonances, shown in blue, with the sum of the deconvolution to give the overall fit to the spectrum in red. The unit cell of $LiFeV_2O_7$ is shown in the inset, housing three unique Li positions.

**Table 5.1:** Chemical shifts and relative peak areas of the isotropic resonances in the $^7$Li NMR spectrum of $LiFeV_2O_7$

| Peak Label | Chemical Shift (ppm) | Rel. Integral |
|---|---|---|
| **1** | 106 | 0.35 |
| **2** | 115 | 5.65 |
| **3** | 143 | 3.00 |
| **4** | 147 | 1.00 |
| **5** | 215 | 1.15 |
| **6** | 219 | 1.35 |

### 5.3.2 $^7$Li Solid-State NMR of Pristine $LiFeV_2O_7$

As per diffraction studies by Benabed *et al.,*[1] the iron vanadate framework of $LiFeV_2O_7$ houses three unique Li atoms in a 1:1:1 ratio. Despite the apparent similarity of all three sites, they are magnetically inequivalent and observable by $^7$Li NMR. In fact, the $^7$Li MAS NMR of as-prepared $LiFeV_2O_7$ exhibits more Li environments than would be expected based on the structure determined by single crystal XRD. Despite three unique equally occupied chemical environments for Li, the $^7$Li NMR spectrum (**Figure 5.1)** is fit to a minimum of 6 sites, separated into three distinct chemical shift pairs, where each frequency region contains two unique sites very close in chemical shift. The chemical shift values and relative peak areas determined from a deconvolution of the spectra are provided in **Table 5.1**. The ratio of each of the individual peaks within a given chemical shift pair is variable, and depends on the particular synthesis. The comparison of $^7$Li NMR spectra of alternate synthesis trials is provided in Appendix I at the end of this thesis. Based on the integrated intensities and chemical Li environments, crystallographic sites Li1 and Li3 are expected to appear at similar chemical shifts, and are therefore encompassed by the highest intensity peak at 115 ppm. The Li2 site is predicted to give rise to the peak at 143 ppm based on the relative peak area ratio. Preliminary density functional theory calculations performed in VASP confirm this assignment, the details of which are provided in Appendix A1. This leaves an additional 4 peaks that are unaccounted for by the proposed crystal structure. Despite their significant appearance in the $^7$Li NMR spectrum, the PXRD of individual powder samples give no indication of crystalline paramagnetic impurities that could account for the peaks corresponding to an impurity phase in addition to pure $LiFeV_2O_7$. The anomaly is therefore hypothesized to arise from small amounts of Fe or V reduction in the pristine material resulting in the additional NMR peaks. Alternatively, the unidentified sites could result from disordering between the $Li^+$ and $Fe^{3+}$ ions whereby the cations switch atomic positions due to their comparable atomic radii. This phenomenon has been observed in a variety of other Li-Fe materials, in some cases even having a significant impact on the ultimate electrochemical behaviour of the material such as is observed for $LiFePO_4$.[8] This type of defect can be especially difficult to identify by X-ray diffraction alone due to the poor scattering ability of Li atoms.

Efforts to more thoroughly characterize the pristine material by other diffraction methods are ongoing, however; $^7Li$ NMR decidedly reveals structural Li disorder not identified by routine characterization techniques. The role that such a disorder might play in the ultimate electrochemical performance is also not yet understood, as despite apparent differences in the degree of disorder with sample preparation, no correlation to experimental capacity or voltage profile has been made. Future efforts combining an NMR study with systematic electrochemical cycling as a function of synthesis could potentially provide insight into the source of this disorder, and would complement the work presented here nicely.

Solid-state NMR was further utilized as means to identify possible Li ion dynamics in pristine $LiFeV_2O_7$. Both 2D EXSY and 1D selective inversion experiments were made use of in the quantification of Li-Li exchange rates between the highly resolved peaks exhibited by this material. In both cases no evidence of ion dynamics on a measurable timescale were observed, despite the ability to efficiently probe individual exchange pairs due to the peak separation in the MAS spectrum. The measured spin-lattice relaxation rates are 1.5 ms, 2.7 ms and 3.5 ms for each of the three frequency regions at 230, 145 and 105 ppm respectively, suggesting that any exchange occurring significantly slower than this timescale is not measurable by these methods. Despite slow ion dynamics, the ability to cycle this material at slow rates implies that while diffusion is not absent, kinetic limitations for Li ion transport play a role, as was shown by Benabed *et al.*[1].

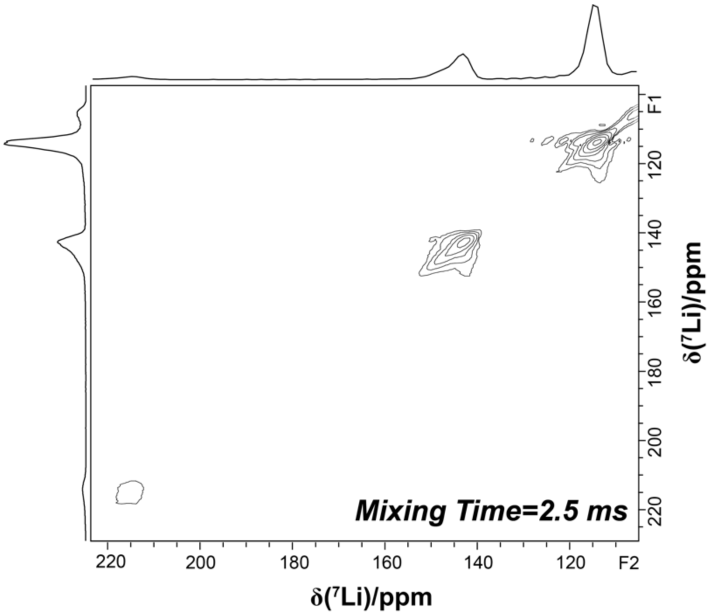

**Figure 5.2:** $^{7}$Li 2D EXSY spectrum of pristine $LiFeV_2O_7$ with a 2.5 millisecond mixing time. No crosspeaks indicate that there is a lack of fast Li-Li exchange in the structure at room temperature.

### 5.3.3 *Ex Situ* $^7$Li Solid-State NMR investigation of Structural Changes in $Li_xFeV_2O_7$

Electrochemical cells incorporating $LiFeV_2O_7$ cathodes were assembled and cycled between 3.4-2.3 V at a slow rate of C/100. All cells used for *ex situ* $^7$Li MAS NMR experiments were cycled at McMaster University in the Goward lab. In good agreement with electrochemical cycling data performed at UdeM by Y.Benabed in the Dollé lab, several voltage plateaus intermixed with sloping regions are observed in a simple discharge/charge curve for $LiFeV_2O_7$. A total capacity of 80 mAh/g (out of a theoretical 97 mAh/g) was achieved for a typical cell cycled in house, somewhat less than those cycled by the Dollé group, where 100 mAh/g was achievable, corresponding to >100% of the theoretical capacity. This discrepancy is attributed to minor differences in electrode and cell construction. Whereas powder X-ray diffraction experiments were performed for a series of cycled $Li_{1+x}FeV_2O_7$ cathodes by Y. Benabed under the supervision of M. Dollé, *ex situ* $^7$Li MAS NMR spectra were collected at various intervals along the discharge curve and compared to diffraction results.

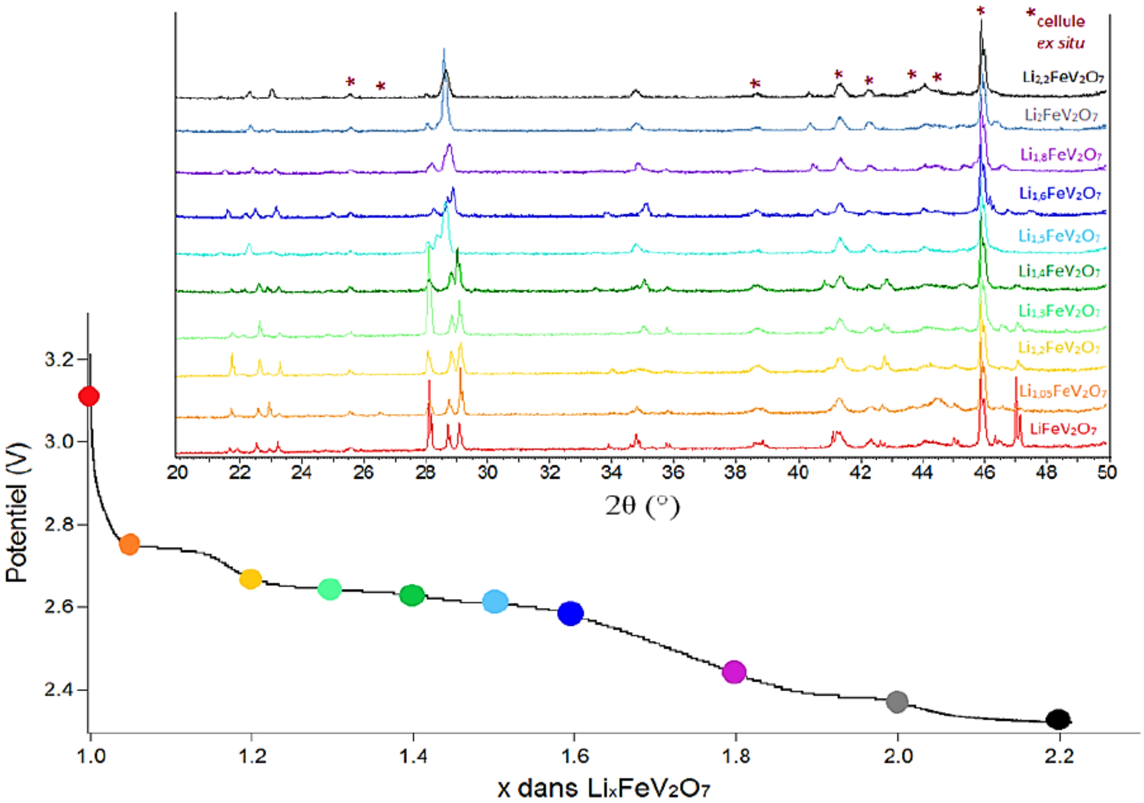

**Figure 5.3:** *Ex Situ* XRD results obtained from Benabed *et al*. depicting the change to the diffraction pattern during electrochemical discharge of $LiFeV_2O_7$ cathodes. A very gradual shift in the powder pattern is observed up until the teal diffraction pattern, corresponding to the $Li_{1.5}FeV_2O_7$ phase.

The $^7Li$ NMR results as a function of electrochemical cycling are depicted along with a single discharge/charge cycle in **Figure 5.4**. Upon discharging to a voltage of 2.65 V, significant broadening of the peaks was observed in the $^7Li$ MAS spectrum, as expected due to the transformation of the transition metal from $Fe^{3+}$ to $Fe^{2+}$. The change from a high-spin $d^6$ to a $d^7$ electron configuration at the transition metal effectively decreases the anisotropy of the magnetic susceptibility of the metal, thus creating a broadening effect in the isotropic resonances of nearby Li nuclei. This uniform broadening across the spectrum is also consistent with the formation of a solid-solution with $Fe^{2+}$ atoms being mixed throughout the structure rather than a phase separation between oxidized and reduced phases. This is in agreement with the *ex situ* XRD results from Dollé and coworkers,[1] depicted in **Figure 5.3,** which revealed no significant changes in the diffraction pattern other than a small shift in the reflections to reflect expansion of the unit cell to accommodate additional Li atoms for addition of up to 20% of the insertable Li equivalent. This systematic broadening of the NMR lineshapes continues until 2.45 V is reached, which corresponds to insertion of about 0.5 equivalents of Li. At this voltage, a sudden narrowing of the peaks is observed, and three new resonances are observed until discharging to 2.35 V (~0.7 Li added) where the broadening resumes until full charge. Together with the appearance of the narrow peaks, an additional, broad signal is retained likely from the primary phase undergoing a solid-solution phase change. The $^7$Li MAS NMR suggest solid-solution in combination with specific biphasic regions as evidenced by the coexistence of a collection of narrow and broad resonances. This structural change is mirrored by the *ex situ* XRD data at $Li_{1.55}FeV_2O_7$ where the once gradually shifting reflections begin to change in a non-uniform fashion. This sudden change in the $^7$Li NMR coupled with the changing XRD pattern could be indicative of a structural rearrangement that occurs in order to accommodate more Li atoms into the parent structure. This unidentified second phase is observed by $^7$Li NMR both on the first discharge and charge processes, as well as after multiple charge cycles, indicating that its formation is robust and highly reversible. Determination of the structural origin of the chemical shifts is nontrivial, as the lack of high-quality powder XRD data has so far prevented a refinement of the powder pattern to determine quantitative changes to the atomic parameters and unit cell.

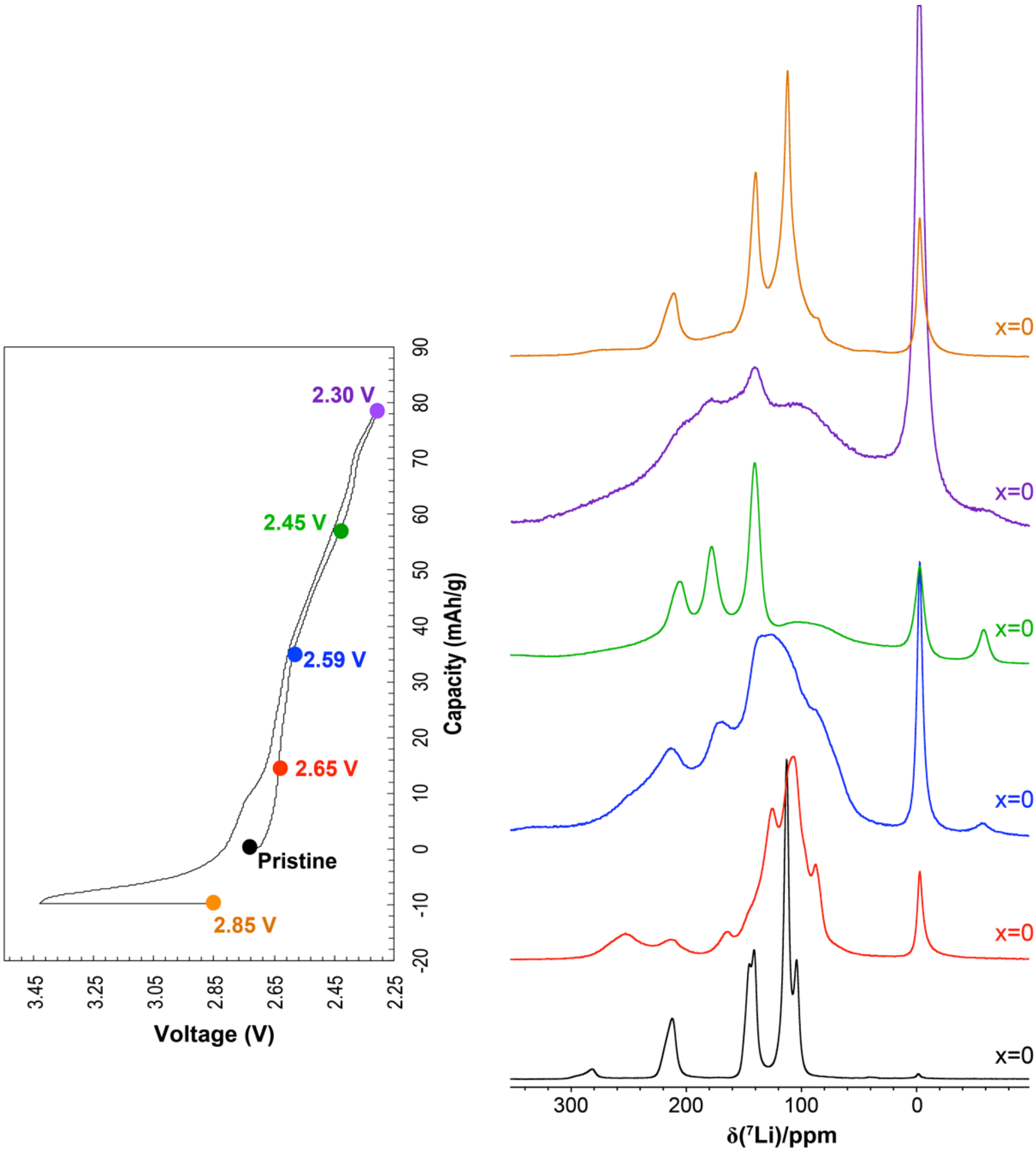

**Figure 5.4:** Stack of $^7$Li spectra as a function of state of discharge as labeled on the electrochemical curve on the left. Coloured spectra are matched to the voltage to which $LiFeV_2O_7$ electrodes were discharged. The approximate composition of $Li_{1+x}FeV_2O_7$ for each spectrum is denoted on the right hand side.

Upon recharging the cell to the initial $LiFeV_2O_7$ stoichiometry, the original peak positions are almost completely recovered with only small changes to the relative intensities and shifts that could be indicative of a partially irreversible transformation of the structure. This recovery of the structure is crucial, especially for phases shown to undergo structural transitions, as it implies that all transformations are fully reversible, and will be less likely to contribute to capacity fade over extended cycling times.

### 5.3.4 Li-Li Exchange Rates in Cycled $Li_{1+x}FeV_2O_7$ Electrodes

As already discussed, favourable Li ion dynamics are an essential component of any good cathode material, as it contributes to capacity retention at fast cycling rates. $^7$Li 2D EXSY NMR experiments were therefore used to explore ion dynamics in cycled $Li_{1+x}FeV_2O_7$ cathodes *ex situ*. Although the time consuming nature of these two-dimensional experiments make them unviable for use in quantitative studies, especially with the small sample size of the cycled electrodes, it is an excellent way to identify possible exchange partners with a single experiment and minimal data analysis. Interestingly, there is no evidence of Li dynamics along the discharge pathway until the appearance of the anomalous second phase discussed in section 5.3.3 that forms around the composition of $Li_{1.55}FeV_2O_7$. **Figure 5.5** depicts the 2D EXSY spectra collected for a $Li_{1+x}FeV_2O_7$ cathode with composition x=0.55. The Li mobility concurrently disappears upon the conversion of this phase to $Li_2FeV_2O_7$ at the end of discharge. This unique mobility has lead to the denotation of the phase corresponding to the three narrow resonances in the $^7$Li MAS NMR spectra within the composition window of ~x=0.5 to x=0.6 henceforth as the *mobile phase*.

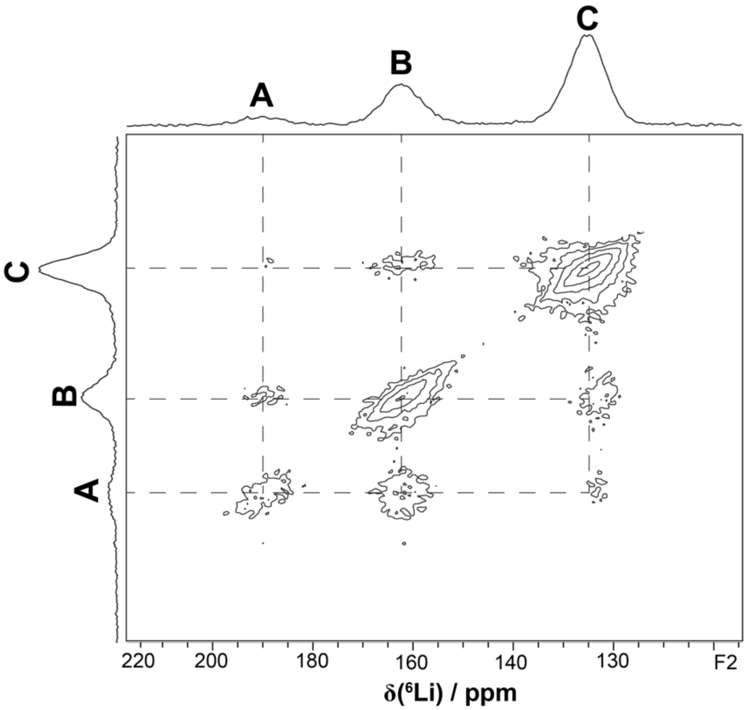

**Figure 5.5:** $^7$Li 2D EXSY spectrum collected at 320 K with a mixing time of 2 ms on a sample of $Li_{1.55}FeV_2O_7$ discharged to 2.45 V corresponding to x=0.55. Clear off-diagonal peak intensity is visible between the three most intense peaks, indicating fast ion hopping in this phase.

The region over which the mobile phase exists was probed by the assembly of a series of cathodes extracted over the voltage window surrounding the initial observation of this phase, namely between 2.5 V and 2.35 V on discharge, where outside of this region the mobile phase is not observed. Three electrodes discharged to 2.5 V, 2.45 V and 2.39 V were used to quantitatively study Li-Li exchange between the three sites in the mobile phase, labeled A, B, and C in order of decreasing resonance frequency. These three discharge voltages correspond approximately to compositions of x=0.5, 0.55, and 0.6 in $Li_{1+x}FeV_2O_7$. **Figure 5.6** depicts the deconvolution of the overlapping peaks in the spectrum for each of the three discharged cathodes. The chemical shifts and peak widths for the three exchanging Li sites are tabulated in **Table 5.2**, with no significant trend in chemical shift or linewidth trends with increased discharge. Selective inversion experiments were chosen to study Li-Li exchange in this material as they offer an efficient and accurate method for quantifying slow exchange in the solid state.[9-12] A series of experiments wherein each of the three peaks were individually inverted were carried out at five temperatures between 300-340 K. In addition to the variable temperature exchange experiments, a $T_1$ measurement using a standard inversion recovery pulse sequence was implemented so as to monitor any relaxation property changes as a function of temperature.

**Table 5.2:** Trend in relative peak area and chemical shift of the 3 peaks corresponding to the mobile phase (A, B, and C) and the additional broad resonance D. No significant changes are observed implying a stable structure undergoing small alterations such as unit cell volume expansion.

| **Rel. Peak Area** | *Peak Label* | | | |
|---|---|---|---|---|
| | **A** | **B** | **C** | **D** |
| **$Li_{1.5}FeV_2O_7$** | 0.17 | 0.27 | 0.36 | 1 |
| **$Li_{1.55}FeV_2O_7$** | 0.19 | 0.34 | 0.48 | 1 |
| **$Li_{1.6}FeV_2O_7$** | 0.22 | 0.38 | 0.51 | 1 |
| **Chemical Shift (ppm)** | *Peak Label* | | | |
| | **A** | **B** | **C** | **D** |
| **$Li_{1.5}FeV_2O_7$** | 215 | 179 | 146 | 98 |
| **$Li_{1.55}FeV_2O_7$** | 212 | 180 | 145 | 94 |
| **$Li_{1.6}FeV_2O_7$** | 212 | 181 | 144 | 99 |

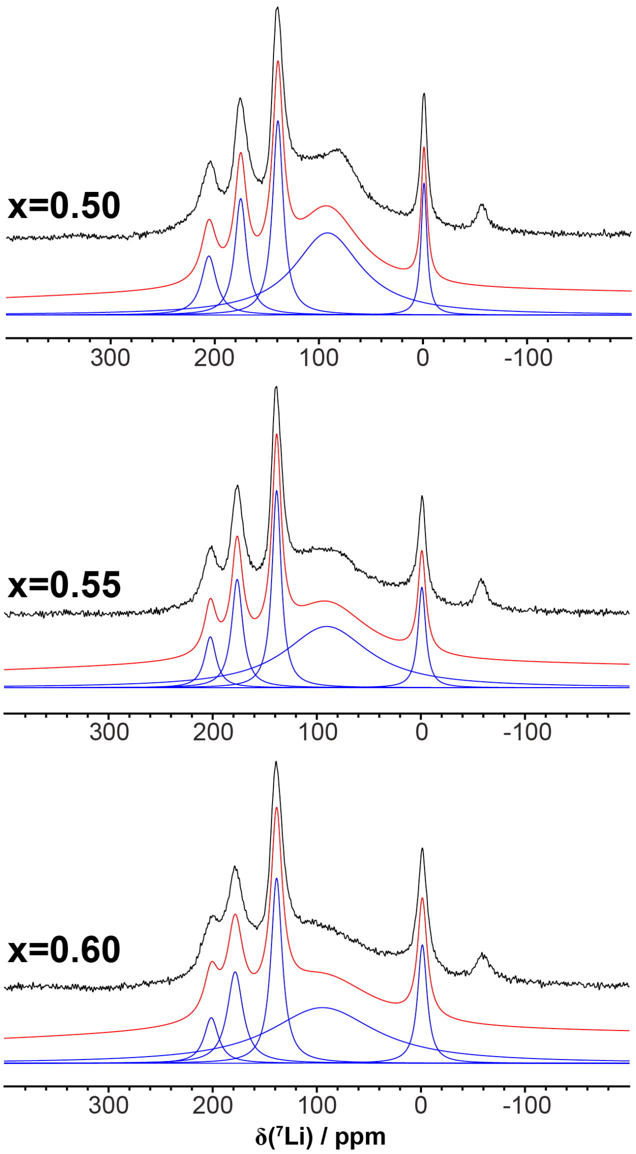

**Figure 5.6:** Deconvoluted $^{7}$Li MAS spectra of three compositions of the mobile phase observed upon discharge of $LiFeV_2O_7$ cathodes. From top to bottom the three samples were discharged to 2.5 V, 2.45 V, and 2.39 V, corresponding to $Li_{1+x}FeV_2O_7$ compositions of x=0.5, 0.55, and 0.6.

The large number of overlapping sites in the MAS $^{7}$Li NMR spectrum underlines the complex nature of this material during the electrochemical process. In order to obtain site-specific rate constants for Li-Li exchange, every spectrum collected using each individual mixing time in an SI experiment array was fit using the same four primary peaks, three belonging to the A, B, and C resonances of the mobile phase, and the last a large broad peak thought to exist as a separate phase. Preliminary 2D EXSY measurements gave no indication that the broad site is involved in Li-Li exchange with the mobile phase, and thus its contribution to the rates is not considered in the analysis shown here. Additionally, the peak present at 0 ppm in all spectra belongs to $LiPF_6$ electrolyte salt or other diamagnetic Li salts formed on the surface of the electrode during charging. Despite a washing procedure to remove these species, in all cases residual amounts of these compounds remain and show up in the NMR spectrum. Their chemical shift (close to 0 ppm) combined with the long relaxation time relative to a typical paramagnetic species confirms that they are not part of the cathode active phase. Upon plotting the experimental peak areas as a function of mixing time in the SI experiment, Li-Li exchange is evident, especially for the $Li_A$-$Li_B$ exchange pair. This is observed by the characteristic transient decrease in intensity at moderate mixing times due to the chemical exchange of nearby Li atoms with the inverted site. This transient well changes across the measured temperature range, with an increase in the depth of the well with increasing temperature (**Figure 5.7**). Furthermore, upon plotting the build-up of the inverted peak as a function of temperature, a significant change in the rate at which the intensity returns to equilibrium is observed, indicative of a temperature–dependent rate process governing the peak intensities. This behaviour is in contrast to the non-selective inversion recovery $T_1$ measurement, where the primary source of nuclear relaxation is the presence of local fields induced by nearby nuclei and unpaired electrons. The large magnetic moment of the electron makes it the dominant source of relaxation as discussed in Chapter 2. These relaxation mechanisms all lack significant temperature dependence over the limited range accessed with the SI and NSI experiments, and thus the NSI curves are not expected to change with temperature. This is demonstrated in **Figure 5.7**, and can be used as confirmation of an exchange process, as any magnetic exchange due to Li spin diffusion is not expected to be temperature dependent.

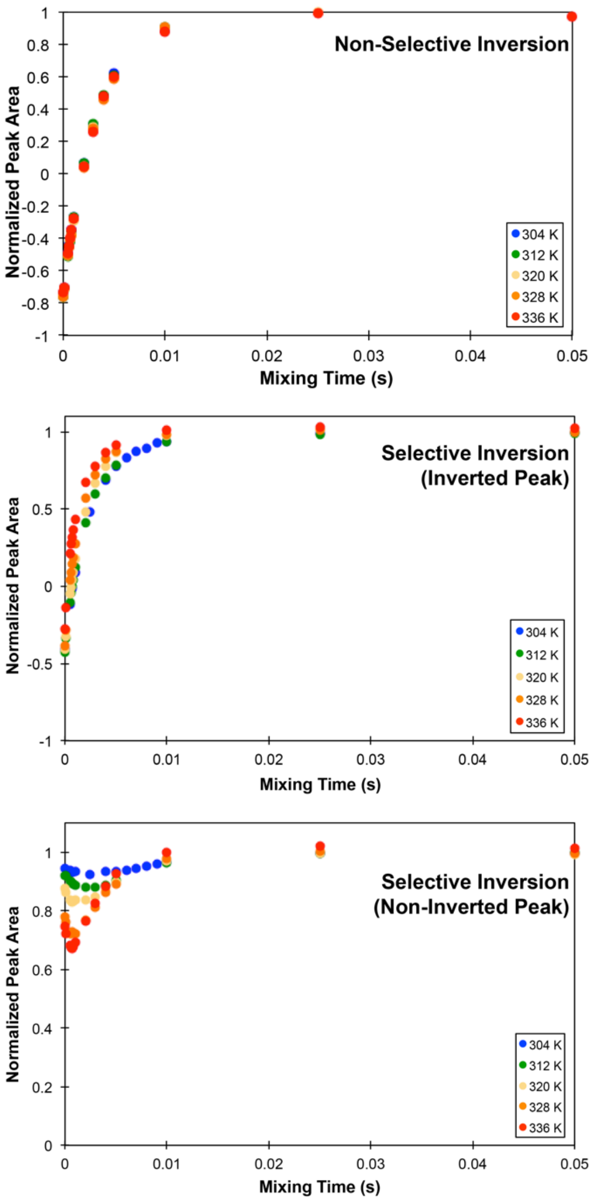

**Figure 5.7:** Plots of peak area dependence on mixing time with varying temperature. For the non-selective inversion experiment the inverted peak shows no temperature dependence on the magnetization build-up to equilibrium. In contrast, both the build-up and transient decrease in magnetization is temperature dependent in the SI experiment due to the exchange rates varying with temperature.

The process of data fitting was carried out in the CIFIT program developed by A.D. Bain at McMaster University.[13,14] This method allows the data to be fit to both relaxation

($T_1$) and rate constants (k) to describe the magnetization intensity as a function of mixing time as described in Chapter 3. The data was fit accordingly, using fixed values for spin-lattice relaxation constants as determined by the individual non-selective inversion recovery experiments for each sample. Some examples of the results of the CIFIT approach are shown in **Figure 5.8**. In general the fit of the modeled peak intensity matches well with experimental data, resulting in reasonable error bars for the predicted rate constants. Larger error is observed for the $Li_B$-$Li_C$ exchange pair, likely due to the overlap with the broad peak corresponding to a separate phase not involved in exchange. This overlap likely introduces additional error into the measured peak area obtained from the deconvolution of the spectrum that is translated to the resulting rate constant. Reasonable values are nevertheless obtained in all cases, with the $Li_A$-$Li_B$ pair being the most mobile Li exchange pair in all samples. Rate constants for this pair are 510-635 $s^{-1}$ for the three samples at the highest measured temperature; contrasted with 130-240 $s^{-1}$ for both $Li_A$-$Li_C$ and $Li_B$-$Li_C$ pairs. **Table 5.3** provides the values of the rate constants for each of the three samples across the five temperatures studied.

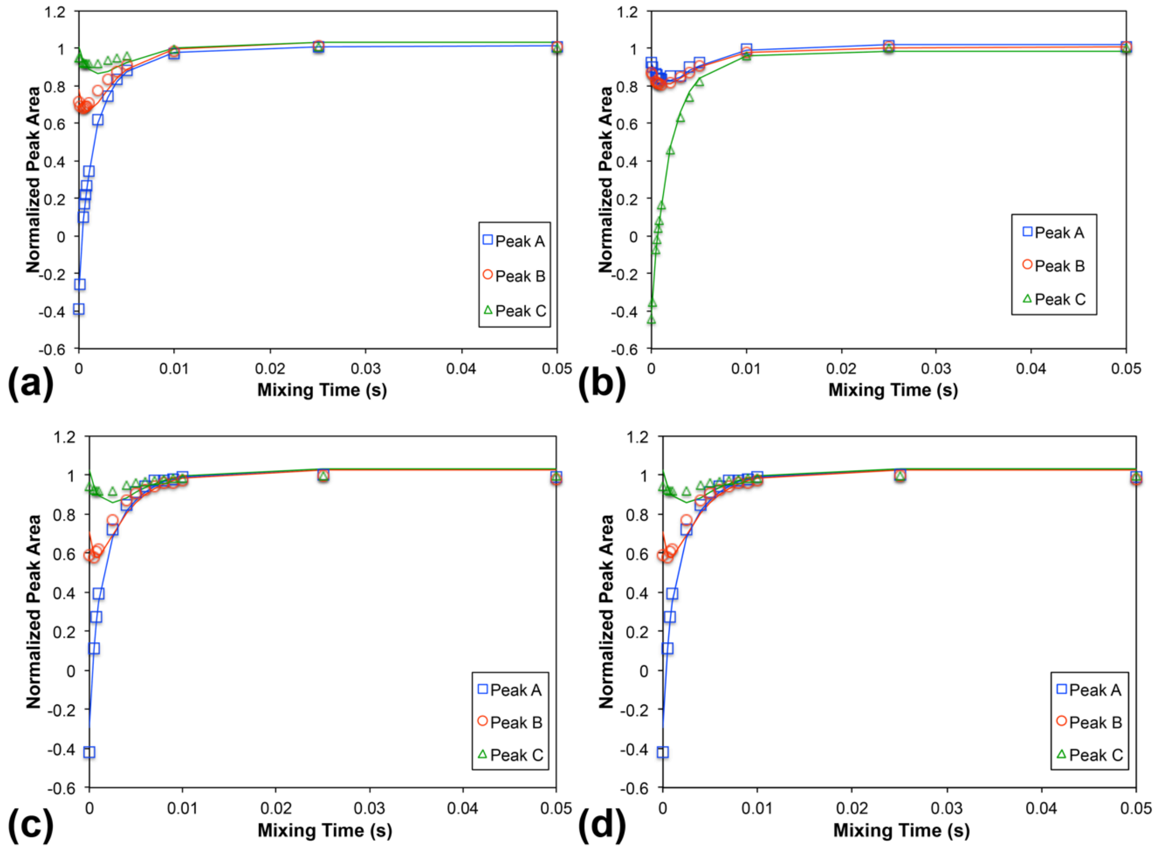

**Figure 5.8:** Selected examples of CIFIT fitting result (solid lines) for **(a)** x=0.6 with Peak A inverted at 320 K, **(b)** x=0.6 with Peak C inverted at 320 K, **(c)** x=0.55 with Peak A inverted at 336 K, and **(d)** x=0.5 with Peak A inverted at 336 K.

For the three samples studied with decreasing discharge voltages, the overall lithiation of the electrode should increase. This is coupled with a statistically significant increase of the rate constant as depicted by the chart in **Figure 5.9** for all of the exchange pairs with increasing discharge. Based on diffraction results from Benabed *et al.*, this composition region follows a solid-solution reaction, implying a gradually changing structure involved in the electrochemical process. This is congruent with the gradually increasing rate constants with the steady structural change leading to faster Li exchange.

**Table 5.3:** Calculated rate constants and error for each of the three exchange pairs in three compositions of the mobile phase

| | **Sample: x=0.5** | | |
|---|---|---|---|
| **T (K)** | **$k_{AB}$ ($s^{-1}$)** | **$k_{AC}$ ($s^{-1}$)** | **$k_{BC}$ ($s^{-1}$)** |
| 304 | 55 ± 10 | 20 ± 8 | 8 ± 5 |
| 312 | 125 ± 10 | 24 ± 5 | 40 ± 3 |
| 320 | 173 ± 20 | 37 ± 5 | 60 ± 5 |
| 328 | 328 ± 30 | 65 ± 10 | 110 ± 10 |
| 338 | 519 ± 60 | 133 ± 10 | 136 ± 10 |

| | **Sample: x=0.55** | | |
|---|---|---|---|
| **T (K)** | **$k_{AB}$ ($s^{-1}$)** | **$k_{AC}$ ($s^{-1}$)** | **$k_{BC}$ ($s^{-1}$)** |
| 304 | 75 ± 10 | 40 ± 10 | N/A* |
| 312 | 120 ± 10 | 30 ± 5 | 10 ± 5 |
| 320 | 210 ± 25 | 75 ± 20 | 50 ± 5 |
| 328 | 325 ± 40 | 100 ± 10 | 100 ± 10 |
| 338 | 510 ± 90 | 130 ± 10 | 135 ± 20 |

| | **Sample: x=0.6** | | |
|---|---|---|---|
| **T (K)** | **$k_{AB}$ ($s^{-1}$)** | **$k_{AC}$ ($s^{-1}$)** | **$k_{BC}$ ($s^{-1}$)** |
| 304 | 145 ± 20 | 50 ± 10 | 35 ± 5 |
| 312 | 230 ± 30 | 80 ± 10 | 60 ± 10 |
| 320 | 365 ± 50 | 130 ± 10 | 135 ± 10 |
| 328 | 530 ± 80 | 175 ± 10 | 140 ± 20 |
| 338 | 635 ± 110 | 240 ± 20 | 160 ± 20 |

*not obtained with a reasonable value or error, therefore not included

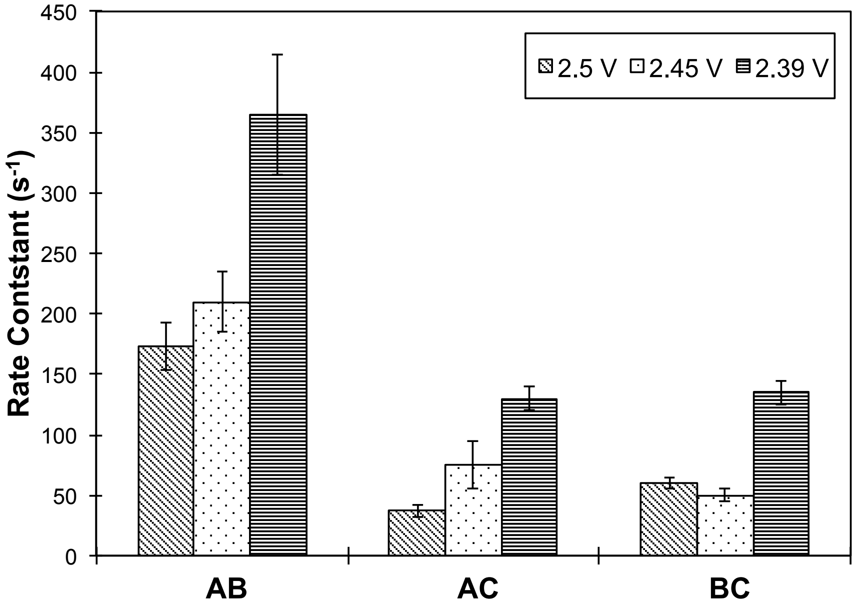

**Figure 5.9:** Trend in rate constants at 320 K for each of the three exchange pairs depicting the overall increase in rate constant with discharge. The decreasing discharge voltage (three columns, left to right) corresponds to an increasing lithium content in $Li_{1+x}FeV_2O_7$ with compositions x=0.5, 0.55 and 0.6.

The rate constants determined as a function of temperature additionally allow for the calculation of an energy barrier for each of the three Li exchange processes over the observable composition range of the mobile phase. Using the Eyring analysis method, the plot of ln(k/T) vs 1000/T yields the energy barrier via the slope of the line. In all cases a good linear fit to the data is obtained, with the highest quality fits coinciding with the dominant $Li_A$-$Li_B$ exchange pair. This likely is due to the combination of the peak overlap of the $Li_C$ site with the broad Li resonance corresponding to the immobile phase in the $^7$Li NMR, as well as the relatively low exchange rates observed for these processes that are inherently more difficult to observe by NMR as they approach the rate of the $T_1$ limit. The results from each of the Eyring plots are provided in **Figure 5.10**, demonstrating the linear fits to the experimental data. The linear fit performed accounted for the error associated with the rate constant values using an instrumental weighting procedure in the fitting procedure so as to rely more heavily on the most accurate data in determination of the energy barriers as per Equation 5.1:

$$w_i = \frac{1}{\sigma_i^2} \tag{5.1}$$

where $w_\mathrm{i}$ is the weighting of the data point and $\sigma_\mathrm{i}$ is the error associated with the rate constant obtained from CIFIT.

The values for activation energy are found to range from 0.19-0.66 eV across all of the possible exchange pairs for the three measured samples. In general, the activation energy decreases as a function of overall lithiation (**Figure 5.11**), suggesting that as Li ions are forced into the structure, they are able to exchange with each other more easily. This trend is less obvious for the $\mathrm{Li_A}$-$\mathrm{Li_C}$ and $\mathrm{Li_B}$-$\mathrm{Li_C}$ exchange pairs, likely due to the significantly greater error associated with the values for these exchange pairs. Nevertheless, the relatively higher rate constants and low error associated with the energy barriers for the $\mathrm{Li_A}$-$\mathrm{Li_B}$ exchange pair make it the most interesting from an electrochemical standpoint, as it likely contributes most significantly to the overall Li diffusion pathway.

**Table 5.4:** Activation energies for all three Li-Li exchange pairs in three compositions of the mobile phase formed on discharge of $LiFeV_2O_7$ electrodes.

| | **Activation Energy (eV)** | | |
|---|---|---|---|
| **Sample** | **AB** | **AC** | **BC** |
| x=0.5 | 0.54 ± 0.04 | 0.66 ± 0.06 | 0.43 ± 0.05 |
| x=0.55 | 0.50 ± 0.01 | 0.36 ± 0.07 | 0.53 ± 0.12 |
| x=0.6 | 0.42 ± 0.04 | 0.35 ± 0.02 | 0.19 ± 0.12 |

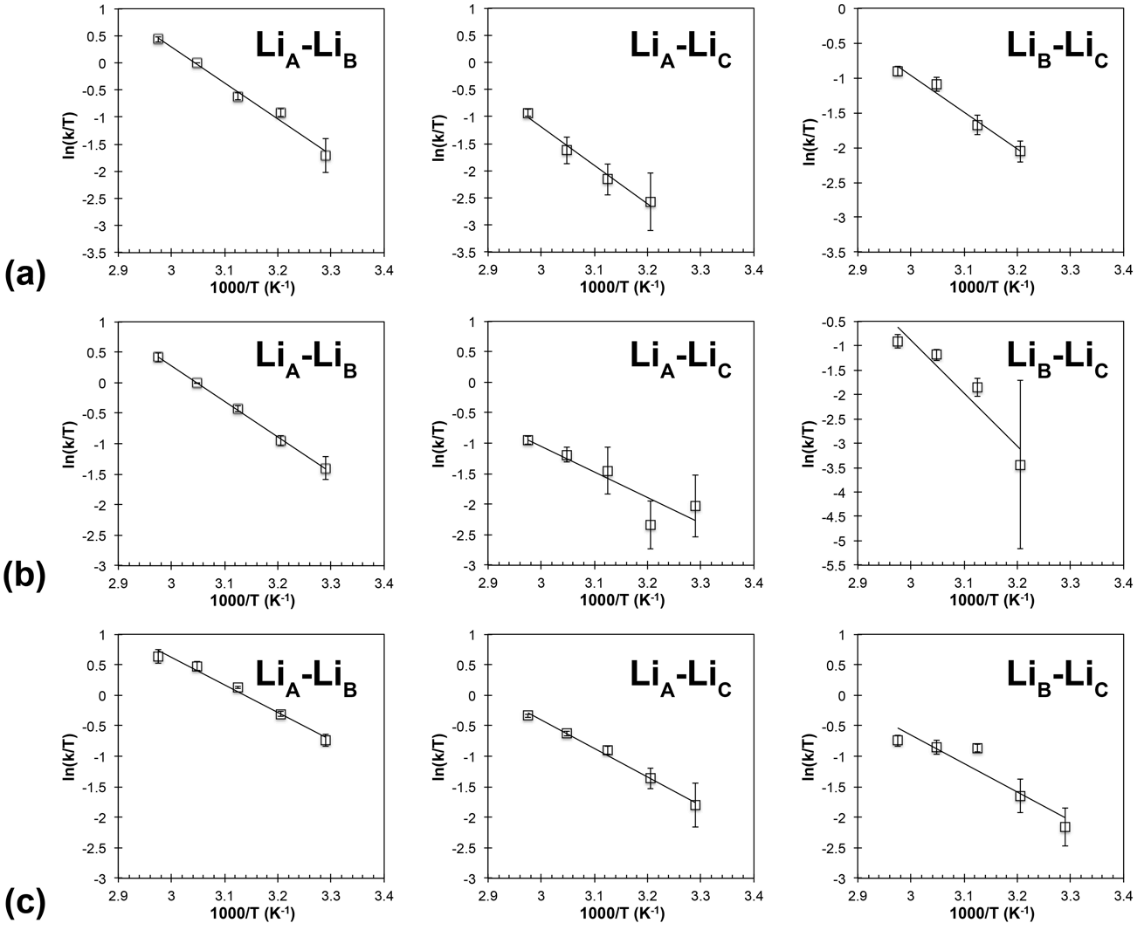

**Figure 5.10:** Eyring plots depicting the linear fits to experimental rate constants to obtain the activation energies for Li-Li exchange in $Li_{1+x}FeV_2O_7$ samples discharged to **(a)** 2.5 V (x=0.5), **(b)** 2.45 V (x=0.55), and **(c)** 2.39 V (x=0.6).

Without confirmed structural information about the mobile phase, it is difficult to rationalize the changing rate constants and energy barriers, or to contrast the differences between the three possible Li-Li exchange pairs. The collection of further diffraction data is underway by Dollé *et al.* in order to understand details of the apparent phase change near the $Li_{1.55}FeV_2O_7$ composition. The insight provided by the quantitative NMR kinetics experiments permits the speculation of possible models to explain the changing dynamics in the mobile phase as a function of discharge. The known solid-solution region is first confirmed by a lack of significant NMR changes in the mobile phase over the composition range around x~0.55. The increasing Li mobility suggests that while the

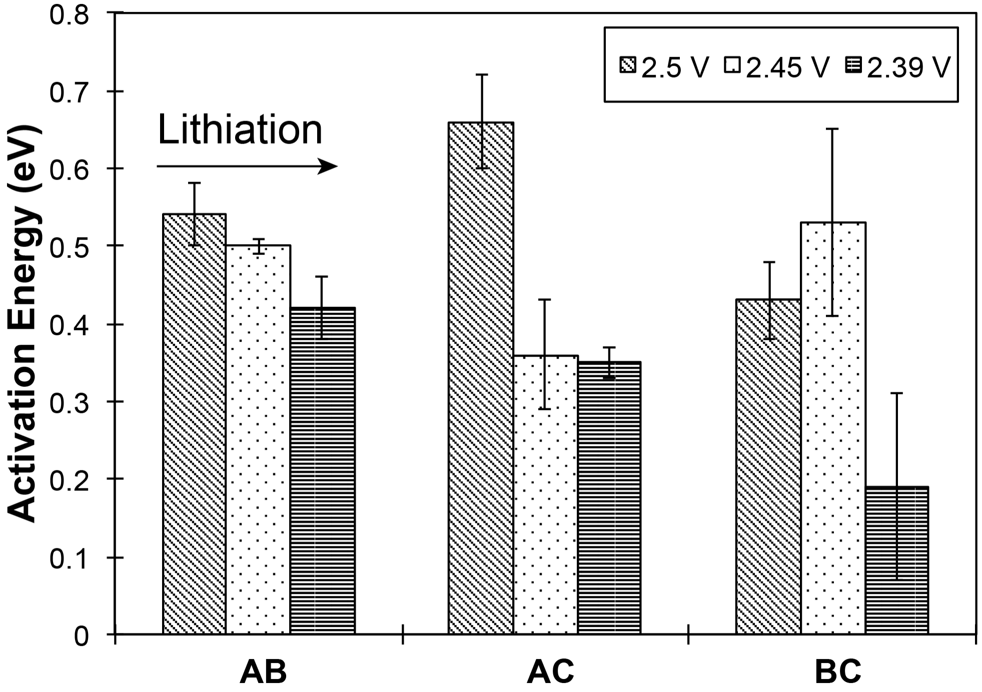

**Figure 5.11:** Trend for the activation energies determined for each of the three exchange pairs as a function of lithiation. The three $Li_{1+x}FeV_2O_7$ samples studied were discharged to 2.5 V (x=0.5), 2.45 V (x=0.55) and 2.5 V (x=0.6).

overall unit cell is not changing significantly, there is a small change in unit cell parameters to accommodate addition Li atoms into the structure as commonly observed in the charge/discharge process for cathode materials. This is corroborated by the very slight changes in chemical shifts exhibited by the mobile phase with lithiation, where even small changes in Li-Fe distances due to unit cell expansion are reflected in the chemical shifts in the $^{7}$Li NMR spectrum. Without an accurate unit cell the expected chemical shift trends cannot be hypothesized for mobile phase compositions, however the small changes are not likely to be due to a large structural rearrangement. Qualitative analysis of the XRD patterns shown in **Figure 5.3** agrees with this, as demonstrated by the shift of the reflections near the $2\theta$ region of 29° to lower angles. Furthermore, the insertion of Li atoms into the lattice is likely coupled with an expansion of the overall cell volume in an attempt for the structure to accommodate the additional $Li^{+}$ atoms. This expansion would likely overall widen the pathway by which the Li atoms travel to exchange with one another, decreasing the coulombic repulsion between $Li^{+}$ and $Fe^{3/2+}$ cations and making the process energetically more favourable. Should this be accurate, a decrease in the energy barrier for Li-Li hopping is expected, and agrees nicely with the experimental values obtained by $^{7}$Li SI results. While a reasonable hypothesis, this proposal remains unconfirmed without additional information and further analysis is ongoing.

## 5.4 Summary

This chapter presents the first example of the quantitative experimental study of Li-Li exchange rates and energy barriers as a function of *ex situ* electrochemical cycling by

NMR or otherwise. The novel iron vanadate cathode material, $LiFeV_2O_7$ was investigated by various $^7Li$ solid-state NMR methods in order to identify structural and dynamics properties both before and during charge/discharge. The initial spectroscopy of the as-prepared lithium iron vanadate reveals a consistent Li structural disorder that is highly dependent on synthesis conditions and is not visible by other diffraction methods used in this study thus far. This disorder can be attributed to small amounts of metal reduction (either Fe or V) and/or anti-site disorder where Li and Fe atoms swap positions to generate new magnetic environments for Li atoms that are readily observed by $^7Li$ ssNMR spectroscopy. This is an excellent example that demonstrates the importance of NMR techniques to study Li cathode materials, as structural disorder of the light Li atom is often not described by routine X-ray diffraction methods.

A detailed *ex situ* NMR study was additionally performed using cycled $Li_{1+x}FeV_2O_7$ electrodes, where a phase transformation was observed near the x=0.55 composition; a result that is in good agreement with the XRD data from collaborators in the Dollé lab at Université de Montréal. This phase transformation was discovered to generate the so-called mobile phase, which exhibits the first evidence of Li ion dynamics in this system. Furthermore, rate constants for each of the three Li-Li exchange pairs in the mobile phase were obtained by variable temperature selective inversion experiments, followed by an analysis to yield energy barriers as a function of Li composition. The observation of an increasing exchange rate and decreasing energy barrier with further state of discharge (and thus higher overall lithium content) suggests that the structure opens such that it becomes more amenable to Li diffusion with lithiation. This can be explained most simply by an overall unit cell expansion, causing the Li diffusion pathway to become less hindered by nearby cation repulsion and lowering the barrier to exchange.

Although this phase is still of interest and further study is required to generate a reasonable structural model for the observed mobile phase formed upon discharge, the results presented in this chapter provide rich information regarding the changing Li kinetics during the electrochemical process. $LiFeV_2O_7$ remains a new and exciting development in the field of vanadate frameworks for Li ion battery cathode materials, and will hopefully open the door for other unique materials based on this structure type with excellent electrochemical activity.

## 5.5 References

(1) Benabed, Y.; Castro, L.; Penin, N.; Darriet, J.; Dollé, M. *Chem. Mater.* **2017**, *29* (21), 9292.

(2) Grey, C. P.; Cheetham, A. K.; Dobson, C. M. *J. Magn. Reson., Ser. A* **1993**, *101* (3), 299.

(3) Patoux, S.; Richardson, T. J. *Electrochemistry Communications* **2007**, *9* (3), 485.

(4) Pralong, V.; Gopal, V.; Caignaert, V.; Duffort, V.; Raveau, B. *Chem. Mater.* **2011**, *24* (1), 12.

(5) Murphy, D. W.; Christian, P. A.; DiSalvo, F. J.; Carides, J. N. *J. Electrochem. Soc.* **1979**, *126* (3), 497.

(6) Sanstakeuchi, E.; Piliero, P. *Journal of Power Sources* **1987**, *21* (2), 133.

(7) Wadsley, A. D. *Acta Crystallographica* **1957**, *10* (4), 261.

(8) Islam, M. S.; Driscoll, D. J.; Fisher, C. A. J.; Slater, P. R. *Chem. Mater.* **2005**, *17* (20), 5085.

(9) Davis, L. J. M.; Goward, G. R. *J. Phys. Chem. C* **2013**, *117* (16), 7981.

(10) Davis, L. J. M.; He, X. J.; Bain, A. D.; Goward, G. R. *Solid State Nucl. Magn. Reson.* **2012**, *42* (C), 26.

(11) Smiley, D. L.; Davis, L. J. M.; Goward, G. R. *J. Phys. Chem. C* **2013**, *117* (46), 24181.

(12) Smiley, D. L.; Tessaro, M. Z.; He, X.; Goward, G. R. *J. Phys. Chem. C* **2015**, *119* (29), 16468.

(13) Bain, A. D. *The CIFIT Program*. July 31, 2000, pp 1–16.

(14) Bain, A. D.; Duns, G. J.; Rathgeb, F.; Vanderkloet, J. *J. Phys. Chem.* **1995**, *99* (48), 17338.

# Chapter 6: Structure and Dynamic Properties of $Na_2FePO_4F$ As Determined by $^{23}Na$ Solid-State NMR

## 6.1 Introduction

This chapter presents the results of a detailed investigation of layered $Na_2MPO_4F$ materials primarily by solid-state NMR methods in combination with electrochemical measurements and powder x-ray diffraction characterization. Using *ex situ* methods, the desodiation mechanism is elucidated in potential cathode material, $Na_2FePO_4F$. A comparison between the NMR properties of the electrochemically active $Na_2FePO_4F$ (paramagnetic) and a structurally analogous reference structure $Na_2MgPO_4F$ (diamagnetic) demonstrates the distinct contributions from hyperfine and quadrupole NMR interactions respectively. The remaining bulk of this chapter will focus on the electrochemically interesting variant, $Na_2FePO_4F$, specifically probing Na ion dynamics using 2D EXSY as well as a detailed *ex situ* NMR and XRD study of the material as Na ions are removed from the structure electrochemically. The majority of the results and analysis discussed in this chapter were reported in a *Chemistry of Materials* publication in 2016 by D.L. Smiley and G.R. Goward.[1]

## 6.2 Methods

### 6.2.1 Preparation of $Na_2MPO_4F$ Samples (M=Fe, Mg)

A two step solid-state synthetic route initially proposed by Kosova *et al.*[2] was used to prepare pristine carbon-coated $Na_2FePO_4F$ powders. In accordance with the reported method, $Fe(C_2O_4)\cdot 2H_2O$, $Na_2CO_3$, and $NH_4H_2PO_4$ were initially mixed and ball milled for 1 h in acetone before annealing at 575 °C for 2 h with a pause at 350 °C for 1

h. The resulting $NaFePO_4$ powder was ball milled with a stoichiometric quantity of NaF and 3 wt% carbon black, followed by heating to 600 °C for 4 h under flowing Ar gas. The resulting $Na_2FePO_4F/C$ samples were characterized by PXRD. Preparation of $Na_2MgPO_4F$ powder was carried out via the standard solid-state method reported in literature,[3] whereby $Na_2PO_3F$ and $MgCO_3$ were mixed stoichiometrically, ball milled for 12 h and heated initially to 350 °C for 6 h. The powder was then further heated to 625 °C for 6 h following an intermittent grinding.

### 6.2.2 Electrochemical Measurements

Cathodes were prepared by grinding the as-synthesized $Na_2FePO_4F/C$ in a 75:15:10 weight % ratio with carbon black (CB) and polyvinylidene fluoride (PVDF) in N-methyl-2-pyrrolidone (NMP) solvent to create a slurry. This slurry was then cast onto Al foil and dried under vacuum for 12 hours at 120 °C. The dried cast was punched into discs 1.27 cm in diameter that were incorporated into coin cells. Sodium ion cells were prepared with 0.6M $NaPF_6$ in 30:70 EC/DMC (by volume) solution mixed in-house and a metallic sodium counter electrode. These cells were cycled on a multichannel potentiostat at a rate of C/20 using a standard galvanostatic cycling procedure. Cells extracted for *ex situ* NMR measurements were washed with acetonitrile in an argon filled glove box before preparation for NMR.

### 6.2.3 Solid-State NMR and Powder X-ray Diffraction Measurements

Sodium-23 ssNMR spectra were acquired at a Larmor frequency of 79.39 MHz (1.5 μs solid $\pi/2$ pulse) on a Bruker wide bore 300 MHz spectrometer. A Bruker 1.3mm double resonance probe was employed for fast MAS rates of 50-65 kHz. All spectra were referenced to 1M NaCl at 0 ppm. For experiments with 25 kHz MAS spinning rates, a custom-built double resonance probe housing 1.8 mm diameter rotors was employed. Deconvolutions of the $^{23}$Na spectra were carried out in Bruker's Topspin (version 3.1) Solids Lineshape Analysis (SOLA) tool. Each peak and corresponding spinning sidebands were fit individually using a Gaussian/Lorentzian model. Details of the parameters from the deconvolution are provided in the supporting information. The quadrupolar parameters for $Na_2MgPO_4F$ were fit using the same SOLA software fitting only the central quadrupole lineshape.

Powder X-ray diffraction (PXRD) data for the as-synthesized powders were collected on a PANalytical diffractometer using Cu Kα radiation from $2\theta=10°$ to $60°$. *Ex situ* 2D diffraction data were collected at the MAX Diffraction Facility at McMaster University, with a Bruker Smart6000 CCD area detector and a Bruker 3-circle D8 goniometer using a Rigaku RU200 Cu Kα rotating anode to collect a range of 5° to 98° ($2\theta$). Air sensitive samples were packed into capillaries and data collected in the transmission geometry.

## 6.3 Results and Discussion

### 6.3.1 Motivation

The layered fluorophosphate class of intercalation materials of the form $A_2FePO_4F$ (A=Li, Na) has demonstrated potential as a cathode material for both lithium and sodium ion batteries.[3,4] First reported in 2009, Nazar and coworkers demonstrated the viability of $Na_2FePO_4F$ for future sodium ion batteries.[3,4] Initial electrochemical tests were completed by cycling the sodium fluorophosphate cathode versus lithium metal, forming a Na-Li hybrid battery reportedly exhibiting an average charge potential of 3.3 V and a reversible capacity of 115 $mAhg^{-1}$.[3] The structure was found by X-ray diffraction (XRD) to crystallize in a layered-like framework made up of $FeO_4F_2$ octahedra and $PO_4$ polyhedra, between which Na atoms reside in two unique crystallographic environments denoted Na1 and Na2, as depicted in **Figure 6.1**. Chemical oxidation of the parent phase to yield $NaFePO_4F$ caused very little change to the structural framework, with only the Na1 site remaining occupied after chemical desodiation.[3,4] This result was used as evidence of increased Na2 site mobility relative to Na1, likely making this site responsible for bulk Na diffusion during electrochemical cycling.

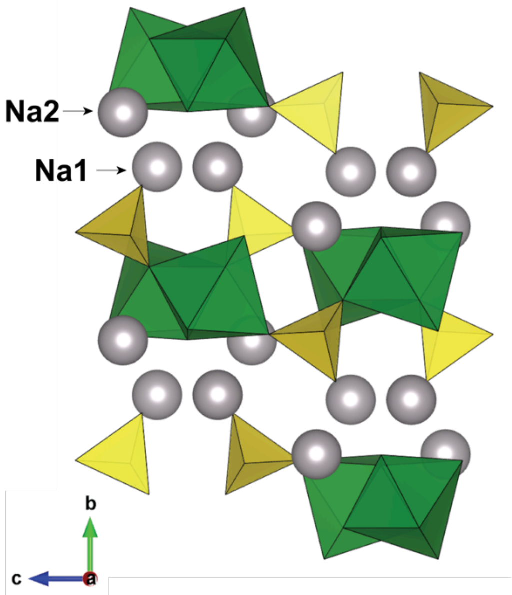

**Figure 6.1:** Unit cell of the reported orthorhombic $Na_2FePO_4F$ structure, depicting the two unique Na positions forming layers between $FeO_4F_2$(green) and $PO_4$ (yellow) polyhedra.

A variety of modified synthetic methods for preparation of $Na_2FePO_4F$ with improved electrochemical performance have been proposed since the original discovery, including new synthetic pathways for nanosizing the material, as well as an assortment of methods that use carbon sources to act both as a particle growth inhibitor and a conductive coating for improved electronic conductivity.[2,5-12] Furthermore, this promising electrochemical behaviour has prompted the modeling of diffusion pathways in an effort to identify the mechanism of Na ion migration in this material.[13] In 2013, Tripathi *et al.*[13] demonstrated the possibility for $Na^+$ diffusion along the a- and c-axes using atomistic modeling to confirm the original prediction by Ellis *et al.*[3] stating that diffusion should occur primarily within the Na ion plane, and not across layers. The simulation results suggest a network of Na ions that include $Na^+$ hops between connecting Na1-Na1 and Na1-Na2 sites to form an extensive diffusion pathway throughout the material with sufficiently low activation energy barriers for alkali ion hopping.[13] The work presented in this chapter builds upon the existing experimental and theoretical literature to better understand the behaviour of the Na ions before, during, and after electrochemical cycling. Primarily using $^{23}Na$ solid-state NMR, the distribution of Na ions at intermediate states of charge is elucidated, as well as an estimation of the ion exchange timescale as determined by exchange spectroscopy.

### 6.3.2 NMR Comparison between Diamagnetic and Paramagnetic Sodium Cathode Materials

The relative adolescence of sodium ion batteries compared to their lithium counterparts becomes apparent upon evaluation of the number of total publications that investigate cathode materials for the two battery types. While many of the characterization methods used to study lithium are indifferent to the change in alkali ion, solid-state NMR specifically probes a single nucleus and as already discussed in Chapters 2 and 3, the nuclear spin properties of Li and Na are not identical. While there are many examples of quantifying quadrupole coupling parameters in a wide variety of Na-containing molecules, as well a few examples of Na NMR used to investigate paramagnetic sodium cathode materials,[14-17] there have been no reported attempts to decouple these two interactions which tend to dominate the NMR spectrum.

Based on the known crystal structure for this material, the distortion of the octahedral environment around both Na1 and Na2 sites in $Na_2FePO_4F$ is expected to produce an observable non-Gaussian NMR line shape due to a detectable quadrupole coupling interaction. In order to observe this effect in the absence of paramagnetic line broadening, a diamagnetic structural analogue ($Na_2MgPO_4F$) was synthesized and investigated by $^{23}$Na NMR. A direct comparison of the 1D MAS NMR spectra of $Na_2MgPO_4F$ and $Na_2FePO_4F$ illustrates the acute effect of the addition of a paramagnetic transition metal to the otherwise equivalent structure. The massive broadening and overall shift of the isotropic resonances is coupled with a significant increase of the spinning sideband intensities for the resonance of the paramagnetic material relative to the diamagnetic equivalent (**Figure 6.2a**). Moreover, the excellent chemical shift resolution of the two crystallographic sites is almost completely lost in the diamagnetic example, necessitating the use of multiple-quantum magic angle spinning (MQMAS) and/or deconvolution methods as shown in **Figure 6.2** to identify the two unique Na line shapes in the $^{23}$Na spectrum of $Na_2MgPO_4F$. A fit of the line shapes reveals two distinct Na environments with comparable quadrupole coupling constants of 1.5 and 1.6 kHz for sites A and B respectively, a result that might be expected due to the similar coordination motifs of the Na1 and Na2 crystallographic environments. This non-zero coupling effect can be justified upon consideration of the distortion of the Na octahedral due in part to the inclusion of 2 F atoms in the first coordination sphere rather than a higher symmetry $NaO_6$ configuration. When overlaying the $^{23}$Na NMR spectra of the Mg and Fe analogs it becomes clear that the chemical shifts, line widths, and spinning sideband manifolds are largely independent of the quadrupolar interaction in this material, and thus the interpretation of the spectra requires primarily the consideration of the effect of the paramagnetic Fe ion on the Na environments. In reality, some residual effects of the quadrupolar interaction are evident, such as the nutation rates of the Na spins even in the paramagnetic variant of the material. This phenomenon will be discussed in greater detail in Chapter 8 of this thesis.

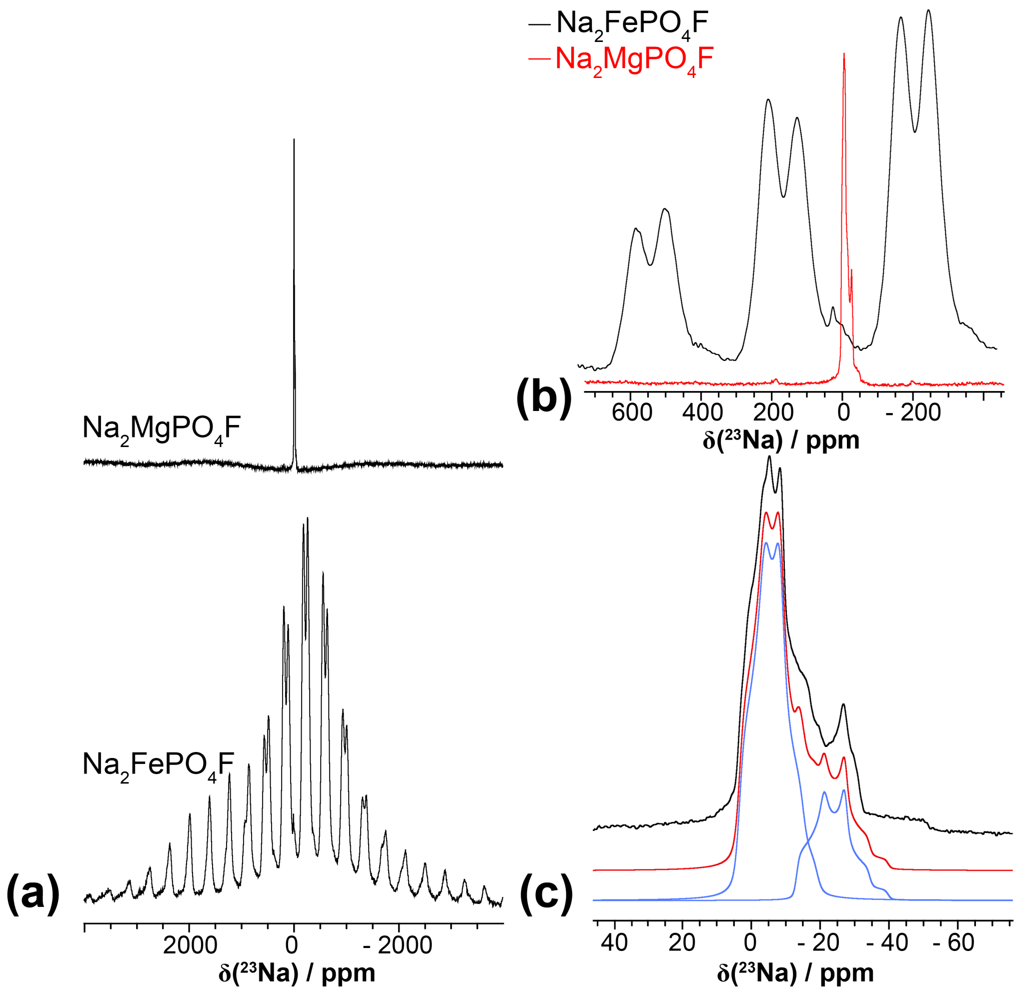

**Figure 6.2:** **(a)** $^{23}$Na MAS NMR spectra of $Na_2MgPO_4F$ (diamagnetic) and $Na_2FePO_4F$ (paramagnetic) demonstrating the effect of unpaired electrons on the experimental spectrum. **(b)** Comparison of the isotropic sodium resonances for $Na_2MgPO_4F$ and $Na_2FePO_4F$ spectra in a. **(c)** Fit of the second order quadrupolar lineshape for the two crystallographic sites in $Na_2MgPO_4F$.

### 6.3.3 $^{23}$Na NMR Characterization of Pristine $Na_2FePO_4F$

Sodium-23 ssNMR with fast MAS (>60 kHz) is implemented here in an effort to characterize the structure and ion mobility in the layered fluorophosphate cathode material, $Na_2FePO_4F$. The 1D $^{23}$Na NMR spectrum is depicted in **Figure 6.3**, where two distinct chemical shifts dominate the spectrum at +440 ppm and -175 ppm in a 0.85:1

integration ratio of the isotropic shifts, labeled sites A and B respectively. Deviation of this ratio from 1:1 is rationalized by a marked difference in the anisotropy of the two sites as will be discussed below, making the ability to infer the relative populations from the isotropic resonances alone difficult. Additional complications with the quantitative integration are likely due to small differences in the nutation frequency of each site, as will be examined in Chapter 8. Evidence of two Na-containing impurities at -127 ppm and -230 ppm are present in small quantities of 8 and 2% of the total $^{23}$Na signal respectively, the latter being attributed to residual $NaFePO_4$ from the solid-state synthesis. A small amount (~2%) of diamagnetic NaF and/or $Na_2CO_3$ remaining from the synthetic process are present around 0 ppm. As will be shown forthwith, none of the aforementioned impurities demonstrate any observable electrochemical activity, and thus their presence does not affect the results presented herein.

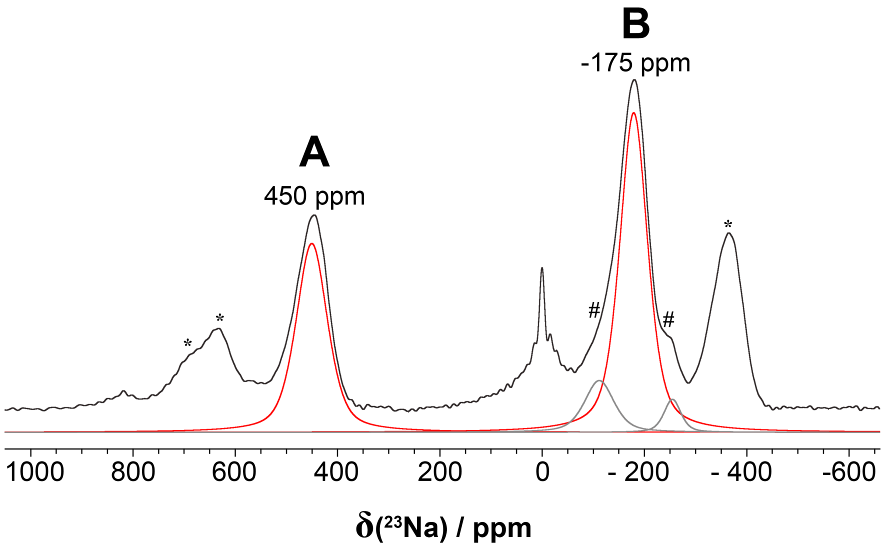

**Figure 6.3:** 1D $^{23}$Na MAS spectrum of as-prepared $Na_2FePO_4F$ with the experimental spectrum shown in black, and a fit of each isotropic site in red or grey. Sites A and B correspond to the two crystallographic Na sites in pristine $Na_2FePO_4F$ with the small peaks around -127 ppm and -205 ppm corresponding to unknown defect or impurity sites.

Isotropic peaks A and B in the spectrum are assigned to the two crystallographically unique Na sites in the orthorhombic $Na_2FePO_4F$ structure. The robust assignment of paramagnetic shifts in related Li fluorophosphate cathode materials is notoriously difficult, owing to the lack of exact 90- or 180-degree Li-O-Fe interactions that give rise to predictable $^{7}$Li chemical shifts in the layered transition metal oxide structures. While the mechanism of unpaired electron spin density transfer from the transition metal to Na ion is expected to be the same as in analogous Li structures, prediction of the strength of that paramagnetic contribution due to incomplete orbital overlap can prove difficult.[18,19] As such, absolute certainty of paramagnetic shift assignments is elusive in materials of this type without the help of complex DFT calculations.[19-21] The results of these calculations for $Na_2FePO_4F$ and the ultimate assignment of the NMR shifts are examined in Chapter 7.

### 6.3.3 *Ex Situ* $^{23}$Na NMR and PXRD of Cycled $Na_2FePO_4F$/C

Ultimately, the success of a cathode is contingent upon the ability of the structure to withstand the removal of Na ions during electrochemical cycling. Efforts to understand changes to the local $Na_2FePO_4F$ structure during charge and discharge are undertaken here utilizing *ex situ* ssNMR techniques. In particular, polyanionic-based cathodes are attractive cathode candidates for Na ion batteries as their lack of significant structural change during cycling ultimately yields high capacity retention over many cycles.[6-8,11,12] There is therefore motivation to experimentally observe the rearrangement of Na ions within this particular polyanionic framework structure during electrochemical charge and discharge. Fortunately, the sensitivity of the sodium shift in $Na_2FePO_4F$ to the local environment allows for small structural and/or electronic changes to be readily captured by $^{23}$Na solid-state NMR. Sodium ion batteries containing carbon-coated $Na_2FePO_4F$ cathodes were assembled and cycled to various states of charge/discharge, demonstrating voltage profiles with two distinct regions centered at 2.9 V and 3.1 V versus Na metal upon charging, in excellent agreement with literature electrochemical tests.[3,4] Cycled coin cells were carefully deconstructed and the recovered cathodes were handled exclusively in a dry argon atmosphere with no exposure to moisture or air during testing. The 1D $^{23}$Na NMR spectrum of each cycled cathode as well as the electrochemical curve for a typical $Na_2FePO_4F$ cell is shown in **Figure 6.4**.

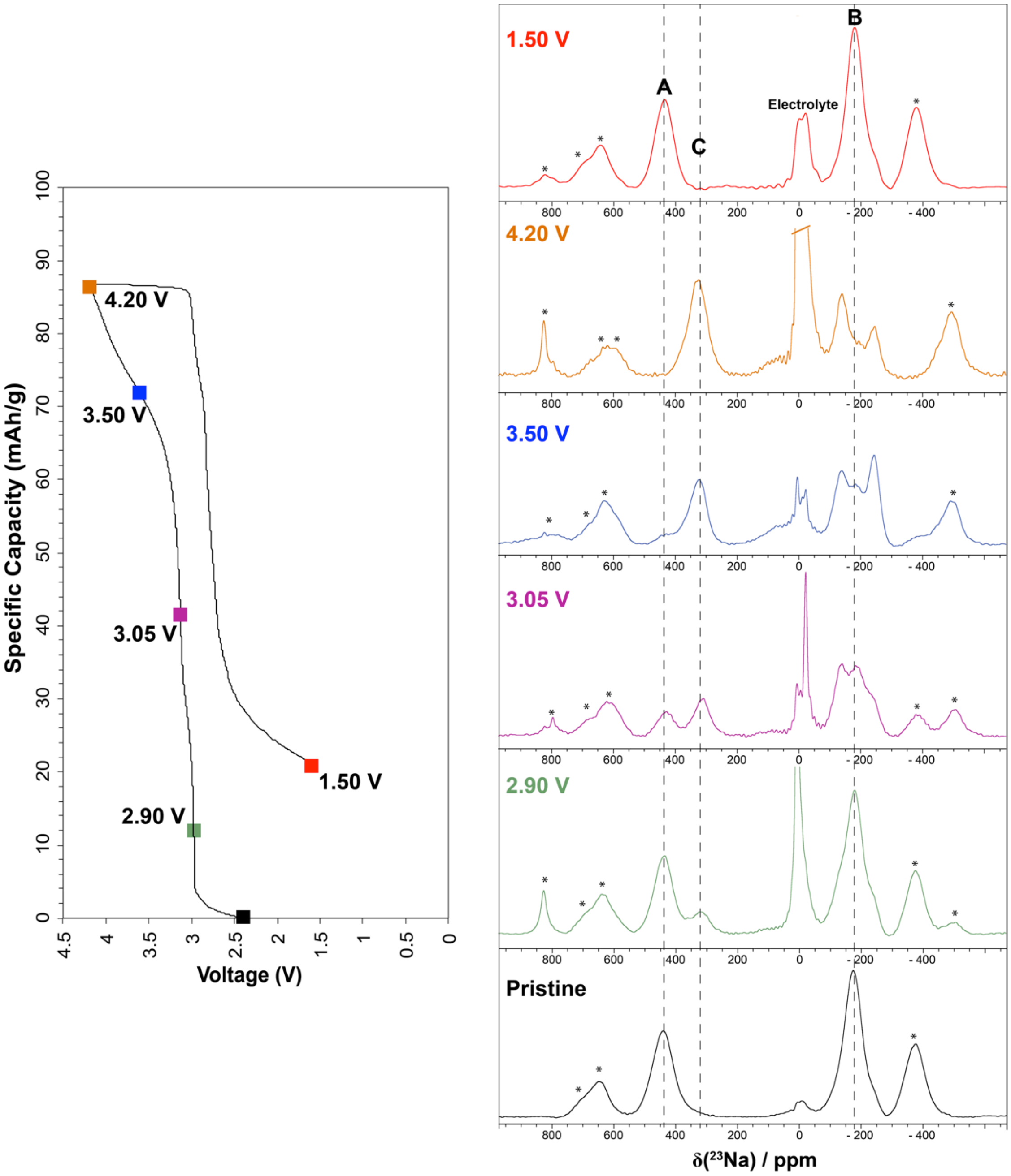

**Figure 6.4:** Galvanostatic cycling curve of a typical $Na_2FePO_4F$ cathode versus Na metal. The voltage points at which cathodes were extracted for study by NMR are labeled with a coloured box that corresponds to the $^{23}$Na MAS spectra on the right hand side. The spectra depict the changing intensity of the original peaks with the concurrent growth of a 'new' site believed to belong to the fully oxidized phase of the material, $NaFePO_4F$.

Upon partially charging the cathode a new Na site centered at +350 ppm (labeled here as site C) is evident in the $^{23}$Na NMR spectrum coupled with the partial loss in intensity of the original A and B sites that correspond to Na ions in the original $Na_2FePO_4F$ phase. This dramatically different chemical shift is not thought to arise from Na ions in an entirely new crystallographic environment, but rather is indicative of Na ions within an environment now surrounded by $Fe^{3+}$ ions as a result of the electrochemical oxidation process. Further cycling to the fully charged state yields only the new site C and a small amount of electrochemically inactive impurities at -127 and -230 remaining from the solid-state synthesis, as discussed above. Upon subsequently discharging the cell, site C is completely diminished accompanied by the reappearance of sites A and B with a full recovery of the initial relative intensities. Over the course of a complete charge-discharge cycle, the ratio of site A to site B remains relatively constant with no more than a 15% variance attributable to the poor signal-to-noise of spectra at intermediate states of charge. This chemical shift behaviour can be explained simply by consideration of possible Na environments in the pristine $Na_2Fe^{2+}FePO_4F$, partially oxidized $Na_{2-x}Fe^{2+/3+}PO_4F$, and fully oxidized $NaFe^{3+}FePO_4F$ phases. Site assignment is relatively straightforward in the samples obtained at the beginning and end of the redox process; with sites A and B corresponding to ions in positions Na1 and Na2, influenced exclusively by $Fe^{2+}$ TM ions, and site C consistent with $Na^+$ occupying the Na1 position (the sole remaining Na site as per literature[3]) in $NaFePO_4F$, where the chemical shift is dominated by paramagnetic interactions with only the $Fe^{3+}$ ion. The most informative results arise from partially charged/discharged samples corresponding to mixed $Fe^{2+}/Fe^{3+}$ species, where the apparent coexistence of both the original $Na_2FePO_4F$ phase and the fully oxidized $NaFePO_4F$ phase is indicative of a so-called two phase desodiation mechanism occurring at all states of charge. There is no evidence of Na ions in a mixed TM environment resulting from a combination of partial $Fe^{2+}$ and partial $Fe^{3+}$ contributions that change with the state of charge, as would be expected for a solid-solution mechanism. A schematic visual representation of the proposed mechanism is depicted in **Figure 6.5** where the Na occupancies in the crystal structure at varying states of charge as determined by $^{23}$Na NMR are correlated to the electrochemical cycling curve.

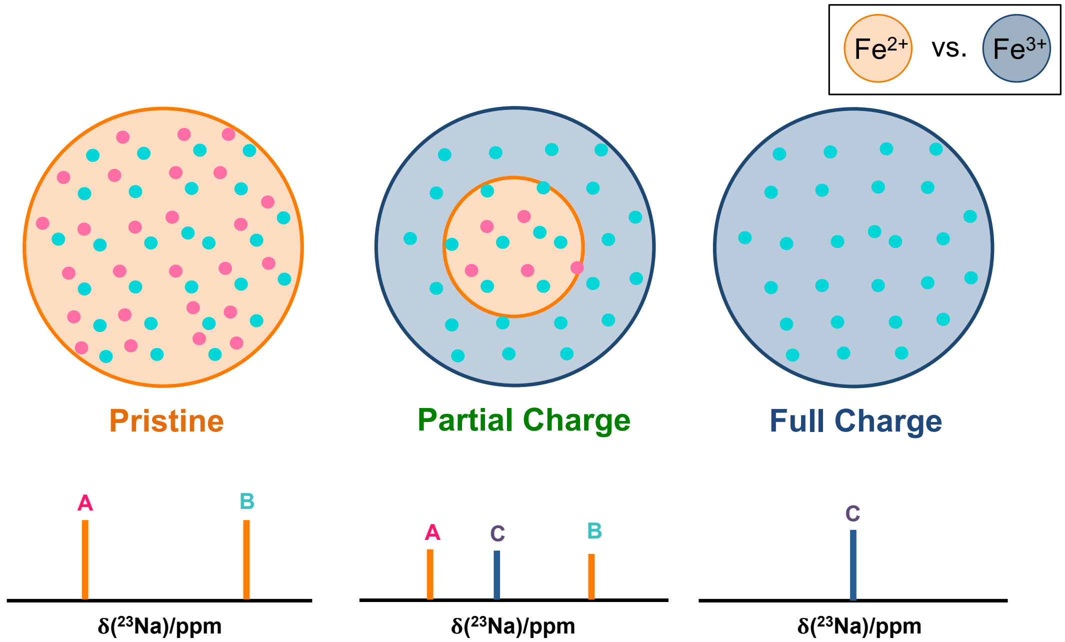

**Figure 6.5:** Proposed desodiation mechanism in $Na_2FePO_4F$ based on the collected *ex situ* NMR data. The schematic represents distinct $Na_2FePO_4F$ particles that make up the electrode, where at partial states of charge there is a distinct phase separation between the pristine and fully charged states rather than a uniform intermediate phase.

This proposal of a two-phase extraction process of the Na ions from $Na_2FePO_4F$ is in contrast to the original assumption that this material desodiates via a solid-solution mechanism.[3] The previous interpretation was based in part on X-ray diffraction results reported by Nazar and coworkers[3] for $Na_{1.5}FePO_4F$ and $NaFePO_4F$ phases generated by chemical oxidation, which demonstrated the presence of a single phase in each case, with the latter exhibiting the full removal of Na ions from the Na2 site and otherwise full retention of the parent structure. Moreover, the apparent sloping voltage profile in the electrochemical curves is often suggestive of solid-solution formation providing further evidence to support the initial hypothesis. The possibility for this solid-solution behaviour was thus carefully considered in light of the NMR results obtained; however, there is little justification for a true solid-solution based on the NMR data shown here. In the event of solid-solution formation, both $Fe^{2+}$ and $Fe^{3+}$ would surround the Na ions at all intermediate states of charge, resulting in a $^{23}Na$ chemical shift that varies with relative $Fe^{2+}/Fe^{3+}$ content. For instance, the chemical shift of Na1 in the pristine material would be expected to gradually migrate to the final $Fe^{3+}$-derived chemical shift, experiencing all intermediate possibilities along the way. This process would be easily traceable via $^{23}Na$ NMR, where the state of charge could be estimated simply by measuring the chemical shift of the Na1 ion in a partially oxidized environment. Rather than such a chemical shift evolution, a single new site is observed at 350 ppm, that changes in intensity but remains at a constant chemical shift irrespective of the state of charge. Therefore, it is concluded that $Fe^{2+}$ and $Fe^{3+}$ domains are wholly isolated from each other, resulting in $^{23}Na$ chemical shifts dominated either by interactions with $Fe^{2+}$ OR $Fe^{3+}$, but not both simultaneously. This finding is in good agreement with Mössbauer results for partially charged/discharged samples, suggesting $Fe^{2+}/Fe^{3+}$ ions are isolated from one another, and do not form a mixed valence $Fe^{2.5+}$-type state.[3,22]

In addition to ssNMR measurements, *ex situ* PXRD at various states of charge was performed for electrochemically cycled $Na_2FePO_4F$ cathodes. The diffraction results for an uncycled cathode as well as three samples cycled to 3.16, 3.4, and 3.5 V are depicted in **Figure 6.6**. A full interpretation including a refinement of the PXRD data was not possible owing to the difficult nature of the samples, however the analysis of some key peaks in the diffraction pattern provide some insight into the composition of the partially charged samples. As was observed via $^{23}$Na NMR, samples at partial states of charge (3.16 V, 3.4 V, and 3.56 V) along the initial charging curve appear to be comprised of a mixture of distinct phases, nominally $Na_2FePO_4F$, $NaFePO_4F$, and an $NaFePO_4$ impurity present in the uncycled cathodes. Closer analysis of two regions (**Figure 6.6b** and **6.6c**) reveal the changing ratio of $Na_2FePO_4F$ to fully oxidized $NaFePO_4F$ as the material is desodiated electrochemically. At intermediate states of charge, two unique sets of reflections are observed, one for $Na_2FePO_4F$ and the other for the fully desodiated $NaFePO_4F$ phase, rather than a gradual change in 2θ value as the material is cycled. This coexistence of two unique phases during charging is in excellent agreement with the results observed by ssNMR, further supporting the two-phase desodiation mechanism proposed here for $Na_2FePO_4F$.

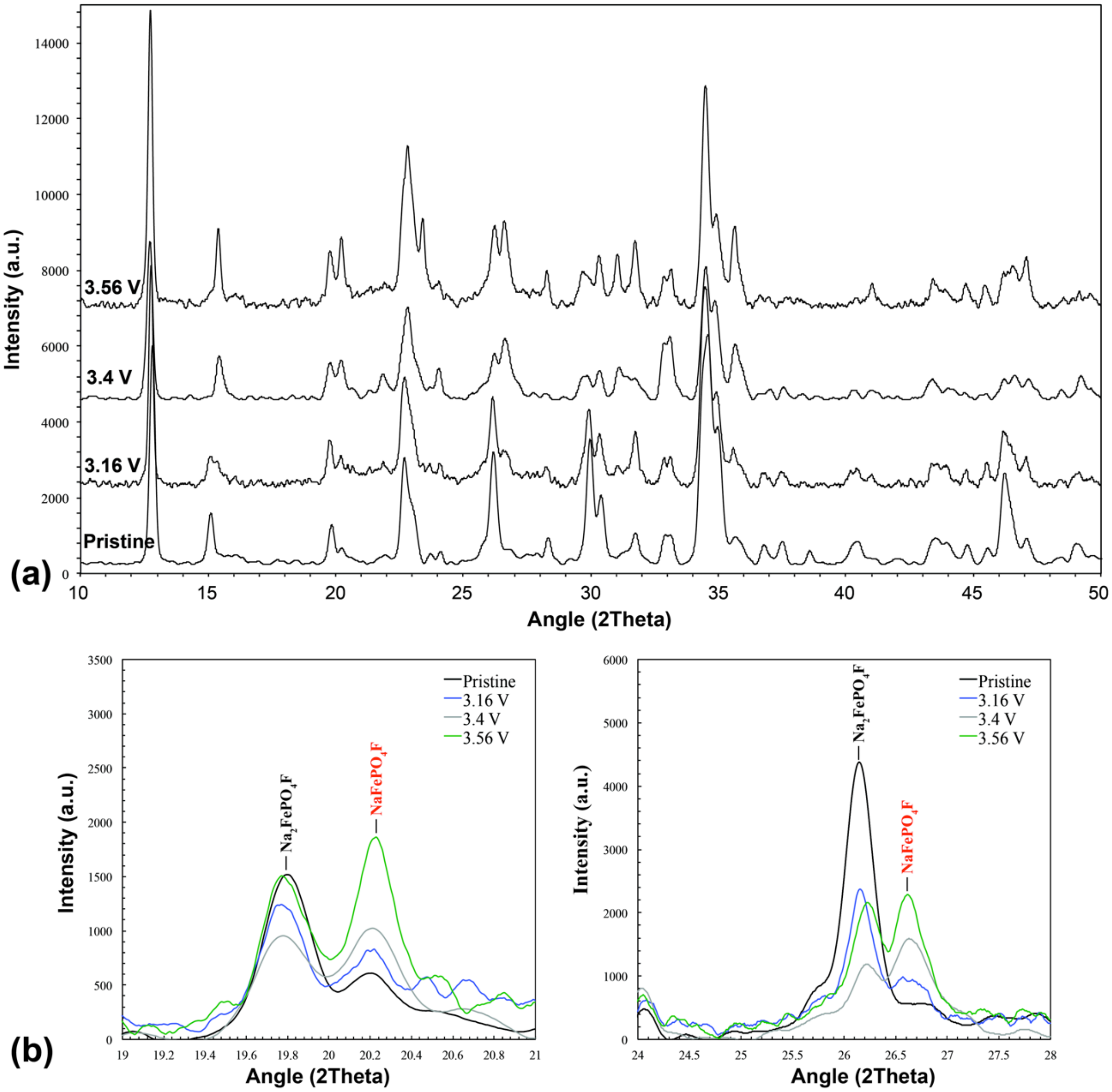

**Figure 6.6: (a)** *Ex situ* powder X-ray diffraction of $Na_{1+x}FePO_4F$ cathode materials cycled to various compositions; pristine (uncycled), 3.16 V, 3.4 V, and 3.56 V. The latter three compositions are partially desodiated, and contain a mixture of $Fe^{2+}$ and $Fe^{3+}$ ions. **(b)** A closer look at two distinct angle ranges where the changing composition with state of charge is especially evident.

Further NMR measurements of cathodes cycled beyond the initial charge-discharge cycle reveal that this two-phase desodiation mechanism does indeed persist over multiple cycles (see **Figure 6.7**), appearing to be highly reversible. The robust nature of the flurophosphate framework is evident, with the local Na environment remaining unchanged even after more than 40 full charge/discharge cycles.

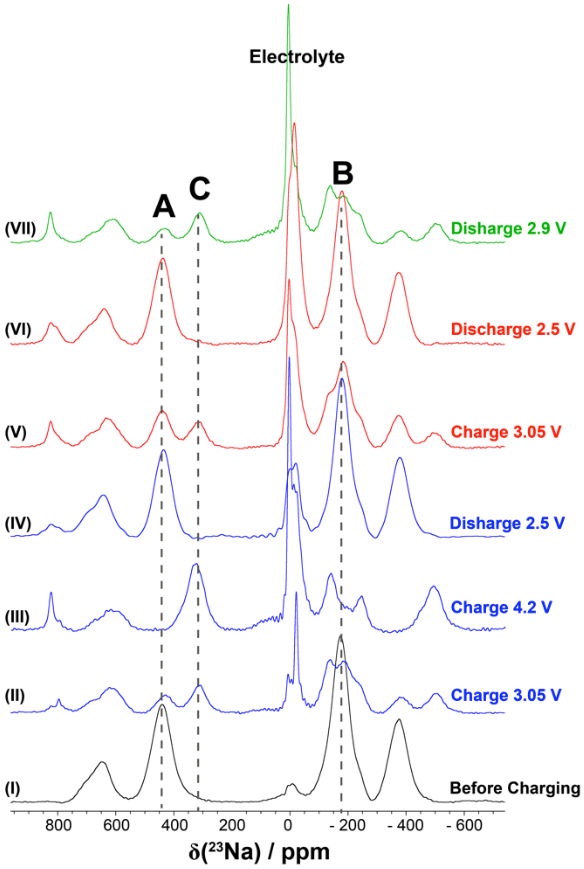

**Figure 6.7:** 1D MAS *ex situ* $^{23}$Na NMR spectra of $Na_2FePO_4F$ (I) prior to cycling, (II-IV) on the 1st cycle, (V,VI) on the 3rd cycle, and (VII) on the 41st cycle.

### 6.3.5 Na Ion Dynamics in Pristine and Electrochemically Cycled $Na_2FePO_4F/C$ by $^{23}$Na NMR

Although the fluorophosphate family of materials, and indeed polyanionic compounds in general, often form robust structural motifs, there are in some cases ion mobility limitations that ultimately prevent their commercial use.[23,24] Ion exchange rates are typically a good predictor of cathode rate capability, as they provide insight into local ion dynamics in the structure independent of particle size and thus grain boundary effects. Quantification of these exchange rates in similar Li polyanionic materials by $^{6,7}$Li NMR has been very successful in a number of cases via the use of both one- and two-dimensional NMR methods including Selective Inversion (SI) [23,25-27] and 2D Exchange Spectroscopy (2D EXSY) [28,29]. In theory, these methods can be extended to the study of similar Na cathode materials, where $^{23}$Na ssNMR can be utilized to probe the ion exchange between crystallographically unique Na sites. For both 1D and 2D NMR exchange experiments, a simple requirement is that the lifetime of spin polarization is long enough to capture changes in resonance frequency resulting from chemical exchange. In short, the exchange rates must be faster than or equal to the inherent nuclear spin relaxation times for the ions of interest. In many cases, this significantly limits the timescale of exchange that can be probed by these methods, and is largely sample dependent. Alkali ion cathode materials of this type typically exhibit fast nuclear relaxation of the site of interest ($^{7}$Li, $^{6}$Li, or $^{23}$Na) owing primarily to the paramagnetic nature of the samples.[20] The spin-lattice relaxation rates ($T_1$) were measured for both sites in $Na_2FePO_4F$ and were found to be 7.5 and 1.5 ms for sites A and B respectively. As a result, the 2D EXSY mixing time, or period during which $^{23}$Na nuclei are allowed to exchange with one another, is in practice limited to a maximum of 5 ms before signal is completely lost to relaxation. This severely restricts the measurable timescale for Na ion exchange via this method as compared to similar studies of analogous lithium polyanionic structures, where $T_1$'s were more favourable, allowing for detection of comparatively slow ion exchange processes. [23-26,28]

Several methods were employed in an attempt to observe and quantify Na1-Na2 exchange in $Na_2FePO_4F$, including variable temperature experiments, $^{23}$Na 2D EXSY, and Selective Inversion NMR. Variable temperature 1D spectra show no evidence of coalescence between the unique crystallographic sites. Additionally, 2D EXSY experiments over a temperature range of 295-340 K exhibit no visible cross peak intensity.

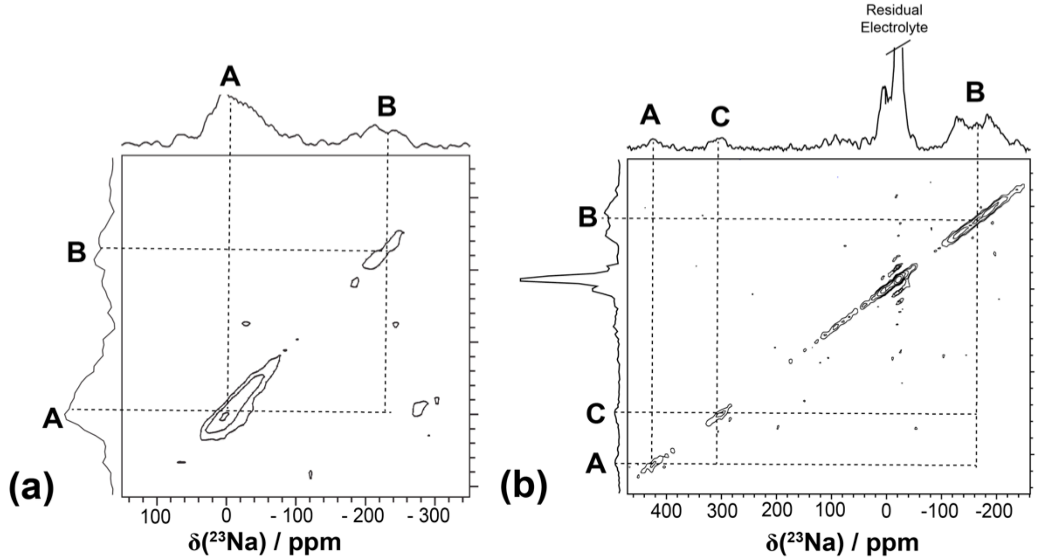

**Figure 6.8:** 2D EXSY $^{23}$Na MAS spectra of **(a)** pristine $Na_2FePO_4F$ at 335 K with a 5 ms mixing time, and **(b)** cycled $Na_2FePO_4F$ at 335 K with a 2 ms mixing time. The peak labeled as 'Residual electrolyte' is due to incomplete removal of $NaPF_6$ or other diamagnetic Na species that remain on the surface of the electrode even after the standard washing procedure.

In all cases, the NMR studies reveal that fast (>200 Hz) Na1-Na2 exchange does not occur in $Na_2FePO_4F$ at room temperature. An example 2D EXSY spectrum is depicted in **Figure 6.8a,** where the lack of cross peaks at even the longest achievable mixing time (5 ms) is evident in pristine $Na_2FePO_4F$. All selective inversion studies only further corroborate the results of the 2D EXSY experiment, with no Na ion exchange on the observable timescale. Atomistic modeling data reported by Tripathi *et al.*[13] in 2013 suggested that the available pathways for Na ion diffusion in $Na_2FePO_4F$ include a combination of Na1-Na1 and Na1-Na2 site hops. The results of the 2D EXSY experiment presented here indicate that either ion motion occurs via an alternate pathway that does not involve Na1-Na2 exchange, or that the ion diffusion is slow in this material overall. In the case of the latter, where the ion mobility is inherently limited, the results obtained from 2D EXSY NMR suggest that Na1-Na2 exchange is expected to occur at a rate of less than 200 Hz at 340 K based on the lack of observable cross peaks in the 2D EXSY spectrum up to mixing times of 5 milliseconds. It is noted that there is evidence of very slow alkali ion exchange in a similar Li fluorophosphate cathode material, $Li_2VPO_4F$,[48] where the Li-Li exchange timescale was determined to be on the order of 20 Hz, a rate too slow to be captured by the analogous $^{23}$Na 2D EXSY experiment in the material of interest here.

Finally, in order to confirm that the appearance of a new site in the NMR spectra of electrochemically cycled cathodes is in fact a new Na environment and not a result of chemical exchange between sites A and B, 1D variable temperature NMR and 2D EXSY experiments of partially charged $Na_{1+x}FePO_4F/C$ samples were undertaken and are depicted in **Figure 6.8b**. No evidence of coalescence or crosspeak intensity is observed; confirming that site C does not arise from partial A-B exchange, and is indeed a unique Na environment. Moreover, exchange experiments performed at intermediate states of charge provided analogous results to that of the pristine sample, wherein any exchange between unique sites is limited to motion slower than that of the measurable timescale via this experiment.

While this ion exchange rate limit is slow relative to the fast Li ion diffusion in other polyanionic Li phosphate materials such as $Li_3V_2(PO_4)_3$[30] and $Li_3Fe_2(PO_4)_3$[26,29], it is in good agreement with results for other Li fluorophosphates structures, such as $LiVPO_4F$,[50] where the addition of the fluoride anion appears to impose an attractive hold on the Na atom, thus impeding alkali ion mobility. The comparatively sluggish ion kinetics in $Na_2FePO_4F$ at typical operational temperatures would certainly contribute to its lack of commercial viability for high rate applications. It is therefore deduced that despite excellent structural stability as demonstrated by the robust nature of the Na chemical shift upon multiple electrochemical cycles, the material ultimately suffers from relatively limited intrinsic ion motion, preventing it from competing with current state-of-the-art materials. This is not to say that attempts to enhance ionic conductivity are unwarranted, and strategies such as carefully controlling particle size may help to maximize the diffusion through a real electrode. Indeed, the structural stability of the fluorophosphates is highly attractive, and therefore efforts to obtain commercially viable materials based on this structure should continue to be pursued.

## 6.4 Summary

The layered fluorophosphate cathode material $Na_2FePO_4F$ was synthesized and investigated here by *ex situ* ssNMR and X-ray diffraction techniques. Variable temperature 2D EXSY studies confirmed that chemical exchange between $Na^+$ atoms residing in unique crystallographic sites is not rapid, and if it does indeed occur as predicted, the ion hopping rate does not exceed 200 Hz in either the pristine or partially desodiated materials. *Ex situ* NMR studies of electrochemically cycled cathodes yielded novel information regarding the de-intercalation mechanism in $Na_2FePO_4F$, where the results are wholly indicative of a two-phase desodiation mechanism in this material. The results from *ex situ* NMR experiments were corroborated by PXRD data of partially charged cathodes that suggested two distinct phases present in varying quantities at several states of charge. All results reported here indicate that while the two phase mechanism of Na intercalation is highly reversible and the framework is structurally very robust, poor ion dynamics are likely what ultimately limit this cathode material, particularly at fast cycling rates. Efforts to optimize electrodes derived from this framework should therefore be focused on improvement of Na ion diffusion properties.

## 6.4 References

(1) Smiley, D. L.; Goward, G. R. *Chem. Mater.* **2016**, *28* (21), 7645.

(2) Kosova, N. V.; Podugolnikov, V. R.; Devyatkina, E. T.; Slobodyuk, A. B. *Materials Research Bulletin* **2014**, *60*, 849.

(3) Ellis, B. L.; Makahnouk, W. R. M.; Rowan-Weetaluktuk, W. N.; Ryan, D. H.; Nazar, L. F. *Chem. Mater.* **2010**, *22* (3), 1059.

(4) Ellis, B. L.; Makahnouk, W. R. M.; Makimura, Y.; Toghill, K.; Nazar, L. F. *Nat. Mater.* **2007**, *6* (10), 749.

(5) Kawabe, Y.; Yabuuchi, N.; Kajiyama, M.; Fukuhara, N.; Inamasu, T.; Okuyama, R.; Nakai, I.; Komaba, S. *Electrochemistry Communications* **2011**, *13* (11), 1225.

(6) Langrock, A.; Xu, Y.; Liu, Y.; Ehrman, S.; Manivannan, A.; Wang, C. *Journal of Power Sources* **2013**, *223* (C), 62.

(7) Song, W.; Ji, X.; Wu, Z.; Zhu, Y.; Yao, Y.; Huangfu, K.; Chen, Q.; Banks, C. E. *J. Mater. Chem. A* **2014**, *2* (8), 2571.

(8) Brisbois, M.; Krins, N.; Hermann, R. P.; Schrijnemakers, A.; Cloots, R.; Vertruyen, B.; Boschini, F. *Materials Letters* **2014**, *130* (C), 263.

(9) Brisbois, M.; Caes, S.; Sougrati, M. T.; Vertruyen, B.; Schrijnemakers, A.; Cloots, R.; Eshraghi, N.; Hermann, R. P.; Mahmoud, A.; Boschini, F. *Solar Energy Materials and Solar Cells* **2016**, *148* (C), 67.

(10) Law, M.; Ramar, V.; Balaya, P. *RSC Adv.* **2015**, *5*, 50155.

(11) Yan, J.; Liu, X.; Li, B. *Electrochemistry Communications* **2015**, *56* (C), 46.

(12) Cui, D.; Chen, S.; Han, C.; Ai, C.; Yuan, L. *Journal of Power Sources* **2016**, *301*

(C), 87.

(13) Tripathi, R.; Wood, S. M.; Islam, M. S.; Nazar, L. F. *Energy Environ. Sci.* **2013**, *6* (8), 2257.

(14) Carlier, D.; Blangero, M.; Ménétrier, M.; Pollet, M.; Doumerc, J.-P.; Delmas, C. *Inorg. Chem.* **2009**, *48* (15), 7018.

(15) Carlier, D.; Cheng, J. H.; Berthelot, R.; Guignard, M.; Yoncheva, M.; Stoyanova, R.; Hwang, B. J.; Delmas, C. *Dalton Trans.* **2011**, *40* (36), 9306.

(16) Billaud, J.; Clément, R. J.; Armstrong, A. R.; Canales-Vázquez, J.; Rozier, P.; Grey, C. P.; Bruce, P. G. *J. Am. Chem. Soc.* **2014**, *136* (49), 17243.

(17) Xu, J.; Lee, D. H.; Clément, R. J.; Yu, X.; Leskes, M.; Pell, A. J.; Pintacuda, G.; Yang, X.-Q.; Grey, C. P.; Meng, Y. S. *Chem. Mater.* **2014**, *26* (2), 1260.

(18) Castets, A.; Carlier, D.; Trad, K.; Delmas, C.; Ménétrier, M. *J. Phys. Chem. C* **2010**, *114* (44), 19141.

(19) Kim, J.; Middlemiss, D. S.; Chernova, N. A.; Zhu, B. Y. X.; Masquelier, C.; Grey, C. P. *J. Am. Chem. Soc.* **2010**, *132* (47), 16825.

(20) Grey, C. P.; Dupré, N. *Chem. Rev.* **2004**, *104* (10), 4493.

(21) Middlemiss, D. S.; Ilott, A. J.; Clément, R. J.; Strobridge, F. C.; Grey, C. P. *Chem. Mater.* **2013**, *25* (9), 1723.

(22) Lee, I. K.; Shim, I.-B.; Kim, C. S. *J. Appl. Phys.* **2011**, *109* (7), 07E136.

(23) Davis, L. J. M.; Goward, G. R. *J. Phys. Chem. C* **2013**, *117* (16), 7981.

(24) Davis, L. J. M.; He, X. J.; Bain, A. D.; Goward, G. R. *Solid State Nucl. Magn. Reson.* **2012**, *42* (C), 26.

(25) Smiley, D. L.; Tessaro, M. Z.; He, X.; Goward, G. R. *J. Phys. Chem. C* **2015**, *119* (29), 16468.

(26) Smiley, D. L.; Davis, L. J. M.; Goward, G. R. *J. Phys. Chem. C* **2013**, *117* (46), 24181.

(27) Langer, J.; Smiley, D. L.; Bain, A. D.; Goward, G. R.; Wilkening, M. *J. Phys. Chem. C* **2016**, *120* (6), 3130.

(28) Cahill, L. S.; Chapman, R. P.; Britten, J. F.; Goward, G. R. *J. Phys. Chem. B* **2006**, *110* (14), 7171.

(29) Davis, L. J. M.; Heinmaa, I.; Goward, G. R. *Chem. Mater.* **2010**, *22* (3), 769.

(30) Cahill, L. S.; Kirby, C. W.; Goward, G. R. *J. Phys. Chem. C* **2008**, *112* (6), 2215.

# Chapter 7: *Ab Initio* Calculations using Density Functional Theory to Investigate Layered $Na_2FePO_4F$

## 7.1 Introduction

In the previous chapter, layered $Na_2FePO_4F$ proved amenable for study by ssNMR in combination with electrochemical studies in order to observe changes to the sodium environments and surrounding structural atoms during electrochemical cycling. Although the general chemical shift trends can be used to gain useful insight into this material, there is not a robust empirical method for linking local sodium environments in the crystal structure to observed paramagnetic shifts in complex polyanionic materials.[1-3] A more complete discussion of the complex effects of unpaired electrons on the NMR experiment is presented in Chapter 3. Unlike the highly ordered metal-oxide materials that consist primarily of regular 90 or 180-degree Li-O-Metal interactions, a (simplistic) empirical method of assigning a fixed paramagnetic shift contribution from each nearest-neighbour transition metal atom leads to discrepancies in the polyanionic structures that often have contributions from secondary interactions and incomplete orbital overlap due to deviations from ideal octahedral metal geometry. *Ab initio* methods have been used to quantitatively assign paramagnetic shifts to unique crystallographic environments in both Li and Na containing cathode materials with some success. In particular, density functional theory (DFT) is becoming widely accepted as the method of choice for calculating the effect of unpaired electrons on NMR shifts.[1-3] Using first principles calculations, the electron spin density in a unit cell can be calculated, thus allowing for a calculation of the total spin density transferred to the NMR observed nucleus. While both the Generalized Gradient Approximation (GGA) and GGA+U methods have been implemented successfully,[4] in transition metal (TM) compounds GGA+U is traditionally the favoured approach as it aims to minimize the known tendency for GGA calculations to underestimate Li intercalation voltages in phosphates due to an incomplete representation of the transition metal in these materials.[5] The present chapter describes the use of density functional theory within the VASP software package for calculation of $^{23}$Na NMR shifts in layered $Na_2FePO_4F$, as well as a calculation of formation energies for intermediate states of charge in $Na_{1+x}FePO_4F$ to complement and corroborate experimental data presented in Chapter 6.

## 7.2 Experimental

### 7.2.1 VASP Calculations

Ab-initio calculations were performed using Density Functional Theory with a Generalized Gradient Approximation (GGA). The method utilizing Projector Augmented Wave (PAW) with pseudopotentials was chosen, as implemented in the Vienna Ab-initio Simulation Package (VASP). PAW-PBE potentials were used within the framework of VASP. This method was selected as an alternative for an all-electron method due to the large unit cell of the structure of interest (94 atoms). A plane wave basis set with cutoff energy of 600 eV was used for all $Na_2FePO_4F$ calculations, including the supercell calculations with O defect sites. A k-point grid of 8x4x4 was used to sample the reciprocal space for a single unit cell. The lowest energy structural configuration was found by a relaxation of all atomic positions and parameters, using both GGA and

GGA+U methods. In this work GGA+U was performed via Dudarev's approach whereby the "on-site" electron-electron repulsion (U) and exchange interaction (J) are treated as a single parameter that is calculated as a difference such that $U_{eff} = U - J$. All chemical shift calculations used a temperature of 320 K to account for typical heating of the rotor during spinning at 60 kHz.

### 7.2.2 Solid-State NMR

All NMR measurements referenced in this chapter were acquired at the McMaster University NMR facility. Room temperature $^{23}$Na ssNMR spectra were acquired at a Larmor frequency of 79.39 MHz with a 1.5 microsecond π/2 pulse on a Bruker wide bore 300 MHz spectrometer. A 1.3 mm Bruker double resonance probe was used to collect all spectra with magic angle spinning frequencies of 60-65 kHz. Spectra were referenced to a 1M $NaCl_{(aq)}$ solution at 0 ppm. A combination of Hahn echo (90°-τ-180°) and single pulse experiments were carried out to obtain the one-dimensional $^{23}$Na spectra referenced in this chapter with typical pulse delays of 100-200 ms.

### 7.2.3 Magnetic Susceptibility Measurements

The magnetic susceptibility of synthesized $Na_2FePO_4F$ was measured using SQUID (Superconducting Quantum Interference Device) measurements in collaboration with Dr. Patrick Rosa at the Institut de Chimie de la Matière Condensée de Bordeaux (ICMCB). The magnetic moment of the material was measured as a function of temperature between 2-350 K at 1000 Oe and 100 Oe, allowing for the determination of the magnetic susceptibility as a function of temperature. The results obtained by this method were input into paramagnetic shift calculations.

## 7.3 Results and Discussion

The fluorophosphate class of materials is among the most widely studied Na ion cathodes owing to their high structural stability and competitive operating voltage.[4,6-8] Of the possible polymorphs, those containing Fe are particularly attractive as they take advantage of the low cost and environmentally friendly transition metal, Fe. Chapter 6 presented extensive experimental NMR results demonstrating the large difference in both sign and magnitude of the paramagnetic shifts for the Na1 and Na2 sites in $Na_2FePO_4F$. This disparity in chemical shifts was somewhat surprising given apparent similarity of the local Na environments occupying the two distinct sites in the crystal lattice. Moreover, a lack of distinct and exclusive 90 or 180-degree Na-O-Fe interactions makes a conclusive shift assignment unreliable, as the contribution from all neighbouring atoms depend principally on orbital occupancy and geometry relative to the Na site of interest. This chapter will discuss in depth the calculation of the magnitude of the Fermi contact interaction giving rise to the observed chemical shifts in $Na_2FePO_4F$, allowing for the assignment of crystallographic sites to peaks in the $^{23}$Na spectra by *ab initio* methods. Furthermore, DFT will be used to complement experimental *ex situ* NMR data to confirm the already reported desodiation mechanism from a theoretical perspective.

### 7.3.1 Structure Optimization of $Na_2FePO_4F$ in VASP

Before calculation of hyperfine coupling constants in this material, the structure obtained experimentally by single crystal X-ray diffraction was optimized using DFT to yield the most stable atomic arrangement in $Na_2FePO_4F$. The structure was initially relaxed followed by a subsequent calculation of the final energy of the optimized geometry. All calculations carried out on $Na_2FePO_4F$ were spin-polarized with imposed ferromagnetic ordering in an effort to best model the spin state under NMR experimental conditions where there is an excess of spin aligned with the magnetic field. Due to a well-known large self-interaction error associated with the GGA strategy, there is often insufficient localization of electrons on the d-orbitals of transition metal compounds. As such, a "GGA+U" approach is executed here, wherein a Hubbard-like on-site electron-electron repulsion (U) term is added in order to better describe the system of interest. Specifically, Dudarev's method of a single parameter $U_{eff}$ that is equal to the difference between the traditional U (electron-electron repulsion) and J (exchange interaction) terms is defined within the calculation framework. More details regarding DFT in general and the DFT+U approach are discussed in Chapter 3 of this thesis. Several values for $U_{eff}$ (referred to simply as 'U' henceforth) are implemented and compared herein in order to best agree with experimental voltage calculations. The results of optimization by GGA and GGA+U with U values of 3.5 eV and 4.5 eV yielded structural features very similar to those obtained experimentally, as outlined in **Table 7.1**.

**Table 7.1:** Relaxed Cell Parameters for the GGA and GGA+U optimized $Na_2FePO_4F$ unit cell compared to experimental values.

| | **a (Å)** | **b (Å)** | **c (Å)** | **Volume ($Å^3$)** | **Space Group** |
|---|---|---|---|---|---|
| **Exp**[7] | 5.22 | 13.854 | 11.779 | 851.846 | *Pbcn* |
| **GGA** | 5.196 | 13.922 | 11.824 | 855.216 | *Pbcn* |
| **GGA+U** U=3.5 eV | 5.353 | 13.861 | 11.758 | 872.44 | *Pbcn* |
| **GGA+U** U=4.5 eV | 5.35 | 13.863 | 11.763 | 872.523 | *Pbcn* |

The GGA+U approach has the distinct effect of causing a slight contraction of the unit cell along the b and c axes coupled with a significant lengthening along the a-axis coupled with an overall volume expansion relative to standard GGA calculations. Upon closer inspection of the structure, it is evident that this expansion in the a-direction is due to the decreased covalency of the Fe-O and Fe-F bonds that link $FeO_4F_2$ units in a chain of corner-shared (**c**) and face-shared (**f**) polyhedra. **Figure 7.1** demonstrates this c-f-c type linking that is unique to the *a*-direction of the unit cell, with very little impact of the Fe-Fe distances along either the *b* or *c* axes. The Fe-Fe internuclear distances for the c and e type linkages are listed in **Table 7.2** for structures obtained experimentally and computationally. While use of GGA alone tends to underestimate these distances relative to experiment, the GGA+U effectively localizes electron density at the Fe nucleus relative to GGA, resulting in longer Fe-O bond lengths due to decreased electron-sharing and therefore larger polyhedral separation along this chain of metal octahedra.

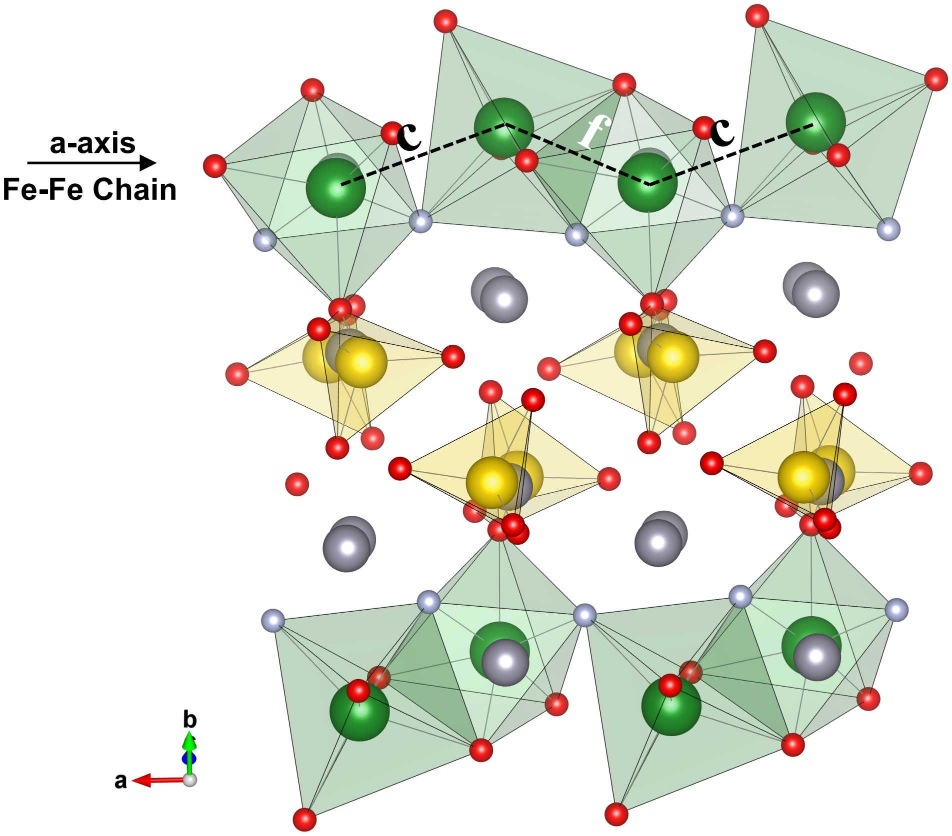

**Figure 7.1:** Depiction of the $Na_2FePO_4F$ structure (determined experimentally), demonstrating the Fe-polyhedra chains formed along the a-axis of the unit cell. Fe-Fe distances resulting from corner-sharing are labeled 'c' and those from face-sharing 'f'. Fe atoms are shown in green with oxygen and fluorine as red and light grey respectively.

**Table 7.2:** Fe-Fe distances between corner and face-shared iron octahedra along the a-direction in $Na_2FePO_4F$ (depicted in Figure 7.1) as determined experimentally and theoretically.

| | **Expt.** | **GGA** | **GGA+U** (U=3.5) | **GGA+U** (U=4.5) |
|---|---|---|---|---|
| **Corner - Shared** | 3.363 Å | 3.313 Å | 3.448 Å | 3.447 Å |
| **Face - Shared** | 2.976 Å | 2.802 Å | 2.998 Å | 2.996 Å |

This effective electron localization that occurs with the application of GGA+U is similarly reflected in the partial density of states (DOS) plots for the Fe 3d electrons in $Na_2FePO_4F$. The DOS plots additionally provide confirmation of the expected orbital occupancies and spin state of the metal, as well as predict the Fe band gap based on the chosen value of U. The comparison of DOS diagrams for GGA versus GGA+U approaches is plotted in **Figure 7.2**, where as expected, a systematic increase of band gap occurs with addition and increasing value of U, again due to the relative localization of electron density at the TM nucleus. The splitting of the down spin $t_{2g}$ orbital even for the GGA calculation indicates that there is local distortion of the Fe octahedral that breaks the degeneracy of this orbital as evidenced by the partial DOS plots. Furthermore, the high-spin $3d^6$ electron configuration is confirmed by appearance of occupied $e_g$ orbitals and a splitting of $t_{2g}$ orbital energies due to electron pairing in only one of the orbitals thus breaking the degeneracy.

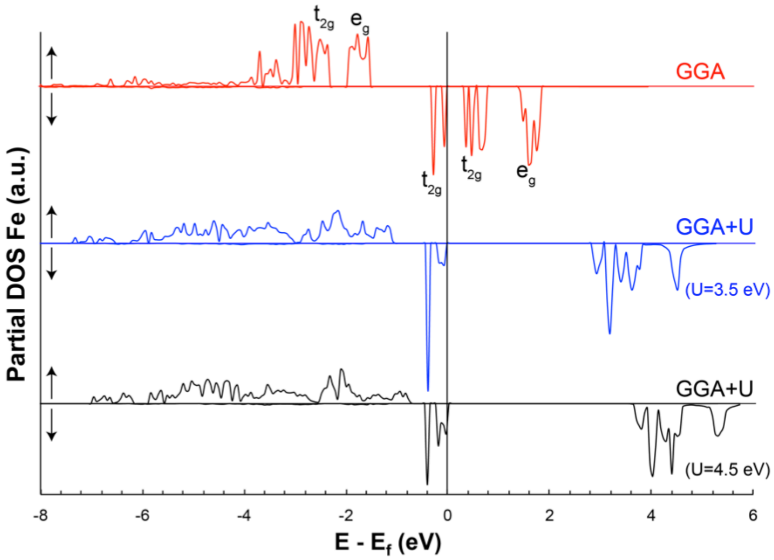

**Figure 7.2:** Partial DOS at Fe for $Na_2FePO_4F$ as calculated with GGA, GGA+U (U=3.5 eV) and GGA+U (U=4.5 eV). The widening of the gap at the Fermi level (denoted by the solid line at $E-E_f=0$) is consistent with the increased localization of d-electron spin density at the Fe site with increasing value of U.

This phenomenon regarding the GGA versus GGA+U approaches for calculation of d-metal compounds is well known, where the purely *ab initio* GGA method does not accurately describe the localization of d-electrons, thus requiring the addition of an interaction energy term to more accurately model the electron density.[5,9] A comparison to similar transition metal phosphate materials can provide some insight into appropriate ranges of U; however, no definitive 'rule' for the choice of U correction to the energy exists, and therefore comparison to known experimental parameters is necessary in order to ensure suitable choice of U.[4,5]

### 7.3.2 Calculation of Theoretical Redox Voltage in $Na_2FePO_4F$

As shown above, the implementation of a GGA+U approach is necessary in order to more correctly reflect the experimentally determined structure, and thus is expected to have a significant impact on calculated parameters such as Fermi contact interactions that will ultimately be used to predict observed chemical shifts in NMR. It is therefore imperative that an appropriate value for U is chosen so as to ensure most accurate representation of the actual electronic structure. Fortunately, the predicted band gap for the 3d atoms in a transition metal structure is highly dependent on choice of magnitude for the U energy correction as well as being a major factor in redox voltage at which the $Fe^{2+} \rightarrow Fe^{3+}$ transition occurs, meaning that by calculating the theoretical redox potential for $Na_2FePO_4F$ and comparing to experimental electrochemical data, an appropriate value for U can be ascertained.

Calculation of the voltage for an electrode due to sodium insertion can be obtained by consideration of the relative chemical potentials of the anode and cathode in an electrochemical cell as per:

$$\mathrm{E} = -\frac{\mu_{\mathrm{Na}}^{\mathrm{cathode}} - \mu_{\mathrm{Na}}^{\mathrm{anode}}}{ze} \tag{7.1}$$

where in the above equation μ represents chemical potential, and *z* and *e* are the number of electrons transferred and the value of electronic charge respectively. If the electrochemical tests are completed using a pure metal anode the chemical potential of the anode remains unchanged over the course of cycling, and thus the variation in open circuit voltage as a function of state of charge is entirely dependent on the changing chemical potential of the cathode as sodium ions are intercalated during charging relative to a constant anode reference potential. To simplify things, the average chemical potential in the cathode can be calculated by considering only the fully charged and discharged states of the cathode, labeled here as $x_1$ and $x_2$ respectively. As per Aydinol *et al.*[10] Equation 7.1 above can be integrated between $x_1$ and $x_2$ to obtain the average open circuit voltage described by:

$$\bar{E} = -\frac{\Delta G_{rxn}}{(x_2 - x_1)zF} \tag{7.2}$$

where F is Faraday's constant (electric charge per mole of electrons) and $\Delta G_{\mathrm{rxn}}$ represents the change in Gibbs free energy for the insertion reaction as follows:

$$(x_2 - x_1)\mathrm{Na(anode)} + \mathrm{Na_{x_1}\ Host\ (cathode)} \rightarrow \mathrm{Na_{x_2}\ Host\ (cathode)} \tag{7.3}$$

Due to negligible entropy and volume effects, $\Delta G_{\mathrm{rxn}}$ can be approximated by consideration only of the relative ground state energies of reactants and products in the above reaction, allowing us to express Equation 7.3 as:

$$\bar{E} = -\frac{E_{\mathrm{Na_{x_2}\ Host\ (cathode)}} - [(x_2 - x_1)\mathrm{E_{Na(anode)}} + E_{\mathrm{Na_{x_1}\ Host\ (cathode)}}]}{(x_2 - x_1)\mathrm{zF}} \tag{7.4}$$

This average insertion voltage can therefore be determined from ground state energies of the fully charged and fully discharged cathode states relative to the Na metal anode, which correspond to $NaFePO_4F$ ($x_1$) and $Na_2FePO_4F$ ($x_2$) respectively for the system described herein.

Theoretical voltages were calculated for the $Na_2FePO_4F$-$NaFePO_4F$ reaction and then compared to experimental electrochemical curves to determine the effect of U on the predicted insertion potential. The results are summarized in **Table 7.3**, where based on the calculated average potential, a U correction of 3.5 eV (yielding $\overline{E}$ =3.14 V) most accurately reproduces the average experimental charging voltage of 3.15 V. The appropriate choice for U of 3.5 eV can therefore be justified by comparison to experimental parameters, specifically the observed cell potential. This allows us to implement the method going forward for calculation of other experimental parameters such as Fermi contact interactions and formation energies in $Na_{1+x}FePO_4F$ for values of x ranging from 0 to 1.

**Table 7.3:** Results from the calculation of the average voltage as a function of calculation method (GGA vs GGA+U) and magnitude of the additional U term (3.0-4.0 eV).

| **Method** | **Structure** | **$E_0$ (eV)** | **Theoretical Voltage** |
|---|---|---|---|
| **GGA<br>(U=0 eV)** | Na Metal<br>$NaFePO_4F$<br>$Na_2FePO_4F$ | -1.304<br>-52.93<br>-56.86 | 2.62 V |
| **GGA+U<br>(U=3.0 eV)** | Na Metal<br>$NaFePO_4F$<br>$Na_2FePO_4F$ | -1.304<br>-51.68<br>-56.07 | 3.07 V |
| **GGA+U<br>(U=3.5 eV)** | Na Metal<br>$NaFePO_4F$<br>$Na_2FePO_4F$ | -1.304<br>-51.52<br>-55.98 | 3.14 V |
| **GGA+U<br>(U=4.0 eV)** | Na Metal<br>$NaFePO_4F$<br>$Na_2FePO_4F$ | -1.304<br>-51.38<br>-55.90 | 3.20 V |

### 7.3.3 Fermi Contact Shift Calculations for $Na_2FePO_4F$ in VASP

With an improved understanding of the effect of GGA as compared to the GGA+U strategy, the paramagnetic shifts for Na atoms in $Na_2FePO_4F$ are determined via calculation of the Fermi contact hyperfine interaction by DFT+U. This is especially imperative for assignment of chemical shifts in complex structures such as phosphates or fluorophosphates where a lack of ideal 90 and 180 degree interactions renders empirical arguments for chemical shift assignments unreliable. DFT therefore is employed here primarily as a method to make a more conclusive site of the experimental chemical shifts for $Na_2FePO_4F$.

Paramagnetic shift calculations in VASP are more accurately described as calculation of the through-bond electron-nuclear coupling interaction known as the Fermi contact interaction (typically denoted as $\mathbf{A_{FC}}$). This interaction is directly related to the electron spin density transferred to the nuclei of interest via Eq. 7.4. By DFT, both an exact value for $A_h$ and a map of electronic spin density in the optimized unit cell are calculated, allowing for the visualization of electron spin density transfer. In addition, a hyperfine coupling constant that describes the coupling of the electron spin density with nuclei in the unit cell is determined and used to calculate the spin density at Na1 and Na2 sites. By convention, 'positive' or 'up' spin is that which is aligned with the magnetic field in the NMR experiment.

Moreover, the spin density in the geometry optimized unit cell can conveniently be separated by unique orbital contributions as defined by the Fe DOS. This separation provides specific spin density maps for particular orbital energies, e.g. contributions from $e_g(\uparrow)$ only. Based on a closer look at the geometry of the Na environments and spin density maps, two significant pathways are identified that contribute significant positive spin to Na1 and negative spin to Na2, both of which are shown in **Figure 7.3**. The electrons in the Fe $e_g$ orbitals are expected to interact strongly with the bridging F atom along the Fe-F-Na1 pathway due to a 173.1° interaction angle, depicted in **Figure 7.3**, that causes the $e_g$ orbitals to point directly toward the F p-orbital lobe which then directly transfers positive electron spin density (depicted as yellow in **Figure 7.3**) to the Na1 atom. This highly favourable transfer of positive electron spin density results in the large positive chemical shift observed in the $^{23}$Na NMR spectrum (+440 ppm) and thus this peak is attributed to the Na1 site. Conversely, the Na2 site, although receiving some positive contributions to the chemical shift, has significant negative spin density (blue in **Figure 7.3**) transfer from the $t_{2g}$ orbitals on Fe directly to the Na2 site through an 82.6° Fe-O-Na interaction (**Figure 7.3(b)**). The $t_{2g}$ lobe containing a single spin-down electron points directly toward the Na2 atom, causing enough negative spin density transfer to result in a net negative chemical shift of -175 ppm for this site.

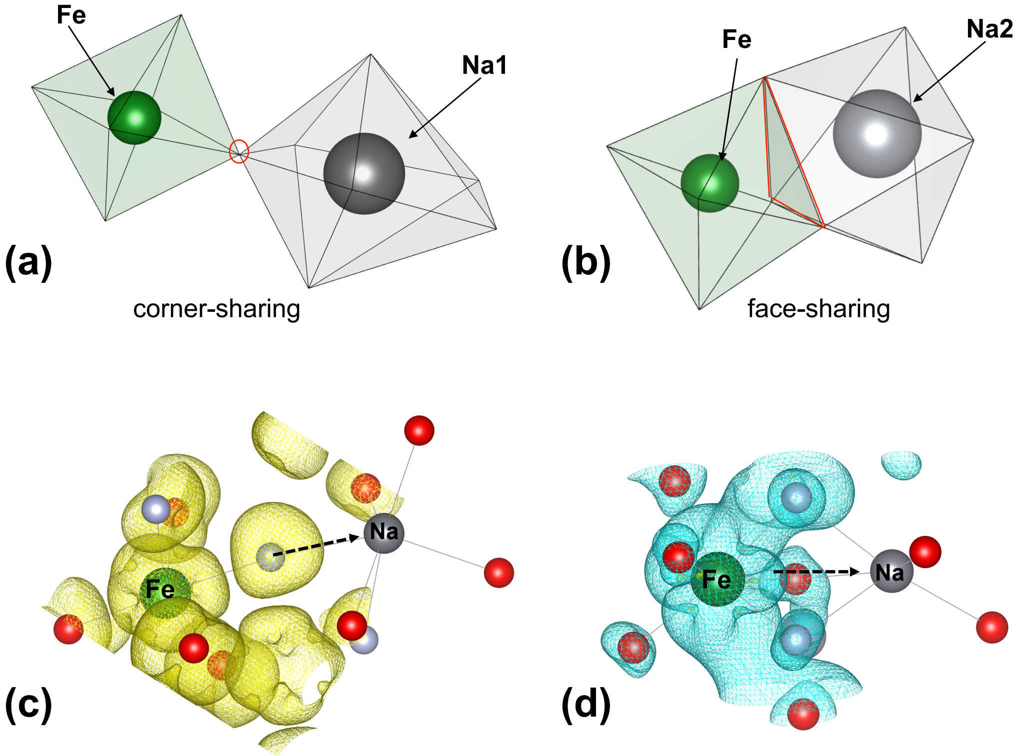

**Figure 7.3** Geometry of the **(a)** Na1 and **(b)** Na2 polyhedra (grey) relative to the $FeO_6F_2$ octahedra (green). **(c)** Positive spin density (yellow) transferred to Na1 through the Fe 3d $e_g$ orbitals via a 180° geometry. **(d)** Negative spin density (blue) transferred via the $t_{2g}$ orbitals to Na2 through a 90° contact through fluorine.

Although the chemical shift difference can be observed visually through generation of spin density maps, the hyperfine coupling constant between the electron spins and each Na nucleus can be calculated in order to quantify the total amount of spin density transferred to each site. Equation 7.5 below is used to calculate this spin density, and uses the hyperfine coupling constant (A) determined by VASP in addition to the total number of unpaired electrons in the unit cell and gyromagnetic ratio of the nucleus to which spin density is being transferred to determine the total amount of spin density at each Na nucleus.

$$\rho = \frac{\mathrm{A}\cdot \mathrm{S}_{\mathrm{tot}}(15.5568)}{\gamma_{\mathrm{N}}} \tag{7.5}$$

The expected paramagnetic contribution to the NMR shift can then be determined by taking into account the spin density at the nucleus (ρ) and the magnetic susceptibility of the material (χ) according to Equation 7.6:

$$\delta(\mathrm{ppm}) = \frac{1}{3\mathrm{SN}_0\mathrm{a}_0{}^3} \cdot \rho \cdot 4\pi \cdot \chi \tag{7.6}$$

where in the equation above S is the total spin magnetic moment (0.5 multiplied by the number of unpaired electrons at Fe), $N_0$ is Avogadro's number, and $a_0$ is the Bohr radius.

By fitting a plot of the inverse of the magnetic susceptibility (1/ χ) versus temperature using the modified Curie-Weiss law, $\chi = C/(T- \Theta_{CW})$, C and $\Theta_{CW}$ are determined from a linear fit (**Figure 7.4**). Using this method, the Curie constant was determined to be $4.24\mu_B$, with a $\Theta_{CW}$ value of -5.55 K. This is in good agreement with the literature values calculated for the same structure of 5.46 and -5.1 for C and Θ respectively.[11] The experimental values were then used to calculate the expected chemical shifts for the Na1 and Na2 sites in $Na_2FePO_4F$ via Equation 7.6.

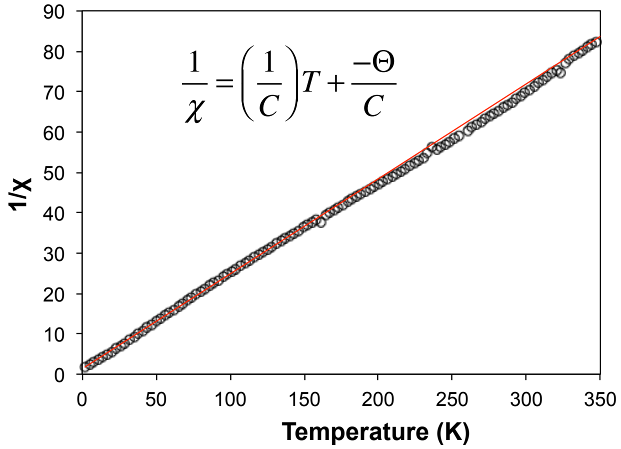

**Figure 7.4:** Linear fit from the results of a SQUID experiment where the magnetic susceptibility as a function of temperature is determined to yield the curie constant (C) and temperature (Θ).

Results from calculations using both the GGA and GGA+U methods are compared to the experimental shift values and reported in **Table 7.4** below.

**Table 7.4**: Calculated chemical shifts for Na1 and Na2 in $Na_2FePO_4F$ by GGA and GGA+U Methods

| **Calculation Method** | **Site Label** | **Observed Shift (ppm)** | **Calculated Shift (ppm)** |
|---|---|---|---|
| **GGA** | Na1 | 445 | 878 |
| | Na2 | -176 | -159 |
| **GGA+U** | Na1 | 445 | 651 |
| **$U_{eff}$=3.5 eV** | Na2 | -176 | -143 |
| **GGA+U** | Na1 | 445 | 583 |
| **$U_{eff}$=4.5 eV** | Na2 | -176 | -128 |

The effect of the additional U term in the GGA+U calculation mirrors what is discussed above, wherein the increased localization of electron density at the transition metal minimizes the spin density transfer to the Na nucleus, thus giving rise to a smaller magnitude chemical shift upon addition and increase of the U correction. Note that in all cases, VASP tends to overestimate the positive contribution to the chemical shift, resulting in the positive frequency shift being calculated as too large, and the negative frequency shift as too small in total magnitude when compared to the experimental results. Despite this overestimation, the calculations give reasonably good agreement between theoretical and experimental results, allowing for an accurate site assignment of Na1 to the +440 ppm chemical shift, and Na2 to the -175 ppm shift (see **Figure 7.5**), contrary to the original assignment based solely on bond lengths and Na-Fe distances.[12]

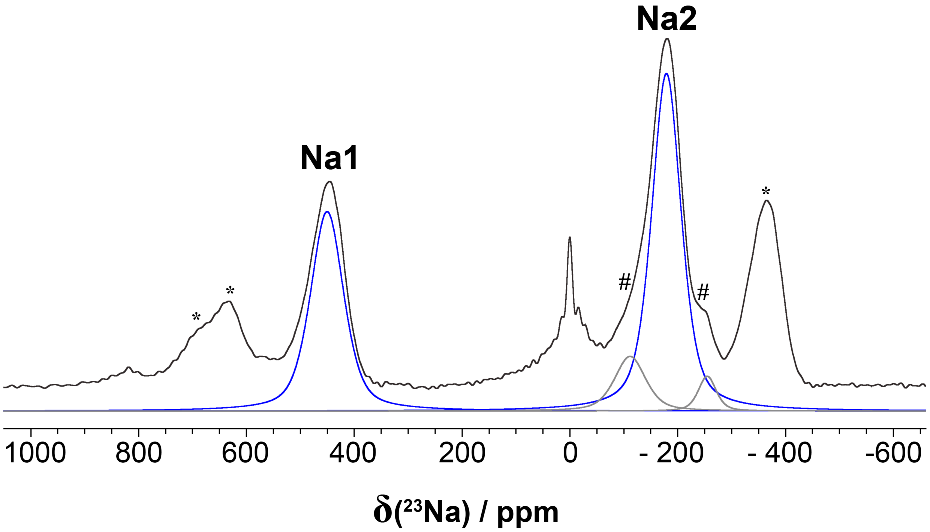

**Figure 7.5:** One-dimensional $^{23}$Na spectrum of $Na_2FePO_4F$ depicting two distinct Na sites, A and B, corresponding to the Na1 and Na2 environments respectively, as determined by DFT+U calculations of the Fermi Contact shifts due to electron-nuclear interactions.

Upon assignment of Na resonances in the spectrum of pristine $Na_2FePO_4F$, the same approach can be used to calculate the expected chemical shift of the oxidized $NaFePO_4F$

phase that appears after electrochemical charging of the material (see Chapter 6). This phase appears afer the electrochemical reaction described by Equation 7.7 below.

$$\mathrm{Na_2Fe^{II}PO_4F \rightarrow NaFe^{III}PO_4F + Na^{+} + e^{-}} \tag{7.7}$$

During electrochemical desodiation, the appearance of a new site was identified as evidence of formation of the fully oxidized $NaFePO_4F$ phase. Based on chemical oxidation experiments reported in literature, it is believed that the Na2 site is fully depopulated during oxidation leaving the rest of the structure largely in tact. DFT is used here to confirm this result by determining if the theoretical NMR shift of the remaining Na1 atoms is in good agreement with experimental observations. Experimentally, what is believed to be the $NaFePO_4F$ phase is observed at a chemical shift of +350 ppm in the $^{23}$Na NMR spectrum. To determine whether the $NaFePO_4F$ structure is lower energy with the Na1 or Na2 sites occupied after oxidation, a calculation of the total energy of the structure was performed using the GGA method. No attempt at a comparison of the GGA method to GGA+U was undertaken for this purpose, as the point of interest is not the absolute energy of the structure, but rather a comparison of the relative energies of the $NaFePO_4F$ configurations. These calculations were done with the assumption that the overall structure does not undergo a significant change upon oxidation, in keeping with the literature X-ray diffraction results[6,7] that suggest preservation of the initial framework with only a small change in volume. The results of the optimized geometry of the Na1 occupied and Na2 occupied structures are provided in **Table 7.5**.

**Table 7.5:** Calculated ground state energies and Fermi contact hyperfine coupling constant for $NaFePO_4F$ with different Na site occupancies.

| Na Site Occupied | Energy Per Formula Unit (eV) | Fermi Contact Hyperfine Coupling (MHz) | Estimated Shift (ppm) |
|---|---|---|---|
| **Na1** | -52.93 | 0.110 | 204 |
| **Na2** | -52.76 | 0.059 | 109 |

The total energy per formula unit for the Na1 occupied structure is lower than that of the Na2 occupied structure, as was shown by experimental X-ray diffraction studies by Nazar and coworkers.[6,7] In addition to the cell parameters, the Fermi contact hyperfine coupling constant was calculated for both structures, both of which gave rise to a positive coupling constant. Without available magnetic measurements for this phase the exact calculation of the expected chemical shift is not possible; however using the theoretical C value for high-spin trivalent iron and a theta value of 0 approximations of the shifts were determined for sodium atoms in Na1 and Na2 positions.[13] The approximated shift of +204 ppm for Na ions housed in the Na1 position more closely reflects the experimental shift at +350 ppm observed upon electrochemical desodiation. The hypothesis of a fully occupied Na1 site in $NaFePO_4F$ is therefore supported theoretically, and can be assigned to the observed 350 ppm site in the NMR data presented in the previous chapter.

### 7.3.4 Formation Energy Calculations for $Na_{1+x}FePO_4F$

The chemical shift calculations provide a method for interpreting the experimental NMR results in terms of assigning observed sites to certain species. However, DFT can be used further to verify the electrochemical phenomena observed by the *ex situ* NMR spectroscopy presented in Chapter 6. Specifically, the most energetically favourable desodiation mechanism can be determined by calculation of the ground state energies of intermediate $Na_{1+x}FePO_4F$ states (with $x$ values ranging from 0 to 1). These energies can then be input into Equation 7.8 to calculate a formation energy ($E_f$):

$$\Delta_f \mathrm{E} = \mathrm{E} - (x\mathrm{E}_{\mathrm{Na2FePO4F}} + (1-x)\mathrm{E}_{\mathrm{NaFePO4F}}) \qquad (7.8)$$

where the energy for any intermediate state (E) is calculated relative to the mixture of reduced and oxidized phases. This effectively compares the existence of a solid solution formation (where the energy of such a configuration is input as $E$ in Equation 7.8 above) to a mixture of distinct phases. If the energy of a solid-solution-like phase is greater than the corresponding biphasic mixture such that $\Delta_f E < 0$, it can be concluded that the biphasic mixture is of lower energy, and therefore thermodynamically favoured over solid solution formation. Conversely, when $\Delta_f E > 0$, this implies the energetically favourable formation of a solid-solution for intermediate phases.

Calculation of this formation energy initially requires calculation of ground state energies for the end members of the expected electrochemical reaction, i.e. the oxidized and reduced phases. In this case, these phases are $NaFePO_4F$ and $Na_2FePO_4F$ respectively, with the results of these structural calculations already discussed previously. For formation energy calculations, the experimentally determined unit cell parameters were used without a geometry optimization step so as not to introduce unwanted variance in calculations of various structures. A variety of solid-solution configurations were chosen, in order to account for different possible sodium site occupancies within the unit cell. In the fully sodiated example ($Na_2FePO_4F$) there are 16 sodium atoms (two equivalent positions) in a single unit cell. To generate intermediate structures of the form $Na_{1+x}FePO_4F$ where $0 < x < 1$, sodium ion site occupancies were randomly chosen in a variety of combinations to determine the lowest energy configuration. In all cases, by using Eq. 7.6 to calculate the formation energies of intermediate states, a $\Delta_f E > 0$ was obtained, implying that the formation of a solid-solution is energetically less favourable relative to two phases. This is shown schematically in **Figure 7.6(a)**, where the distribution of Na atoms in a two-phase versus a solid-solution particle is shown. All formation energies were plotted in **Figure 7.6(b),** demonstrating the probability of phase separation based on ground state energy differences. Note that in this case entropic contributions were not considered. Although this might initially appear problematic due to the possible energy stabilization of the solid-solution phases due to increased entropic mixing, this entropy term in similar iron phosphate derivatives has been shown to be on the order of $0.3k_B$[14], i.e. much smaller than the difference between ground state energies, and therefore not enough to favour solid-solution formation here.

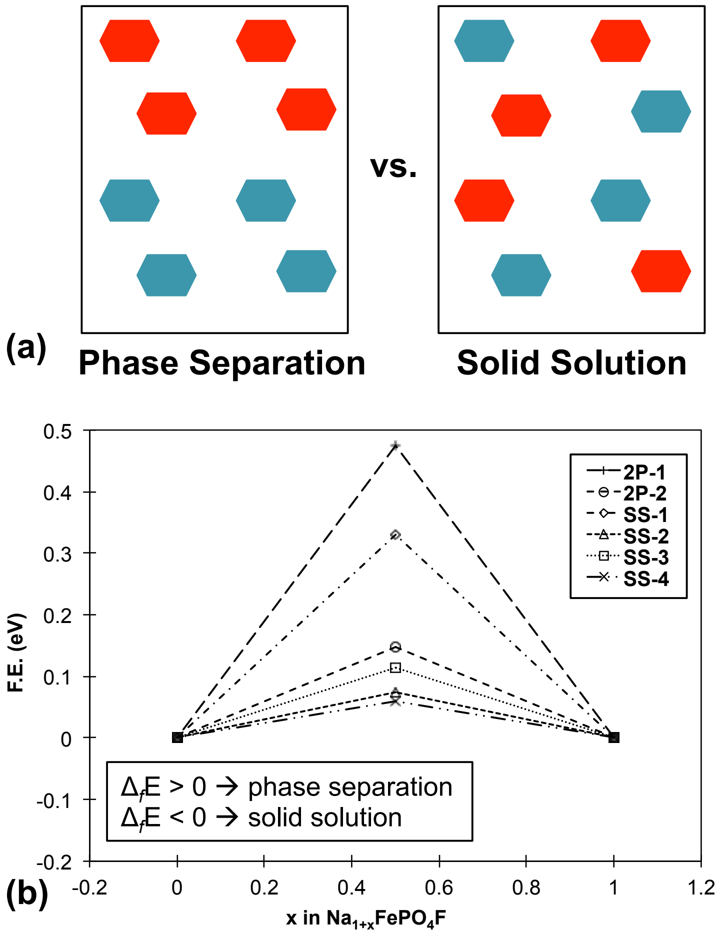

**Figure 7.6: (a)** Schematic representation of Na ion distribution in a phase separated (two-phase) or solid-solution configuration. In the latter, Na ions are ‘randomly’ distributed throughout the structure to create a consistent average Na occupancy throughout a given particle. Conversely, in the phase-separated particle, Na distributions are fixed at the two end members, separated by a thin phase boundary. **(b)** Shows the results of the formation energy calculations for the *x*=0.5 Na stoichiometry ($Na_{1.5}FePO_4F$).

Results of the DFT calculations are therefore in excellent agreement with the experimental *ex situ* NMR results presented in the previous chapter, where the observed biphasic nature of the Na intercalation in $Na_2FePO_4F$ is corroborated by first principles calculations.

## 7.4 Summary

This chapter details the results of a series of ab initio studies carried out in collaboration with Prof. Dany Carlier at the Université de Bordeaux. Following a optimization of experimental structural parameters in the cathode $Na_2FePO_4F$, Fermi contact interactions were calculated and ultimately used to determine paramagnetic NMR shifts for Na atoms in this material. This allowed for the assignment of the two crystallographic Na sites to the two distinct peaks observed in the NMR spectrum at +445 and -175 ppm. The application of the DFT+U approach was also discussed herein, with the use of theoretical insertion potentials as a guide for choice of the U parameter. Based on these calculations, a value of 3.5 eV was chosen as most appropriate for this particular system, as it most accurately reflected the average experimental voltage for the $Na_2FePO_4F$-$NaFePO_4F$ reaction versus Na metal.

The DFT method was further applied to corroborate experimental results presented in Chapter 6, wherein the formation of a two-phase insertion/deinsertion reaction for Na in $Na_{1+x}FePO_4F$ was determined to be thermodynamically favourable relative to creation of solid-solution type intermediates. This work demonstrates the complementary nature of spectroscopy and first principles calculations in understanding paramagnetic cathode materials for battery applications. Both methods will be applied in tandem in the continuation of this work as discussed in Chapter 8, where a combination of a variety of experimental methods and DFT calculations are used to identify anomalous structural effects in sodium iron fluorophosphates cathodes.

## 7.5 References

(1) Clément, R. J.; Pell, A. J.; Middlemiss, D. S.; Strobridge, F. C.; Miller, J. K.; Whittingham, M. S.; Emsley, L.; Grey, C. P.; Pintacuda, G. *J. Am. Chem. Soc.* **2012**, *134* (41), 17178.

(2) Castets, A.; Carlier, D.; Trad, K.; Delmas, C.; Ménétrier, M. *J. Phys. Chem. C* **2010**, *114* (44), 19141.

(3) Kim, J.; Middlemiss, D. S.; Chernova, N. A.; Zhu, B. Y. X.; Masquelier, C.; Grey, C. P. *J. Am. Chem. Soc.* **2010**, *132* (47), 16825.

(4) Broux, T.; Bamine, T.; Fauth, F.; Simonelli, L.; Olszewski, W.; Marini, C.; Ménétrier, M.; Carlier, D.; Masquelier, C.; Croguennec, L. *Chem. Mater.* **2016**, *28* (21), 7683.

(5) Zhou, F.; Marianetti, C. A.; Cococcioni, M.; Morgan, D.; Ceder, G. *Phys. Rev. B* **2004**, *69* (20), 201101.

(6) Ellis, B. L.; Makahnouk, W. R. M.; Makimura, Y.; Toghill, K.; Nazar, L. F. *Nat. Mater.* **2007**, *6* (10), 749.

(7) Ellis, B. L.; Makahnouk, W. R. M.; Rowan-Weetaluktuk, W. N.; Ryan, D. H.; Nazar, L. F. *Chem. Mater.* **2010**, *22* (3), 1059.

(8) Ellis, B. L.; Nazar, L. F. *Current Opinion in Solid State & Materials Science* **2012**, *16* (4), 168.

(9) Cramer, C. J.; Truhlar, D. G. *Phys. Chem. Chem. Phys.* **2009**, *11* (46), 10757.

(10) Aydinol, M. K.; Ceder, G. *J. Electrochem. Soc.* **1997**.

(11) Avdeev, M.; Ling, C. D.; Tan, T. T.; Li, S.; Oyama, G.; Yamada, A.; Barpanda,

P. *Inorg. Chem.* **2014**, *53* (2), 682.

(12) Smiley, D. L.; Goward, G. R. *Chem. Mater.* **2016**, *28* (21), 7645.

(13) Housecroft, C. E.; Sharpe, A. G. *Inorganic chemistry*, 3rd ed.; Prentice Hall, 2007.

(14) Zhou, F.; Maxisch, T.; Ceder, G. *Phys. Rev. Lett.* **2006**, *97* (15), 155704.

# Chapter 8: Investigation of Oxygen Defect Formation in $Na_2FePO_4F$

## 8.1 Introduction

Sodium iron fluorophosphate as a potential cathode material for sodium ion batteries has been a focus of this thesis, with the electrochemical process being tracked by a combination of solid-state $^{23}$Na NMR methods and density functional theory. The electrochemical mechanism by which Na ions are removed from the parent structure was determined to be biphasic in nature as evidenced by solid-state NMR spectra that were characterized with the help of *ab initio* calculations in the preceding two chapters.[1] This mechanism was further supported by formation energy calculations described in chapter 7, where this two-phase mechanism was shown to be lower in energy relative to the contrasting solid-solution hypothesis. This chapter catalogues the attempts to identify and characterize possible structural defects never before reported for this particular fluorophosphate analog. The initial $^{23}$Na NMR studies of sodium iron fluorophosphate revealed two anomalous peaks at low frequencies near the assigned Na2 resonance from the pristine material. This chapter aims to identify and explore the possibility for defect formation in $Na_2FePO_4F$ that is not readily observed by diffraction methods. As will be discussed herein, structural defects are not uncommon, especially in the fluorophosphate family of materials, as the possibility for oxygen substitution at the fluorine sites can generate unique structural features.

The appearance of the extra resonance in the $^{23}$Na NMR spectrum of $Na_2FePO_4F$ was the first evidence of an anomalous sodium environment in the pristine cathode material; however, using this as a starting point, a suite of additional techniques have been applied in an effort to gather information about the proposed defect. This work was carried out in part in collaboration with the Université de Bordeaux, specifically Mössbauer spectroscopy, density functional theory, and electron paramagnetic resonance techniques were all performed at the facilities in France. Moreover, this project is ongoing, and thus a significant amount of experimental data that did not provide direct evidence for defect formation is compiled into Appendix A2 for future reference.

## 8.2 Methods

### 8.2.1 Solid-state NMR

All NMR measurements referenced in this chapter were acquired at the McMaster University NMR facility. Room temperature $^{23}$Na ssNMR spectra were acquired at a Larmor frequency of 79.39 MHz with a 1.5 microsecond $\pi/2$ pulse on a Bruker wide bore 300 MHz spectrometer. A 1.3 mm Bruker double resonance probe was used to collect all spectra with magic angle spinning frequencies of 60-65 kHz. Spectra were referenced to a 1M $NaCl_{(aq)}$ solution at 0 ppm. A combination of Hahn echo (90°-$\tau$-180°) and single pulse experiments were carried out to obtain the one-dimensional $^{23}$Na spectra referenced in this chapter with typical pulse delays of 100-200 ms.

Temperature calibration was performed using a standard $Sm_2Sn_2O_7$ temperature thermometer as per the established method.[2]

### 8.2.2 *Ab Initio* Calculations in VASP

Ab-initio calculations were performed using Density Functional Theory with a Generalized Gradient Approximation (GGA). The method utilizing Projector Augmented Wave (PAW) with pseudopotentials was chosen, as implemented in the Vienna Ab-initio Simulation Package (VASP).[3] PAW-PBE potentials were used within the framework of VASP.[3,4] This method was selected as an alternative for an all-electron method due to the large unit cell of the structure of interest (94 atoms). A plane wave basis set with cutoff energy of 600 eV was used for all $Na_2FePO_4F$ calculations, including the supercell calculations with O defect sites. A k-point grid of 8x4x4 was used to sample the reciprocal space for a single unit cell. The lowest energy structural configuration was found by a relaxation of all atomic positions and parameters, using the Generalized Gradient Approximation method.

### 8.3.3 Powder X-ray Diffraction

Powder X-ray diffraction data for the as-synthesized powders were collected on a PANalytical diffractometer using Cu Kα radiation from $2\theta = 10°$ to $80°$. A Rietveld refinement was kindly performed by Prof. Y. Mozharivskyj in order to assess relative sodium site occupation in pristine $Na_2FePO_4F$ powders prepared by the solid-state method performed in house.

### 8.3.4 Synthesis of Pristine $Na_2FePO_4F$ and Variations

A two step solid-state synthetic route initially proposed by Kosova *et al.*[5] was employed here to prepare pristine carbon-coated $Na_2FePO_4F$ powders. Using this method, $Fe(C_2O_4)\cdot 2H_2O$, $Na_2CO_3$, and $NH_4H_2PO_4$ were initially mixed and ball milled for 1 h in acetone before annealing at 575 °C for 2 h with a pause at 350 °C for 1 h. The resulting $NaFePO_4$ powder was then ball milled with a stoichiometric quantity of NaF and 3 wt% carbon black, followed by heating to 600 °C for 4 h under flowing Ar gas.

Subsequent variations to the original synthetic method were carried out in an effort to generate more significant quantities of the proposed defect site, similar to what was done with $Na_3V_2(PO_4)_2F_3$ samples by Broux *et al.*[6] The details of these synthesis trials will be discussed in greater detail in Appendix A2.

## 8.3 Results and Discussion

### 8.3.1 Motivation

In Chapter 7 of this thesis the $^{23}$Na NMR spectrum of $Na_2FePO_4F$ was reported, where the two most significant peaks were assigned to sodium ions residing in the Na1 and Na2 crystallographic positions in the orthorhombic lattice. An additional two resonances were observed, although at that time further information regarding the origin of these peaks was not given. Here, the assignment of these sites is explored *via* a range of experimental and theoretical methods to identify defect formation and impurities in $Na_2FePO_4F$ samples prepared by a high-temperature route.

The first evidence for any unexpected structural features was observed in the $^{23}$Na MAS spectrum of as-prepared $Na_2FePO_4F$. The result is shown in a deconvolution of the 1D NMR spectrum in **Figure 8.1**, where the as-yet unidentified peaks are highlighted in red and blue. These two peaks at -127 and -230 ppm are not insignificant, although they are small in relative intensity to the pristine sites (accounting for 8% and 2% of the total signal respectively). Furthermore, their large chemical shifts far exceed the typical range for a diamagnetic compound, implying that the Na atoms reside in a paramagnetic phase similar to the pristine material.

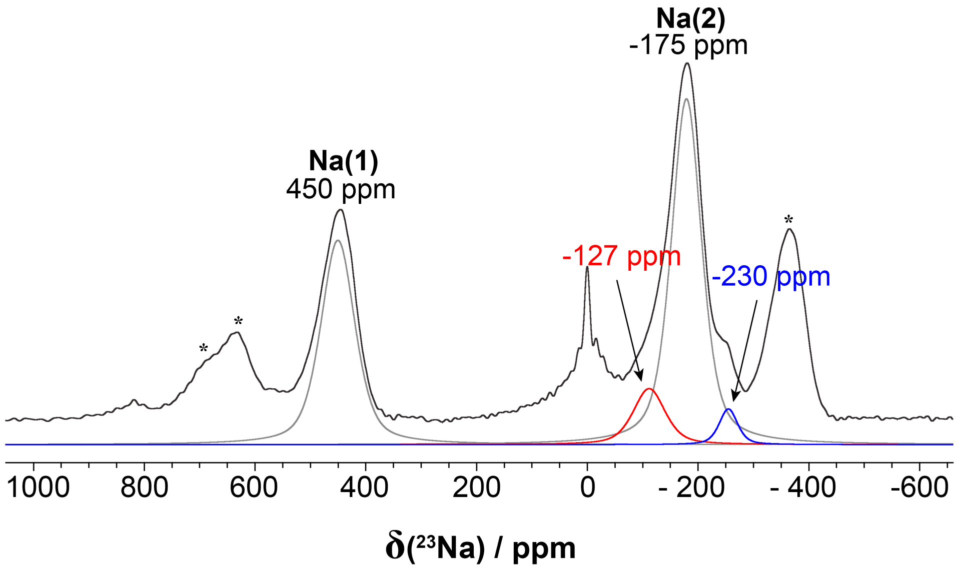

**Figure 8.1:** $^{23}$Na MAS solid-state NMR spectrum of $Na_2FePO_4F$ prepared in house by the reported high temperature method. The dominating chemical shifts corresponding the the pristine phase are shown in grey, while the two ‘unidentified’ peaks of interest at -127 and -230 ppm are depicted in red and blue respectively. Spinning-sidebands are indicated by *.

As discussed in Chapter 6, the unidentified resonances are not thought to be involved in the electrochemical process, owing to their unchanging chemical shift and relative intensity as a function of electrochemical cycling. This could result from a lack of a redox-activity of the paramagnetic transition metal over the voltage window studied due to the distortion of the structure or Fe oxidation state. This lack of electrochemical activity made it possible to accurately study the pristine material without taking into consideration effects from these unidentified peaks. However, although not directly electrochemically active, any additional sodium ions or structural components not participating in the redox process are effectively dead weight in the context of a commercial battery, and thus can ultimately reduce the material's performance.

Within this chapter three possibilities are explored that account for the anomalies in the experimental $^{23}$Na MAS spectrum of $Na_2FePO_4F$ synthesized by a high-temperature solid-state route, with an emphasis on separating impurity phases from inherent structural defects. Two types of impurities, both Na-containing and Na-free, are investigated by powder X-ray diffraction, density functional theory calculations, solid-state NMR, and Mössbauer spectroscopy. The proposal of defect formation involving increased oxygen content to generate $Na_2FePO_4F_yO_{1-y}$ will then be discussed in detail and compared to a vanadium fluorophosphate material known to exhibit similar behaviour.[6,7]

### 8.3.1 Identifying and Removing Na-Containing Impurities Synthetically

Of the two additional peaks in the NMR spectrum depicted in Figure 8.1, the lower frequency resonance at -230 ppm (blue peak in **Figure 8.1**) turns out to be more easily identified. A closer look at the powder X-ray diffraction pattern reveals a series of small reflections that do not correspond to the desired phase, $Na_2FePO_4F$, but rather a similar sodium iron phosphate of the form $NaFePO_4$. Unlike the popular $LiFePO_4$ counterpart, sodium iron phosphate demonstrates poor electrochemical behaviour relative to the fluorophosphates.[5] The theoretical Fermi contact shifts for Na ions in $NaFePO_4$ were calculated by DFT as implemented in VASP, with the goal of assigning at least one of the two unknown peaks to this phase. The Fermi contact shift for Na ions in the single Na environment in $NaFePO_4$ is predicted by DFT to be -226 ppm, in near perfect agreement with the experimentally observed resonance at -230 ppm. This site is therefore attributable to a $NaFePO_4$ impurity resulting from the synthetic process.

Upon assignment of this peak to a known impurity phase, its removal was successfully accomplished by using a massive excess of NaF in the solid-state synthesis (~200%) followed by a washing procedure to remove the sodium fluoride. This method appears to remove the anomalous peak in the $^{23}$Na NMR spectrum at -230 ppm. The synthetic procedure used to produce $Na_2FePO_4F$ was originally reported by Kosova *et al.*, and follows a two-step approach wherein $NaFePO_4$ is originally generated, and subsequently reacted with NaF at high temperatures to yield the desired phase via the reaction equations below.

$$\mathrm{Na_2CO_3 + 2FeC_2O_4 \cdot 2H_2O + 2(NH_4)_2HPO_4 \rightarrow \mathbf{2NaFePO_4} + 4NH_3 + 3CO_2 + 2CO + 7H_2O} \tag{8.1}$$

$$\mathrm{NaFePO_4 + NaF \rightarrow \mathbf{Na_2FePO_4F}} \tag{8.2}$$

The use of a stoichiometric quantity of NaF in the above reaction is insufficient due to loss of the lightweight starting material during the second high-temperature annealing stage, resulting in incomplete conversion of $NaFePO_4$ to $Na_2FePO_4F$ as per Equation 8.2. By adding an excess of NaF, even after the inevitable loss of some of this starting material the reaction can still proceed to completion. This step successfully removes all evidence of $NaFePO_4$ from the $^{23}$Na NMR and PXRD measurements. Additional spectra and diffraction patterns are provided in Appendix A2 to demonstrate this.

### 8.3.2 Sodium-Free Impurities in $Na_2FePO_4F$ Powders

While the removal of $NaFePO_4$ impurity eradicates one of the two unassigned resonances in the NMR spectrum, it does nothing to remove the lower frequency site at -127 ppm (red peak in **Figure 8.1**), implying that the second site is not related to the aforementioned Na-containing impurity phase. In addition to sodium-containing impurities due to incomplete reaction of NaF and $NaFePO_4$ starting materials, a sodium-free defect identified as $Fe_2O_3$ is also observed. Mössbauer spectroscopy performed on synthesized $Na_2FePO_4F$ powders revealed the presence of $Fe_2O_3$ particles via observation of a small quantity of a magnetic component identified by the sextuplet in the Mössbauer spectrum provided in **Figure 8.2**. This is consistent with the qualitative observation of a minimal amount of red powder in addition to the dark grey bulk material after the final high-temperature step in a typical synthesis of this phase. A closer look at the powder X-ray diffraction pattern reveals a single small reflection at a 2θ angle of 35° initially not identified due to overlap with the parent phase. This reflection is in close agreement with

$\gamma$-$Fe_2O_3$ present in the sample. The significant overlap of most of the reflections associated with this phase and the desired $Na_2FePO_4F$ phase make identification by diffraction alone difficult (see **Figure 8.2**). Fortunately, Mössbauer is able to quantify this impurity, finding it to comprise ~10 mol% of the Fe in the sample. Further details regarding the Mössbauer experiments and results are provided below in Section 8.3.3.1.

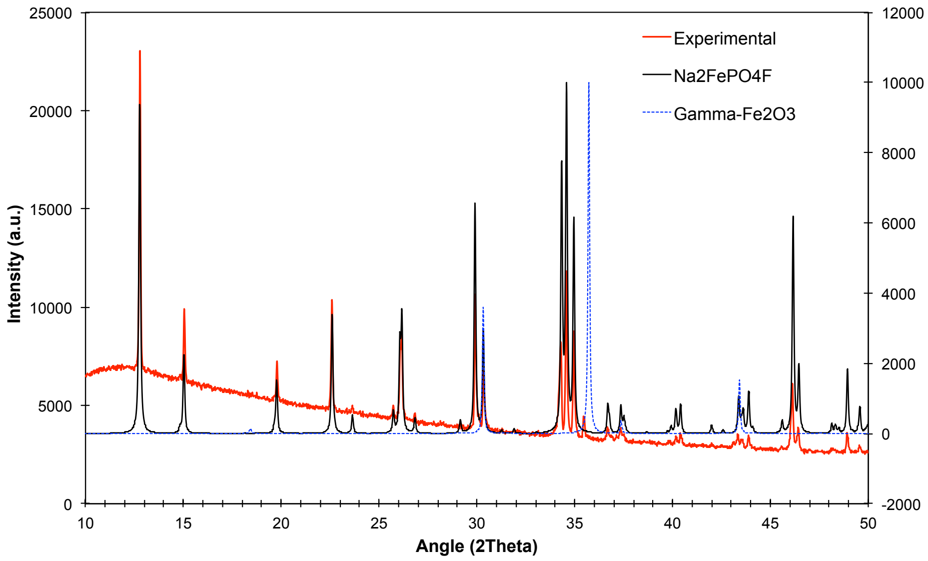

**Figure 8.2:** PXRD pattern of $Na_2FePO_4F$ synthesized by a high-temperature solid-state route with excess NaF. Data was acquired over the course of 13 h. The experimental pattern (red) is compared to the theoretical powder pattern for $Na_2FePO_4F$ (black) and $\gamma$-$Fe_2O_3$ (blue).

The identification of an iron oxide impurity does not, however, account for the remaining Na peak in the NMR spectrum not assigned to either of the crystallographic positions in pristine $Na_2FePO_4F$. No other evidence of an impurity phase by diffraction suggests additional crystalline Na-containing phases. This could indicate that this peak results from Na ions in the same phase as the parent structure, perhaps chemically shifted in the NMR spectrum due to a structural defect inducing a change in the Fermi contact interaction at this site.

### 8.3.3 Identification of O-defects in $Na_2FePO_4F$

Other examples of sodium metal fluorophosphates have been reported in literature; one of which, $Na_3V_2(PO_4)_2F_3$ (NVPF), is among the most widely studied cathode materials in the field of sodium ion batteries due to its superior electrochemical performance. After many conflicting reports regarding the exact structure of this phase,[8-10] specifically relating to unit cell volumes and electrochemical features, Bianchini *et al.*[7] found that the changing F/O ratio with disparity in synthesis conditions was likely the origin of the discrepancies in literature. This defect type appears when oxygen atoms occupy the fluorine sites in the fluorophosphates, effectively converting some of what should be $VO_4F_2$ octahedra into $VO_5F$, and changing the oxidation state of the vanadium from $V^{3+}$ to $V^{4+}$ to accommodate additional $O^{2-}$ into the structure. As exact reaction temperatures and exposure to oxygen or vanadium impurities are likely to be highly variable across research groups, the relative amount of this defect concurrently varies, creating inconsistencies in structural determination of NVPF. Such a discrepancy has not yet been reported for $Na_2FePO_4F$, although this phase has received considerably less attention in the battery community and therefore has not been studied in depth by many unique research groups. The remainder of this chapter aims to explore the possibility for formation of this type of defect in the iron fluorophosphates.

#### *8.3.3.1 Identification of Fe$^{III}$ Species by Mössbauer Spectroscopy*

Mössbauer spectroscopy is an excellent method for determination of the chemical environment around a nucleus as it is sensitive to properties such as valence state, spin state, and magnetic moment.[11] For iron-containing compounds it is possible to perform $^{57}$Fe Mössbauer spectroscopy, where the spectrum is simply the gamma-ray absorption of Fe atoms in the sample versus energy (expressed in units of mm/s). The electrons around the Fe nucleus perturb the nuclear state energies, resulting in a resonant frequency that is defined by the difference in energies between the ground and excited states of the nucleus. Three types of interactions are typically considered in a Mössbauer spectrum, the isomer shift (IS), quadrupole shift (QS) and hyperfine magnetic shift (HMS). The isomer shift provides information regarding the electron density at the nucleus, and can differentiate between valence states of the atom due to differences in screening effects of the nucleus with different d-electron configurations. For example, $Fe^{2+}$ ($d^6$) has a greater number of d-electrons, and thus the nucleus will be better screened from the 4s electrons compared to an $Fe^{3+}$ ($d^5$) ion. IS values for $Fe^{3+}$ nuclei are consequently smaller relative to $Fe^{2+}$ due to decreased screening effects. A comparison of isomer shifts is therefore an excellent way to determine oxidation states in unknown Fe-containing phases.

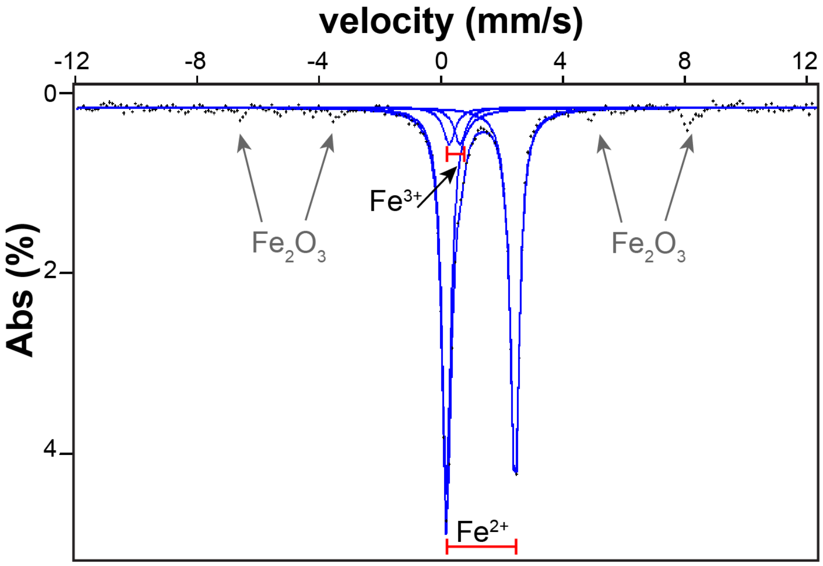

**Figure 8.3:** Mössbauer results for one of the synthesized $Na_2FePO_4F$ powders prepared in house. The two main components are fit with the solid blue lines, where Fe(III) and Fe(II) components each exhibit different splitting, thus allowing them to be distinguished by this method. Small peaks in the baseline are part of the sextuplet resulting from an $Fe_2O_3$ impurity in the sample.

In addition to the isomer shift, the presence of an electric field gradient, or a non-spherical charge distribution about the nucleus, splits the excited state energy levels in the case of $^{57}$Fe (excited state spin $I = \frac{3}{2}$) into two non-degenerate energy levels. In contrast, the ground state energy levels ($I = \frac{1}{2}$) are not split, resulting in two possible transitions between ground and excited states ($\pm\frac{1}{2} \rightarrow \pm\frac{1}{2}$, $\pm\frac{1}{2} \rightarrow \pm\frac{3}{2}$), yielding a splitting of the resonance energies as observed in **Figure 8.3**. Even further splitting of energy levels can occur in samples with magnetic properties, where the energies of the nuclear transitions are split by the magnetic field at the nucleus. This hyperfine magnetic field generated by the sample removes the degeneracies of all the spin states, yielding unique transitions between all possible energy levels in the Mössbauer spectrum typically observed as a sextuplet (specifically for $^{57}Fe$).

The proposed defect necessitates the presence of $Fe^{3+}$ regions in the pristine $Na_2FePO_4F$ structure due to excess $O^{2-}$ in the lattice as in the absence of any defect or impurity all iron is expected to be high-spin $Fe^{2+}$ as per Ellis *et al.*[12,13] Mössbauer was used in an effort to identify and quantify any $Fe^{3+}$ species in a sample of as-prepared $Na_2FePO_4F$. As indicated in **Figure 8.3**, two isomer shifts with distinct quadrupole splitting parameters are observed experimentally, confirming the presence of a small amount of high-spin $Fe^{3+}$ in the sample. Moreover, a weak sextuplet resulting from significant hyperfine splitting of the nuclear energy levels is observed, thus indicating Fe in a magnetic environment, specifically $Fe_2O_3$ as discussed in Section 8.3.2 above. Results of the fit of the Mössbauer spectrum acquired at room temperature are summarized in **Table 8.1**, where the non-magnetic $Fe^{3+}$ accounts for 11% of the total iron in the sample. The remainder of the material is identified as $Fe^{2+}$ by the IS and QS of the dominant signal (1.23 mm/s and 2.25 mm/s respectively), and is consistent with the expected result for $Na_2FePO_4F$.[13] Interestingly, the $Fe^{3+}$ signal reported to arise from formation of $NaFe^{3+}PO_4F$ upon chemical oxidation has very similar properties to the $Fe^{3+}$ signal observed here in the pristine phase. Ellis *et al.* reported an IS of 0.43 mm/s and QS of 0.48 mm/s of the oxidized $Fe^{3+}$ phase, very similar to the 11% $Fe^{3+}$ phase present in the pristine material in this study.[13] This could imply that the $Fe^{3+}$ present in the sample is in a chemical environment very similar to the parent phase, congruous with the O-defect interpretation.

**Table 8.1:** Parameters obtained from the fit of the Mössbauer experiment at 293 K conducted on a typical synthesized $Na_2FePO_4F$ powder. Sites 1 and 2 correspond to Fe(II) and Fe(III) respectively on the basis of the splitting parameter and isomer shift.

| Site | Isomer Shift (mm/s) | Linewidth at Half-height (mm/s) | Quadrupole Splitting (mm/s) | % |
|---|---|---|---|---|
| **1 ($Fe^{2+}$)** | 1.23 | 0.36 | 2.25 | 89 |
| **2 ($Fe^{3+}$)** | 0.39 | 0.45 | 0.36 | 11 |

Low temperature Mössbauer measurements at 4.2 K were performed so as to identify whether the observed non-magnetic trivalent iron atoms exist within the same phase as the parent material, or as separate impurity phase. The results further confirm the presence of magnetic $Fe^{III}$, specifically due to $Fe_2O_3$ existing as an impurity phase mixed with the desired phase. A second, non-magnetically ordered $Fe^{3+}$ component is identified as being likely within the compound forming approximately 8% of the total iron content in the sample. This result is consistent with defect formation in pristine $Na_2FePO_4F$ that results in $Fe^{3+}$ incorporation into the structure. The low temperature Mössbauer data suggests a ratio of 78:8:13 for the $Fe^{2+}$:$Fe^{3+}$:$Fe_2O_3$ components as summarized in **Table 8.2**, indicating that the $Fe^{3+}$ associated with the defect makes up approximately 10% of the $Na_2FePO_4F$ material after accounting for the iron oxide impurity. This is very close to the 8% additional intensity in the peak at -127 ppm of the $^{23}$Na NMR spectrum shown above in **Figure 8.1**. While this does not unequivocally prove the formation of the specific oxygen defect discussed above, it substantiates the hypothesis that the additional peak in the NMR spectrum at -127 ppm is due to Na atoms in close proximity to anomalous $Fe^{3+}$ within the predominantly $Na_2Fe^{II}PO_4F$ lattice.

**Table 8.2:** Parameters obtained from the fit of the Mössbauer experiment at 4.2 K conducted on a typical synthesized $Na_2FePO_4F$ powder. Sites 1 and 2 correspond to Fe(II) and Fe(III) that exist within the majority phase, while Site 3 corresponds to magnetic $Fe_2O_3$ existing as an impurity phase.

| **Site** | **Isomer Shift (mm/s)** | **Linewidth at Half-height (mm/s)** | **Quadrupole Splitting (mm/s)** | **%** |
|---|---|---|---|---|
| **1** | 1.36 | 0.20 | 2.93 | 79 |
| **2** | 0.41 | 0.25 | 0.71 | 8 |
| **3** | 0.45 | 0.45 | N/A | 13 |

### *8.3.3.2 Powder XRD and Rietveld Refinement*

Thus far, the presence of $Fe^{III}$ in the synthesized phase has been confirmed by Mössbauer, and it is likely to coincide with the additional peak in the $^{23}Na$ NMR spectrum at -127 ppm. This does not, however, prove that the origin of the $Fe^{3+}$ atoms is due to extra oxygen atoms replacing fluorine in the lattice. The possibility for sodium deficiency such that one of the two sodium sites is preferentially depopulated resulting in oxidation of $Fe^{2+}$ to $Fe^{3+}$ must first be explored. This simple explanation would account for the additional peak in the NMR spectrum and the structural trivalent iron identified by Mössbauer. To explore this possibility, Prof. Y. Mozharivskyj carried out a refinement of the powder X-ray diffraction pattern for synthesized $Na_2FePO_4F$, where specifically the sodium occupancy in the Na1 and Na2 sites was of interest. The result of this refinement (**Figure 8.4**) reveals Na1 and Na2 site occupancies of 0.97(1) and 1.03(1) respectively, as expected based on the reported crystal structure of $Na_2FePO_4F$.[13] Even the slight variation from an ideal 1:1 ratio does not account for a 10% conversion of total Fe in the structure to $Fe^{3+}$ due to sodium deficiency in the lattice, effectively ruling out this rationalization for the NMR and Mössbauer results.

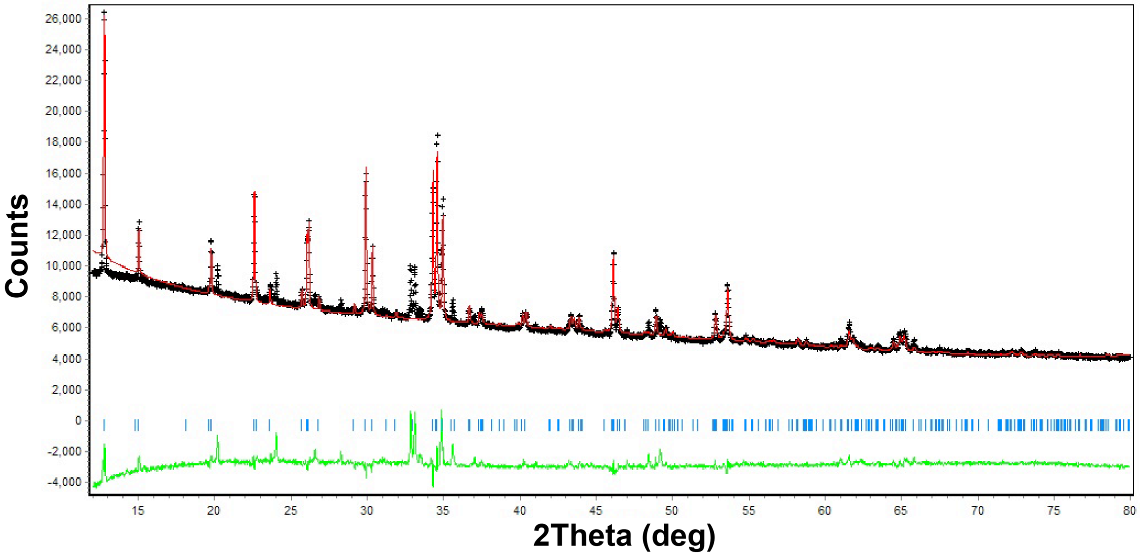

**Figure 8.4:** Powder X-ray diffraction pattern and Rietveld refinement for a synthesized $Na_2FePO_4F$ sample. The fit to the powder pattern is shown in red, with the green line plotting the difference between experiment and fit. Any discrepancies between the two come from identified $NaFePO_4$ and $Fe_2O_3$ impurities in this particular sample.

#### *8.3.3.3 $^{23}$Na Nutation NMR*

One of the major difficulties with sodium NMR in general is the effect of the quadrupole moment of the $^{23}$Na nucleus on the spectrum. Paradoxically, this can also be one of the most useful features of quadrupolar nuclei, in many cases offering rich insight into the bonding and electronic environment of the sodium nucleus.[14-16] The quadrupolar interaction has been largely ignored in the analysis of spectra presented in this thesis thus far, due primarily to the fact that the paramagnetic interaction tends to dominate the spectrum and in reality pose a much larger issue relative to the quadrupole coupling. Furthermore, the traditional second order $^{23}$Na quadrupole lineshapes are not observed for any of the paramagnetic samples investigated over the course of this thesis, and thus chemical shifts and linewidths are attributed entirely to interaction with unpaired electron spin density transferred to the Na nuclei. This is not to say, however, that the quadrupolar interaction is completely invisible; the response of the resonances to the radiofrequency pulse (referred to as nutation – see Chapter 2) follows a highly irregular pattern especially for the peaks exhibited by $Na_2FePO_4F$ despite no other obvious quadrupole-specific effects.

In most cases, such as spin-1/2 or quadrupolar nuclei in high symmetry environments, the assumption is that the magnetic field generated by the radiofrequency pulse dominates the spins response to that pulse relative to other interactions.[14-16] This assumption fails in the event of quadrupolar interactions that are on the order of MHz and therefore comparable to or larger than the radiofrequency. When quadrupole coupling is very small relative to the rf field, the nuclei will behave identically to the spin-1/2 case, following a sinusoidal dependence on pulse length. Conversely, for large quadrupole coupling constants, the interaction results in a nutation frequency that is a sine wave offset by $I + \frac{1}{2}$ where I is the spin number ($I = \frac{3}{2}$ for $^{23}$Na). The complexity arises where the rf and quadrupolar fields are intermediate, resulting in strange and irregular nutation frequencies that depend strongly on the pulse and quadrupolar coupling frequencies relative to each other.[15-17]

The complexity of the nutation curve in the intermediate regime creates difficulties in investigating samples by $^{23}$Na ssNMR, especially for broad paramagnetic samples as the additional issues of fast relaxation play a role at long pulse lengths. The first indication of abnormal nutation behaviour of the Na sites in $Na_2FePO_4F$ arises when attempting to invert the peaks, where at long pulse lengths the peak intensity can be *saturated* but not inverted (see Appendix A2 for spectra). Moreover, the different peaks in the $^{23}$Na MAS spectrum have slightly different responses to the rf field relative to each other; for instance the pulse length yielding maximum intensity differ for each site. Simply put, the nutation frequency of the three sites (Na1, Na2 and the defect site) is not uniform, and likely contains useful information regarding the specific Na environments that correspond to these three peaks. In order to probe this, a simple experiment wherein the pulse length was arrayed and compared to the observed peak area is shown by the graph in **Figure 8.5**.

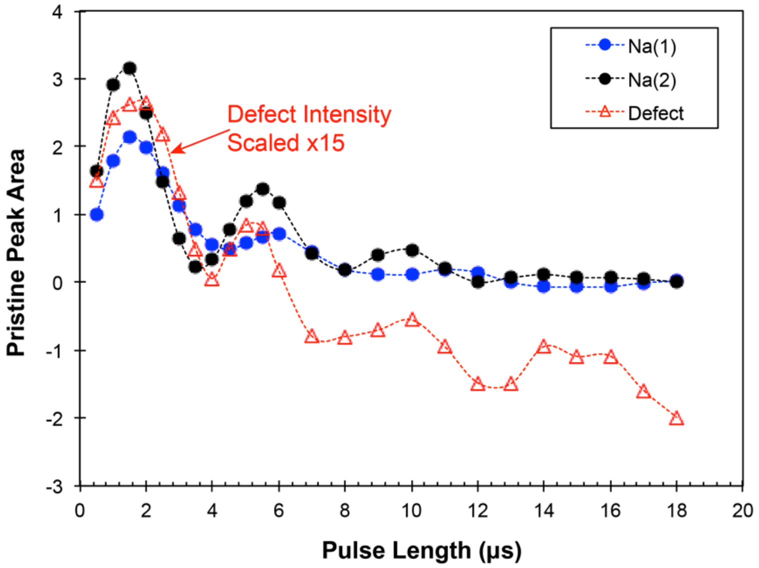

**Figure 8.5:** Plot of peak area as a function of pulse length for the Na1, Na2 and defect Na sites in a typical $^{23}$Na MAS NMR spectrum of $Na_2FePO_4F$ powder.

The difference in nutation behaviour of the three sites is attributed to slight differences in symmetry at each Na site. Although very similar, the Na1 and Na2 sites do exhibit small variations in Na-O or Na-F distances that likely contribute to small changes to the quadrupolar interaction experienced by the nuclei occupying each site. Similarly, the defect site environment is likely altered slightly due to relative Na-O distance changes. This is in good agreement with the O-defect theory, where the alteration of iron octahedra from $FeO_4F_2$ to $FeO_5F$ (see **Figure 8.6**) is bound to cause a local change of Na-O or Na-F distances nearby. For example, the average Na-O distance in a phosphate material such as $NaFePO_4$ is 2.607 Å compared to 2.473 Å in $Na_2FePO_4F$.[5,12,13] This difference, although slight, gives rise to a small change in the electric field gradient at the Na nuclei, resulting in small changes to the nutation behaviour. Although not included as part of this thesis, it would be possible to model the difference in nutation for Na atoms in different environments in an attempt to correlate the observed results to a specific Na site, allowing this nutation frequency to be compared to the proposed defect environment. Even the qualitative observation of differences implies a small local distortion of the Na site environment that could be due to a change in coordination environment consistent with partial oxygen occupancy of fluorine sites in the lattice.

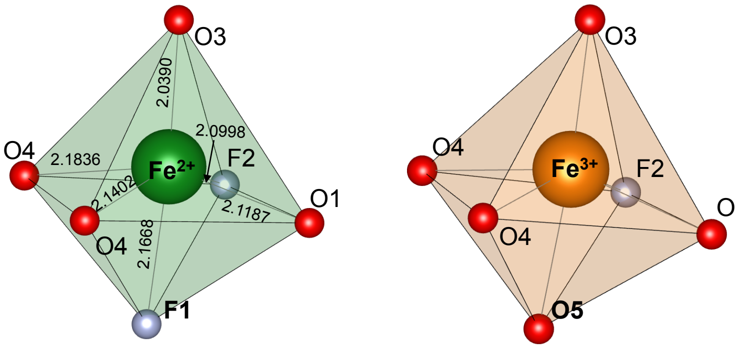

$FeO_4F_2$ $FeO_5F$

**Figure 8.6:** $FeO_xF_y$ octahedra in the pristine (green) and defect (orange) structures. The bond lengths (in Å) and labels given for $FeO_4F_2$ are based on reported unit cell information (2010 Ellis *et al.*). The $FeO_5F$ octahedron on the right is a theoretical arrangement around the $Fe^{3+}$ center.

## 8.4 Summary and Outlook

In addition to the results presented here, a compilation of other techniques used in this thesis in an attempt to synthesize and/or characterize the observed defect are provided in Appendix A2. Extensive NMR experiments including $^{31}P$ MAS spectra and exchange studies were carried out in an attempt to identify unique phosphorus environments and confirm by NMR that the defect is in close contact with the Na sites in the pristine material. Furthermore, a suite of solid-state synthesis trials was conducted in an attempt to synthesize the defect intentionally via alteration of starting materials, and annealing temperatures. Using XRD and NMR to characterize these samples, it was determined that the methods chosen preferentially generated an additional unknown phase likely separate from the $Na_2FePO_4F$ lattice. These results are provided with the intention that they can provide a starting point for the eventual confirmation of the hypothesized defect.

Although not yet fully characterized, the data presented in this chapter provide evidence for the formation of oxygen defects in the sodium iron fluorophosphate structure. The apparent existence of $Fe^{3+}$ within the $Na_2FePO_4F$ lattice by both NMR and Mössbauer in combination with the precedent for oxygen to replace F atoms in other sodium metal fluorophosphates lead to the conclusion that it is likely that this type of defect also exists in the iron-containing phases. This is important to understand from a materials perspective, as it implies that this effect must be considered in the fluorophosphate family of materials as a whole, and the impact on electrochemical cycling needs to be investigated. How the presence of this excess $Fe^{3+}$ in the structure impacts overall performance is not yet understood, and systematic studies are required to characterize first the defect, and next the ultimate impact it has on the material's cathodic properties.

## 8.5 References

(1) Smiley, D. L.; Goward, G. R. *Chem. Mater.* **2016**, *28* (21), 7645.

(2) Grey, C. P.; Cheetham, A. K.; Dobson, C. M. *J. Magn. Reson., Ser. A* **1993**, *101* (3), 299.

(3) Kresse, G.; Furthmüller, J. *Computational Materials Science* **1996**, *6* (1), 15.

(4) Kresse, G.; Joubert, D. *Physical Review B (Condensed Matter and Materials Physics)* **1999**, *59* (3), 1758.

(5) Kosova, N. V.; Podugolnikov, V. R.; Devyatkina, E. T.; Slobodyuk, A. B. *Materials Research Bulletin* **2014**, *60*, 849.

(6) Broux, T.; Bamine, T.; Fauth, F.; Simonelli, L.; Olszewski, W.; Marini, C.; Ménétrier, M.; Carlier, D.; Masquelier, C.; Croguennec, L. *Chem. Mater.* **2016**, *28* (21), 7683.

(7) Bianchini, M.; Brisset, N.; Fauth, F.; Weill, F.; Elkaim, E.; Suard, E.; Masquelier, C.; Croguennec, L. *Chem. Mater.* **2014**, *26* (14), 4238.

(8) Serras, P.; Palomares, V.; Goñi, A.; Gil de Muro, I.; Kubiak, P.; Lezama, L.; Rojo, T. *J. Mater. Chem.* **2012**, *22* (41), 22301.

(9) Le Meins, J. M.; Crosnier-Lopez, M. P.; Hemon-Ribaud, A.; Courbion, G. *J. Solid State Chem.* **1999**, *148* (2), 260.

(10) Hao, X. *Sci Sin Chim* **2012**, *42* (1), 38.

(11) Fultz, B. *Mössbauer Spectrometry*, 1st ed.; John Wiley & Sons, Inc.: Hoboken, NJ, USA, 2012; Vol. 56.

(12) Ellis, B. L.; Makahnouk, W. R. M.; Makimura, Y.; Toghill, K.; Nazar, L. F. *Nat.*

*Mater.* **2007**, *6* (10), 749.

(13) Ellis, B. L.; Makahnouk, W. R. M.; Rowan-Weetaluktuk, W. N.; Ryan, D. H.; Nazar, L. F. *Chem. Mater.* **2010**, *22* (3), 1059.

(14) Kentgens, A. P. M. *Geoderma* **1997**, *80*, 271.

(15) Duer, M. J. *Introduction to Solid-State NMR Spectroscopy*; Wiley-Blackwell, 2005.

(16) Spencer, T. L.; Goward, G. R.; Bain, A. D. *Can. J. Chem.* **2011**, *89* (7), 764.

(17) Keeler, J. *Understanding NMR Spectroscopy*; John Wiley & Sons, 2011.

# Chapter 9: Summary and Outlook

## 9.1 Summary

The importance of climate change and dependence on non-renewable energy sources to power the world has brought the research and development of alternative energy solutions to the forefront of global initiatives. One such solution poised to solve the energy storage issue that plagues renewable energy production is the alkali ion battery. This area is incredibly unique in that it brings together researchers from numerous fields such as chemistry, physics, and materials science (among others) to work toward the common goal of developing an ideal lithium or sodium ion battery. While each individual contribution may appear small, when put together the body of knowledge has already lead to the development and commercialization of battery systems that power electric vehicles, portable electronics, and energy storage stations around the world. The series of experiments, data analysis and tested hypotheses that make up this thesis contribute to this broader area of scientific discovery, primarily from a physical chemistry perspective, in an effort to better understand both the materials of interest as well as the methods that can be used to characterize materials in the future.

The work presented in this thesis has demonstrated the use of multinuclear solid-state NMR methods to study a variety of potential cathode materials for both lithium and sodium ion batteries, with a focus on polyanionic frameworks as an alternative to the layered oxide family that dominates the current battery paradigm. Through exploring an assorted range of cathode materials spanning different battery constructs (i.e. lithium *versus* sodium ion), the underlying theme to the work discussed here is the desire to understand the local environments of the mobile Li or Na ion before, during, and after, battery operation. The critical role the alkali ion plays in these systems is obvious, and yet observing its complex motion and changing surroundings is non-trivial. Solid-state nuclear magnetic resonance is one of the few methods that can afford access to such detailed and specific information, such is the nature of a technique where any single (NMR-active) nucleus can be investigated without being obfuscated by structural atoms. As demonstrated throughout this thesis, both $^{7}$Li and $^{23}$Na NMR spectroscopy accomplish this task, offering excellent environment-specific information down to the crystallographic site occupied by the alkali ion. Combined with the ability to observe various effects in very small sample sizes such as a single battery electrode, ssNMR beautifully complements long-range structural characterization techniques by contributing local information regarding both the structure and dynamics.

The initial portion of this thesis, specifically the studies of electrode materials for lithium ion batteries, examined the use of selective inversion NMR experiments to study and quantify Li-Li exchange in non-ideal cases. In this case non-ideal refers to (a) materials with slow ion dynamics, and (b) materials that have changing dynamics over the course of they're electrochemical life-cycle. The latter chapters were focused on the investigation the details of a potential sodium ion cathode material, $Na_2FePO_4F$, presenting the discovery of and justification for the mechanism of desodiation of this material as it is cycled by a combination of solid-state NMR and density functional theory calculations. Overall, this work contributes to both the field of solid-state NMR spectroscopy, pushing the limits of what is measurable by exchange spectroscopy methods in paramagnetic materials, and the fields of solid-state materials and electrochemistry, providing a detailed understanding of structure types that might be best suited to battery applications in the future.

## 9.2 Contributions and Outlook

### 9.2.1 Measuring Slow Li Ion Dynamics in $Li_2MnP_2O_7$ and $Li_2SnO_3$ by Selective Inversion NMR

In Chapter 4 the selective inversion NMR method for studying chemical exchange was applied to materials exhibiting slow Li ion dynamics that approach the relaxation limit of the experiment. In this chapter the experimental practicalities and challenges were examined for two different Li-containing materials: $Li_2SnO_3$ and $Li_2MnP_2O_7$, both of which house Li ions that exhibit slow rates of chemical exchange, but are vastly different from the perspective of the NMR experiment. This work essentially contrasts the study of chemical exchange more generally in diamagnetic versus paramagnetic materials, where the latter suffers from inherently fast nuclear relaxation rates that impose a limit on what is measurable by this technique.

The study of Li-Li exchange rates in $Li_2MnP_2O_7$ revealed that Li ion exchange, albeit slow, is confined to mobility within the Li tunnel-like layers and is unlikely to occur across distinct tunnels.[1] This diffusion pathway is rather intuitive, given that there is no open pathway through which movement from one Li tunnel to another would be favourable. Although this pathway for Li ion diffusion was discernable by NMR methods, quantification of exchange rates with minimal error was not possible due to the similarity in timescale of nuclear relaxation and chemical exchange. This demonstrated the observable limit of this technique especially as it is applied to paramagnetic materials that have, in general, faster relaxation properties. $Li_2SnO_3$ exhibited similarly slow Li-Li ion exchange rates, however, due to the lack of electron-induced relaxation effects, rate constants as low as 0.7 $s^{-1}$ were determinable by the selective inversion technique.[2] Interestingly, the ultimate diffusion pathway of Li ions through the tin-oxide lattice follows an unusual across-plane mechanism due to the existence of Li vacancies that drive diffusion along a single pathway. The results from this work demonstrate that although there are certainly intrinsic drawbacks associated with this method, even when exchange rates and relaxation time constants are comparable there is still the opportunity to identify possible exchange pathways qualitatively.

### 9.2.2 Identification of Phase Transformations and Ion Hopping Rates in $LiFeV_2O_7$ by $^7Li$ Solid-state NMR During Electrochemical Cycling

The work presented in Chapter 5 demonstrated the use of $^7Li$ solid-state NMR methods to investigate the novel Li cathode material, $LiFeV_2O_7$. In addition to new insight into the local Li environments in the lattice, selective inversion experiments were used to show that ion exchange rates (and thus Li diffusion) is dependent on the state of charge for the $Li_{1+x}FeV_2O_7$ cathodes, with compositions near x=0.5-0.6 exhibiting fast Li ion motion. Furthermore, the ion exchange rates were found to increase over the composition region, in combination with a decrease in the activation energy barrier for exchange, implying that ion exchange becomes more thermodynamically favourable as the material is lithiated. This is proposed to result from an opening of the ion diffusion pathway as the lattice expands to accommodate additional Li ions, resulting in a lower energy barrier for diffusion through the structure.

This study is the first example of a quantitative Li-Li exchange rate determination in a cathode *ex situ*. Typically ion dynamics are probed before charging or discharge whilst the material is in its most thermodynamically stable state. The work presented herein illustrates the need to consider ion mobility during charging, especially where phase changes, however subtle, can create ion exchange pathways that were previously unavailable. The obvious ongoing strategy is to correlate the NMR results to actual experimental information regarding the structure of $Li_{1+x}FeV_2O_7$ phases during cycling. Without this structural component it is impossible to make conclusions with regards to open ion exchange pathways and features that promote Li diffusion in iron vanadates. High quality X-ray and neutron diffraction studies would be extremely helpful in the elucidation of the structure, and are expected to supplement the NMR dynamics analysis well.[3] The need for additional structural insight nicely demonstrates the need for complementary characterization techniques to study solid-state cathode materials in order to derive a complete representation of these complex materials.

### 9.2.3 Structure and Dynamics Properties of $Na_2FePO_4F$ As Determined by $^{23}Na$ Solid-State NMR and *Ab Initio* Calculations

Sodium iron fluorophosphate was chosen for this investigation as one of the first examples of applying $^{23}Na$ solid-state NMR to study a cathode material for sodium ion batteries. The combination of promising electrochemical activity reported by Ellis *et al.*[4] and possibility for ion exchange experiments due to multiple Na sites in the lattice made $Na_2FePO_4F$ a highly suitable material for method testing. It was determined that the extremely fast nuclear relaxation times associated with the Na nuclei in $Na_2FePO_4F$ make quantitative Na-Na exchange rates impossible to obtain by exchange spectroscopy, where the timescale of the NMR experiment is too fast for the slow ion diffusion in this particular material. Although possible in theory, in practice the various paramagnetic Na cathode materials investigated over the course of this thesis all exhibited spin-lattice relaxation times on the order of a few milliseconds or less. Without a larger temporal range over which to probe Na-Na exchange, only very fast ion dynamics would be observable by the NMR methods discussed herein for this sample. In addition to relaxation, complications arising from the quadrupole coupling interaction of the Na ions in these materials leads to complex behaviour such as highly irregular nutation effects that can impact quantitative measurements by ssNMR. Despite these drawbacks, $^{23}$Na NMR spectroscopy has proven to be a useful tool to study site-specific changes in paramagnetic sodium cathode materials.

By cycling coin cells incorporating $Na_2FePO_4F$ as the cathode material, *ex situ* NMR experiments reveal the changing distribution of Na ions in the electrode during charge and discharge. As presented in Chapter 6, a two-phase desodiation mechanism was discovered for $Na_2FePO_4F$ electrodes, where at all intermediate states of charge both the fully reduced $Na_2FePO_4F$ and oxidized $NaFePO_4F$ phases coexist.[5] The resolution afforded by the NMR spectroscopy allowed for the observation of unique $^{23}$Na NMR peaks for each of these phases, making it possible to track their relative amount during cycling.

With the help of DFT calculations, the signals were appropriately assigned to the various Na sites in both the reduced and oxidized variants of the fluorophosphate, confirming the proposed biphasic behaviour of the material. Furthermore, formation energy calculations of intermediate $Na_{1.5}FePO_4F$ compositions corroborated this mechanism, revealing that formation of a biphasic particle is less energetically costly than a solid-solution mixture. The use of theoretical calculations were instrumental in the verification of NMR results, which can in some cases be ambiguous due to complex paramagnetic interactions giving rise to unusual NMR shifts. By combining structural insight afforded by DFT with experimental corroboration, a reliable understanding of various aspects of relevant sodium cathode materials was developed.

### 9.2.4 Investigation of Oxygen Defect Formation in $Na_2FePO_4F$

In Chapter 8 of this thesis, efforts to identify possible oxygen-induced defect formation in $Na_2FePO_4F$ were presented. Despite exhaustive experimental efforts (reported in Appendix A2), full confirmation of the proposed structural defect was not obtained. It has been shown in similar metal fluorophosphate materials that the possibility for oxygen to occupy the site of a fluorine atom results in a structural defect forcing nearby $V^{3+}$ atoms to oxidize, affording $V^{4+}$.[6,7] Thus far, evidence of oxidized Fe (from $Fe^{2+}$ in pristine $Na_2FePO_4F$ to $Fe^{3+}$) has been confirmed by Mössbauer spectroscopy, and this trivalent iron has been correlated to an addition peak in the $^{23}$Na

NMR spectrum. The chemical shift and nutation behaviour of the extraneous site in the NMR spectrum imply that there are sodium atoms in a distorted environment close to $Fe^{3+}$ centers. Additional low-temperature Mössbauer studies suggest that the extraneous $Fe^{3+}$ (and thus the extra NMR site) belong in the same phase as pristine $Na_2FePO_4F$, all consistent with the proposed defect wherein extra oxygen content occupies fluorine crystallographic positions in the lattice.

Attempts thus far to synthesize this defect in larger quantities have thus far been thwarted, despite attempts at forcing $Fe^{3+}$ into the material and controlling the F/O ratio with starting materials in the synthesis. Nevertheless, it is possible that further optimization of synthetic conditions can produce the desired defect in a controlled manner such that it can be characterized by NMR and diffraction methods to confirm the structural origin of the effect. Furthermore, the preliminary Density Functional Theory calculations provided in Appendix A2 can be improved and optimized, including the successful calculation of an O defect in a larger supercell to mitigate exaggeration of the effects on surrounding atoms. Calculation of formation energies of this defect variety relative to other possibilities would be able to determine whether or not this type of structural rearrangement is energetically feasible or identify other possibilities that correlate with the experimental results presented in Chapter 8.

Should the proposed defect be confirmed by a combination of synthetic or theoretical methods, this would be extremely interesting from an electrochemical perspective, as the role that such a defect plays in the ultimate performance of the material would need to be understood. The use of flurophosphate cathodes has been proposed in both lithium and sodium ion batteries, and the systematic formation of a defect site in these materials has not yet been reported. This discovery would shed light on a large field of materials development for alkali ion battery cathode materials, and perhaps influence new synthetic routes to materials in this class.

## 9.3 Concluding Remarks

In the preceding chapters, exchange NMR methods were applied to various materials to discover unique ion diffusion pathways in these materials, as well as track Li mobility changes *ex situ* in a novel material. Furthermore, the use of $^{23}$Na ssNMR to study sodium cathode materials is in its infancy relative to Li, and the findings summarized herein shed light on the possibilities and limitations of this method moving forward.

Observed as a whole, the work presented in this thesis demonstrates the use of solid-state NMR methods to investigate various cathode materials for both lithium and sodium ion batteries. The focus has been on observing site-specific changes of the charge-carrying ion in polyanionic cathode alternatives, by providing a combination of structural and mobility-related information. In order to improve existing batteries, a deeper chemical understanding of the process underlying the energy storage mechanism is absolutely critical, and the work presented in this thesis aims to contribute a small part to this ever-evolving field.

## 9.4 References

(1) Smiley, D. L.; Tessaro, M. Z.; He, X.; Goward, G. R. *J. Phys. Chem. C* **2015**, *119* (29), 16468.

(2) Langer, J.; Smiley, D. L.; Bain, A. D.; Goward, G. R.; Wilkening, M. *J. Phys. Chem. C* **2016**, *120* (6), 3130.

(3) Benabed, Y.; Castro, L.; Penin, N.; Darriet, J.; Dollé, M. *Chem. Mater.* **2017**, *29* (21), 9292.

(4) Ellis, B. L.; Makahnouk, W. R. M.; Rowan-Weetaluktuk, W. N.; Ryan, D. H.; Nazar, L. F. *Chem. Mater.* **2010**, *22* (3), 1059.

(5) Smiley, D. L.; Goward, G. R. *Chem. Mater.* **2016**, *28* (21), 7645.

(6) Bianchini, M.; Brisset, N.; Fauth, F.; Weill, F.; Elkaim, E.; Suard, E.; Masquelier, C.; Croguennec, L. *Chem. Mater.* **2014**, *26* (14), 4238.

(7) Broux, T.; Bamine, T.; Fauth, F.; Simonelli, L.; Olszewski, W.; Marini, C.; Ménétrier, M.; Carlier, D.; Masquelier, C.; Croguennec, L. *Chem. Mater.* **2016**, *28* (21), 7683.

# Appendix A1: Additional NMR and Ab Initio Calculations for Lithium Iron Vanadate

## A1.1 $^{7}$Li NMR of $LiFeV_2O_7$ Synthesis Trials

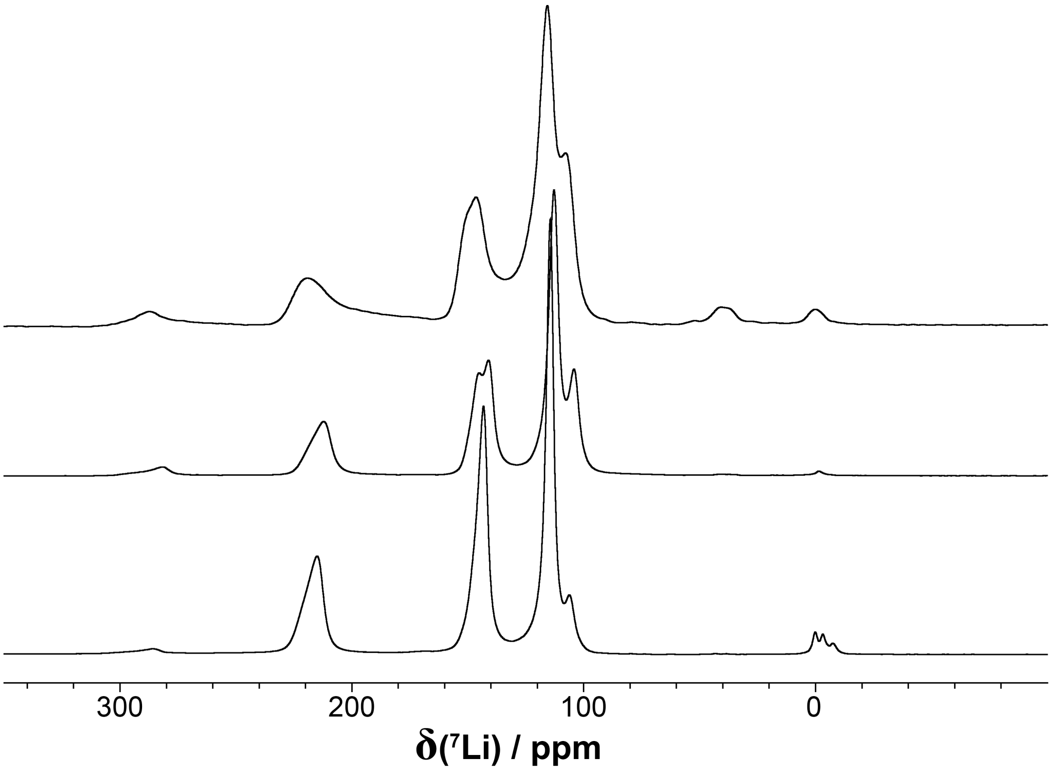

**Figure A1 - 1:** $^{7}$Li MAS NMR spectra of three $LiFeV_2O_7$ samples from different synthesis batches. Despite the same synthetic procedure, differing peak ratios are observed, implying a disorder in the Li sites that is difficult to control synthetically.

## A1.2 Ab Initio Calculations of the Fermi Contact Shifts in $LiFeV_2O_7$

Ab-initio calculations were performed using Density Functional Theory with a Generalized Gradient Approximation (GGA). The method utilizing Projector Augmented Wave (PAW) with pseudopotentials was chosen, as implemented in the Vienna Ab-initio Simulation Package (VASP). PAW-PBE potential were used within the framework of VASP. A plane wave basis set with cutoff energy of 600 eV was used for all calculations. A k-point grid of 2x4x2 was used to sample the reciprocal space for a single unit cell.

**Table A1 - 1:** Table of Calculated Fermi Contact Shifts for $LiFeV_2O_7$ based on structural data obtained by Benabed *et al.*[1]

| Site Label | Fermi Contact Shift (ppm)[a] | Experimental Shift (ppm) |
|---|---|---|
| **Li1** | 352 | 115 |
| **Li2** | 496 | 143 |
| **Li3** | 308 | 115 |

[a]Calculation used theoretical values of the curie constant (C=5.92) for $Fe^{3+}$ with Θ=0 K.

**Table A1 - 2:** Table of Calculated Fermi Contact Shifts for a proposed $Li_{1.5}FeV_2O_7$ structural model. Structural model was obtained from Y. Benabed based on the electrochemical curve. Clearly, the number of expected Li sites does not coincide with the observed NMR spectrum.

| Site Label | Fermi Contact Shift (ppm)[a] | Fermi Contact Shift (ppm)[b] |
|---|---|---|
| **Li1** | -20 | -102 |
| **Li2** | -16 | -77 |
| **Li3** | -94.4 | -460 |
| **Li4** | 26 | 128 |
| **Li5** | 325 | 1585 |
| **Li6** | 121 | 587 |
| **Li7** | -608 | -2965 |
| **Li8** | -52 | -255 |
| **Li9** | -435 | -2121 |

[a]Calculation used magnetic susceptibility information from $LiFeP_2O_7$, [b]Calculation used estimated magnetic susceptibility information from Y. Benabed

## A1.3 Vanadium Reduction during Electrochemical Cycling

To further complicate the electrochemical cycling of $LiFeV_2O_7$, vanadium reduction is believed to play an important role in the discharge/charge cycle, likely accounting for the additional capacity corresponding to the insertion of an extra 0.1 Li observed by the

Dollé group. Although not yet confirmed by synchrotron XRD measurements, the sudden appearance of narrow peaks in the $^7$Li NMR *ex situ* spectra could be due in part to the onset of $V^{4+} \rightarrow V^{3+}$ activity in the electrochemical redox process. The unusually narrow peaks in the middle of discharge followed by a broadening could indicate that the reduction of the $V^{4+}$ atoms is affecting the chemical shifts and peak widths at mid-charge, until the majority of the $Fe^{3+}$ is converted to $Fe^{2+}$ and the peaks are once again significantly broadened and a single final phase is obtained low potentials.

## A1.4 References

(1) Benabed, Y.; Castro, L.; Penin, N.; Darriet, J.; Dollé, M. *Chem. Mater.* **2017**, *29* (21), 9292.

# Appendix A2: Additional Attempts to Characterize Defects in $Na_2FePO_4F$

## A2.1 Assignment of $NaFePO_4$

Preparation of pristine $Na_2FePO_4F$ phases yielded in all cases the expected phase with the addition of varying amounts of $NaFePO_4$ impurity depending on the synthetic method chosen. Due to the formation of various unknown side products with the synthesis method reported by Nazar and coworkers, a two-step preparation method outlined by Kosova *et al*. was used for all active material in the electrochemical cells published in the ex situ NMR study of this phase. Despite the use of a small excess (~3-15%) of NaF in the second reaction step combining $NaFePO_4$ and NaF to generate $Na_2FePO_4F$, additional $NaFePO_4$ was found to be consistently present in small quantities in all pristine samples. This resulted in an additional signal in the Na NMR spectrum that overlaps with the Na2 chemical shift of $Na_2FePO_4F$. Upon depopulation of the Na2 site electrochemically, yet another peak in the NMR spectrum was found to be hidden underneath the larger Na2 peak. Although neither of the two additional sites in the NMR spectrum appeared to have any effect on electrochemical cycling, it is necessary to confirm the origin of the two unknown peaks so as to fully understand the structure and electrochemical behaviour of the parent phase.

The chemical shift of pure $NaFePO_4$ was established by a DFT calculation by the GGA method to be -226 ppm, almost exactly the same as one of the experimentally observed additional peaks residing at -230 ppm. This confirms that the low frequency site in the experimental spectrum does indeed correspond to an $NaFePO_4$ impurity.

This assignment was further verified by the eventual formation of a $NaFePO_4$-free phase obtained by use of a massive excess of sodium fluoride followed by a water-wash to remove unreacted NaF salt to yield a final $Na_2FePO_4F$ product devoid of $NaFePO_4$ according to powder X-ray diffraction and $^{23}$Na NMR (**Figure A2-1**). Despite a positive identification of one of the two unknown sites in the NMR spectrum, the lower frequency site at -140 ppm is still unidentified. Electrochemical cycling and subsequent NMR of the 'pure' $Na_2FePO_4F$ F phase synthesized without NFP impurity still shows the additional signal, suggesting that this additional peak is not related the known impurity.

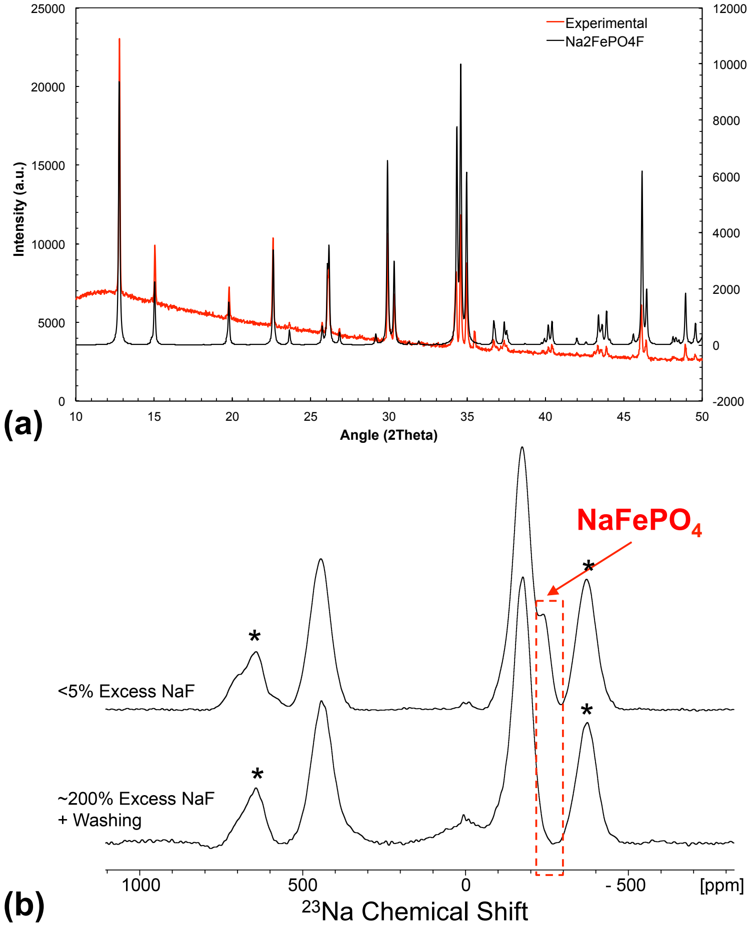

**Figure A2 - 1:(a)** PXRD pattern of prepared $Na_2FePO_4F$ compared to the theoretical powder pattern found in literature. **(b)** $^{23}Na$ MAS NMR spectra of $Na_2FePO_4F$ prepared with and without excess NaF.

## A.2.2 Attempted Synthesis of O-defect in $Na_2FePO_4F_yO_{1-y}$ Samples

All experimental results thus far are in good agreement with the oxygenation of the parent $Na_2FePO_4F$ phase (approximately 10% according to Mossbauer and NMR) where O atoms replace F atoms in the lattice resulting in oxidation of nearby Fe atoms to $Fe^{3+}$. Ideally, a concrete assignment of the existing evidence to such a structural phenomenon could be made by synthesis of the defect in varying amounts and characterization by

Mössbauer, X-ray diffraction, and NMR. This was attempted by the varying of synthesis parameters used to prepare $Na_2FePO_4F$ initially, followed by XRD and NMR analysis to observe any changes to the structure.

A series of samples were prepared as per the report by Broux *et al.* where a series of NVPF samples with varying oxygen content were generated by changing relative $Fe^{II}/Fe^{III}$ and F/O ratios in the starting materials. In this example, $FePO_4$ and $FeC_2O_4{\cdot}2H_2O$ were used as the $Fe^{3+}$ and $Fe^{2+}$ sources respectively, with NaF and $Na_2CO_3$ used to control the O:F ratio. As demonstrated in **Figure A2-2**, this did not result in the desired effect of increasing the amount of the defect-related site in the $^{23}$Na NMR spectrum. Furthermore, analysis of the XRD patterns revealed systematic formation of a new phase that likely corresponds to the congruently increasing peak near 0 ppm in the NMR spectrum of these materials. Additional alteration of other synthesis parameters such as heating time and temperature did not result in any systematic change in defect concentration either by diffraction or NMR. While it is believed that the successful synthesis of the O-rich phase is necessary for full structural characterization of the proposed defect, it has not been completed thus far.

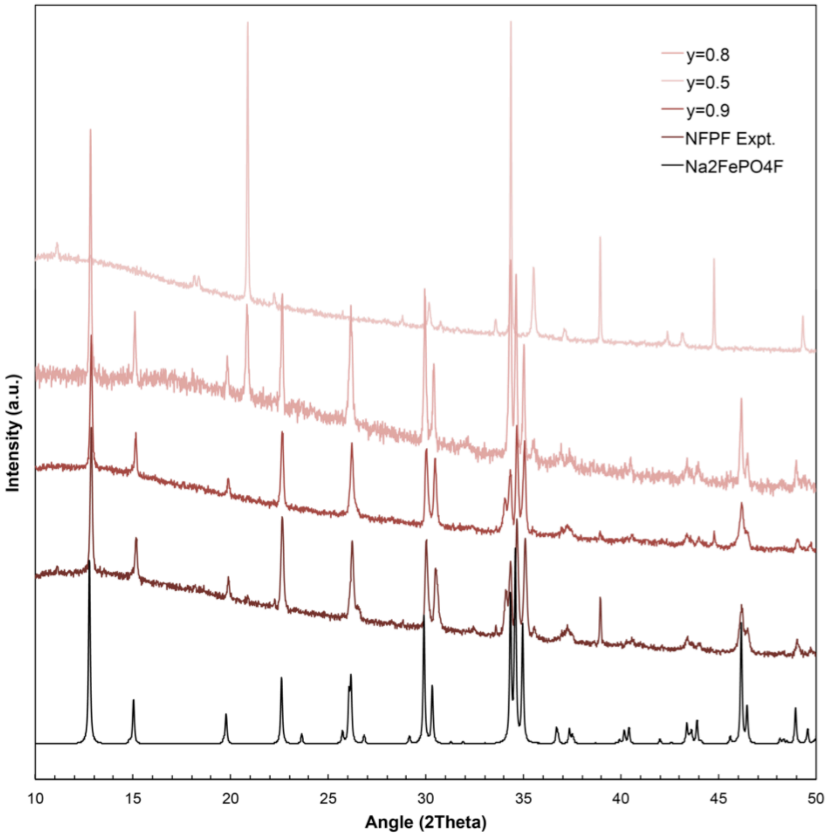

**Figure A2 - 2:** PXRD patterns of $Na_2FePO_4F_yO_{1-y}$ samples prepared with varying amounts of oxygen. Rather than a gradual change in the peaks consistent with defect formation, the appearance of a new (impurity phase) is evident.

## A2.3 DFT Calculations of O-Defect in $Na_2FePO4F_yO_{1-y}$

Density functional theory has proven very useful in aiding the analysis of experimental NMR data when it comes to $Na_2FePO_4F$. It was similarly utilized here in an effort to calculate the chemical shift expected for a Na nucleus in close proximity to the proposed defect environment and thus a near-$Fe^{3+}$ environment. The change in electron configuration of the nearby transition metal should have a massive impact on the NMR shift, a change that should be reflected in the *ab initio* calculation of the shift.

Several unexpected challenges arose upon attempts to calculate this shift, namely the large size of the unit cell. The typical unit cell for $Na_2FePO_4F$ is already close to 100 atoms, relatively large compared to similar materials. Ideally, a supercell is generated to avoid over-concentration of the defect, resulting in a significant impact of a single atom exchange on the remainder of the unit cell. Due to computational time constraints, the use of the typical unit cell rather than a supercell was used here to calculate the effect of replacement of a single F atom with O. Of the 8 available F sites to replace in the unit cell, the total energy, magnetic moment and Na shifts were calculated for four examples, the result of which is shown in **Figure A2-3**. As demonstrated there, the replacement of the F atom at the F8 position with oxygen yields the lowest energy structure with the most reasonable magnetic moment estimate. The importance of this parameter is related to the conversion of a single $Fe^{2+}$ to $Fe^{3+}$ to accommodate the additional negative charge of oxygen. The closer this value **S** is to the theoretical value (33) is indication of a calculated structure that more closely matches the expected electron configuration.

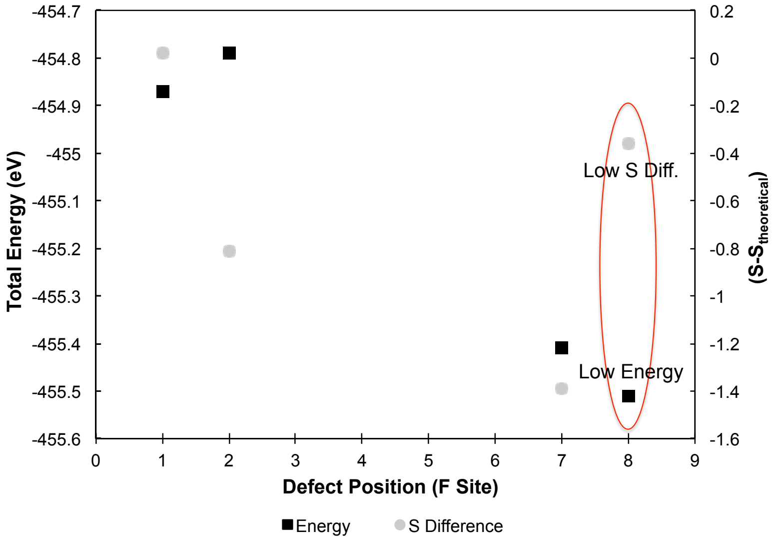

**Figure A2 - 3:** Calculated total energy and deviation from ideal magnetic moment for various $Na_2FePO_4F$ structures where one of the 8 F atoms is replaced by O. The label on the x-axis refers to the crystallographic F site that is chosen for replacement. The configuration where F8 is replaced by O yields the lowest energy structure, in combination with a realistic value for S (the total magnetic moment in the unit cell).

As the F8 defect position appears to be most favourable based on this preliminary set of calculations, the calculated Na shifts (**Table A2-1**) based on this new structure are provided below. The large number of different Na shifts resulting from this calculation is likely due to the lack of a supercell used in this case. In a relatively ‘small’ cell, changing a single Fe atom oxidation state has a large impact on each of the 16 Na atoms in the unit cell. This is clearly not reflected experimentally, where only a single additional NMR site is observed. While it is conceivable that there might be another peak existing as a shoulder in the spectrum, it isn’t likely that there are 15 additional peaks gone unnoticed in the experimental spectrum. Furthermore, the ratio of the extra peak to the pristine phase is not consistent with this, as according to the calculation each of the 16 shifts should be equally intense. Further calculations using a supercell are therefore necessary in order to calculate the expected shift for this type of defect site in $Na_2FePO_4F_yO_{1-y}$.

**Table A2 - 1:** Calculated chemical shifts for each of the 12 unique Na environments in $Na_2FePO_4F$ when one of the F atoms in the unit cell is exchanged for O.

| **Na Position** | **Calc. Shift** |
|---|---|
| Na1 | 1484 ppm |
| Na2 | 1441 ppm |
| Na3 | 1495 ppm |
| Na4 | 2700 ppm |
| Na5 | 1484 ppm |
| Na6 | 1441 ppm |
| Na7 | 1496 ppm |
| Na8 | 2700 ppm |
| Na9 | -171 ppm |
| Na10 | -64 ppm |
| Na11 | 139 ppm |
| Na12 | 726 ppm |
| Na13 | -171 ppm |
| Na14 | -64 ppm |
| Na15 | 139 ppm |
| Na16 | 726 ppm |

## A2.4 Multinuclear NMR Studies to Identify Defect

In addition to that presented in Chapter 8, additional NMR experiments were performed in an effort to identify the origin of the defect in $Na_2FePO_4F$. Phosphorus NMR was chosen as a method to do this, as it is expected that $Fe^{3+}$ in the sample will have an effect on the nearby $^{31}P$ chemical shifts. Based on calculations, the shift for phosphorus in pristine (defect-free) $Na_2FePO_4F$ should be close to 5000-6000 ppm. This is a slight underestimation, with the experimental isotropic shift found to be closer to 7000 ppm.

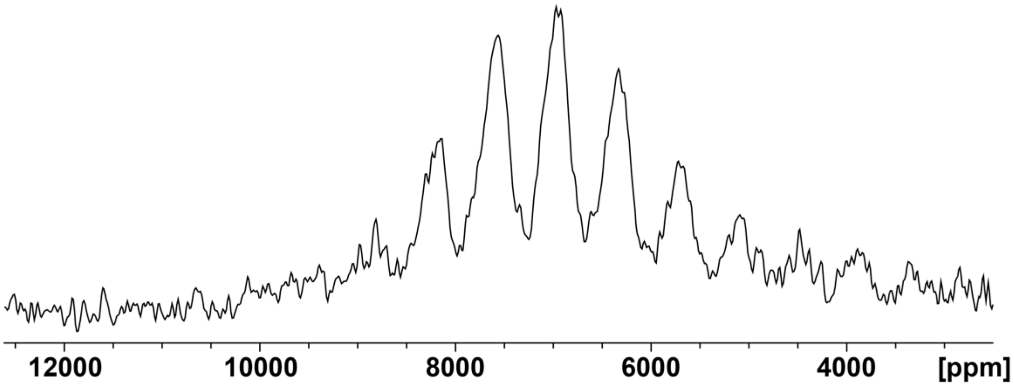

**Figure A2 - 4:** $^{31}P$ MAS spectrum of synthesized $Na_2FePO_4F$ on a 2.35 T Bruker spectrometer using a probe housing rotors of 2.5mm diameter. A Hahn echo experiment was used with 90° pulse lengths of 1.05 μs and a recycle delay of 1s.

Despite observation of the isotropic resonance, the peak width is extremely broad, meaning that observation of a shoulder corresponding to 10% of the signal shifted due to nearby $Fe^{3+}$ is extremely unlikely. Although successful in the related $Na_3V_2(PO_4)_2F_3$ study, the broadening due to $Fe^{2+}$ is too significant to achieve the required resolution.

Exchange experiments, both 2D EXSY and selective inversion, were employed in the hope that chemical or magnetic exchange could be observed between the parent phase and the defect site. Likely a result of the extremely fast nuclear relaxation rates as discussed in Chapter 6, no evidence of exchange was observed. This is not entirely surprising, given that exchange between the pristine Na(1) and Na(2) sites is not observed despite them being in the same phase.

In addition to NMR, EPR was attempted in collaboration with M. Duttine at the ICMCB. Unfortunately, due to a large excess of magnetic $Fe_2O_3$ as identified by Mössbauer, any peaks due to $Fe^{2+}$ or $Fe^{3+}$ corresponding to the fluorophosphates were not observed. In order to make use of the EPR method, which in theory can distinguish between the two Fe oxidation states, a synthesis free of iron oxide impurity must be developed.

## A2.5 Nutation Behaviour of Na Sites in $Na_2FePO_4F$

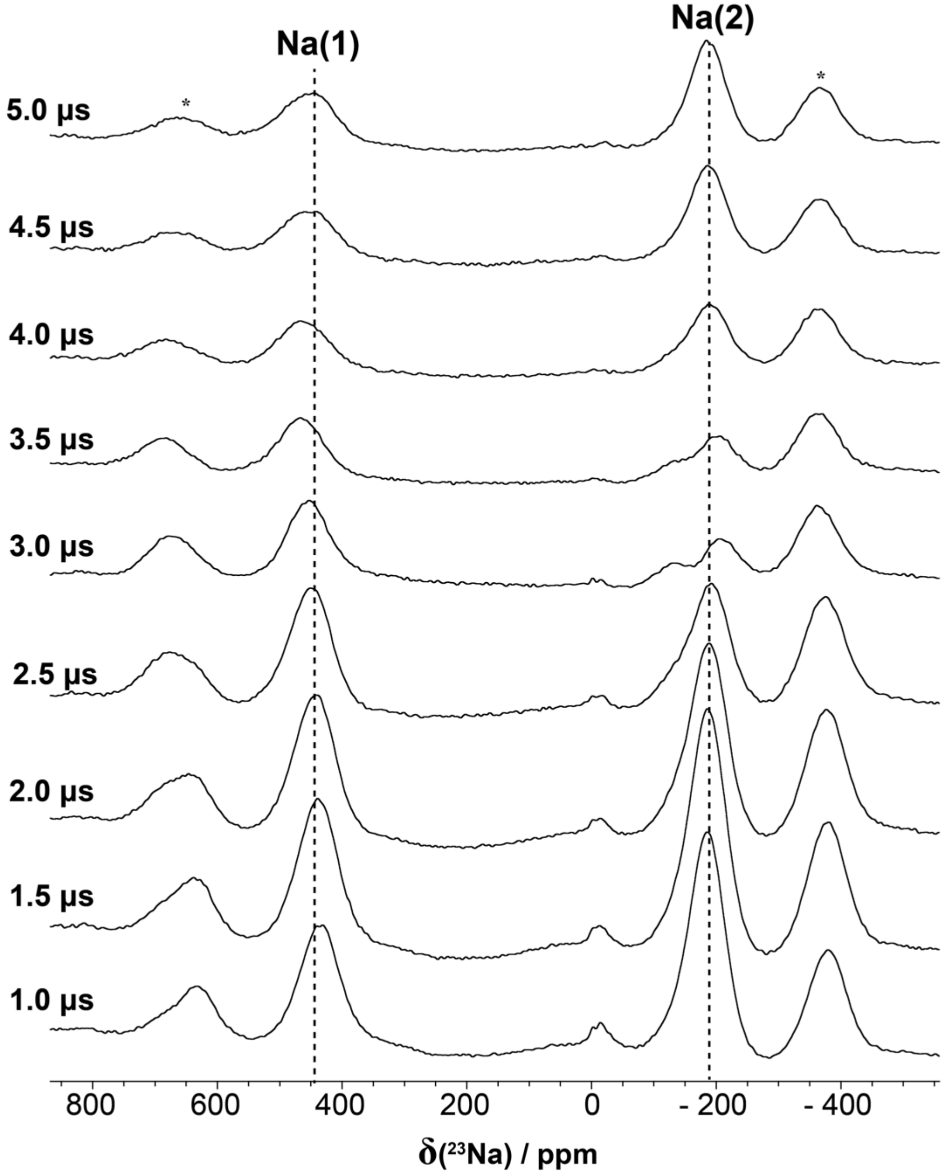

**Figure A2 - 5:** $^{23}$Na MAS NMR spectra of $Na_2FePO_4F$ prepared by a high-temperature synthesis route at different pulse lengths (shown on spectra) with the same power level. A non-sinusoidal behaviour is evident for all three sites, implying a quadrupolar coupling interaction on the order of the radiofrequency pulses.